REDUNDANCY IN LONG-SPAN BRIDGES FOR RISK MITIGATION IN A MULTI-HAZARD ENVIRONMENT

AUGUST 2022
FHWA-RC-22-0002

U.S. Department of Transportation
Federal Highway Administration

Federal Highway Administration
RESOURCE CENTER
Office of Innovation Implementation

FOREWORD

This study was part of the Federal Highway Administration Hazard Mitigation Research Program addressing bridge vulnerabilities to single or multiple hazards. The major objective of the program is developing measures, as well as analysis and design tools and methodologies, for hazard mitigation and adaptation. This report presents the results of a study on the redundancy and robustness of long-span cable-supported bridges in the event of sudden loss of single or multiple members. The bridge systems considered in this work are a tied-arch bridge, a cable-stayed bridge, and a suspension bridge.

The work in this research presents detailed information on the: (1) development of finite element models of three example bridges, (2) investigation of the bridges' behavior under sudden loss of single or multiple cables, (3) investigation of the bridges' behaviors under over-loading through pushdown analyses, (4) a new structural robustness evaluation method and a robustness index which are applicable for long-span bridges, and (5) investigation of the robustness and redundancy of the three example bridges using the proposed robustness evaluation method. The results show that: (1) the effect of single cable loss on each bridge can be captured explicitly, demonstrating the applicability of the new method, especially for long-span bridges, (2) in spite of the adverse effect of single cable loss, there was no significant reduction in the reliability and robustness of all three long-span bridges, i.e., they are very robust against single cable loss scenarios, and (3) with the successive loss of more cables, progressive collapse of the entire bridge, similar to un-zipping collapse, was triggered in the cable-stayed and suspension bridges. The tied arch bridge exhibited different behavior, because the main arch element underwent inelastic buckling after the loss of some cables.

Shay K. Burrows P.E.
Resource Center Director
Federal Highway Administration
Office of Innovation Implementation

TECHNICAL REPORT DOCUMENTATION PAGE

1. Report No. FHWA-RC-22-0002	2. Government Accession No.	3. Recipient's Catalog No.
4. Title and Subtitle Redundancy in Long-Span Bridges for Risk Mitigation in a Multi-Hazard Environment		5. Report Date May 2021 6. Performing Organization Code
7. Author(s) A.K. Agrawal (ORCID: 0000-0001-6660-2299), Sherif El-Tawil, Qian Chen and Hong-fan Wang		8. Performing Organization Report No.
9. Performing Organization Name and Address The City College of New York 160 Convent Ave, New York, NY 10031		10. Work Unit No. 11. Contract or Grant No. DTFH61-14-D-00010/693JJ318F000170
12. Sponsoring Agency Name and Address Office of Infrastructure Research and Development Federal Highway Administration 6300 Georgetown Pike McLean, VA 22101-2296		13. Type of Report and Period Covered Final Report, July 2018 – December 2020 14. Sponsoring Agency Code HRDI-20

15. Supplementary Notes
The Federal Highway Administration (FHWA) Study Manager was Waider Wong (FHWA).

16. Abstract
As a critical part of the infrastructure system, long-span bridges can be exposed to extreme conditions, such as floods, scours, and hurricanes, or severe dynamic loads, for example due to seismic shaking, blast, or impact. In spite of their importance to the resilience of adjacent communities, their redundancy and ability to mobilize alternative load paths when needed are not as well understood as for shorter span bridges. Traditional design approaches are unable to provide explicit measures of residual safety of such bridges, and the current redundancy evaluation approach suggested by the NCHRP Report 776, which was proposed based on short to medium-span bridges, is inappropriate for long-span bridges. Therefore, a new performance-based method was developed in this research to quantitatively evaluate the redundancy and robustness of long-span bridges, especially after abnormal loading events that result in member loss. Three long-span cable supported bridges (i.e., a cable-stayed bridge, a tied-arch bridge, and a suspension bridge) were selected, and detailed implicit and explicit finite element models were developed for them. The explicit models were employed to investigate the dynamic behavior of the bridges under various cable loss scenarios and critical live load distributions. The simulation results showed that only structural members in the vicinity of cable loss were primarily affected to a certain degree, while the overall performance of the bridges was affected only slightly. The progressive collapse behavior of the bridges was additionally studied by successively removing members until system failure occurred. The behavior of the bridges subjected to over loading was examined through pushdown analyses for both the intact and damaged states with single cable loss, and critical limit states were identified for each bridge. A new performance-based robustness evaluation method and a robustness index, well-suited for both short-span and long-span bridges, were presented and verified on short to medium-span bridges. Using the new method, the robustness of the three long-span bridges was quantitatively evaluated for the limit states identified through the pushdown analyses. The results showed that: (1) the effect of single cable loss on each bridge can be captured explicitly, demonstrating the applicability of the new method, especially for long-span bridges, and (2) despite the adverse effects of single cable loss, there was no significant reduction in the reliability and robustness of all three bridges, i.e., they are very robust against single cable loss scenarios.

17. Key Words redundancy, robustness, long-span cable-supported bridges, progressive collapse	18. Distribution Statement No restrictions. This document is available to the public through the National Technical Information Service, Springfield, VA 22161. http://www.ntis.gov

19. Security Classif. (of this report) Unclassified	20. Security Classif. (of this page) Unclassified	21. No. of Pages 255	22. Price N/A

Form DOT F 1700.7 (8-72) Reproduction of completed page authorized.

SI* (MODERN METRIC) CONVERSION FACTORS				
APPROXIMATE CONVERSIONS TO SI UNITS				
Symbol	**When You Know**	**Multiply By**	**To Find**	**Symbol**
		LENGTH		
in	inches	25.4	millimeters	mm
ft	feet	0.305	meters	m
yd	yards	0.914	meters	m
mi	miles	1.61	kilometers	km
		AREA		
in^2	square inches	645.2	square millimeters	mm^2
ft^2	square feet	0.093	square meters	m^2
yd^2	square yard	0.836	square meters	m^2
ac	acres	0.405	hectares	ha
mi^2	square miles	2.59	square kilometers	km^2
		VOLUME		
fl oz	fluid ounces	29.57	milliliters	mL
gal	gallons	3.785	liters	L
ft^3	cubic feet	0.028	cubic meters	m^3
yd^3	cubic yards	0.765	cubic meters	m^3
		NOTE: volumes greater than 1,000 L shall be shown in m^3		
		MASS		
oz	ounces	28.35	grams	g
lb	pounds	0.454	kilograms	kg
T	short tons (2,000 lb)	0.907	megagrams (or "metric ton")	Mg (or "t")
		TEMPERATURE (exact degrees)		
°F	Fahrenheit	5 (F-32)/9 or (F-32)/1.8	Celsius	°C
		ILLUMINATION		
fc	foot-candles	10.76	lux	lx
fl	foot-Lamberts	3.426	candela/m^2	cd/m^2
		FORCE and PRESSURE or STRESS		
lbf	poundforce	4.45	newtons	N
lbf/in^2	poundforce per square inch	6.89	kilopascals	kPa
APPROXIMATE CONVERSIONS FROM SI UNITS				
Symbol	**When You Know**	**Multiply By**	**To Find**	**Symbol**
		LENGTH		
mm	millimeters	0.039	inches	in
m	meters	3.28	feet	ft
m	meters	1.09	yards	yd
km	kilometers	0.621	miles	mi
		AREA		
mm^2	square millimeters	0.0016	square inches	in^2
m^2	square meters	10.764	square feet	ft^2
m^2	square meters	1.195	square yards	yd^2
ha	hectares	2.47	acres	ac
km^2	square kilometers	0.386	square miles	mi^2
		VOLUME		
mL	milliliters	0.034	fluid ounces	fl oz
L	liters	0.264	gallons	gal
m^3	cubic meters	35.314	cubic feet	ft^3
m^3	cubic meters	1.307	cubic yards	yd^3
		MASS		
g	grams	0.035	ounces	oz
kg	kilograms	2.202	pounds	lb
Mg (or "t")	megagrams (or "metric ton")	1.103	short tons (2,000 lb)	T
		TEMPERATURE (exact degrees)		
°C	Celsius	1.8C+32	Fahrenheit	°F
		ILLUMINATION		
lx	lux	0.0929	foot-candles	fc
cd/m^2	candela/m2	0.2919	foot-Lamberts	fl
		FORCE and PRESSURE or STRESS		
N	newtons	2.225	poundforce	lbf
kPa	kilopascals	0.145	poundforce per square inch	lbf/in^2

*SI is the symbol for International System of Units. Appropriate rounding should be made to comply with Section 4 of ASTM E380.
(Revised March 2003)

TABLE OF CONTENTS

LIST OF FIGURES

LIST OF TABLES

CHAPTER 1. INTRODUCTION

BACKGROUND

Based on the 2020 National Bridge Inventory database, there are currently 818 highway bridges in the United States with a maximum span longer than 122 m (400 feet). Although they account only for 0.132% of the total 618,458 highway bridges, they are crucial links in the current transportation network and essential to the daily operation of cities, especially large metropolitan areas. For example, the George Washington Bridge connecting Manhattan (New York City) with Fort Lee (New Jersey) carried 275,000 ~ 300,000 vehicles per day in 2016 (Rodrigue, 2020).

Because of numerous advantages such as high structural efficiency, cables have been widely adopted in these long-span bridges, such as hangers in arch bridges, stay cables in cable-stayed bridges and suspenders in suspension bridges. Of the 818 highways bridges mentioned above, there are 109 arch-through bridges, 58 cable-stayed bridges and 70 suspension bridges. However, as key structural components for the bridges, cables are especially vulnerable to damage, even failure, due to various reasons, such as corrosion (e.g., Nanfang'ao Bridge, (TTSB 2020)), fatigue, combination of corrosion and fatigue, fire (e.g., Rio-Antirrio Bridge and Mezcala Bridge (Zoli and Steinhouse 2007)), explosion, vehicle or vessel impact (Qingzhou Bridge (Zoli and Steinhouse 2007)), improper design (e.g., Kutai Kartanegara Bridge (Kawai et al. 2014)), etc. For the bridges subjected to such cable damage or failure, their continued stability and performance can be broadly attributed to "redundancy". However, the redundancy of these long-span cable supported bridges, especially after cable loss, is not yet well understood. Many long-span cable-supported bridges with cable failures have survived without collapse, whereas some bridges have collapsed when cables were locally damaged. Therefore, there is an urgent need for a methodology that can quantitatively evaluate the redundancy of these types of bridge.

Progressive Collapse of Structures

Long span bridges are a critical part of the infrastructure system that enables the necessary functions of society. These bridges could be subjected to extreme events during their service life, such as fire, blast, vehicular or vessel impacts, hurricanes, etc. These events can cause local damage to the structural system, which may progress into a partial or total failure of the entire bridge structural system, even collapse. A notable characteristic of the failure of many large structural systems is that the outcome is disproportionate to the initiating local damage. This type of structural response is termed "progressive collapse".

As a critical structural engineering issue, progressive collapse was first identified during the collapse of the Ronan Point Tower (London, 1968). After that, many more similar collapses have been observed, such as Capitan Arenas (Barcelona, 1972), Skyline Plaza (Virginia, 1973), the roof of Hartford Civic Center (Connecticut, 1978), Alfred P. Murrah Federal Building (Oklahoma, 1995), the Sampoong Department Store (Seoul, 1995), World Trade Center Towers (New York, 2001), the roof of Transvaal Water Park (Moscow, 2004), and the Achimota Melcom Shopping Centre (Acra, 2012). Based on investigations of these collapses and assessments and mitigation of their initiating events, several definitions of progressive collapse were proposed in the literatures (Allen and Schriever 1972; Gross and McGuire 1983; GSA 2003; ASCE/SEI 7-10; Ellingwood et al. 2007; Kokot and Solomo 2012). However, one of the most widely accepted definitions of progressive collapse in the engineering profession was proposed by Ellingwood (2006): "A progressive collapse initiates as a result of local structural damage and develops, in a chain reaction mechanism, into a failure that is disproportionate to the initiating local damage." The local damage can be initiated by events such as extreme hazards, design or construction error, overloads, etc.

Following the collapse of the Ronan Point Tower (London, 1968), the risk of progressive collapse has been included in building codes and design recommendations in many counties, such as the United Kingdom, Canada, Denmark, and France. The collapses of Alfred P. Murrah Federal Building (Oklahoma, 1995) and World Trade Center Towers (New York, 2001) due to terrorist attacks caused significant concerns among the general public in the United States and highlighted the need to develop new guidelines against progressive collapse. Accordingly, new standards and recommendations for buildings have been proposed to protect against progressive collapse in the United States (GSA 2003; DOD 2009). Adam et al. (2018) summarized four widely recognized design approaches against progressive collapse in current design codes: (1) tie force prescriptive rules, (2) alternate load path (ALP) method, (3) key element design methods, and (4) risk-based methods.

Progressive Collapse of Bridges

Currently, the existing guidelines that address progressive collapse (e.g., GSA 2003; DOD 2009) were developed exclusively for buildings. There has not been any parallel development in design guidelines or provisions against progressive collapse for bridges. Existing guidelines for buildings may not be suitable for bridges because of the differences in the configurations of the two types of structural systems and in the nature and intensity of their permanent, live and transient loads. Bridges are also subjected to much harsher conditions than buildings because of direct exposure to adverse environmental conditions, such as flooding, scours, hurricanes, etc., and dynamic loads such as earthquakes, vehicular loads and impact. Hence, bridges, especially long-span bridges, are generally more vulnerable to collapse in the event of localized failure because they inherently have less or no redundancy and unidentified ALPs. Zoli and Steinhouse (2007) noted that long-span bridges are generally not designed to be resistant to progressive collapse. Due to reasons of structural efficiency, many long span bridge forms, including suspension bridges, cable-stayed bridges and truss bridges, are intrinsically non-redundant, i.e., they incorporate elements whose localized failure could precipitate progressive collapse. Some notable progressive collapses of long-span bridges are summarized in the next section.

Long-span Bridge Collapses after Local Member Damage

Tacoma Narrows Bridge

The first Tacoma Narrows Bridge was a three-span suspension bridge in Washington State and it opened to traffic in July, 1940. The main span was 853.4 m (2,800 feet) long and the total length was 1,810.2 m (5,939 feet). It was the third longest suspension bridge in the world by main span. On November 7, 1940, the bridge deck oscillated severely in an alternative twisting motion, due to the resonance from vortex shedding and aeroelastic flutter. Finally, several suspenders in the main span ruptured, triggering a progressive collapse of the entire bridge. Figure 1 shows the failure process of the bridge.

Source: Wide World/Library of Congress (LC-USZ62-46682).

Figure 1. Photo. Collapse of Tacoma Narrows Bridge.

Silver Bridge

The Silver Bridge was a three-span eyebar-chain suspension bridge built in 1928, over the Ohio River, connecting West Virginia and Ohio. The main span was 213.5 m (700 feet) long and the total length was 681.2 m. On December 15, 1967, it collapsed due to corrosion cracking and stress concentration in a local member (a defective eyebar), resulting in the loss of 46 lives and nine injuries, as shown in Figure 2. The collapse of Silver Bridge sparked national interests in the safety inspection and maintenance of bridges, resulting in the creation of the National Bridge Inspection Standards in 1971 (Hartmann and Weingroff 2021). Follow-up studies of this bridge's collapse led to further understanding of the redundancy of fracture-critical bridges.

Source: NTSB.

Figure 2. Photo. Collapse of Sliver Bridge.

Seongsu Bridge

The suspended span of the Seongsu Bridge, a Gerber-type truss bridge across the Han River in Seoul, Korea, collapsed on October 21, 1994, killing 32 people and injuring 17 (Cho et al. 2001). The suspended trusses were connected to an anchor truss by vertical hangers. This structural failure was caused by improper welding of the steel trusses of the suspension structure beneath the concrete slab roadway. Figure 3 shows a photograph of the bridge after the collapse of the suspended span.

Source: © 1994 최광모 (licensed under CC BY-SA 4.0).

Figure 3. Photo. Collapse of Seongsu Bridge.

Kutai Kartanegara Bridge

The Kutai Kartanegara Bridge was a three-span suspension bridge built in 2001, over the Mahakam River in Indonesia. The total length was 470 m, consisting of a 270 m center-span and two 100m side-spans, as shown in Figure 4(a). On November 26, 2011, the entire bridge collapsed, as shown in Figure 4(b), when workers were conducting maintenance on the bridge. At least 20 people were killed, 40 people were injured and 19 people were reported missing in the accident. Kawai et al. (2014) suggested that the collapse was triggered by the sudden failure of a suspender clamp in the center span, and the subsequent failure of other clamps led to a zipper type progressive collapse of the entire bridge.

Source: © 2011 Arief R. Randan (Ezagren).

(a) Before collapse.

Source: © 2011 Katakutu (licensed under CC BY-SA 3.0).

(b) After collapse.

Figure 4. Photo. Collapse of Kutai Kartanegara Bridge

I-35W Mississippi River Bridge

The I-35W Mississippi River Bridge was a three-span continuous steel truss bridge over the

Mississippi River in Minneapolis, Minnesota, built in 1967, as shown in Figure 5(a). The main span was 139.0 m (456 feet) long and the total length was 301.1 m (988 feet). On August 1, 2007, it collapsed, as shown in Figure 5(b), resulting in the death of 13 people and injury of 145. The subsequent investigation conducted by the National Transportation Safety Board suggested that the collapse was mainly caused by undersized gusset plates-13mm (0.5 inches) thick at joints U10 and U11, which were inadequate to support the intended load on the bridge (NTSB 2008a-d). The study also highlighted the significant role played by redundancy and alternate load paths in preventing such failures (Hao 2010).

Source: © 2006 Todd Murray (licensed under CC BY-SA 3.0).

(a) Before collapse.

Source: NTSB.

(b) After collapse.

Figure 5. Photos. Collapse of I-35W Mississippi River Bridge.

Gongguan Bridge

The Gongguan Bridge was a three-span concrete arch bridge in Fujian, China, built in 1999 and the three spans were 80 m, 100 m and 80 m long, as shown in Figure 6(a). On July 14, 2011, the partial deck of one side span collapsed due to rupture of several hangers, as shown in Figure 6(b), resulting in the loss of one driver and 22 passengers injured in a tourist bus. The investigation showed that the collapse was mainly caused by the corrosion and fatigue failure of the hanger wires, and an overloaded truck running on the bridge may have triggered the collapse.

Source: © 2013 Empa (https://www.empa.ch/web/empa/disclaimer)
(a) Before collapse.

Source: © 2013 Empa (https://www.empa.ch/web/empa/disclaimer).
(b) Bridge deck after collapse.

Figure 6. Photo. Collapse of Gongguan Bridge.

Morandi Bridge

The Morandi Bridge was a cable-stayed bridge over the river Polcevera in Genoa, Italy, as shown in Figure 7(a). It was designed in the early 1960s by the well-known Italian engineer Riccardo Morandi and was opened to traffic in 1963. It was noticeable that the bridge girder was supported by very few stays, i.e., two per span. On August 14, 2018, a 210 m (690 feet) section of the bridge collapsed during a rainstorm, as shown in Figure 7(b), resulting in 43 dead and 16 injured. Calvi et al. (2019) suggested that the collapse was caused by the loss of a stay, possibly due to fatigue problems in the tendons near the tip of tower, or by the deterioration of the connection between the stay and transverse links.

Source: © 2010 Davide Papalini (licensed under CC BY-SA 3.0).
(a) Before collapse.

Source: © 2018 Salvatore1991 (licensed under CC BY-SA 4.0).
(b) After collapse.

Figure 7. Photos. Collapse of Morandi Bridge.

Nanfang'ao Bridge

The Nanfang'ao Bridge was a steel tied-arch bridge in Yiyuan, Taiwan, as shown in Figure 8(a). It was opened to the public in 1998. The total length was 140 m (459 feet). On October 1, 2019, the bridge collapsed, killing 6 people and injuring 12. A video camera nearby captured the collapse process. It showed that a hanger snapped from its top connection with the arch first, then more hangers snapped in progression until the entire bridge collapsed, as shown in Figure 8(b).

Source: © 2013 玄史生 (licensed under CC BY-SA 3.0).
(a) Before collapse.

Source: © 2019 Military News Agency (cropped).

(b) Bridge deck after collapse.

Figure 8. Photo. Collapse of Nanfang'ao Bridge.

Although the examples above discussed bridges that collapsed, there are several examples of bridges that didn't collapse following damage to a local member.

On May 7, 1975, the main girder of the Lafayette Street Bridge over the Mississippi River in St. Paul, Minnesota was found to have a crack that originated at the lateral bracing gusset to the transverse stiffener weld area due to the lack of fusion (Fisher et al. 1977). Brittle failure of the girder in the central span occurred following the penetration of the crack through the web thickness of the girder. However, collapse of that one girder did not lead to the collapse of the entire bridge.

The Lewes, Yukon River Bridge, located approximately 32 km (20 mile) south of the City of Whitehorse in Canada and carrying the Alaska Highway, is a two-span Warren through-truss bridge. It was damaged because of impact by an over-height vehicle in 1982. The impact damaged many tension members, including a bottom chord member near the midspan, which opened by approximately 2 inches after the accident (Beauchamp et al. 1984). Significant vertical deflection and horizontal displacement at the roller support were also observed. However, the bridge survived without collapse. The bridge was restored to its fully functional condition by replacing all damaged members. Interestingly, it was observed by Beauchamp et al. (1984) that the bridge did not collapse because the floor system, acting as an equivalent bottom chord, took over most of the broken truss's dead load. Similarly, one of the web verticals near the mid-span of the East Brough's Bridge, a Pratt through-truss, in London, Ontario, Canada, was severed because of an impact by a bus in 2000 (Jelinek and Bartlett, 2002). Although the bridge was heavily damaged, it escaped complete collapse.

On January 20, 2017, a resident engineer on an active painting job noticed a fractured truss member (U19-19') in the north truss of the Delaware River Bridge, as shown in Figure 9 (FHWA 2017). The bridge continued to perform under full live load during the period when the failure occurred and when it was discovered. This is another example that shows that certain truss systems, even after the loss of a member, can still carry full traffic load.

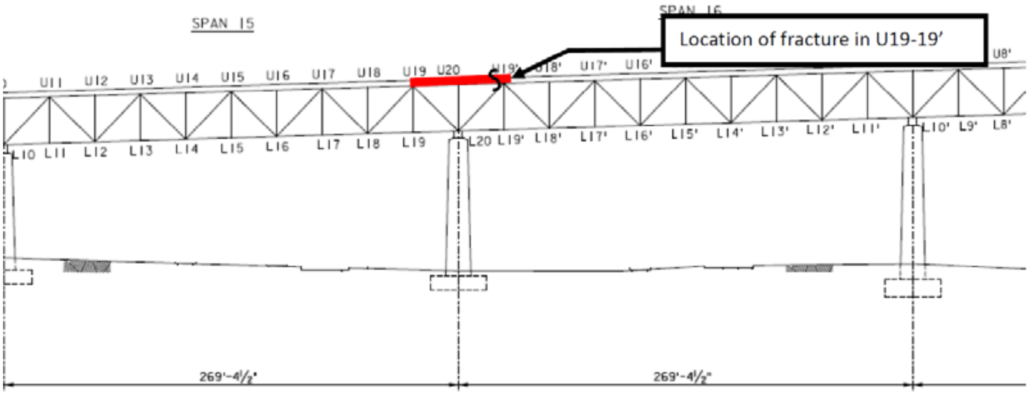

Source: FHWA.

(a) Elevation view of the truss with fractured member.

Source: FHWA.

(b) Close up photo of the fractured member.

Figure 9. Sketch and Photo. Fractured upper chord member of the Delaware River Bridge.

FHWA (2013) investigated the after-fracture performance of a two-line, simple-span truss bridge that was part of the Milton-Madison Bridge (between Milton, Kentucky and Madison, Indiana) and was slated for explosive demolition. During the testing, a built-up bottom chord member at the mid-span of the bridge was completely severed through a controlled blast test. Figure 10 shows one-half of the lower chord severed. It was observed that the total removal of the bottom chord member did not cause collapse of the bridge. In fact, the analysis presented in FHWA (2013), Diggelmann et al. (2013), and Cha et al. (2014) shows that the bridge likely could have remained functional under normal service loads even after complete loss of the bottom chord member.

Source: FHWA.

Figure 10. Photo. Blast-induced Fracture of the bottom chord member in the Old Milton-Madison Bridge on Madison, IN side.

From the study of bridges that survived local member damage, it was noted by Liu et al. (2013) that both the East Brough's and Lewes Bridges should have collapsed if the load path in these bridges was from the floor system to the panel point of the main truss, and joints were pin connections that structurally isolated the main trusses from each other and from the floor system, assumptions that are made in typical truss bridge design. In reality, there were structural features in these two bridges that facilitated ALPs to enhance their redundancy. Some of these prominent features were: (i) truss connections idealized as pinned were actually rigid joints consisting of the gusset plates with many fasteners to transfer moments, (ii) trusses that were designed to carry loads independently were interconnected by lateral and diagonal bracings, floor trusses and sway frame members, and (iii) the floor system that was assumed not to contribute to stiffness, strength, or load sharing between the trusses was rigidly connected to the trusses at the floor beams. Isolated studies have also documented the effects of these structural features on the behavior of trusses. For example, Nagavi and Aktan (2003) have shown that 3-D finite element models with rigid joints simulated more accurately the behavior of a steel through-truss bridge with riveted gusset plates, especially the inelastic response, than conventional 2-D and 3-D truss models. Floor system-truss interaction has been observed during the monitoring of a railroad through-truss bridge by DelGrego et al. (2008).

REDUNDANCY VERSUS ROBUSTNESS

The examples above showed that while some bridges suffered progressive collapse when local damage occurred, others did not. The qualities used in the literature to describe the resistance to progressive collapse are typically “redundancy” and “robustness”. These terms are frequently used interchangeably even though they are not precisely the same.

A report from the ASCE Disproportionate Collapse Committee (ASCE 2020) defines redundancy as the “Availability of alternative load paths for redistribution of loads from paths that have been compromised by a hazard scenario.” Robustness is defined as “Insensitivity to initial damage. A structure is robust if an initial damage does not lead to disproportionate collapse.” The commentary in the ASCE report notes that a definition of robustness requires reference to specified design objectives and, in this case, robustness depends on both the bridge’s structural system and the location and amount of initial damage. AASHTO LRFD Bridge Design Specifications (AASHTO 2017) defines redundancy as “the quality of a bridge that enables it to perform its design function in the damaged state”. The AASHTO approach is not quite clear because it does not define the precise “quality” that is important to ensure. As written, the AASHTO definition is a hybrid between ASCE’s definitions for redundancy and robustness.

In this work, the following definitions are used for these two qualities:

- *Redundancy* is defined as the ability of a bridge’s structural system to seek an alternative load path to achieve a given level of structural performance after the occurrence of local structural damage when a specific risk materializes. Redundancy is a structural system characteristic that is dependent upon the location of damage.
- *Robustness* is a measure of a bridge’s tolerance to damage. When faced with an adverse and unforeseen event, a robust bridge will not violate its performance objectives in a manner that is disproportionate to the severity of the event.

RESEARCH MOTIVATION AND NEEDS

Long-span cable-supported bridges play a key role in the transportation infrastructure. Cables, including suspenders and hangers, are the most vulnerable structural components of these types of bridges during extreme events. The damage or failure of these slender members can cause severe problems including major or complete collapse of the bridge, as has happened in the past.

A few studies were conducted on long-span cable-supported bridges focusing on the impact of cable loss, such as Wolf and Starossek (2009 and 2010), Qiu et al. (2014), Lonetti and Pascuzzo (2014), Bi et al. (2015), Das et al. (2016), Hashemi et al. (2016), etc. However, the topic is not yet well understood, and key questions remain about how to quantify the redundancy and robustness of these types of bridges. While some NCHRP studies focused on the redundancy of bridges, e.g., NCHRP Reports 406, 458 and 776, they all addressed regular short-to-medium span highway bridges, and it is not clear if they are applicable to long-span cable-supported bridges.

In current design practice, the bridge system is considered reliable or safe under the condition that each component satisfies its strength requirement for all load cases. However, optimization of the entire bridge system to meet the member design criteria may not provide sufficient levels of redundancy at the system level to withstand an accidental single point failure or local damage resulting from intentional threats or other hazards. Because of their operational importance for economic, social, and security requirements and high repair or replacement costs, long-span bridges should have sufficient load path redundancy and the capability to survive during extraordinary events beyond the scope of conventional design criteria. In other words, these bridges should be robust and not suffer progressive collapse in the event of local structural damage or any single point failure.

This work is motivated by the identified gap in the literatures and the need to develop new methodologies to quantitatively evaluate the redundancy and robustness of long-span cable-supported bridges, especially when they are subjected to localized damage.

RESEARCH OBJECTIVES AND OUTCOME

The main objective of this research is to develop a method to quantitatively evaluate the redundancy and robustness of long-span cable-supported bridges, especially in the event of sudden loss of single or multiple members. Specific objectives of this study include,

(1) Develop an integrated framework and performance-based criteria to quantify the redundancy and robustness of three types of long-span cable-supported bridges: suspension bridges, cable-stayed bridges and suspended tied-arch bridges.

(2) Study the relationship between redundancy and robustness, system performance, and overall bridge stability and safety.

(3) Use the developed redundancy and robustness assessment methods to investigate the performance of several representative long-span bridges under localized damage.

In summary, the main outcome of this research is to propose a quantitative redundancy and robustness evaluation method for long-span cable supported bridges, especially after an abnormal event.

SUMMARY OF THE CHAPTERS OF THIS REPORT

The detailed work performed to achieve the research's objectives can be described in the chapters of this report as follows.

Chapter 1 introduces an overview of this research and the structure of the research report.

Chapter 2 summarizes past research on redundancy and robustness, including the definitions, quantitative measures and considerations in current bridge design codes.

Chapter 3 introduces the three long-span cable supported bridges selected for evaluation in this research. The bridges and their detailed finite element models are described. Both implicit and explicit models are developed for each bridge. The explicit models are developed in LS-DYNA® and verified through comparisons with the results of the implicit models, experimental data and refined analysis models.

Chapter 4 investigates the behavior of the three bridges under single hanger/cable/suspender loss scenarios. The design live load patterns are introduced, and the behavior of the intact bridges under these live load patterns is analyzed. The behavior of the bridges under sudden single hanger/suspender loss scenarios is then investigated. The collapse behavior of the bridges is further studied by successively removing members until system failure occurs.

Chapter 5 presents the behavior of bridges subjected to over loading. Pushdown analysis is conducted on the intact bridges and the corresponding damaged bridge with single hanger/cable/suspender loss. Various cable loss scenarios and live load distribution patterns are considered. Based on the results of pushdown analysis, the limit states of each bridge are identified for subsequent redundancy and robustness analyses.

Chapter 6 proposes a new performance-based robustness evaluation method and a robustness index for bridges, especially for long-span bridges, considering the shortcomings of the current approach suggested by NCHRP Reports. The new method is used to evaluate a simple example bridge-a three-span steel I-Girder bridge in the NCHRP Report 776, including the intact status and damaged conditions with various damage scenarios.

Chapter 7 investigates the robustness of the three long-span bridges using the proposed robustness evaluation method introduced in Chapter 6. First, based on the identified typical limit states in Chapter 5 and proposed generalized first-order reliability method in Chapter 6, reliability indexes of these limit states were calculated for both intact bridges and damaged bridges with single cable loss. Uncertainties such as the applied load, section properties and material properties have been considered. Then, based on the calculated reliability indexes for both intact and damaged bridges, robustness indexes of the identified limit states were calculated for each bridge.

Chapter 8 presents a summary of the work carried out in this report, key conclusions resulting from the research and some recommendations for future research.

CHAPTER 2. LITERATURE REVIEW

INTRODUCTION

This chapter discusses the literatures on bridge redundancy and robustness. First, general ideas about these two structural qualities are presented. Then, techniques for quantifying their value are discussed followed by how various codes and specifications around the world incorporate redundancy and robustness in bridge design.

DEFINITIONS OF REDUNDANCY AND ROBUSTNESS

While static indeterminacy is often used to impart a measure of structural redundancy, it has long been known that the mere presence of “more” members than necessary for structural stability is not enough to prevent collapse; each member should possess sufficient reserve capacity in the event of an accidental damage to one of the bridge members. Accidental load combinations are explicitly considered in only a relatively few domains, such as the nuclear industry (IAEA 2016). Some design codes (e.g., Eurocode 1991) account for progressive collapse prevention by providing prescriptive rules on detailing, ductility, continuity, bridging, and avoid prescribing specific events to be considered during design. In some cases, depending on the risk category, checking for the presence of adequate tie forces or alternate paths after notional removal of key member(s) is required. Examples of “threat independent” specifications can be found in the Eurocode (1991), which recommend structures to withstand abnormal events “without being damaged to an extent disproportionate to the original cause”. The alternate load path (ALP) method (GSA 2003), which specifies the extent and location of load bearing elements to be removed, is threat independent as well, but is unable to provide a measure of reserve capacity (Agrawal et al. 2020). In this context, redundancy in bridges is related to ALPs that are defined as changes in the load paths and load distribution experienced by other members in the event of loss of a critical member.

The concept of redundancy and ALP is rather more developed for buildings than bridges. The General Services Administration (GSA 2003) criteria utilize the alternate path method (APM) to prevent progressive collapse and allow the use of both linear static and non-linear dynamic analysis to identify structural members in the alternate path structure. Redundancy of a structure tends to promote an overall more robust structure and helps to ensure that ALPs are available in the case of local failure in a critical member. Additionally, redundancy in a structure generally provides multiple locations for yielding to occur. This increases the probability that the damage may be constrained. GSA (2016) upgraded the progressive collapse requirements of explicit design for loss of vertical load-bearing elements in GSA (2003) by adopting a threat-based approach and alternate path methodology (APM) in UFC 04-023-03 (DoD 2009). This method requires the structure to be able to bridge over vertical load-bearing elements that are notionally removed one at a time at specific plan and elevation locations.

A detailed framework for addressing issues related to low probability/high consequence events during progressive collapse of buildings can be found in Ellingwood (2006). This work also summarizes measures for progressive collapse risk mitigation and identifies challenges for implementing general provisions in national standards, such as ASCE Standard 7: Minimum design loads for buildings and other structures. To reduce the probability of progressive collapse, it may be necessary to design key elements in a structural system to withstand stipulated “abnormal” loads that are far more than what otherwise would be required under a normal design condition to facilitate the development of ALPs. Redundancy, as a key to prevent progressive collapse through ALPs, means there should not be any critical element whose failure would initiate a series reaction of successive loss of members that would take down the structure. For each critical element, there should be one or more redundant counterparts to take over the critical load scenario in case the critical member fails (Ellingwood and Dusenberry 2005). El-Tawil et al. (2007) investigated the progressive collapse of steel frame structures using a macromodel based simulation approach and noted that the collapsing system continually seeks ALPs to survive in the dynamic process. Their work shows that a nonlinear APM is useful for judging the ability of a system to absorb the loss of a critical member. Compared to an elastic APM analysis, inelastic APM simulation provides more resolution, shows failure progression, and provides information on the likelihood of complete versus partial collapse. Izzuddin et al. (2008) investigated the alternate path method for buildings and showed that ALPs are beneficial for improving redundancy and structural robustness in buildings.

For bridges, while load path redundancy may currently be considered in the classification of fracture critical members for design and fabrication (Lwin 2012), structural and internal redundancy considerations have not yet been codified in AASHTO LRFD Specification. However, two recent AASHTO Guide Specifications (AASHTO 2018a, b) provide prescriptive guidance on selection of members to be removed, analysis methods, evaluation of bridges for different types of analysis following a member loss, and internal redundancy evaluation of built-up members.

Codes, such as the Canadian Standards Association (CSA) CAN/CSA-S6-14 (CSA 2014), have been permitting engineers to consider redundancy through system behavior. In one of the earliest works on ALP in bridges, Sanders et al. (1975) tested the load capacity of the single-lane Hubby truss bridge over Des Moines River that was scheduled for removal by cutting its vertical member at one cross-section. The test results showed that the cutting of the member did not result in significant decrease in load carrying capacity of the bridge. Sanders et al. (1975) attributed this capability of redistribution of loads to the frame action inherent in trusses and semi-continuous nature of the deck truss. Csagoly and Jaeger (1979) analyzed failure of several bridges to support the presence of multiple load paths in bridges, where load redistribution took place after damage to a critical member. They also noted that the construction of single-load path bridges was prohibited by the 1979 Ontario Highway Bridge Design Code.

Frangopol and Curley (1987) proposed various indexes to quantify redundancy in terms of strengths of intact and damaged systems without identifying ALPs that contribute to redundancy. Sirisak (1996) investigated the structural integrity of truss bridges. They noted that the joints in these bridges may be more rigid than pinned joints, and a bridge truss, which is otherwise assumed statically determinate, may be highly indeterminate and may show significant reserve strength when loaded beyond the classical limit load determined by the limit state of a single member. If the joints are treated as rigid, the failure of a member may not lead to an immediate collapse of the bridge and ALPs may be found. In such a situation, it may be more prudent to evaluate the system strength without exclusively concentrating on component or member strength to identify ALPs. Recently, Williamson et al. (2010) investigated the safety of reinforced concrete bridges against blast loads and recommended increasing redundancy of reinforced concrete bridges by proving multiple load paths. This includes, but not limited to, decreasing spacing of longitudinal girders and stringers, decreasing deck beam spacing, etc. While local damage to the bridge deck and/or supporting bridge girders is undesirable, redundancy and ductility will often allow internal forces to redistribute when damage occurs to these components, thus allowing an ALP to be realized in order to maintain global stability.

Robustness is a relatively recent performance requirement placed on structures, in line with the evolving paradigm in engineering from “preventing trouble” to “managing trouble” (Blockley 1992). For a robust structure, the effects of an initial damage should be confined locally, i.e., the structure should be able to dynamically redistribute the existing loads plus loads caused by the damage and attain a new stable equilibrium configuration and not suffer collapse. The presence of a weak failure path through a structural system can significantly reduce its robustness.

In the literatures, several researchers have defined structural redundancy and robustness. Structural redundancy in bridges can be defined as the ability of an efficiently design bridge system that meets member design criteria to continue to carry load and redistribute the load among its remaining members after one or several critical structural members or components exceed their load carrying capacities so that collapse is avoided and some level of service is maintained (NCHRP Reports 406, 458; Frangopol and Curly 1987).

Robustness is defined as the capability of performing without failure under unexpected conditions. Thus, structural robustness could be defined as the capability of a structural system to survive extraordinary circumstances, beyond the scope of conventional design criteria (Björnsson 2010). This definition is similar to the one advanced by De et al. (1989), who suggested that structural robustness would represent the ability of a structure to survive and continue to carry some load after the removal of one or several structural components as opposed to structural redundancy, which considers the reserve strength of an overloaded structure. Other researchers have defined robustness as the ability of a structure to resist the progression of collapse following a sudden initial local damage (Starossek 2009; Starossek and Haberland 2010). While the initial definition considers the ability of a damaged structure to continue to carry some load, the alternate definition implies the ability of the system to survive the dynamic release of energy associated with an extreme damaging event such as impact or blast.

Traditionally, the term redundancy has been used to describe the ability of the system to avoid collapse, whether the initial failure is sudden due to an exceptional and unexpected loading event, is caused by a slow decay in member capacity, or is the result of member overloading. Redundancy is, however, related to robustness. Together, both characteristics define a system’s ability to survive and continue to carry load after the capacity of individual members are exceeded or after the removal of individual members or components from the system whether the removal is associated with quick release of embedded energy or due to a slow process.

QUANTITIVE MEASURES OF REDUNDANCY AND ROBUSTNESS IN PREVIOUS RESEARCH

Several definitions of redundancy and robustness have been proposed in the literature. These measures could be categorized into the following three types: deterministic, probabilistic and risk-based measures.

To assess the structural tolerance to local damage, Frangopol and Curley (1987) proposed a deterministic indicator of redundancy in terms of the reserve strength of the damaged and intact structure, as described by Equation (1).

$$R = \frac{L_{intact}}{L_{intact} - L_{damaged}} \tag{1}$$

where L_{intact} is the overall collapse load of structure without damage and $L_{damaged}$ is the overall collapse load of structure considering some damage in one or more members. In addition to that, Frangopol and Curley (1987) also proposed three redundancy factors based on reliability theory, as introduced in Equation (2),

$$R_1 = \frac{\beta_{system,\ collapse} - \beta_{weakest\ member}}{\beta_{system,\ collapse}}$$
$$R_2 = \frac{\beta_{system,\ collapse} - \beta_{system,\ first\ member}}{\beta_{system,\ collapse}} \tag{2}$$
$$R_3 = \frac{\beta_{system,\ collapse}}{\beta_{system,\ collapse} - \beta_{system,\ damaged}}$$

where R_1 is the redundancy factor with respect to the weakest member, R_2 is the redundancy factor with respect to failure of any first member, and R_3 is the redundancy factor with respect to a given damaged state of the system.

According to previous NCHRP research studies (Ghosn & Moses 1998; Liu et al. 2001; Ghosn, et al. 2014), redundancy is measured by means of three parameters related to three different limit states by both deterministic and probabilistic method, as described by Equation (3) and Equation (4).

$$R_u = \frac{LF_u}{LF_1};\ R_f = \frac{LF_f}{LF_1};\ R_d = \frac{LF_d}{LF_1}. \tag{3}$$

where LF_u, LF_f, LF_d and LF_1 are load factors related to the system ultimate limit state of the intact bridge, functionality limit state of the intact bridge, ultimate limit state of the damaged bridge, and first member failure of the intact bridge; R_u, R_f and R_d are the redundancy factors for the ultimate limit state, functionality limit state, and damaged condition.

The limit values for the redundancy factors are also introduced and calibrated by three reliability indexes though the application of serval short-to-medium span bridges, as described by Equation (4).

$$\Delta\beta_u = \beta_{ult} - \beta_{member}$$
$$\Delta\beta_f = \beta_{funct} - \beta_{member} \tag{4}$$
$$\Delta\beta_d = \beta_{damaged} - \beta_{member}$$

Lind (1995) also proposed a probabilistic measure of redundancy based on structural vulnerability by Equation (5). It measures the structural effects of an assumed damage to a system indicating its relative increased sensitivity to further damage,

$$V_d = \frac{P(R_d, S)}{P(R_0, S)} \tag{5}$$

where R_d is the resistance of the damaged system, R_0 is the resistance of the intact system, and S is the applied load. In Equation (5), $P(R, S)$ is the probability of system failure as a function of both load and system resistance.

Starossek and Haberland (2008) proposed a stiffness-based measure by comparing the determinants of system matrices for an active system of an intact versus a damaged structure, as described in Equation (6),

$$R_s = min\left(\frac{\det K_i}{\det K_0}\right) \quad (6)$$

where det K_i and det K_0 are the determinants of the stiffness matrices for the damaged and intact structures respectively.

In a related study, Starossek and Haberland (2009) also proposed another measure by a quantification of the damage progression caused by initial damage, which is introduced by Equation (7),

$$R_d = 1 - \frac{p}{p_{lim}} \quad (7)$$

where R_d is the damaged based robustness indicator, "p" is the maximum extent of additional damage resulting from the assumable initial damage "i", and p_{lim} is the acceptable damage progression.

Brett and Lu (2013) proposed a robustness index based on system sensitivity to any damage or exposure. The system sensitivity to the exposure is introduced by Equation (7), then the system robustness is evaluated by Equation (8),

$$S = \frac{\delta G}{\delta X} \quad (8)$$

where G is a global system property, X is a generic system variable against which the "abnormal exposure" may be measured. Then the robustness index R is evaluated by Equation (9) below,

$$R = \frac{1}{1+S} \quad (9)$$

Besides these methods, there are other quantitative measures, such as method based on topology in terms of member connectivity by Agrawal et al. (2006) and energy-based measures in terms of strain energy released at some specified damage vs. energy required to cause some pre-defined system failure by Xu and Ellingwood (2011). However, these redundancy or robustness evaluation measures are either proposed for short-to-medium span bridges or the proposed measures are on the conceptual level and they are too complex for long-span bridges.

CONSIDERATIONS OF REDUNDANCY AND ROBUSTNESS IN BRIDGE DESIGN CODES

Although bridge redundancy and robustness have been studied by various researchers around the world, rigorous methods for evaluation of these characteristics haven't yet found their way into bridge design or evaluation specifications.

In the current AASHTO LRFD Specification (AASHTO 2020), only the term "redundancy" is used while "robustness" is not discussed at all. Redundancy is considered by a load modifier η_R in the design equation of the strength limit state. The Specification provides a 5% penalty for non-redundant members and 5% credit for redundant members during component design. However, determination of whether a member is redundant or not is subjective and is mainly based on an engineer's judgement. In current manual for bridge evaluation, system factors φ_s have been introduced to account for redundancy in load rating.

The term "redundancy" does not appear at all in the current version of Eurocode and the term "robustness" appears only once. However, in the current revision of Eurocode (prEN 1990:2019), the requirements for robustness say that, "A structure should be designed to have an adequate level of robustness so that during its design service life it will not be damaged by adverse and unforeseen events, such as the failure or collapse of a structural member or part of a structure, to an extent disproportionate to the original cause". The robustness is treated as a property of structure and environment, including event, damage, function losses (or limit states) and consequences. The revision of Eurocode (prEN 1990:2019) to strengthen robustness requirement starts from the prescriptive rules and commonly applied engineering design methods to provide basic or upgraded levels of robustness but leaves an opening for quantitative and risk-based methods if these become more common in practice in the future. The code also provides detailed guidance on design measures to enhance structural robustness for practicing engineering, such as strategies for designing for identified accidental actions and designing for general enhanced robustness.

The Canadian code CAN/CSA-S6-14 (CSA 2014) encourages the use of redundant structures for new bridge design, but does not provide any rewards or penalties to promote their use over single load path structures. For bridge evaluation and rehabilitation, CAN/CSA-S6-14 permits a reduction of 10% to 20% in the evaluation live load factor for redundant, ductile and inspectable bridge. For long span bridge projects, various approaches have been applied to provide some level of redundancy, such as demonstrating that viable ALPs exist; demonstrating the presence of internal redundancy in a component; provision for additional structural capacity; protection of a key structural component; and demonstrating safety against progressive collapse.

The South Korean code doesn't consider redundancy and robustness explicitly, although research on related topics, such as disaster resilience of cable-stayed bridges and reliability-redundancy trade-off analysis for design aid, have been ongoing in South Korea.

The Japanese design code doesn't recommend specific consideration of structural redundancy. However, the following two recommendations for redundancy appear in JSCE Code on Standard Specifications for Steel and Composite Structures (JSCE 2007b): (i) "it is important to secure good redundancy in the road network", and (ii) "the methods of nonlinear structural analysis can be applied to designing redundancy in the overall structure."

For long-span bridges, the Post-Tensioning Institute (PTI 2001) and SETRA (2002) were the only guidelines that proposed explicit guidance on cable loss events for cable-stayed bridges to prevent progressive collapse. The guidelines require all cable-stayed bridges to withstand the loss of any one cable without the occurrence of structural instability. A load case called "Loss of one cable" is provided to cater to this situation. Two methods are suggested to calculate the cable loss dynamic force in this load case: 1) static analysis using a static equivalent 2.0 factor with elastic superposition, and 2) nonlinear dynamic analysis with full permanent load and live load.

The research discussed above on bridge system redundancy or robustness measures as mainly focused on short to medium span bridges. The conclusions from most of the available studies cannot be extrapolated to long-span cable-supported bridges. It is clear from the literature survey above that system redundancy and robustness measures for long-span bridges have seldom been studied in depth and further research is necessary to fill the gap. The research presented in this report is focused on achieving this goal.

Bridge Redundancy Considerations in Specifications

AASHTO specifications (AASHTO 2014) define redundancy as "the quality of a bridge that enables it to perform its design function in the damaged state". In general, redundancy in truss bridges could be classified as (i) internal (member) redundancy, (ii) structural redundancy, and (iii) load path redundancy (FHWA 2013). A structural system can have internal redundancy because of multiple parallel elements within a member, such as built-up members made from many different plates and other structural shapes that are bolted or riveted together. Fracture in one part of such members may be arrested by other parts of the member. Structural redundancy is directly related to static indeterminacy of the structure. For example, continuous-span structures would have structural redundancy. Load path redundancy is based on available paths for load redistribution in the event of failure of a critical member. All three forms of redundancies may play a role in preventing the collapse of a bridge after the failure of a critical member. However, the specific contribution of each aspect to the overall redundancy of a long-span bridge is not yet well understood.

The AASHTO Load and Resistance Factor Design (LRFD) Bridge Design Specifications (2012) explicitly considers redundancy during bridge design by introducing a load modifier which is the product of factors related to ductility, redundancy, and operational importance of the structure (AASHTO LRFD 2012 Article 1.3.2.1). However, it may have a negligible effect on bridge design, particularly for bridges with single-point vulnerabilities and the potential for abrupt member loss. The current design standard-AASHTO LRFD Bridge Design Specifications (2018) suggests that non-redundant element must be designed for 1.05 times force effect of design loads. However, no instructions are provided on how to conduct a proper analysis, or what level of live load the bridge should be able to carry in its damaged state. More importantly, a non-redundant bridge may be vulnerable to collapse due to sudden loss of a critical member, even if it had been designed with full consideration of the redundancy load modifier required by the design standard.

More recently, the AASHTO Guide Specifications for Analysis and Identification of Fracture Critical Members and System Redundant Members (AASHTO 2018a) was published to address the issue of load-path redundancy in different types of bridges, including truss bridges. This guide specification provides prescriptive recommendations on the selection of members to be removed during redundancy analysis, such as failure of tension shear diagonal or tension chord. It also provides load factors for Redundancy-I case when loads are applied before the failure (so that the effect of dynamic amplification can be captured), and Redundancy-II (for normal use of the bridge without wind after a member failure). Both linear method with dynamic amplification factor and dynamic method (where member removal can be simulated) are recommended in this Guide Specifications. However, it does not provide an approach to quantify redundancy. Rather, it provides guidance on design and evaluation of a bridge following the damage of a fracture critical member.

The AASHTO Guide Specifications for Internal Redundancy of Mechanically Fastened Built-up Steel Members (AASHTO 2018b) provides guidance on evaluation of internal redundancy in built-up members that are traditionally designed as fracture critical members. This guide specification also provides guidance on special inspection interval for fracture critical members.

The NCHRP Report 776 proposed a displacement-based approach to evaluate redundancy of bridge. However, the research was solely based on short to medium span bridges, and it does not address major bridges exposed to multiple hazards. Moreover, the specified redundancy factor may not be applicable to long-span cable-supported bridges because of inherent complexities in such bridges, which may be significantly different from one bridge to another.

Barth et al. (2014) suggested that a sound explanation of load-path redundancy could lead to a more efficient and reasonable manner of designing and rating of highway bridges, thereby avoiding structure collapse and potential disasters. Load factors applicable for the analysis of a damaged structure are currently lacking (Grubb et al. 2015). Furthermore, the dynamic effects of sudden member loss reported in FHWA (2013) are still not considered in the current AASHTO approach. Advancement in the development of design guidelines or provisions to protect against progressive collapse of bridges in U.S. is still lacking, although many high-profile progressive collapses of bridges have been observed over the last several decades.

Designing bridges to resist progressive collapse is a challenge that can be met if the design processes can assure the presence of ALPs and structural redundancy in the event of any local damage or failure. A bridge that has load path redundancy would perform well under different hazard conditions, irrespective of the nature of the hazard. Even if significant damage results from a severe intensity hazard, well-designed bridges would have inherent abilities to maintain global stability and safe functionality following the damage.

CHAPTER 3. FINITE ELEMENT MODELING

INTRODUCTION

This chapter presents detailed information on the finite element models of the three bridges considered in this work. For each bridge, both explicit and implicit models were developed. While explicit models were developed for the LS-DYNA® platform (Hallquist 2006), implicit models were developed in other software, namely ANSYS® (ANSYS Inc. 2013), Midas Civil (Midas IT. 2012) and SAP 2000® (CSI 2019). Implicit methods are adequate for modeling bridge response when the material behavior is elastic or mildly nonlinear. Explicit analysis methods are preferable when dealing with scenarios that entail highly nonlinear material behavior, contact and rapid load application, e.g., associated with sudden member loss. Explicit schemes analyze the dynamic behavior by solving finite-difference equations, whereas implicit methods require formation and manipulation of the global mass, stiffness and damping matrices at each time step, processes that are prone to numerical difficulties, especially for highly nonlinear structures with many degrees of freedom, like long-span bridges. One of the objectives of developing both explicit and implicit models was to verify the accuracy and correctness of the basic finite element models by comparing certain aspects of their behavior against each other, as the theoretical bases of both techniques are different. Since implicit models are computationally efficient and require shorter calculation time, they were used for preliminary parametric analyses prior to performing the more time-consuming explicit simulations of member removal.

CABLE-STAYED BRIDGE MODEL

The Cooper River Bridge, also known as the Arthur Ravenel Jr. Bridge, was selected to represent cable-stayed bridges in this research project. The Cooper River Bridge connects downtown Charleston to Mount Pleasant across the Cooper River in South Carolina, USA. A photograph of the bridge is shown in Figure 11.

Source: © 2007 bbatsell (licensed under CC BY-SA 2.5)

Figure 11. Photo. View of the Cooper River Bridge.

The bridge has a total length of 3,296 feet. It consists of one 1,546 feet long main span, two 650 feet long side spans, and two 225 feet approach side spans on both sides. Carrying two-way traffic, the bridge has four vehicular lanes in each direction plus one walkway on the south side. The total width of the bridge deck is 140 feet in main and long side spans, the width changes to 120 feet in the approach side spans. The diamond-shape pylons are 568.5 feet high and are connected to the girders by 64 stayed cables in each plane. All cables are regularly spaced at 47 feet distance along the deck, except for the first and the last four back stays in the side spans.

Implicit Model

The implicit model of the Cooper River Bridge was developed in Midas Civil (Midas IT. 2012) as shown in Figure 12. The model accounts for the stayed cables, bridge pylons, piers, girder members, floor beams, stringers, diaphragms, secondary bracing members, concrete deck, elastomeric bearings and nonstructural components. The stayed cables were modeled by cable elements. The bridge pylons, piers and all the steel structural members, such as girders, floor beams, stringers, diaphragms and secondary bracing members, were modeled by general 3-D beam elements. The concrete bridge slabs were modeled by plate elements. The effects of other nonstructural components were included as equivalent forces, which were converted to masses during eigenvalue analysis.

The support components were modeled using fictitious beam elements with large stiffness. Internal connections between end piers and floor beams are shown in Figure 13. Moment in x-x, y-y and z-z directions were released for support beams on the two end-piers to simulate pin connections. The internal connections between the middle auxiliary piers and floor beams are shown in Figure 14. Moment in the transverse direction was released to simulate revolute (pin) connections. Lateral bearings connecting the main girder members to the bridge pylons were modeled by an elastic link element with defined stiffness based on the design details of the bearings. Miscellaneous connections between cables and bridge pylons; cables and main girders; concrete bridge slabs and floor beams were modeled by rigid links, which were intended to model existing physical separations among them.

Fixed boundary conditions were applied to the bases of the pylons and piers and interactions between soil and piles were ignored. Linear elastic materials were used for all the structural components in the implicit model. Overall, the entire model consisted of 6,361 nodes, 4,123 beam elements, 128 cable elements, 1,872 plate elements and 3,525 rigid links. A summary of component models and element types is shown in Table 1.

Table 1. Element types in the implicit model of the Cooper River Bridge.

Structural Members	Element type
Stayed Cables	Single Cable Element
Bridge Pylons and Piers	Beam Element
Structural Steel Member (Girder, Floor Beam, Stringer and others)	Beam Element
Concrete Deck	Plate Element
Lateral Elastomeric Bearings	Elastic Link with Defined Stiffness
Miscellaneous Connection	Rigid Link
Nonstructural Elements (Barrier and others)	Equivalent Force
Support on Substructure	Fictitious Beam Element

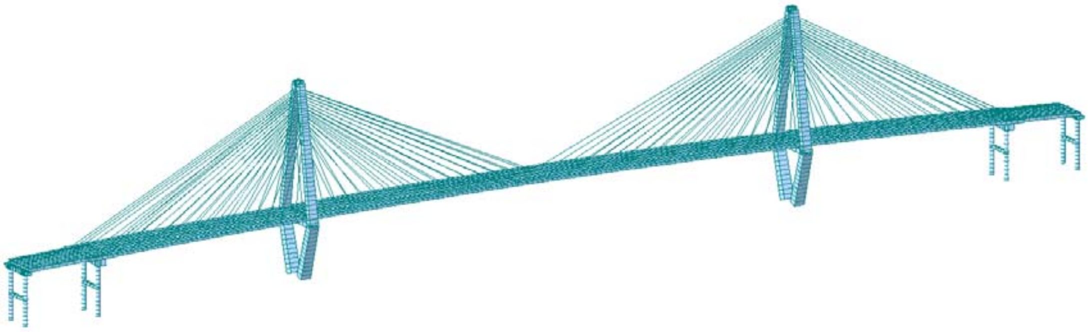

Source: FHWA.

Figure 12. Illustration. Implicit model of the Cooper River Bridge.

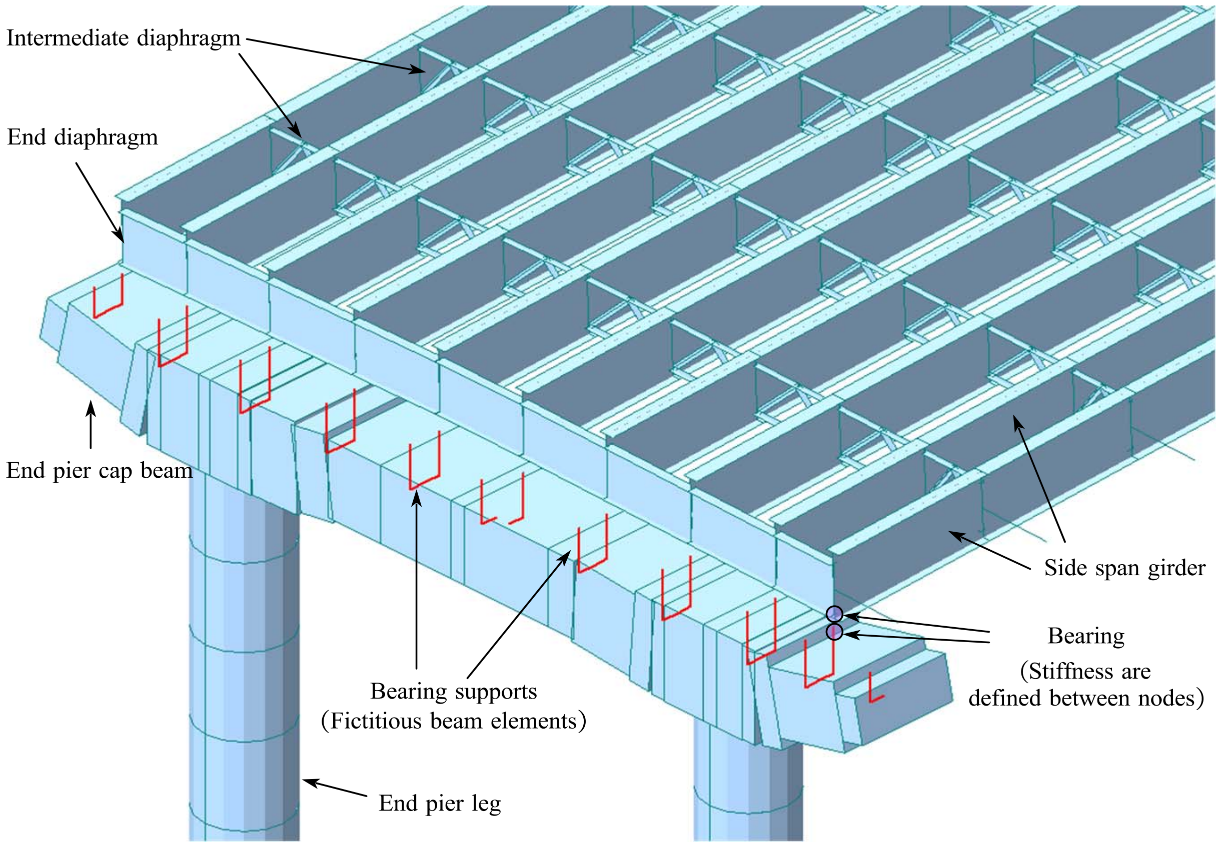

Source: FHWA.

Figure 13. Illustration. Internal connections between end piers and floor beam.

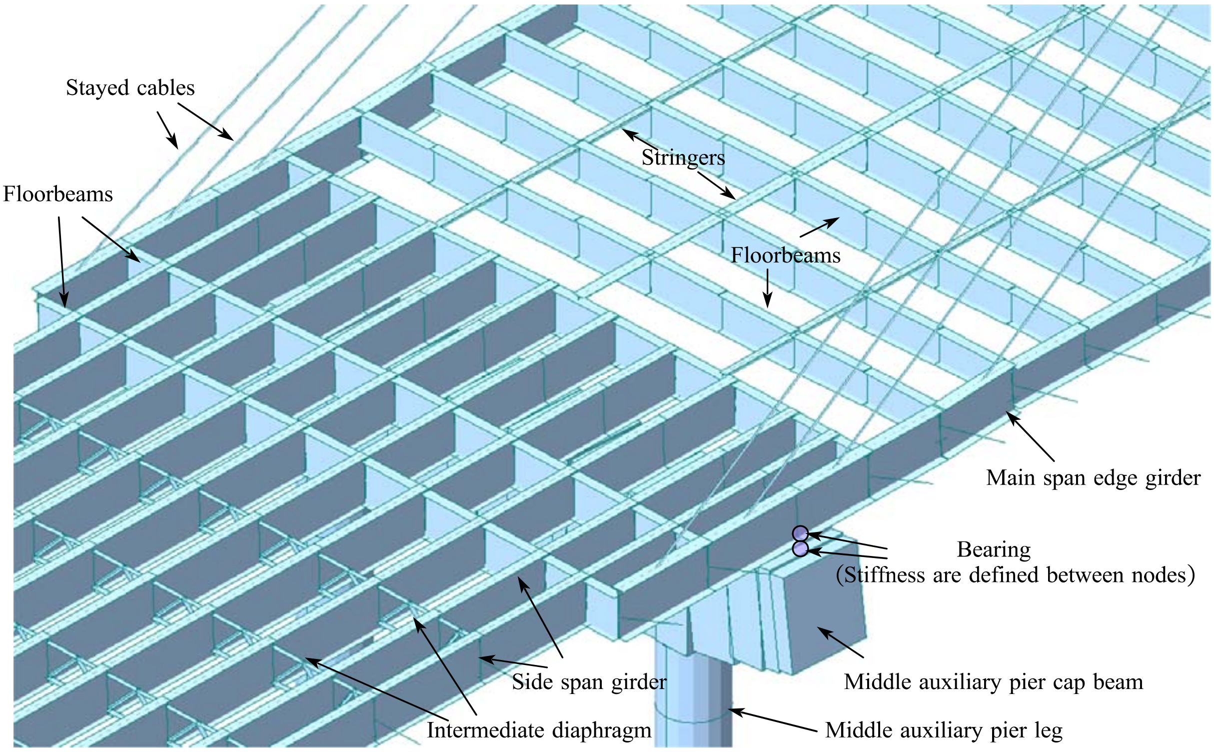

Source: FHWA.

Figure 14. Illustration. Internal connections between middle auxiliary piers and floor beams.

Explicit Model

In order to investigate the dynamic response of cable-stayed bridges following sudden loss of a critical element, a 3-D finite element model of the Cooper River Bridge was developed in LS-DYNA®, as shown in Figure 15. The basic geometry of the explicit model is the same as that of the implicit model. Table 2 summarizes element types and material models used to model different structural components of the bridge. Overall, the explicit model consisted of 12,968 nodes, 6,039 beam elements, 1,872 shell elements, 1,611 mass element and 2,132 nodal rigid bodies. The detailed material nonlinearity considerations for each of the structural components are introduced in the following sub-sections.

Table 2. Element and material information for the explicit model of the Cooper River Bridge.

Structural Members	Element Types	Material Information
Stayed Cables	Multiple truss elements	*MAT_PLASTIC_KINEMATIC
Bridge Pylons and Piers	Belytschko-Schwer resultant beam	*MAT_MOMENT_CURVATURE_BEAM
Structural Steel Members (Girders, Floor Beam, Stringer and others)	Hughes-Liu beam with cross-section integration	*MAT_PLASTIC_KINEMATIC
Concrete Deck	Fully-integrated shell element	*MAT_PLASTICITY_COMPRESSION_TENSION
Bearings	Discrete beam element	*MAT_NONLINEAR_ELASTIC_DISCRETE_BEAM
Miscellaneous Connections	*CONSTRAINED_NODAL_RIGID_BODY	
Nonstructural Elements (Barriers and others)	Mass element	
Support on Substructures	Belytschko-Schwer resultant beam	*MAT_RIGID

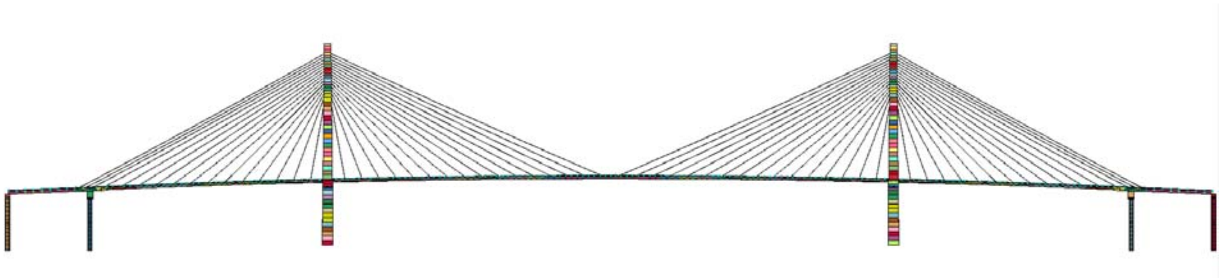

Source: FHWA.

(a) Elevation view.

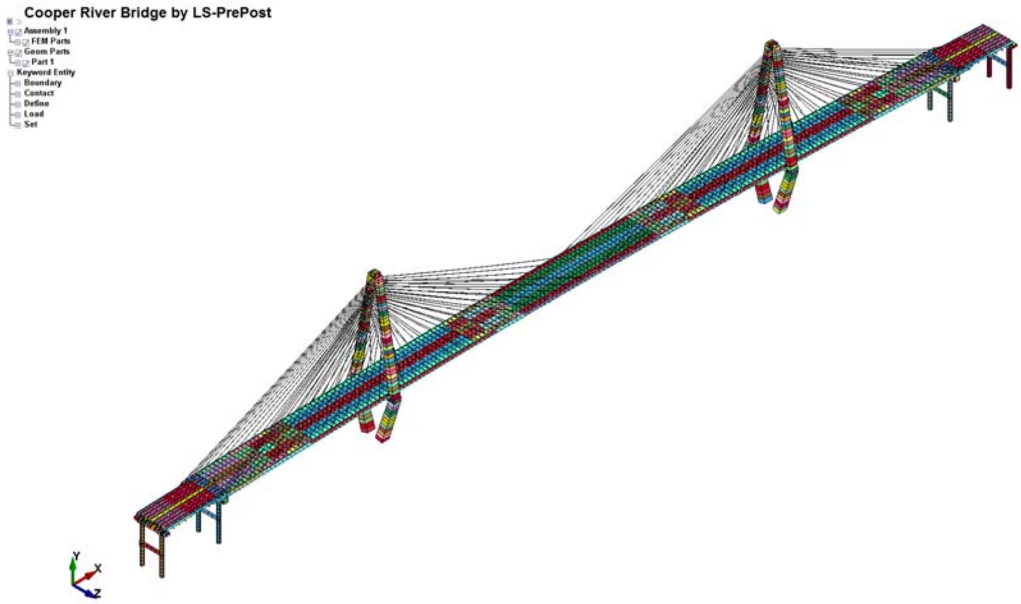

Source: FHWA.

(b) Isometric view.

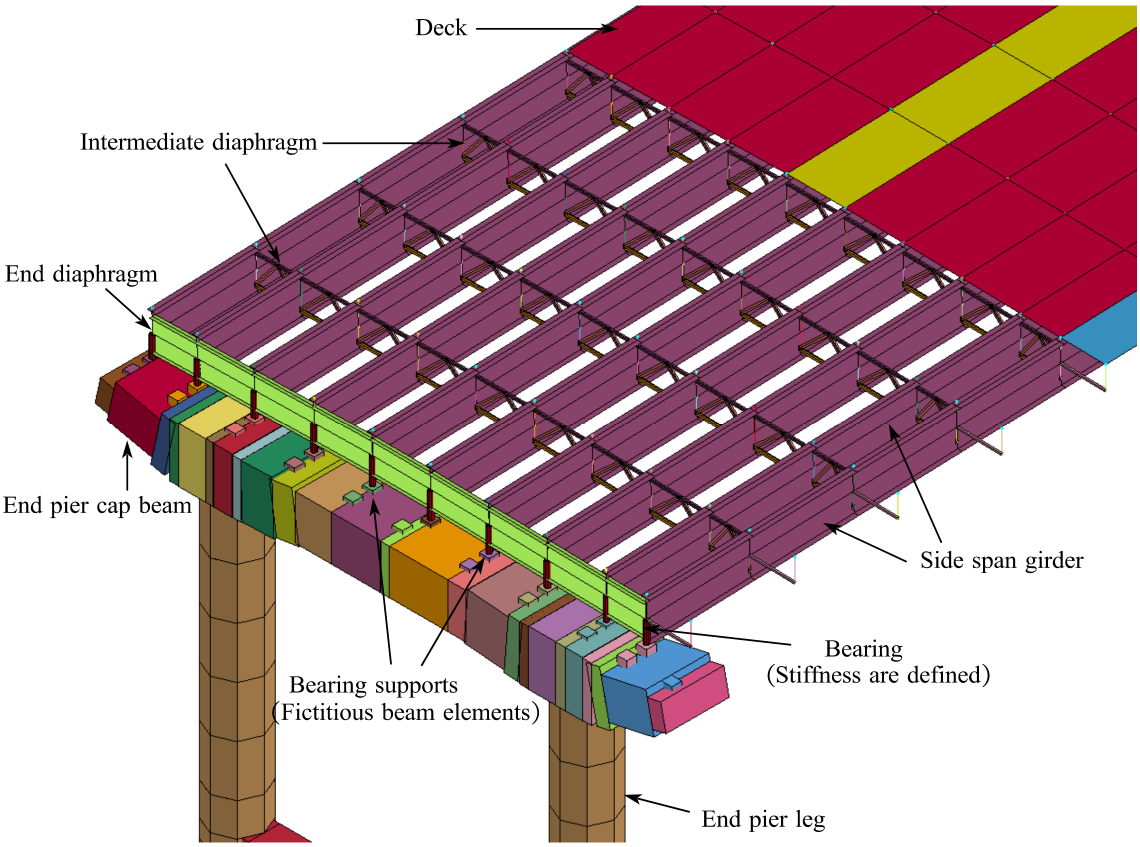

Source: FHWA.

(c) Components information near end pier.

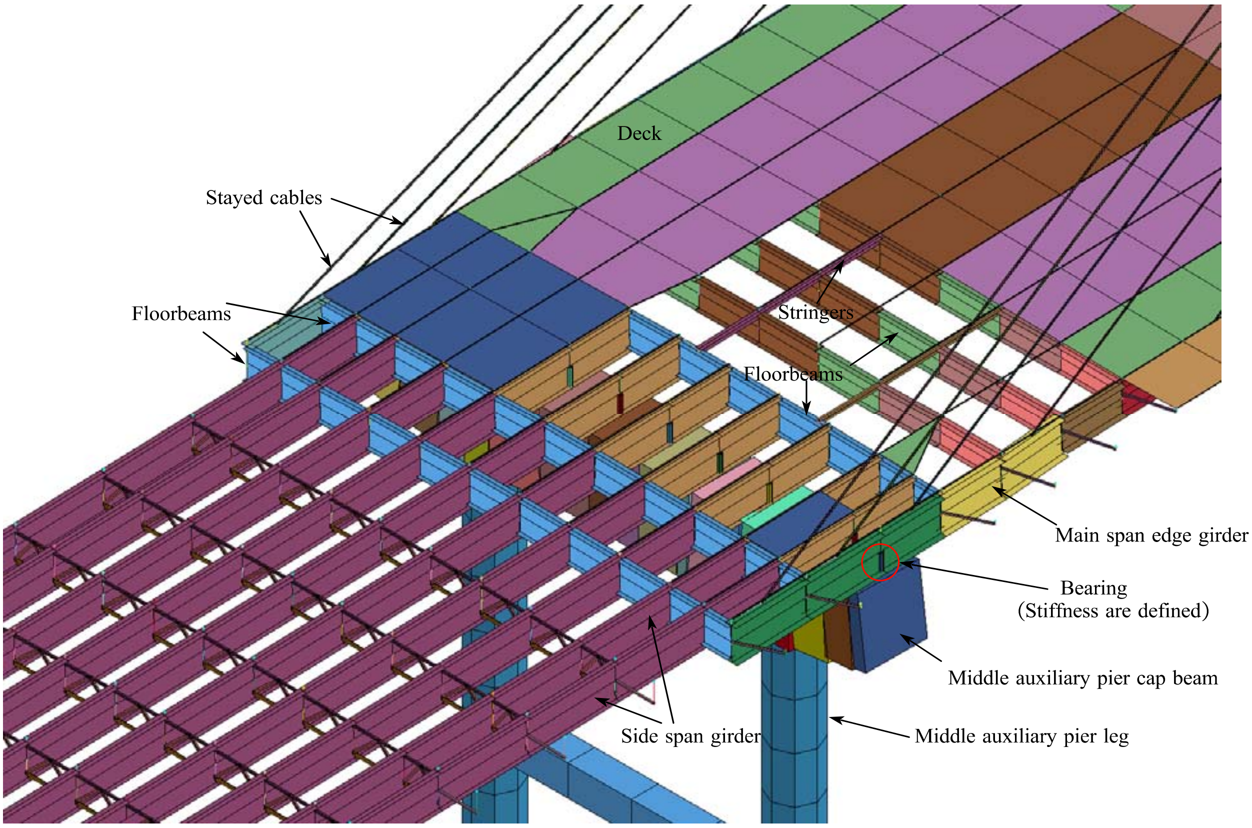

Source: FHWA.

(d) Components information near middle auxiliary pier.

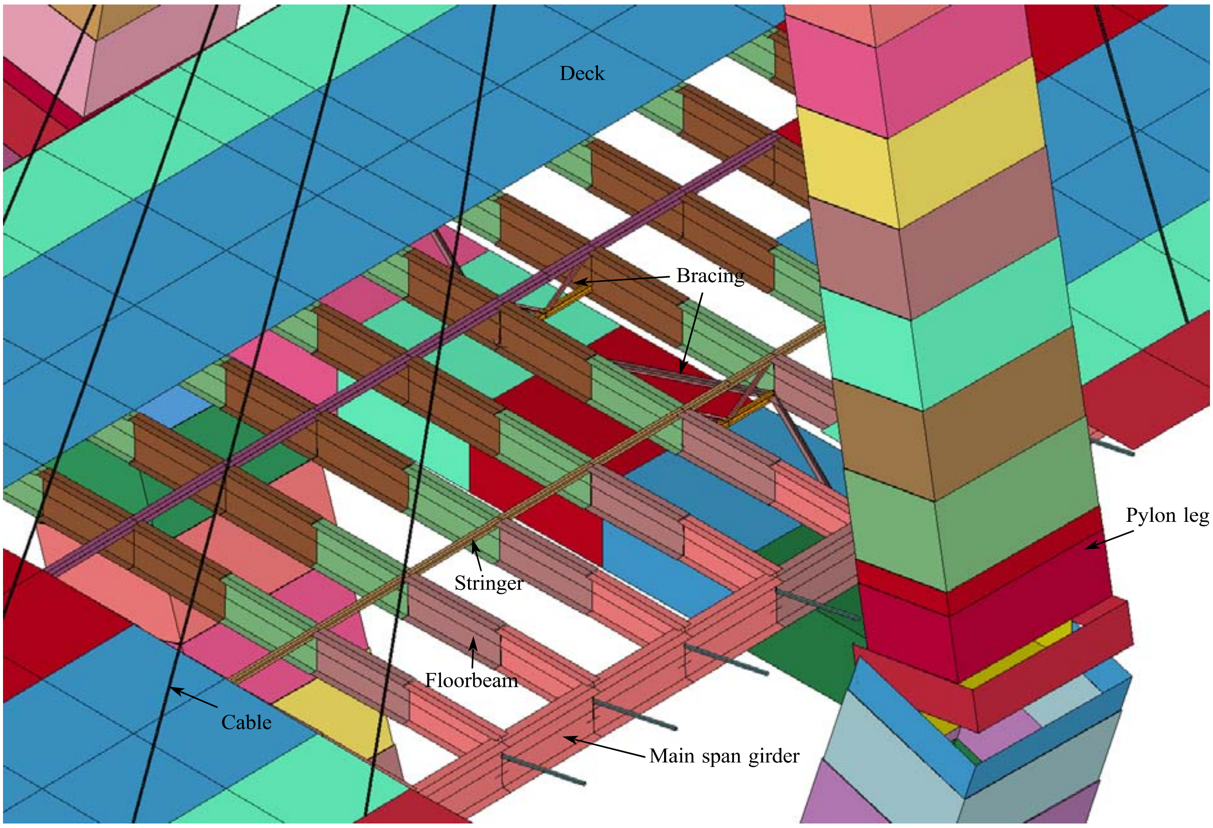

Source: FHWA.

(e) Components information near pylon leg.

Figure 15. Illustrations. Explicit model of the Cooper River Bridge.

Structural Steel Members

Structural steel components, including girder members, floor beams, stringers, steel diaphragms and secondary bracing members were modeled by Hughes-Liu beam elements with cross section integration. Approximately 20 to 30 integration points were used for each section depending on the section shape. The material nonlinear behavior of these components was modeled by the material model *MAT_PLASTIC_KINEMATIC (*MAT_003). This material model is cost-effective and provides an elastoplastic behavior with kinematic hardening behavior as shown in Figure 16.

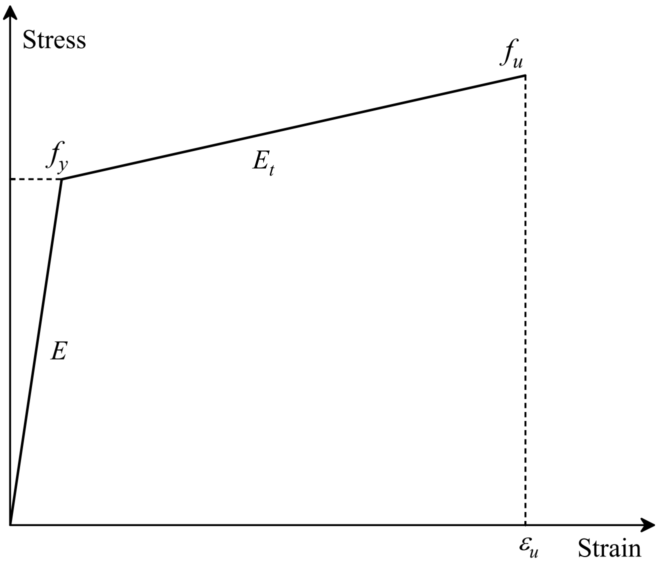

Source: FHWA.

Figure 16. Illustration. Material model of structural steel members.

Bridge Pylon

The bridge pylon legs are primarily subjected to biaxial bending moments and axial force during a member loss situation. To avoid the complexity of modeling detailed reinforcement explicitly while considering the interaction between axial forces and bending moments, the material nonlinearity of the reinforced concrete bridge pylon was characterized by a simplified model *MAT_MOMENT_CURVATURE_BEAM (*MAT_166) with Belytschko-Schwer beam elements. In this formulation, different user-defined moment curvatures can be provided as a function of axial force level and a failure criterion could be set up based on the ultimate curvature at each section.

The modeling approach is demonstrated by comparing LS-DYNA simulation results with test results in Vecchio and Shim (2004) who conducted a series of beam tests to investigate the behavior of reinforced concrete elements. In these tests, simply supported beams with span length of 21 feet (6,400 mm) were pushed down by a concentrated load at the center point with a servo-controlled MTS universal testing machine, as shown in Figure 17. Test cases A3 and B3 were selected for comparison. The section details and material information for this test setup are shown in Figure 18 and Table 3 (Vecchio and Shim 2004).

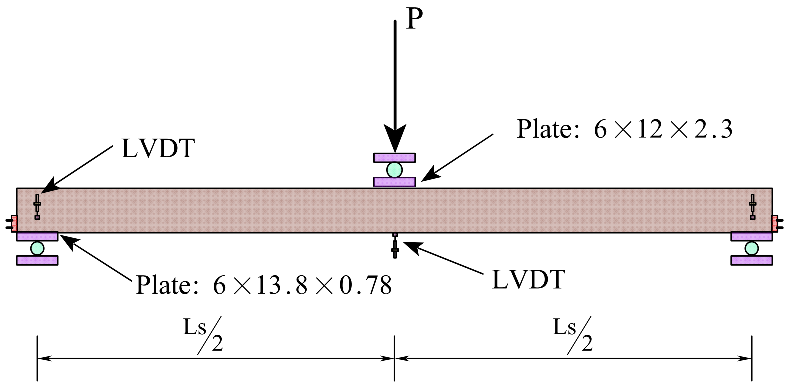

Source: © ASCE (with permission from ASCE).

Figure 17. Illustration. Test set up by Vecchio and Shim (Case A3 and B3).

Table 3. Material properties of the test beams.

Reinforcement				
	Area (inch^2)	f_y (ksi)	f_u (ksi)	E (ksi)
M10	0.155	45.7	66.7	29,000
M25	0.775	64.5	89.2	31,900
M30	1.085	63.2	101.5	29,000
Concrete				
	f'_c (ksi)	f'_{sp} (ksi)	ε_0 (inch/inch)	E_c (ksi)
A3	6.3	0.454	0.0019	4974.8
B3	6.3	0.454	0.0019	4974.8

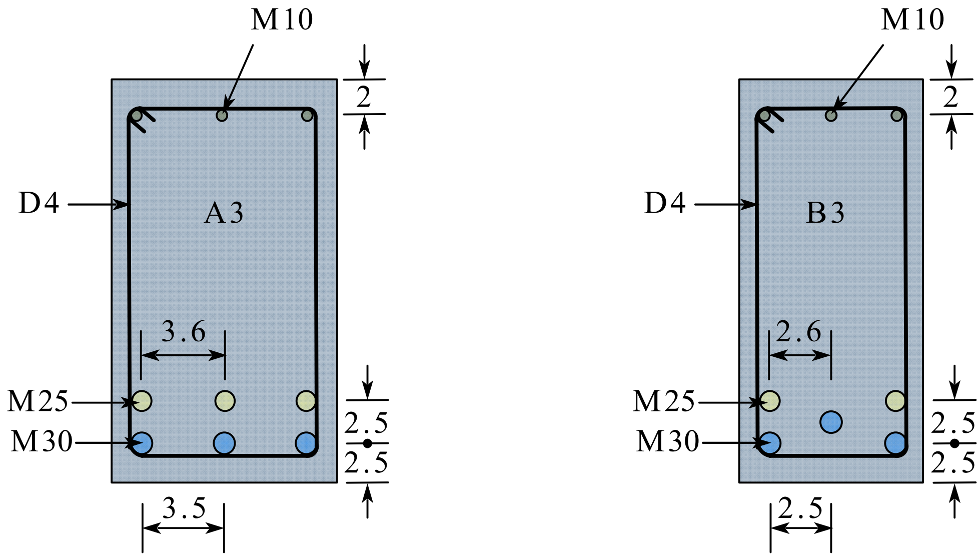

(a) Case A3 (b) Case B3

Source: © ASCE (with permission from ASCE).

Figure 18. Illustrations. Cross-section details of test beams (unit: inch).

The two beams (Case A3 and B3) were modeled in LS-DYNA® by using the aforementioned modeling scheme. A separate section analysis was conducted in SAP 2000® to get the moment curvature curves under axial loads that ranged from the section's axial tension capacity to its axial compression capacity. Twelve moment curvature curves under six different axial forces were selected as the input data in the material model for each case, as shown in Table 4, Figure 19 and Figure 20. Pushdown analysis of these two beams were conducted in LS-DYNA® by applying *BOUNDARY_PRESCRIBED_MOTION_NODE at the center nodes of the test beams. The comparisons of load displacement curves obtained from test results and LS-DYNA simulations are shown in Figure 21. It is observed from this figure that the selected modeling scheme is able to capture the flexural behavior of the beams well.

Table 4. Axial forces for input data of the moment curvature curves (unit: kips).

Case	N1	N2	N3	N4	N5	N6
Case A3	-875.0	-656.2	-437.6	-218.8	0.0	289.2
Case B3	-674.7	-506.1	-337.3	-123.8	0.0	6.2

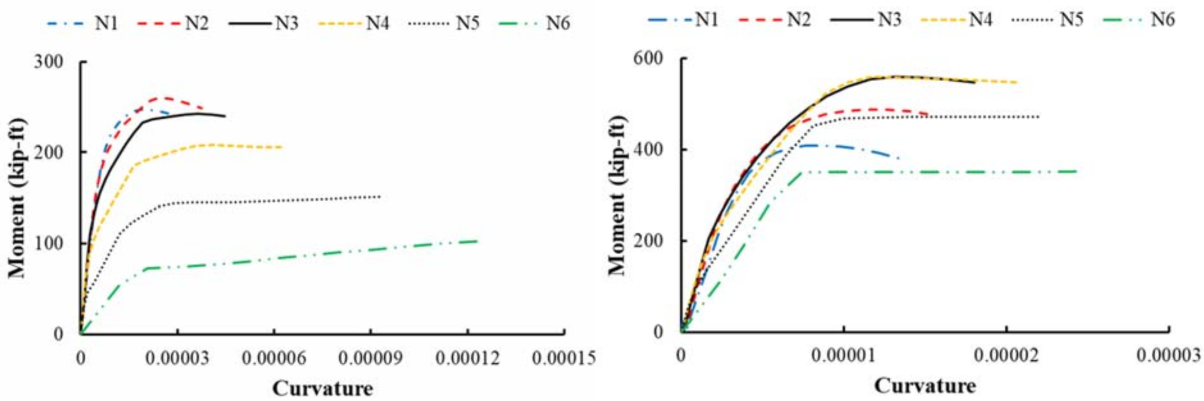

Source: FHWA. Source: FHWA.

(a) Moment-curvature curves about weak axis. (b) Moment-curvature curves about strong axis.

Figure 19. Graphs. Moment curvature curves under different axial forces of Case A3.

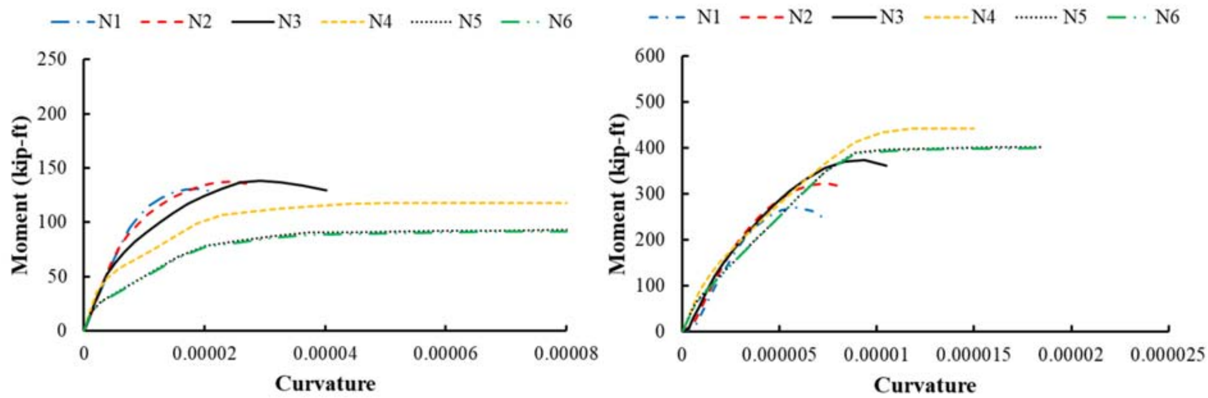

Source: FHWA.

(a) Moment-curvature curves about weak axis.

Source: FHWA.

(b) Moment-curvature curves about strong axis.

Figure 20. Graphs. Moment curvature curves under different axial forces of Case B3.

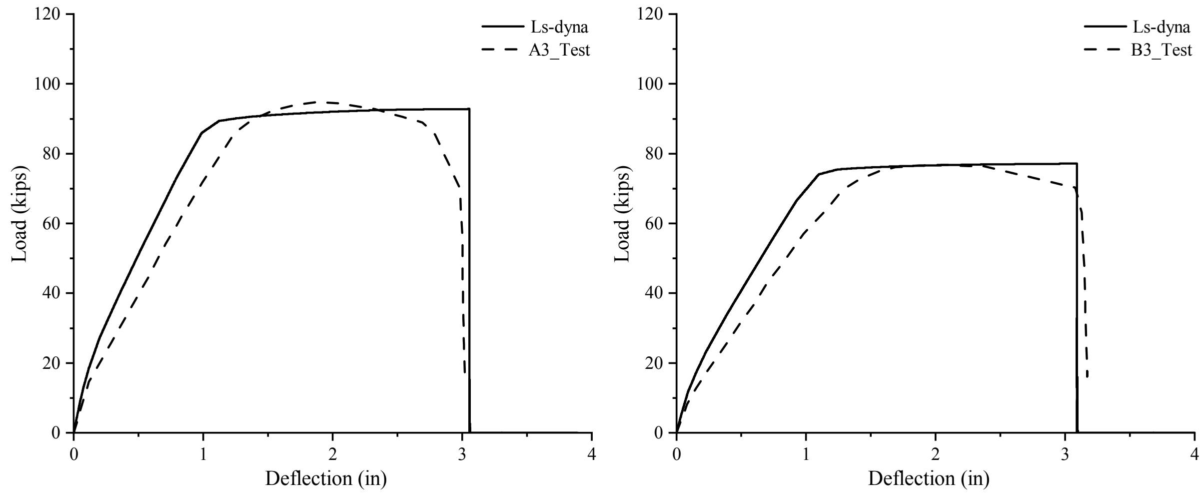

Source: FHWA.

(a) Case A3.

Source: FHWA.

(b) Case B3.

Figure 21. Graphs. Load-displacement responses.

Stay Cables

There are 128 cables with different cross-section areas and pre-tensioning forces in the Cooper River Bridge. The stay cables consist of 0.62 inches diameter uncoated, seven wire, weldless, low-relaxation strands complying with the requirements of ASTM A416, Grade 270. According to AASHTO LRFD Bridge Design Specifications (AASHTO 2012), the elastic modulus (E) is 28,500 ksi and the tensile strength (f_u) is 270 ksi with ultimate strain (ε_u) 6%. The yield strength (f_y) is 90% of the tensile strength (f_u) for the cables. Each cable was modeled with 10 truss elements in order to accurately represent the sag effect. Material nonlinear response was modeled by the material model *MAT_PLASTIC_KINEMATIC (*MAT_003). The input parameters for this model are shown in Table 5. The ADD_THERMAL_EXPANSION option was used to give *MAT_003 a thermal expansion capability. The pre-tensioning forces based on the design calculations were applied as an equivalent thermal load (achieved by decreasing the temperature in cable elements) during 0.1 seconds by using the command *LOAD_THERMAL_CONSTANT_NODE.

Table 5. Input parameters for *MAT_003 (Cable ASTM A416 Grade 270).

f_y (ksi)	E_t (ksi)	E (ksi)	ε_u
243	524.5	28,500	6%

Computations from finite element simulation and theoretical calculations of the vertical sag of a single cable under pre-tensioning force as well as self-weight were compared to demonstrate the validity of the approach. In this example, a single plane cable with two pinned ends were modeled by 10 truss elements in LS-DYNA®. Similarly, this cable was also modeled by 10 cable elements in Midas Civil. The section, material properties, pre-tensioning force were obtained from the longest cable in North Plane of the cable-stayed bridge, as shown in Table 6. The geometric dimensions are shown in Figure 22. The simulation results of vertical sag computed from LS-DYNA® and Midas Civil are compared in Figure 23.

Table 6. Section and material properties for the example cable.

Area (feet^2)	**Density** (kip/feet^3)	**Elastic modulus** (ksf)	**Poison ratio**	**Pre-tension** (kip)
0.1453	0.57	4,104,000	0.3	1,828.5

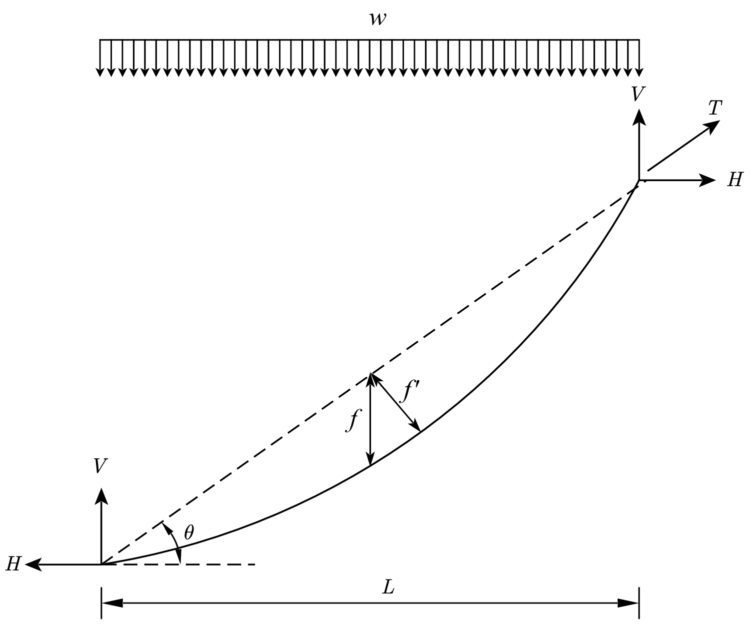

Source: FHWA.

Figure 22. Illustration. Geometric dimension of the single cable example (*L* = 675 feet).

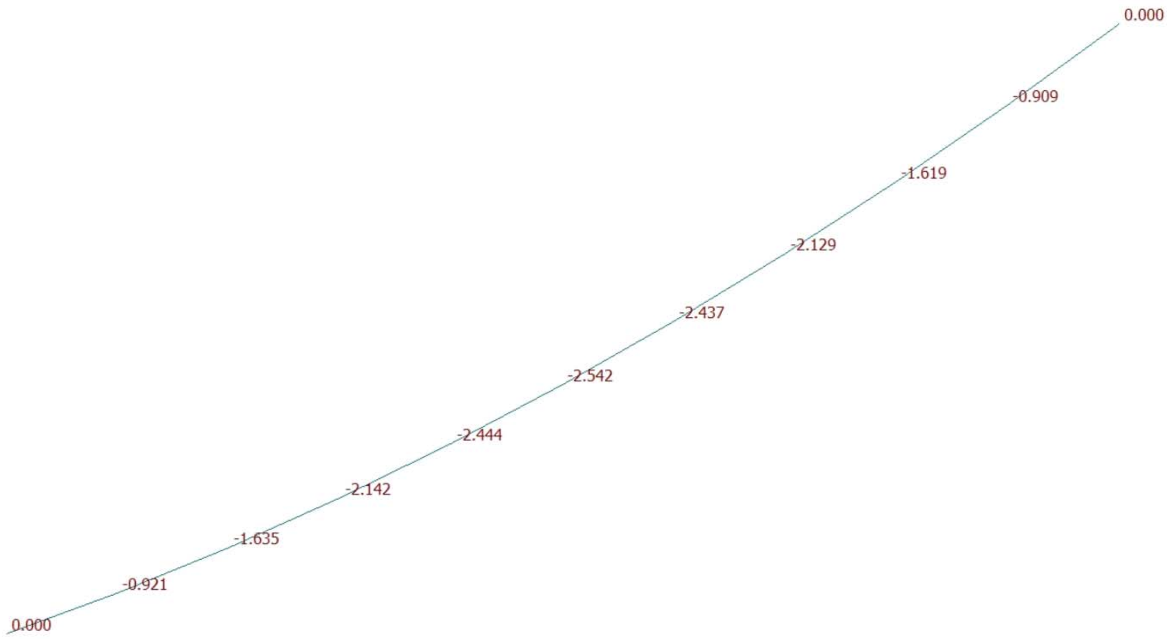

Source: FHWA.

(a) Vertical sag of single cable example in Midas Civil (unit: feet).

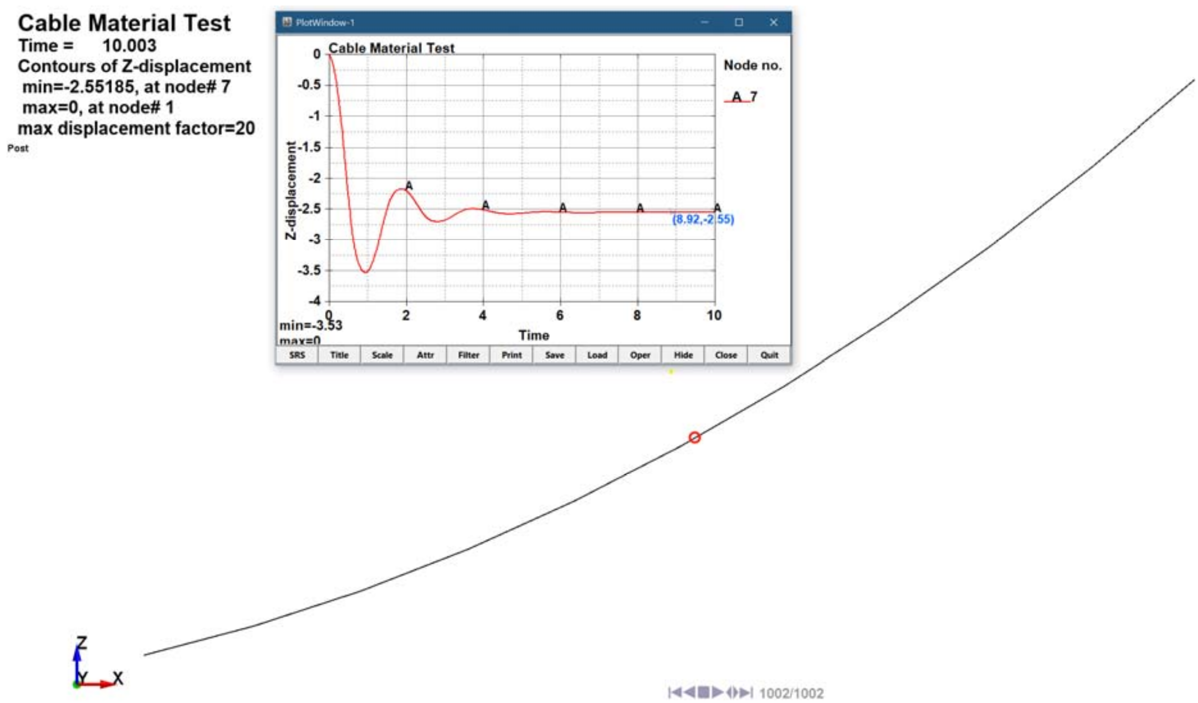

Source: FHWA.

(b) Vertical sag of single cable example in LS-DYNA® (unit: feet).

Figure 23. Illustrations. Finite element simulation results of cable vertical sag.

Based on Gimsing and Georgakis (2011), the vertical sag in the cable could be computed from Equation (10),

$$f = \frac{wL^2}{8H}\cos\theta \quad (10)$$

Where w = uniform load per unit length of horizontal projection, f = cable sag, L = span and H = the horizontal component of cable force.

Comparison of the vertical sag of the cable from simulations and to that from theoretical analysis is shown in Table 7. It is observed that the FEM results differ from the theoretical results by less than 1%, which validates the cable modeling approaches employed in both LS-DYNA® and Midas Civil.

Table 7. Comparison of vertical sag between FE simulations and theoretical analysis.

	Theoretical Results	LS-DYNA	Difference	Midas Civil	Difference
Vertical Sag (feet)	2.549	2.552	0.12%	2.542	-0.28%

Using the aforementioned cable modeling method, single cable analysis was conducted for each cable in the bridge to compute its deformed geometry under self-weight and initial tension force. This information was then used to model the cable geometries in the explicit bridge model.

Bridge Deck and Post-Tensioning Strands

The bridge deck was modeled using fully-integrated four-node isotropic shell elements. The bridge deck was connected to the underlying steel girder members and floor beams though rigid links, using *CONSTRAINED_NODAL_RIGID_BODY. To avoid the complexity of modeling detailed reinforcement explicitly, the material nonlinearity of the bridge deck was considered by a simplified model introduced and calibrated by Alashker et al. (2011). This simplified model emphasizes the tensile membrane response of the concrete deck, since its flexural resistance becomes insignificant at large deformation levels near the ultimate states. The uniaxial material response was based on the following assumptions: (1) the concrete slab is the only source for compressive resistance, and it has zero tensile strength, and (2) the steel reinforcement mesh is the only source of tensile resistance. The Kent and Park Model (1971) was employed for the nonlinear stress-strain relationship for concrete in compression. The equivalent tensile stress-strain relationship due to reinforcement was defined by Equation (11),

$$F_{t,eq}(\varepsilon) = \frac{F_{t,R}(\varepsilon)A_R}{A_{eq}} \quad (11)$$

where $F_{t,eq}(\varepsilon)$ is the equivalent tensile stress at strain ε, A_{eq} is the equivalent area of the concrete shell element per unit width; $F_{t,R}(\varepsilon)$ is the stress values in the steel reinforcement mesh at strain ε, and A_R is the area of the mesh reinforcement per unit width. This equivalent behavior was implemented by *MAT_PLASTICITY_COMPRESSION_TENSION (*MAT_124) in LS-DYNA®, which can model distinct tension and compression relationships. The typical stress-strain relationship of the composite deck model is shown in Figure 24.

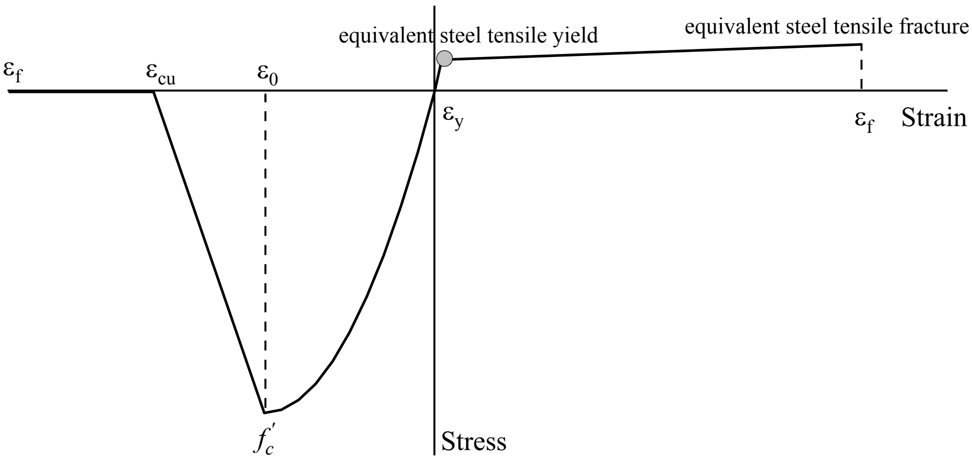

Source: FHWA.

Figure 24. Illustration. Equivalent stress-strain relationship of deck elements.

Post-tensioning strands were used at the center of main span and near the middle auxiliary piers in order to prevent cracking in the concrete deck. In the explicit model, these post-tensioning strands were modeled by truss elements with *MAT_PLASTIC_KINEMATIC (*MAT_003). These elements shared common nodes with the adjacent shell elements of the concrete deck. A close-up view of the deck with post-tensioning strands is shown in Figure 25. Like the stay cables, thermal expansion was also considered in the material model by the *ADD_THERMAL_EXPANSION option. The pre-tensioning and the post-tensioning forces obtained from the design drawings were induced by cooling the strands, which thermally shrank to apply pre-tensions. Assumed pre-stressing losses of 35% were considered for all post-tensioning strands. The post-tensioning sequence was not considered in the explicit model.

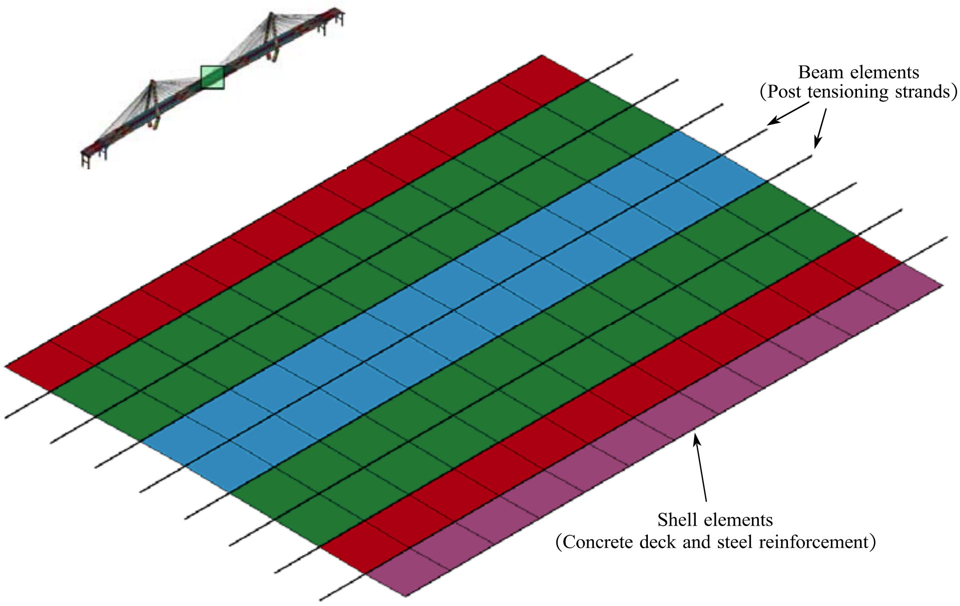

Source: FHWA.

Figure 25. Illustration. Bridge deck model with post-tensioning strands.

Elastomeric Bearings

The elastomeric bearings at end piers and middle auxiliary piers were modeled by discrete beam elements with *MAT_LINEAR_ELASTIC_DISCRETE_BEAM (*MAT_066), which has six springs with each spring acting along one of the six local degrees of freedom. Stiffness of the springs acting along the released degrees of freedom were set to zero in both explicit and implicit models.

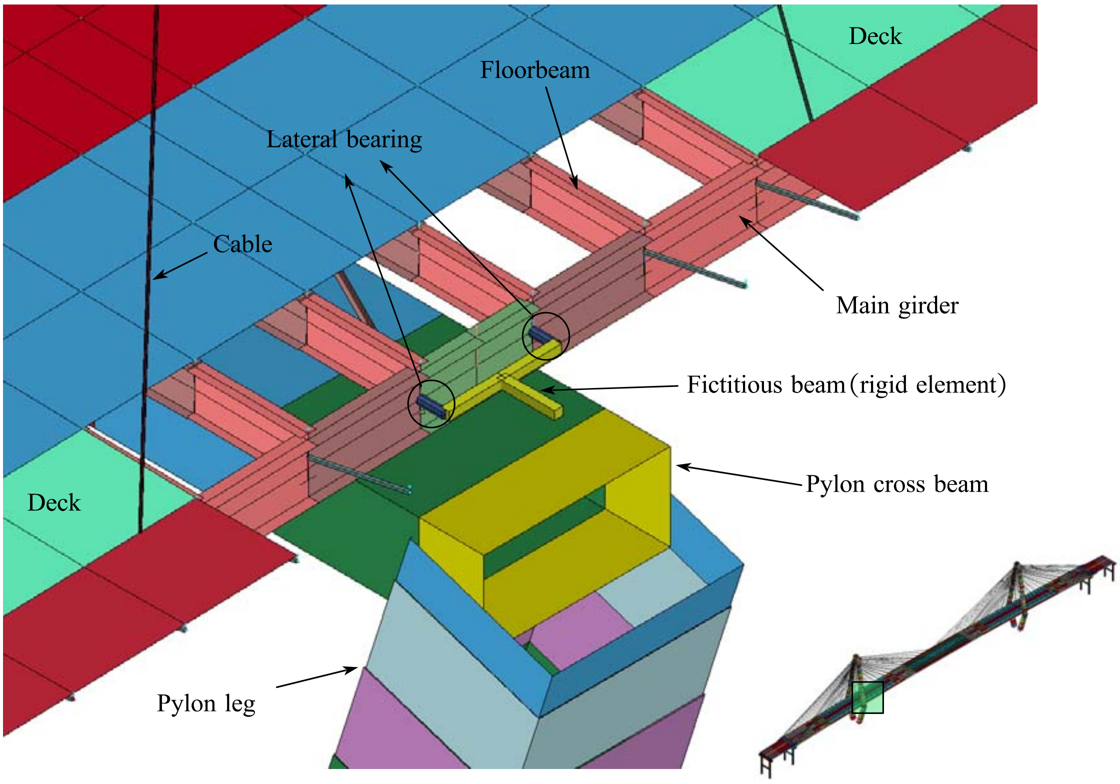

Source: FHWA.

Figure 26. Illustration. Lateral elastomeric bearings connecting girder members to pylons.

The lateral elastomeric bearings connecting the girder to the pylons, as shown in Figure 26, were modeled by discrete beam elements with *MAT_NONLINEAR_ELASTIC_DISCRETE_BEAM (*MAT_067). The translational stiffness of the lateral elastomeric bearings and their ultimate deformations in each direction are shown in Table 8.

Table 8. Stiffness and ultimate deformations of the lateral elastomeric bearings.

Global Direction	Longitudinal	Vertical	Compression
Stiffness (kip/inch)	19.11	40.81	622.33
Ultimate deformation (feet)	2.969	1.615	0.245

Note: Ultimate deformation in compression is based on the design drawing, other information is based on design information.

Accuracy of the FE Models

In order to ensure accuracy of both implicit and explicit models, cross validation was first conducted between both models under dead load. The bridge was built through multiple construction stages and sequences. Achieving the same construction sequence in the finite element model as in the real structure is difficult and would require significant simulation time. Hence, the dead load analysis was simplified in the finite element modeling scheme. In the implicit model, all related loads were applied as a nonlinear load combination under the dead load. In the explicit model, the application of dead load was conducted by the following steps.

Stage 1: Time range 0 to 8 seconds: Pretension forces in the cables and self-weight of the main structures were applied in this stage. A global damping of 80% of critical was applied to prevent excessive vibrations associated with sudden application of the loads. Based on the construction plans, post-tensioning in the deck was applied once the deck was completed. Thus, the post-tensioning strands did not contribute to stiffness during this stage and the Young's Modulus of the strands were reduced to 5% of their normal value to reflect this fact.

Stage 2: Time range 8 to 20 seconds: The stiffness of the post-tension strands was increased to its normal value and the post-tensioning forces were applied. This stage was also accompanied by large global damping (i.e., 80% of critical damping) to prevent numerical problems associated with excessive vibrations and shortening of the post-tensioning strands.

The results under dead load in the explicit model were extracted at the end of Stage 2 and compared to the results from the implicit model. The data compared included vertical displacements, reaction forces, cable forces and mode shapes for the two models.

Vertical Displacements

The vertical deflections along the main girder in both models are shown in Figure 27. The deflection was measured from the initial camber position of the girder. The maximum downward deflection was located at the center with a value equal to approximately 1.4 feet. The main girder near the two pylons suffered an upward displacement of approximately 0.25 feet because of pre-distortion of the bearings on the bridge pylons. A comparison of the results shows good agreement between the two models.

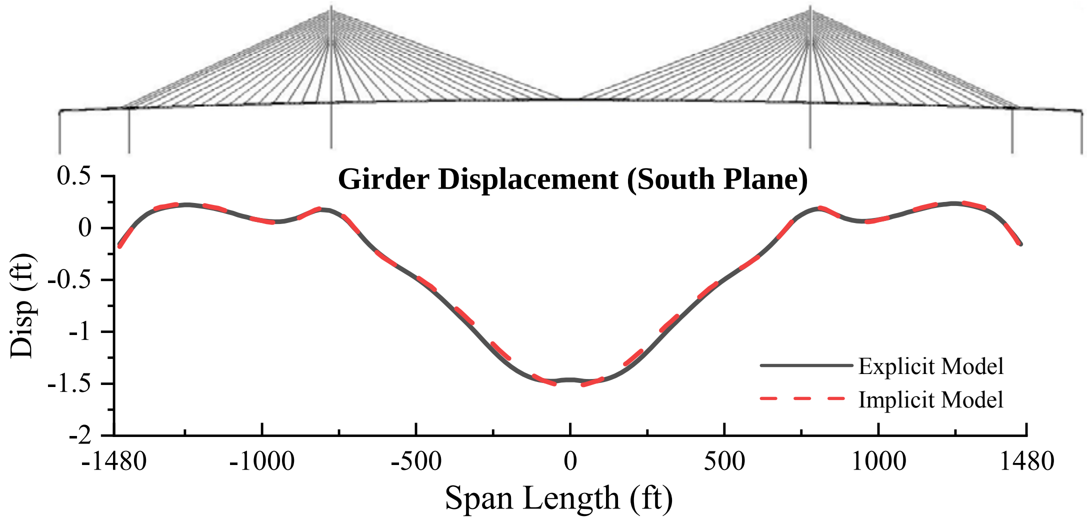

Source: FHWA.

Figure 27. Graph. Comparison of girder vertical deflection in the Cooper River Bridge.

Reactions Forces and Cable Stresses

The reaction forces at the base of piers and tower legs are shown in Table 9. A comparison of cable stresses in each plane is shown in Figure 28. The maximum difference of cable stresses in both planes is within 5%. The results show good agreement between the implicit and explicit models.

Table 9. Comparison of reaction force and total weight of the Cooper River Bridge.

Vertical Reactions (Two Legs)	**Implicit Model** (kips)	**Explicit Model** (kips)	**Difference** (%)
East End Pier	11,248.84	11,380.16	1.2
East Middle Pier	15,136.44	15,104.69	-0.2
East Pylon	75,426.55	75,568.73	0.2
West Pylon	75,438.35	75,688.09	0.3
West Middle Pier	15,135.82	15,110.08	-0.2
West End Pier	11,270.68	11,409.45	1.2
Total Weight	203,656.68	204,261.20	0.3

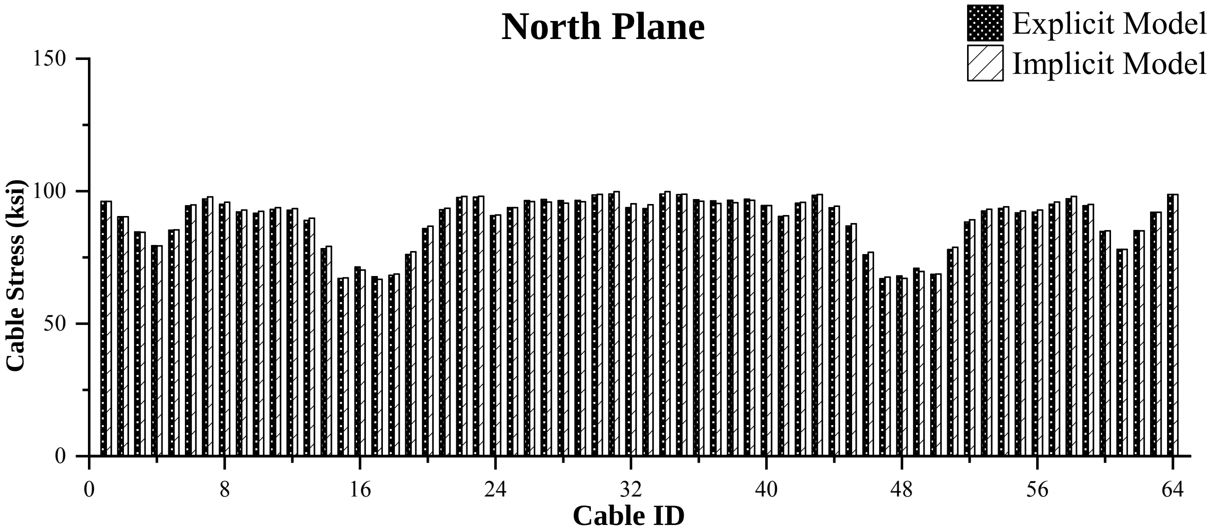

Source: FHWA.

(a) North Plane.

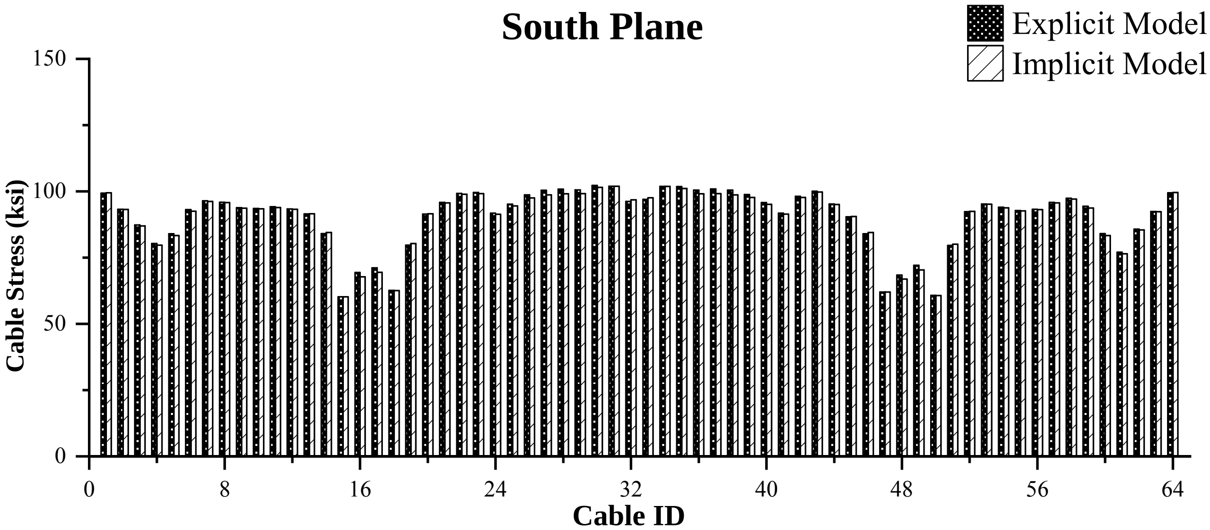

Source: FHWA.

(b) South Plane.

Figure 28. Graphs. Comparison of cable forces in the Cooper River Bridge.

Modal Analysis

The first ten mode shapes and natural frequencies obtained by the implicit and explicit models of the bridge are listed in Figure 29 and Table 10. In order to eliminate local modal shapes in cables and unstable results, only one single element with equivalent elastic modulus adjusted by Ernst's Equation (Ernst 1965) was used for each stay cable. Also, an elastic material model was used for the bridge pylons in the explicit modal analysis.

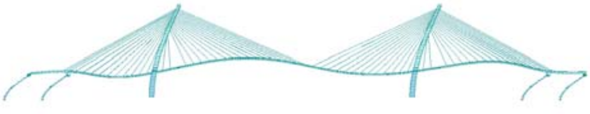

(1) Mode 1 (f = 0.216 Hz; T = 4.625 seconds)

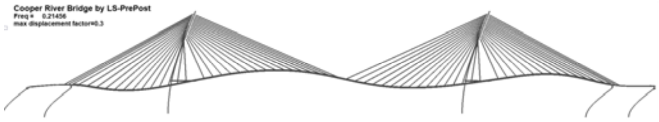

(1) Mode 1 (f = 0.215 Hz; T = 4.661 seconds)

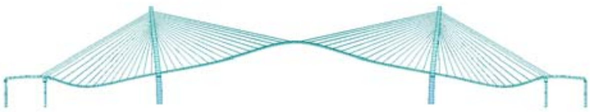

(2) Mode 2 (f = 0.251 Hz; T = 3.983 seconds)

(2) Mode 2 (f = 0.247 Hz; T = 4.044 seconds)

(3) Mode 3 (f = 0.301 Hz; T = 3.321 seconds)

(3) Mode 3 (f = 0.304 Hz; T = 3.292 seconds)

(4) Mode 4 (f = 0.316 Hz; T = 3.166 seconds)

(4) Mode 4 (f = 0.309 Hz; T = 3.239 seconds)

(5) Mode 5 (f = 0.366 Hz; T = 2.734 seconds)

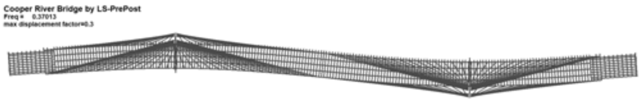

(5) Mode 5 (f = 0.370 Hz; T = 2.702 seconds)

(6) Mode 6 (f = 0.483 Hz; T = 2.071 seconds)

(6) Mode 6 (f = 0.475 Hz; T = 2.104 seconds)

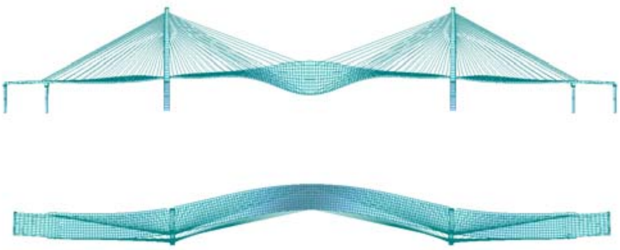

(7) Mode 7 (f = 0.489 Hz; T = 2.044 seconds)

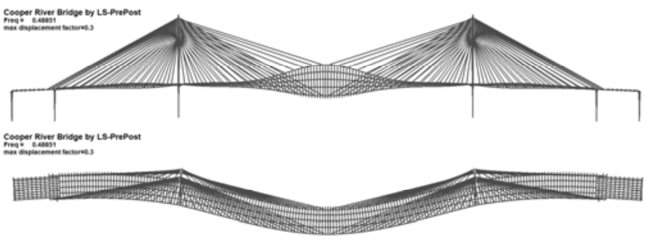

(7) Mode 7 (f = 0.489 Hz; T = 2.047 seconds)

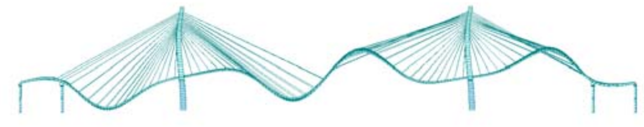

(8) Mode 8 (f = 0.551 Hz; T = 1.814 seconds)

(8) Mode 8 (f = 0.552 Hz; T = 1.182 seconds)

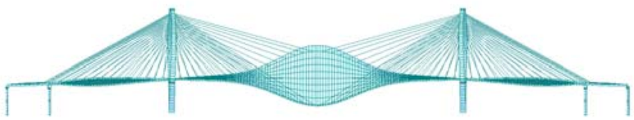

(9) Mode 9 (f = 0.571 Hz; T = 1.753 seconds)

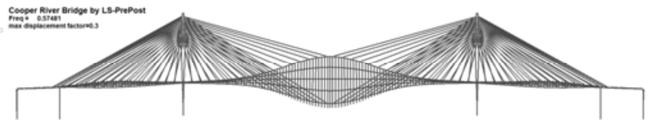

(9) Mode 9 (f = 0.575 Hz; T = 1.740 seconds)

(10) Mode 10 (f = 0.593 Hz; T = 1.687 seconds)

(10) Mode 10 (f = 0.592 Hz; T = 1.688 seconds)

Source: FHWA.

Figure 29. Illustrations. First ten global mode shapes of the Cooper River Bridge.

Table 10. Natural frequencies of the Cooper River Bridge.

Mode No.	Type	Implicit Model Frequency (Hz)	Explicit Model Frequency (Hz)	Difference (%)
1	1st Longitudinal bending	0.216	0.215	-0.7
2	1st Vertical bending	0.251	0.247	-1.5
3	1st Lateral bending	0.301	0.304	0.9
4	2nd Vertical bending	0.316	0.309	-2.3
5	2nd Lateral bending	0.366	0.370	1.1
6	3rd Vertical bending	0.483	0.475	-1.6
7	3rd Lateral bending 1st Torsion	0.489	0.489	-0.1
8	4th Vertical bending	0.551	0.552	0.2
9	2nd Torsion	0.571	0.575	0.7
10	5th Vertical bending	0.593	0.592	-0.1

The comparisons of mode shapes and natural frequencies in Figure 29 and Table 10 show good agreement between the implicit model and the explicit model.

TIED-ARCH BRIDGE

The Whittier Bridge, as shown in Figure 30, is a pair of suspended tied-arch bridges connecting Newburyport and Amesbury over the Merrimack River in Massachusetts, USA. The north bound bridge has been selected as a representative of tied-arch bridges for investigation in this project. The bridge has a total length of 480 feet with four vehicular lanes in one direction plus a 14 feet shared use path for pedestrians and bicycles. The total width of the bridge deck is 100 feet-4 inches. The two lateral arches are 76 feet high with eight cross bracings spread out along the length of the arch to ensure their horizontal stability. The two lateral arches are connected to the lower girders by 36 cross inclined hangers on each side. The hangers are numbered based on their working points along girder members and the spacing between these working points of hangers along girder member is 12 feet.

Source: HNTB.

Figure 30. Photo. A view of the Whittier Bridge.

Implicit Model

An implicit model of the Whittier Bridge was developed in SAP 2000® as shown in Figure 31. The finite element model included the main girders, arch members, inclined hangers, floor beams, stringers, secondary bracing members and concrete deck. The steel arches, girder members, floor beams, stringers, top and bottom bracing were modeled by general 3-D frame elements. Each inclined hanger was modeled by single cable elements. The precast concrete slabs were modeled by plate elements. Roller supports were applied at the north end of the girders and pinned supports were applied at the south end of the girders. Other nonstructural components were considered by equivalent forces, which were converted to masses during modal analysis by adding the specified load pattern as a mass source. The connections between the concrete slabs and floor beams, floor beams and stringers, floor beams and bottom bracing were modeled by body constraints. Linear elastic materials were used for all the structural components. Overall, the entire model consisted of 4,528 nodes, 2,042 frame elements, 2,400 plate elements and 72 cable elements. A summary of component modeling and element types is shown in Table 11.

Table 11. Element type in the implicit model of the Whittier Bridge.

Structural Members	Element type
Inclined Hangers	Single Cable Element
Structural Steel Members (Arches, Girders, Floor Beams, Stringers and others)	3-D Frame Element
Concrete Deck	Plate Element
Miscellaneous Connections	Body Constraint
Nonstructural Elements (Barriers and others)	Equivalent Force

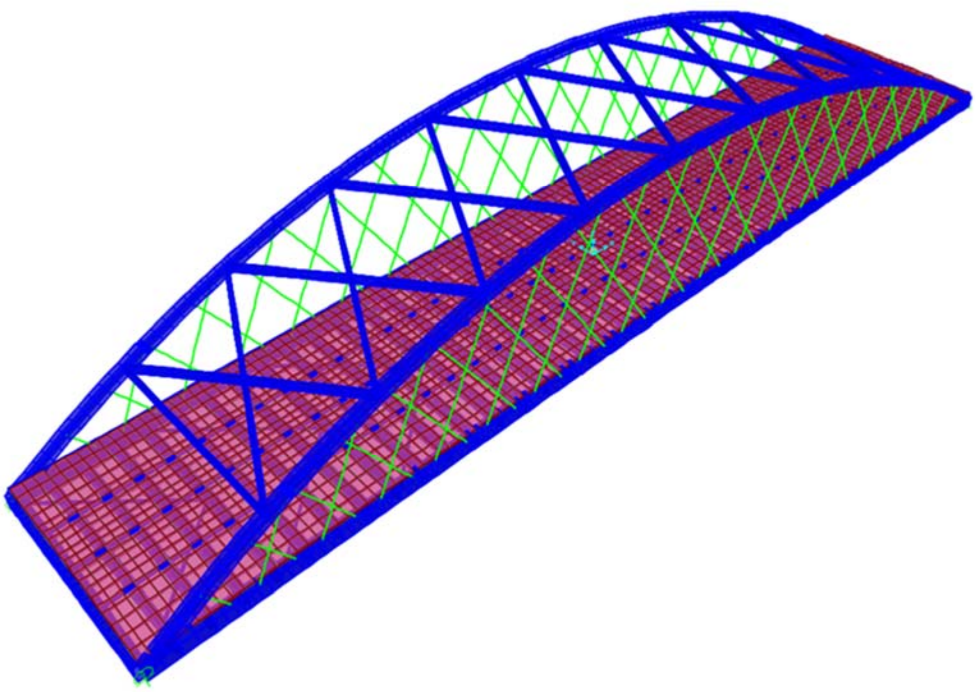

Source: FHWA.

(a) Isometric view.

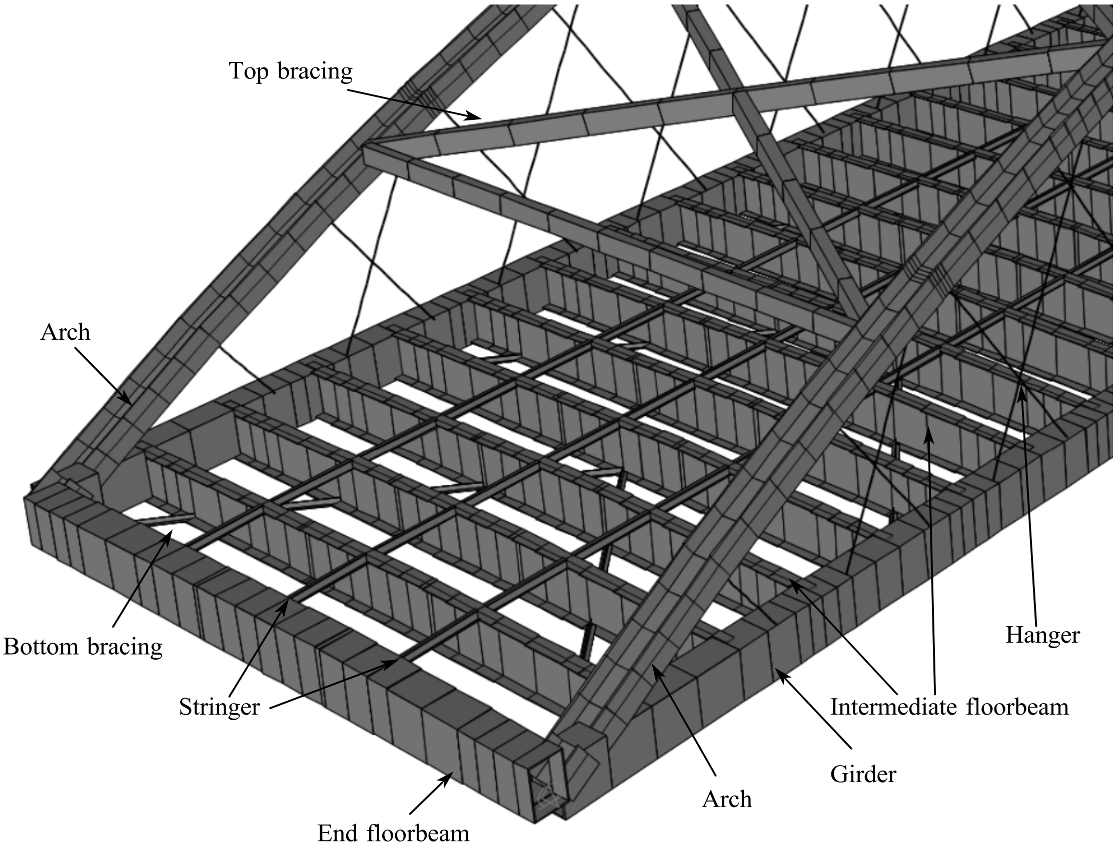

Source: FHWA.

(b) Component information.

Figure 31. Illustrations. Implicit model of the Whittier Bridge.

Explicit Model

Like the cable-stayed bridge, an explicit 3-D finite element model of the Whittier Bridge was developed in LS-DYNA®, as shown in Figure 32. The basic geometry of the explicit model is the same as the implicit model. Table 12 summarizes key aspects of the explicit model. Overall, the model has 6,650 nodes, 2,122 beam elements and 2,400 shell elements. Similar to the explicit model of the cable-stayed bridge, all structural steel members were modeled by Hughes-Liu beam elements with cross section integration; the inclined hangers were modeled by multiple truss elements; post-tensioning strands in the bridge deck were modeled explicitly with truss elements. An assumed total pre-stress loss of 35% was considered in modeling the deck.

Since the hangers in the tied-arch bridge are much shorter than cables in the cable-stayed bridge, five truss elements instead of ten were used for each hanger to reduce the calculation cost. Material nonlinearity in structural steel members and inclined hangers were modeled with an elastic-plastic behavior with kinematic hardening as done in the explicit model of the cable-stayed bridge.

Table 12. Element and material information in the explicit model of the Whittier Bridge.

Structural Members	Element Types	Material Model
Inclined Hangers	Multiple Truss Elements	*MAT_PLASTIC_KINEMATIC
Structural Steel Members (Arches, Girders, Floor Beams, Stringers and others)	Hughes-Liu Beam with Cross-section Integration	*MAT_PLASTIC_KINEMATIC
Concrete Deck	Fully-Integrated Shell Element	*MAT_CONCRETE_EC2
Miscellaneous Connections	*CONSTRAINED_NODAL_RIGID_BODY	
Nonstructural Elements (Barriers and others)	Mass element	

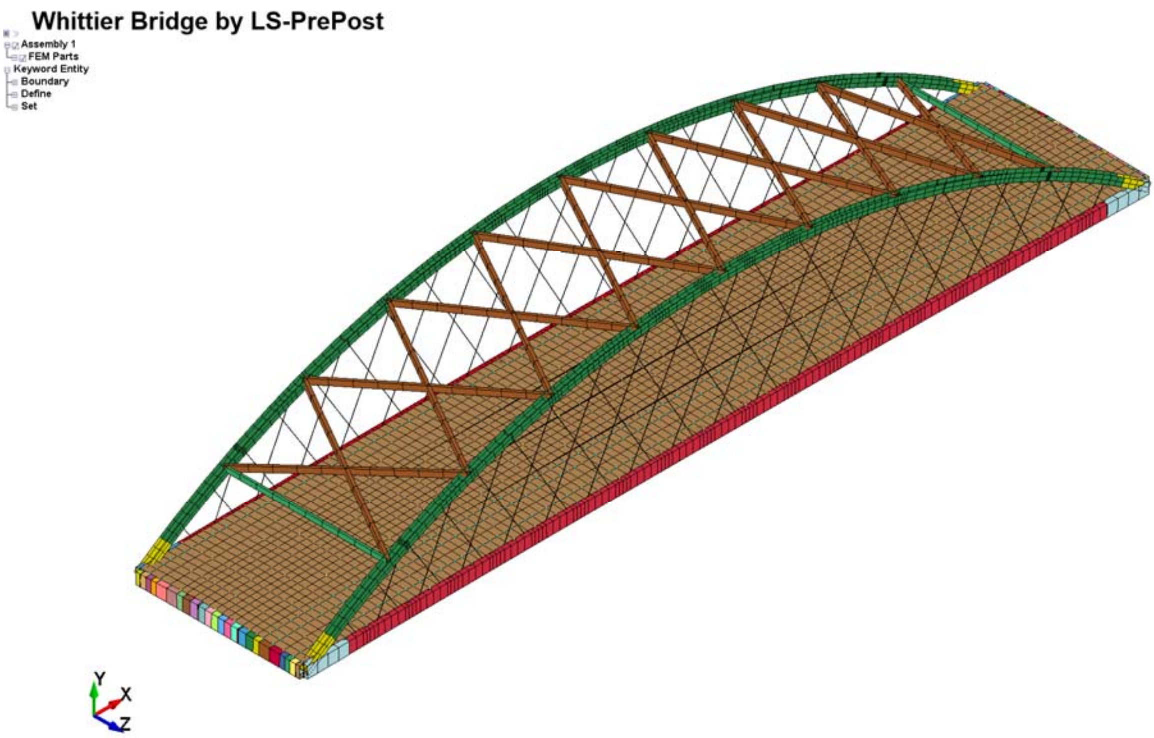

Source: FHWA.

(a) Isometric view.

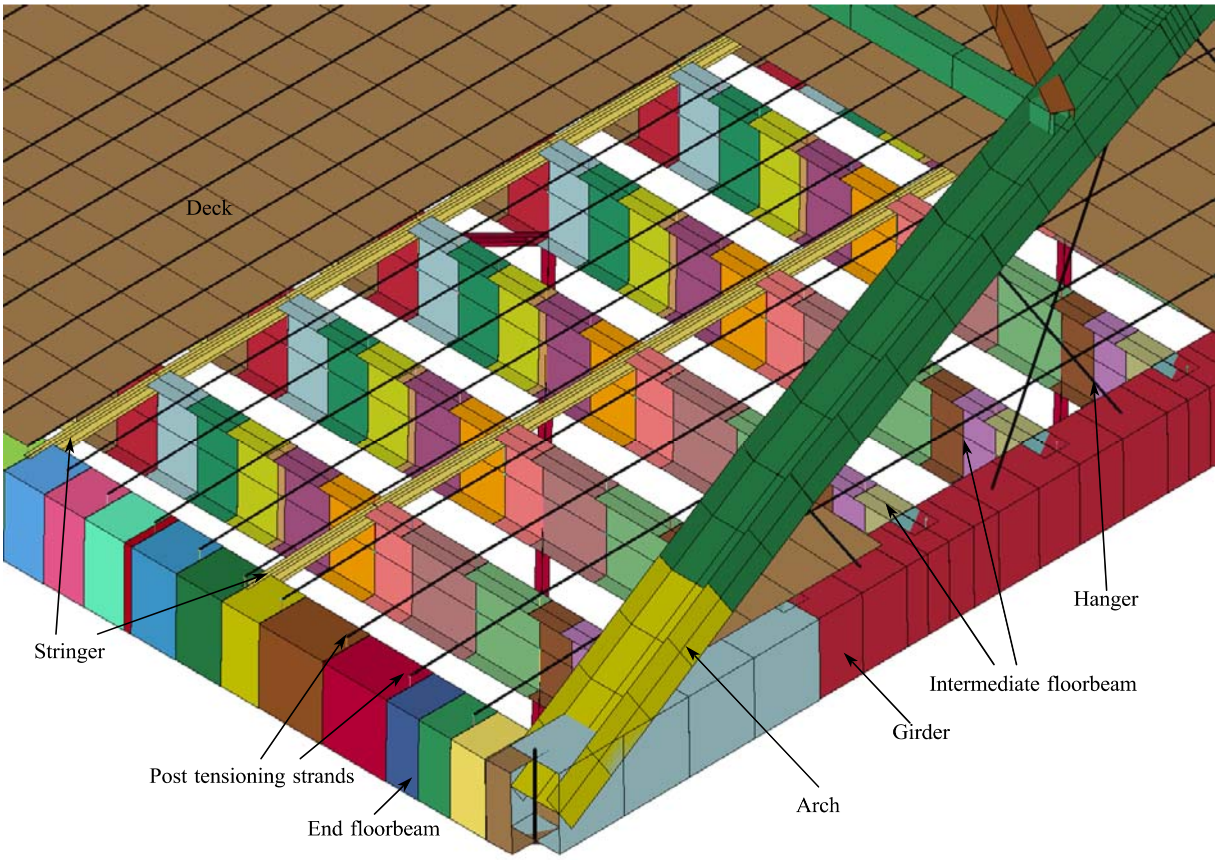

Source: FHWA.

(b) Components information.

Figure 32. Illustrations. Explicit model of the Whittier Bridge.

Bridge Deck

The precast concrete deck was modeled by shell elements with *MAT_CONCRETE_EC2 (*MAT_172), which is widely used in concrete slab modeling, such as Vasudevan (2012), Bojanowski and Balcerzak (2014) and Rackauskaite et al. (2017). This material model can represent a smeared combination of concrete and reinforcement by defining the fraction of reinforcement. Concrete cracking in tension and crushing in compression, and reinforcement yield, hardening and failure criteria are modeled in this material model. The material data and equations governing the behavior are taken from Eurocode 2 (CEN 2004). A non-thermally sensitive concrete model (Type 3) with the stress-strain behavior defined in Figure 33 was used for the precast concrete deck. The compressive behavior of the concrete initially follows the relationship defined by Equation (12), then follows a linear softening response after reaching the ultimate compressive strength. Tensile behavior follows a cracking with tension-stiffening behavior after the tensile capacity is reached.

$$\text{Stress} = FC_{max}\left[\frac{\varepsilon}{\varepsilon_{cl}} \cdot \frac{3}{2+\left(\frac{\varepsilon}{\varepsilon_{cl}}\right)^3}\right] \tag{12}$$

where ε_{cl} is the strain at which the ultimate compressive strength $FC_{\max}$ is reached. The strain ε_{cl} is calculated from the elastic stiffness as $\varepsilon_{cl} = 3FC_{\max}/(2E)$.

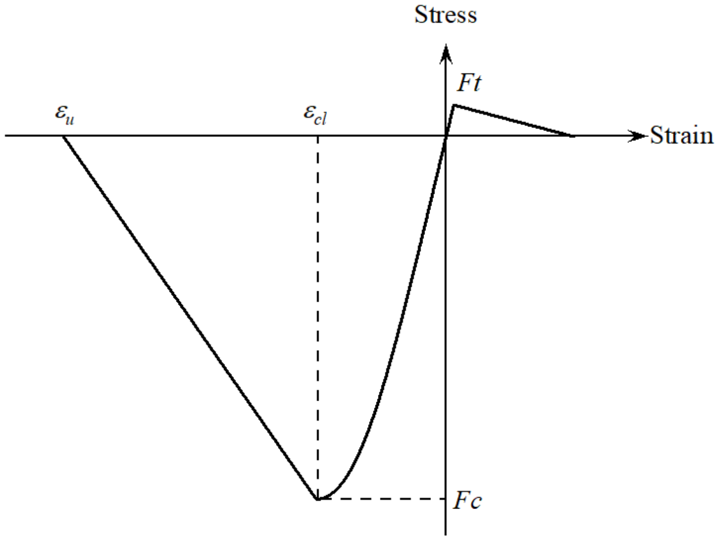

Source: FHWA.

Figure 33. Illustration. Concrete stress strain behavior in *MAT_172.

Concrete unloading behavior in this material model is shown in Figure 34. The elastic modulus is reduced according to the parameter UNLFAC in the material model. The initial elastic modulus is used during unloading and reloading when UNLFAC is zero. On the other hand, no permanent strain exists after unloading if UNLFAC is 1. UNLFAC = 0.5 is used in the concrete deck model, which implies that a permanent strain linearly interpolated between 0 and the extreme value is employed.

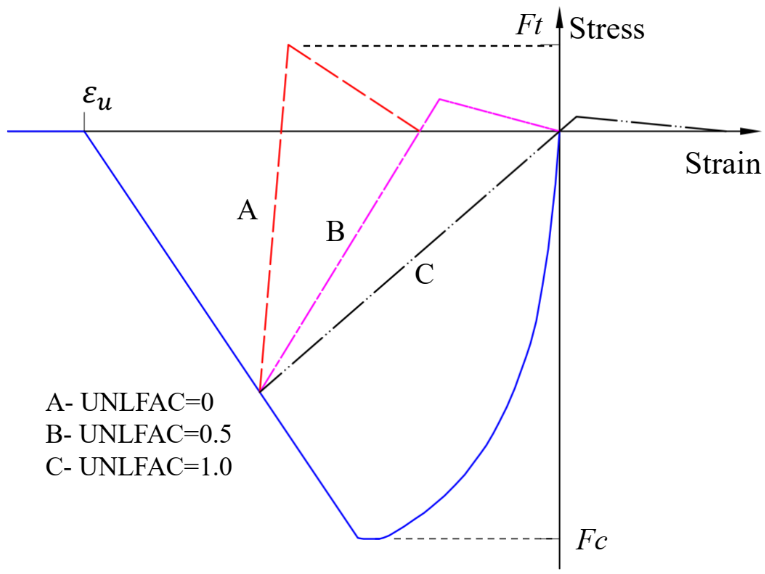

Source: FHWA.

Figure 34. Illustration. Concrete unloading behavior in *MAT_172.

Accuracy of the FE Models

In order to ensure accuracy of both implicit and explicit models, cross validation was conducted between both models under dead load. Like the cable-stayed bridge simulation, all the related loads were applied as a nonlinear load combination under dead load in the implicit model. In the explicit model, the application of dead load was achieved through the following steps.

Stage 1: Time ranges 0 to 10 seconds: During this stage, pretension forces in the hangers and self-weight of the main structure were applied. Large global damping (i.e., 80% of critical damping) was applied to prevent excessive vibrations that could lead to premature failure. The concrete deck did not contribute stiffness during this stage since it was cast after installation of the girders and frames. However, it contributed mass. As such, the deck was modeled, but its Young's modulus and that for the post-tensioning strands were reduced to 5% of their normal values to reduce their contribution to stiffness to the extent practicable. In addition, the concrete deck material was made to behave elastically to prevent unfavorable cracking in the deck during this stage.

Stage 2: Time ranges 10 to 30 seconds: The elastic moduli of the deck and post-tensioning strands were increased to their normal values and the post tensioning forces were applied. As in Stage 1, large global damping (i.e., 80% of critical damping) was employed to prevent numerical problems associated with excessive vibrations.

Stage 3: Time ranges 30 to 40 seconds: The material model of concrete deck was changed from an elastic one to the nonlinear one described earlier. As in Stages 1 and 2, large global damping (80% of critical damping) was still implemented to prevent unfavorable cracking in the deck.

The results of the explicit model under dead load were extracted at the end of Stage 3 when the vibrations had mostly died down. The data included vertical displacements, reaction forces, cable forces and mode shapes for the two models.

Vertical Displacements under Dead Load

The vertical deflection profiles along the main girder in the implicit and explicit models of the tied-arch bridge are compared in Figure 35. The deflection was measured from the initial cambered position of the girder. Similarly, the vertical deflection along the main arch in both models is shown in Figure 36. Overall, the maximum downward deflection on the girder was located at the center with a value equal to approximately 8.9 inches. The maximum downward deflection on the arch was approximately 7.5 inches. The comparison results show good agreement between the two models.

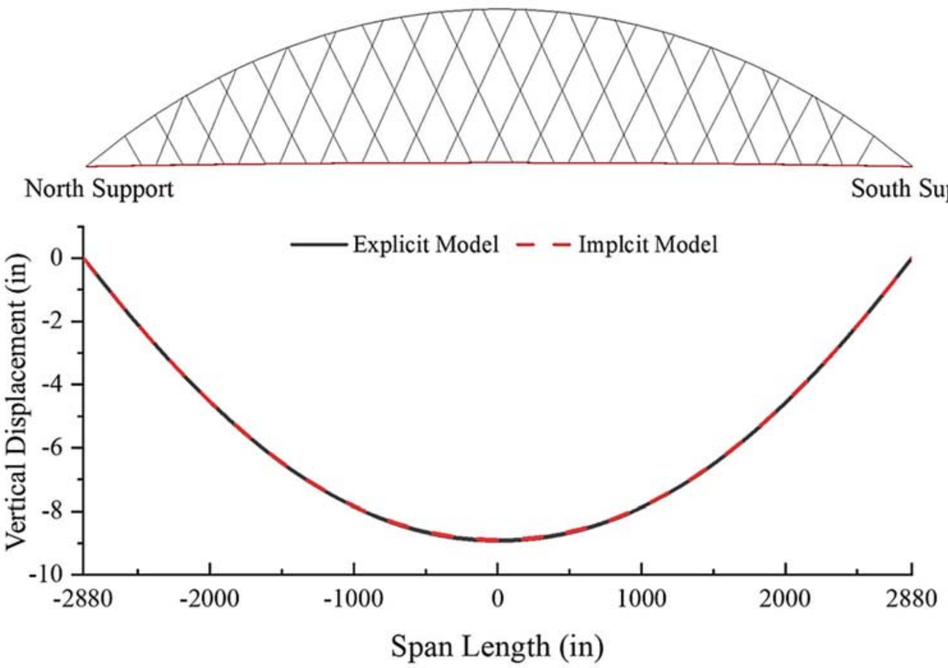

Source: FHWA.

Figure 35. Graph. Comparison of girder vertical deflection in the Whittier Bridge (West Plane)

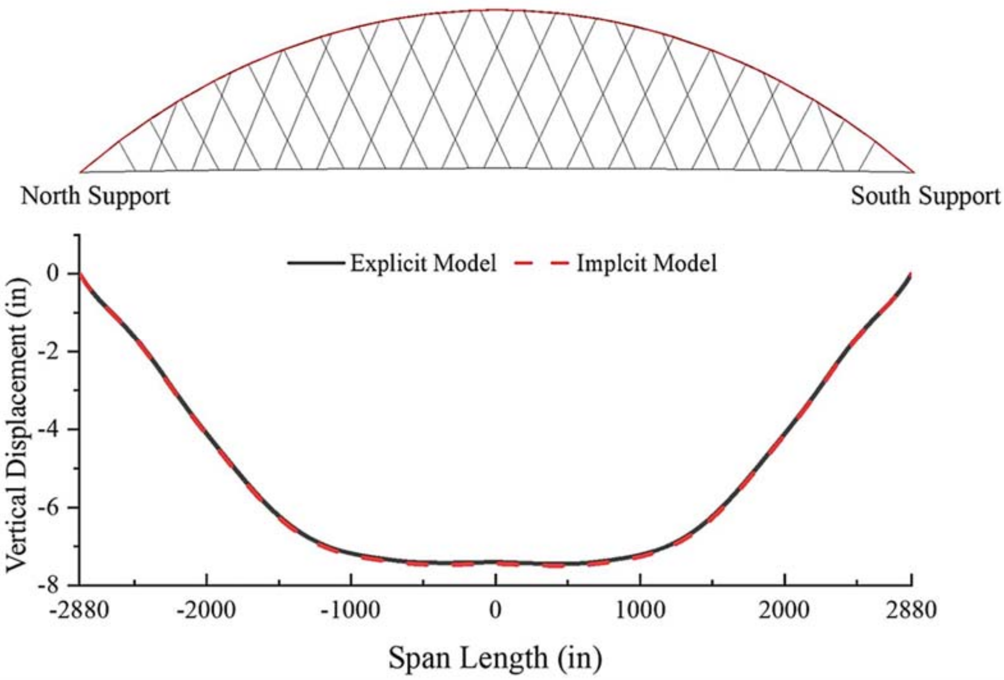

Source: FHWA.

Figure 36. Graph. Comparison of arch vertical deflection in the Whittier Bridge (West Plane)

Internal Forces under Dead Load

The reaction forces at the four corners in the implicit model and explicit model are shown in Table 13. The comparison of hanger forces in each plane is shown in Figure 37. Clearly both models match quite well.

Table 13. Comparison of reaction force and total weight of the tied-arch bridge.

Vertical Reaction	**Design Drawing** (kips)	**Implicit Model** (kips)	**Difference** (%)	**Explicit Model** (kips)	**Difference** (%)
Node 1	3,668	3,691.02	0.6	3,700.40	0.9
Node 153	3,668	3,691.11	0.6	3,699.20	0.9
Node 154	3,668	3,692.46	0.7	3,701.00	0.9
Node 306	3,668	3,690.96	0.6	3,700.20	0.9
Total Weight	14,672	14,765.54	0.6	14,800.80	0.9

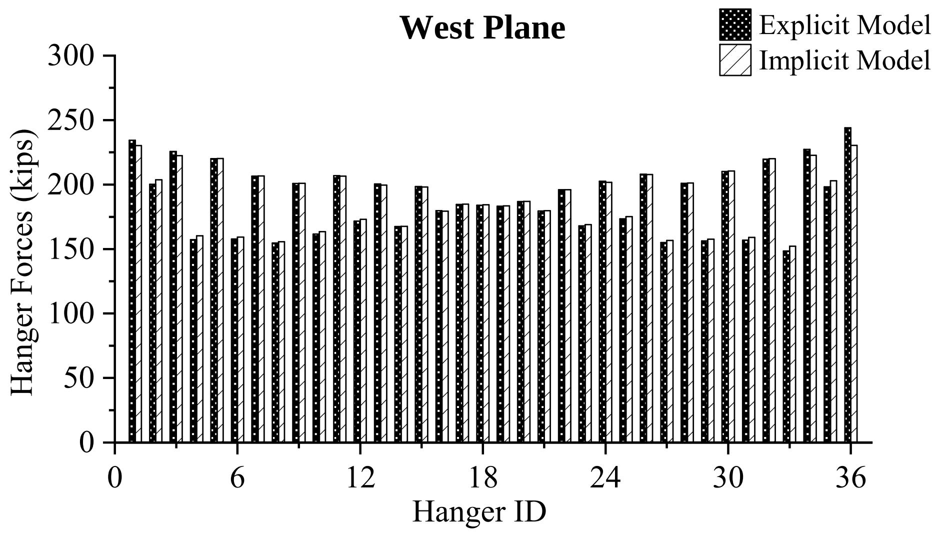

Source: FHWA.

(a) West Plane.

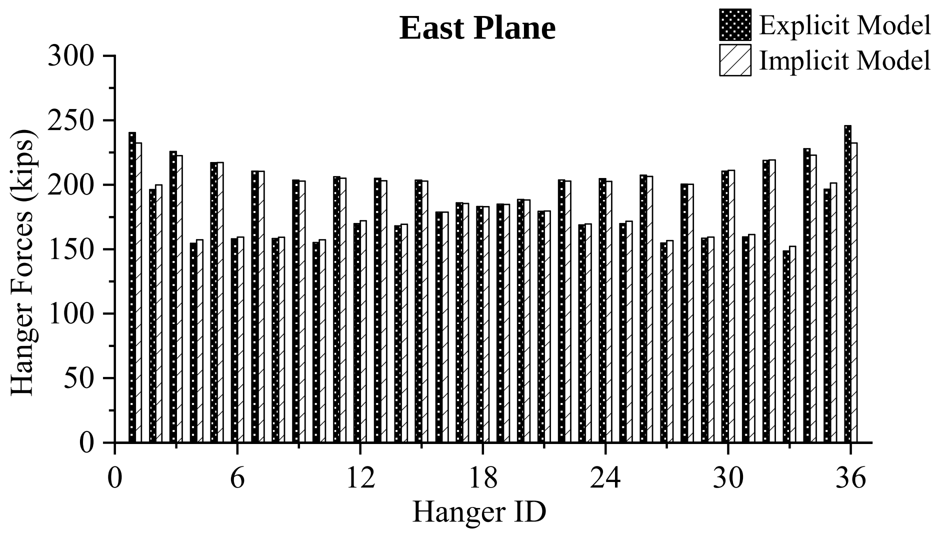

Source: FHWA.

(b) East Plane.

Figure 37. Graphs. Comparison of hanger forces in the Whittier Bridge.

Modal Analysis

The first five mode shapes and natural frequencies obtained by the implicit and explicit models of the bridge are listed in Figure 38 and Table 14. The results show that the mode shapes computed from the implicit and explicit models and corresponding natural frequencies match well.

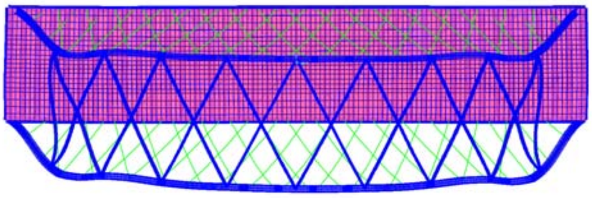

(1) Mode 1 (f = 1.267 Hz; T = 0.789 seconds)

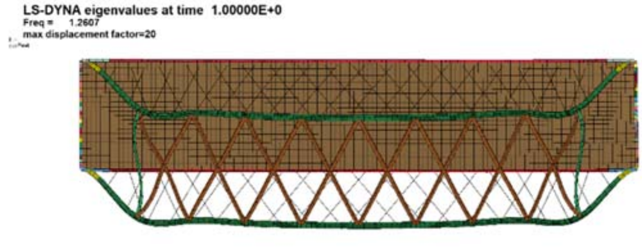

(1) Mode 1 (f = 1.261 Hz; T = 0.793 seconds)

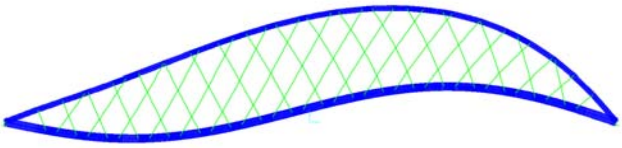

(2) Mode 2 (f = 1.274 Hz; T = 0.785 seconds)

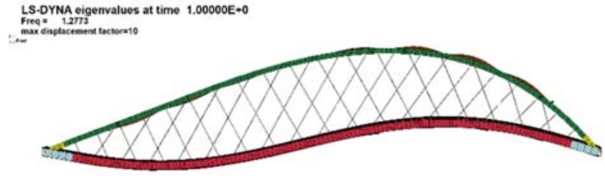

(2) Mode 2 (f = 1.277 Hz; T = 0.783 seconds)

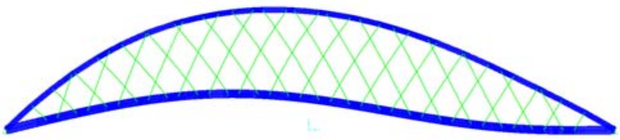

(3) Mode 3 (f = 1.303 Hz; T = 0.767 seconds)

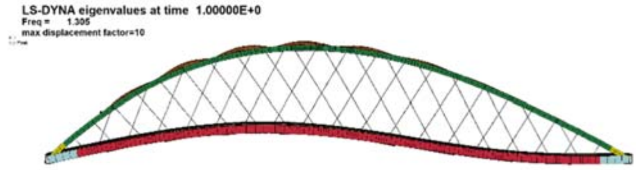

(3) Mode 3 (f = 1.305 Hz; T = 0.766 seconds)

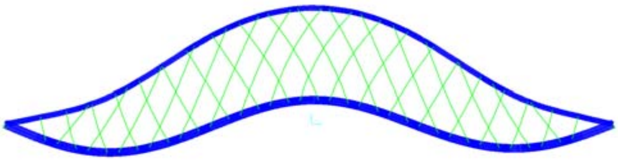

(4) Mode 4 (f = 1.980 Hz; T = 0.505 seconds)

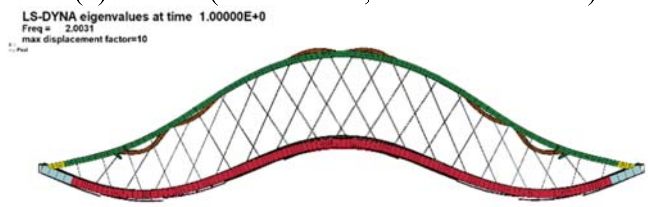

(4) Mode 4 (f = 2.003 Hz; T = 0.499 seconds)

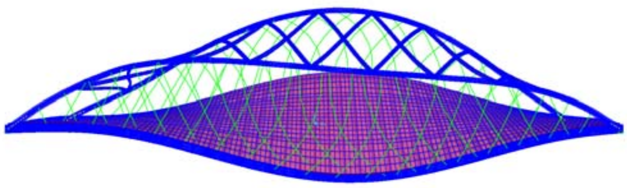

(5) Mode 5 (f = 2.186 Hz; T = 0.457 seconds)

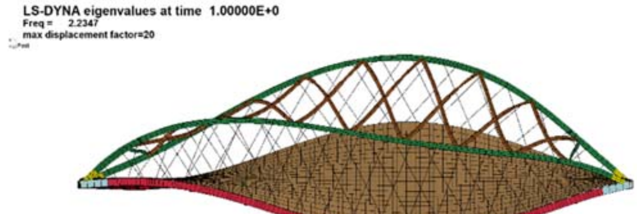

(5) Mode 5 (f = 2.235 Hz; T = 0.447 seconds)

Source: FHWA.

Figure 38. Illustrations. First five global mode shapes of the Whittier Bridge.

Table 14. Natural frequencies of the Whittier Bridge.

Mode No.	**Type**	**Implicit Model Frequency** (Hz)	**Explicit Model Frequency** (Hz)	**Difference** (%)
1	1st Lateral bending	1.267	1.261	-0.5
2	1st Vertical bending	1.274	1.277	0.2
3	2nd Vertical bending	1.303	1.305	0.2
4	3rd Vertical bending	1.980	2.003	1.2
5	1st Torsional	2.186	2.235	2.2

SUSPENSION BRIDGE

The Delaware Memorial Bridge, shown in Figure 39, is a pair of twin long-span suspension bridges linking Delaware and New Jersey above the Delaware River. The 1st structure was opened on August 16, 1951 and the 2nd structure was opened on September 12, 1968. In this research, the 2nd structure of the Delaware Memorial Bridge was selected as a representative of typical suspension bridges.

Source: © 2015 Acroterion (licensed under CC BY-SA 3.0) (cropped)

Figure 39. Photo. A view of the Delaware Memorial Bridge.

The 2nd structure of the Delaware Memorial Bridge was designed in accordance with 1961 AASHO Specifications (AASHO 1961). As shown in Figure 40, it is a three-span suspension bridge with two steel towers. The suspended structure consists of a 2,150 feet-long center span and two 750 feet long side spans. The total length is 3,650 feet. The roadway is 52 feet wide from curb to curb and accommodates four 13-feet wide traffic lanes, as shown in Figure 41.

The suspended structure consists of two stiffening trusses spaced 61 feet apart, floor trusses spaced 15 feet apart and an 8-inch-thick reinforced concrete deck. The concrete deck is supported on floor trusses by 11 rolled-shape steel stringers placed in the transverse direction of the bridge. On each side of the concrete deck, a welded stringer is connected to the concrete deck to accommodate a 3feet-1inch wide sidewalk. As shown in Figure 42, the stiffening trusses are Warren type and are composed of 142 truss panels. The suspended structure is also vertically supported by 69 pairs of suspenders from the main cables.

The bridge has two main cables designed in a 2nd degree parabola configuration with a 1/10 sag to span ratio at the center span. Each main cable was made up of 9,196 No. 6 U.S. gauge galvanized cold-drawn steel wires laid up to in 19 strands of 484 wires each. The equivalent diameter of the cable is 1.57 feet. There are two sizes of suspender strands: 2.50 inch diameter steel strands in the middle section of the center span and 2.3125 inch diameter steel strands at other locations. Each suspender consists of a group of four steel strands. The suspender spacing is 51.85 feet in the center span and 50.43 feet in the two side spans.

The steel towers are 418.08 feet high. Each tower consists of two shafts braced together with a lower strut located around 146 feet from the base and another strut at the top of the tower.

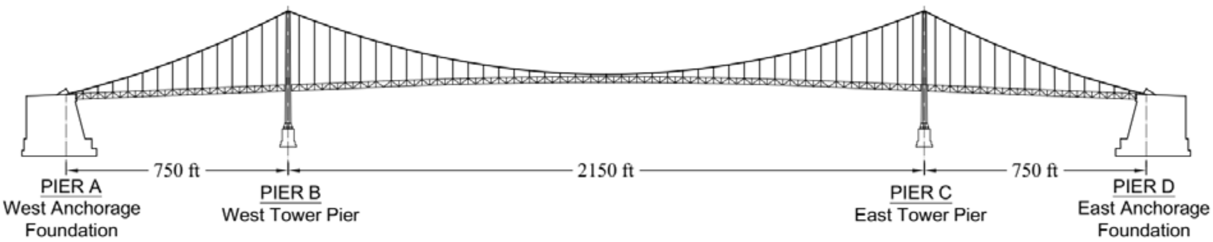

Source: Delaware River and Bay Authority.

Figure 40. Illustration. Elevation view of the Delaware Memorial Bridge.

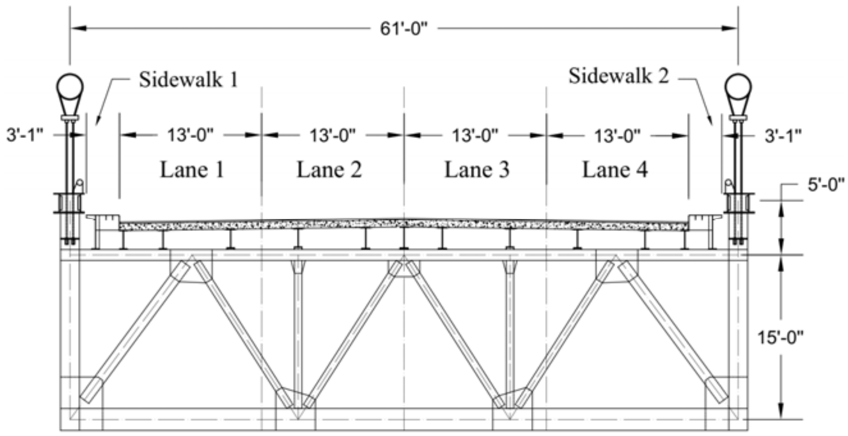

Source: Delaware River and Bay Authority.

Figure 41. Illustration. Cross section of the Delaware Memorial Bridge.

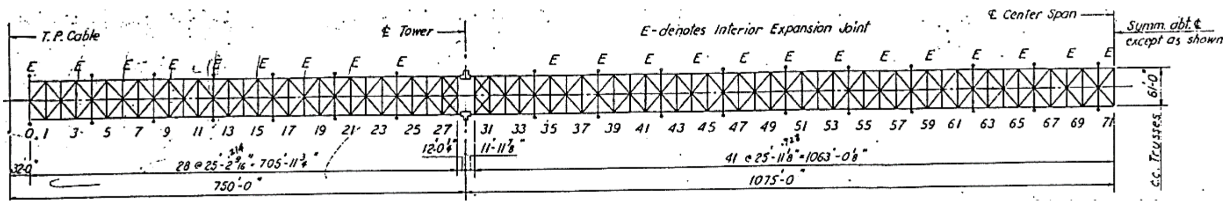

Source: Delaware River and Bay Authority.

(a) Plan view of the stiffening trusses.

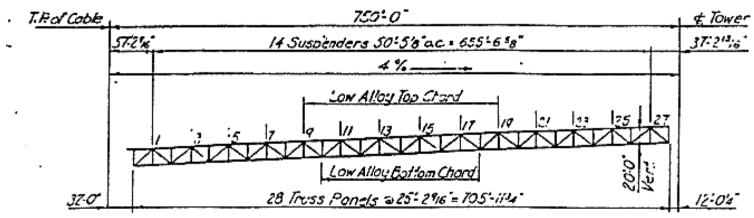

Source: Delaware River and Bay Authority.

(b) Elevation view of the stiffening trusses in a side span.

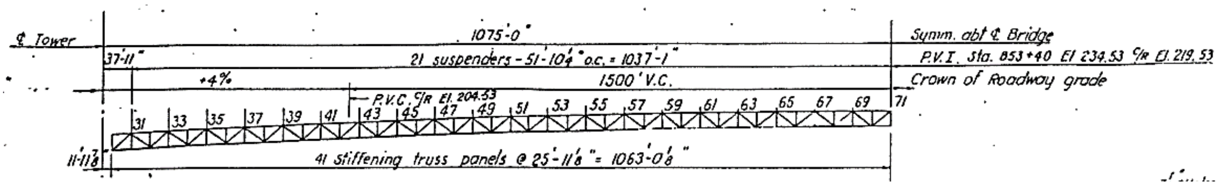

Source: Delaware River and Bay Authority.

(c) Elevation view of the stiffening trusses in the center span.

Figure 42. Illustrations. Configuration of stiffening trusses in the Delaware Memorial Bridge.

Implicit Model

The implicit model of the 2nd structure of the Delaware Memorial Bridge shown in Figure 43 was developed using ANSYS® Mechanical 14.0 (ANSYS 2011). The model accounted for the main cables, steel towers, suspenders, stiffening trusses, steel stringers, concrete deck, tower saddles and nonstructural components such as the inspection catwalk and light poles. The main cables and suspenders were modeled by truss element LINK180, which can take tension only. The tower links were also modeled by a truss element that could take both tension and compression. The bridge towers, stiffening trusses and all other steel structure members, such as stringers, were modeled by BEAM188 elements. The concrete deck was modeled by SHELL181 elements, and MPC184 constraint elements were added between the nodes of stringers and the corresponding nodes of the deck to simulate composite action.

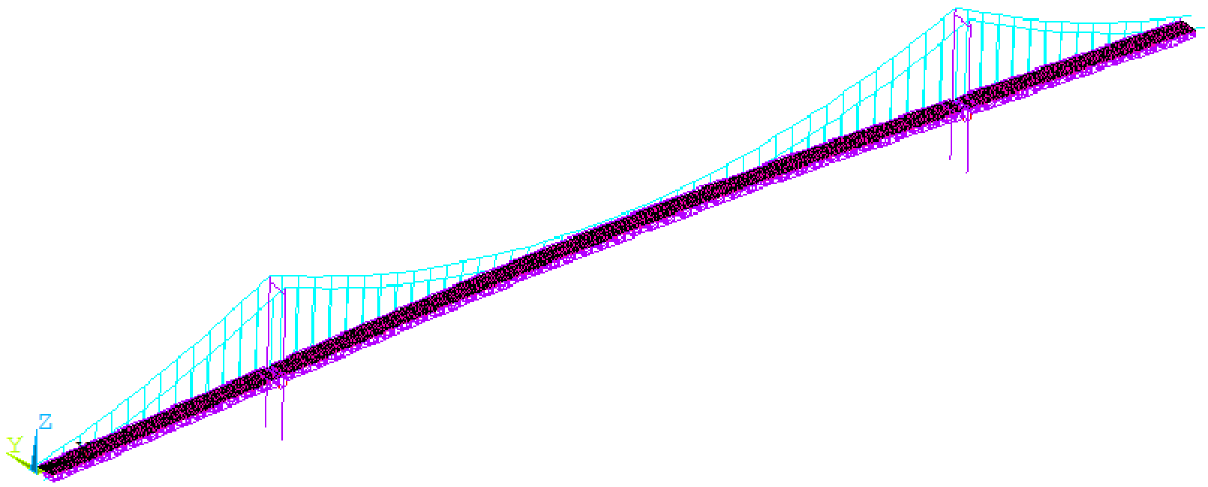

Source: FHWA.

Figure 43. Illustration. The implicit model of the Delaware Memorial Bridge.

The main cables were anchored to the ground at both sides of the bridge with pin connections as shown in Figure 44(a). At the top of the tower, the main cables were supported vertically through the tower saddles. The main cable nodes were coupled with the tower saddle nodes, and the coupling varied with the loading stages. Specifically, for the dead load analysis, only the transverse and vertical degrees of freedom (DOFs) (i.e., UX and UZ) of the nodes were coupled, and the main cable nodes were able to move freely in the longitudinal direction of the bridge (+/-X direction). However, DOFs in all three directions (i.e., UX, UY and UZ) were coupled for the subsequent loads such as live load.

The suspended stiffening trusses at the side spans were simply supported at the bridge abutments. The related boundary conditions are shown in Figure 44(a). The stiffening trusses were connected to the tower through the tower links and wind tongues/shoes, which provided the vertical (+/-Z direction) and lateral (+/-Y direction) supports, respectively. Since general line-type beam elements were used to mode the tower, some virtual massless rigid brackets were added on the lower strut to model the spatial connection with the stiffening trusses. The deck-stringer components were simply supported on the lower strut (cross-beam) through the virtual rigid brackets, which provided both vertical (+Z direction) and lateral (+/-Y direction) supports. The details about these connections are shown in Figure 44(c). Except for the tower links, all these connections between the stiffening trusses and the tower were modeled through DOF coupling constraints. It should be noted that the stiffening trusses were able to move freely in the longitudinal direction (+/-X direction) at the lower strut of the towers, where large expansion joints were installed. More details about modeling of the structural components and the internal connections in the implicit model are introduced in the following section.

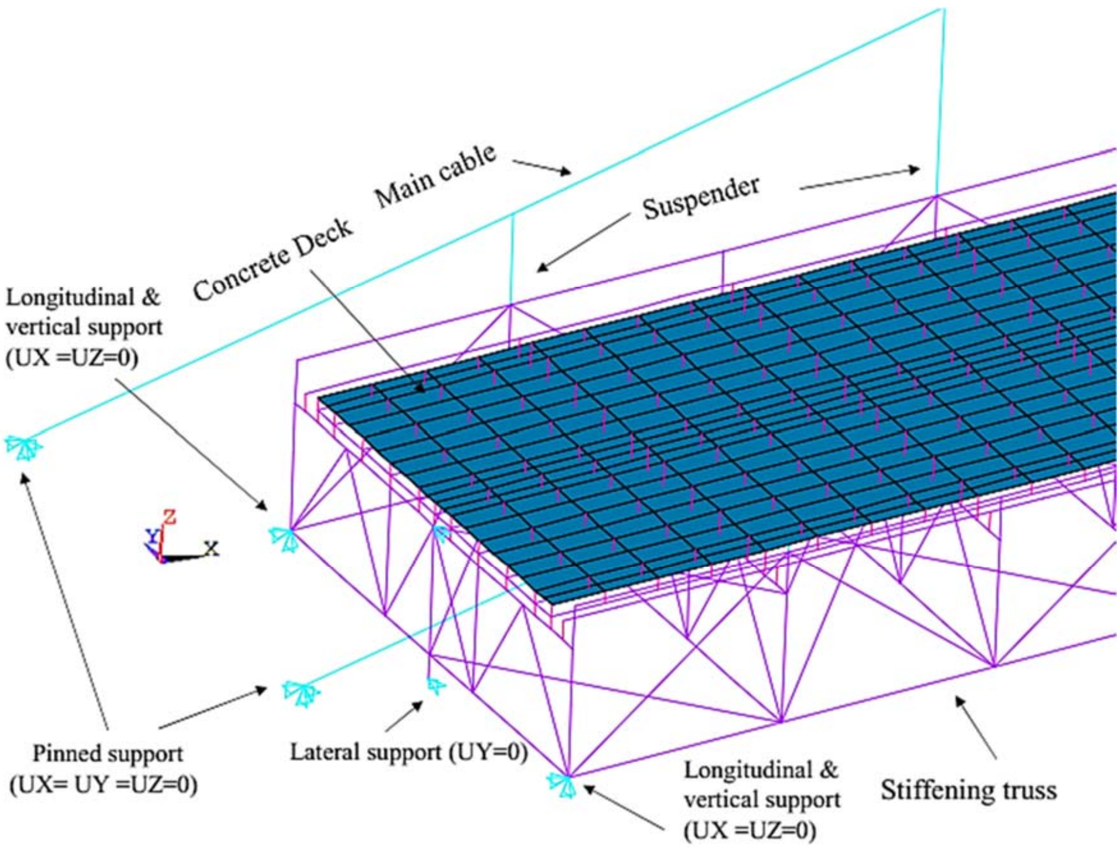

Source: FHWA.

(a) Boundary conditions around bridge abutment.

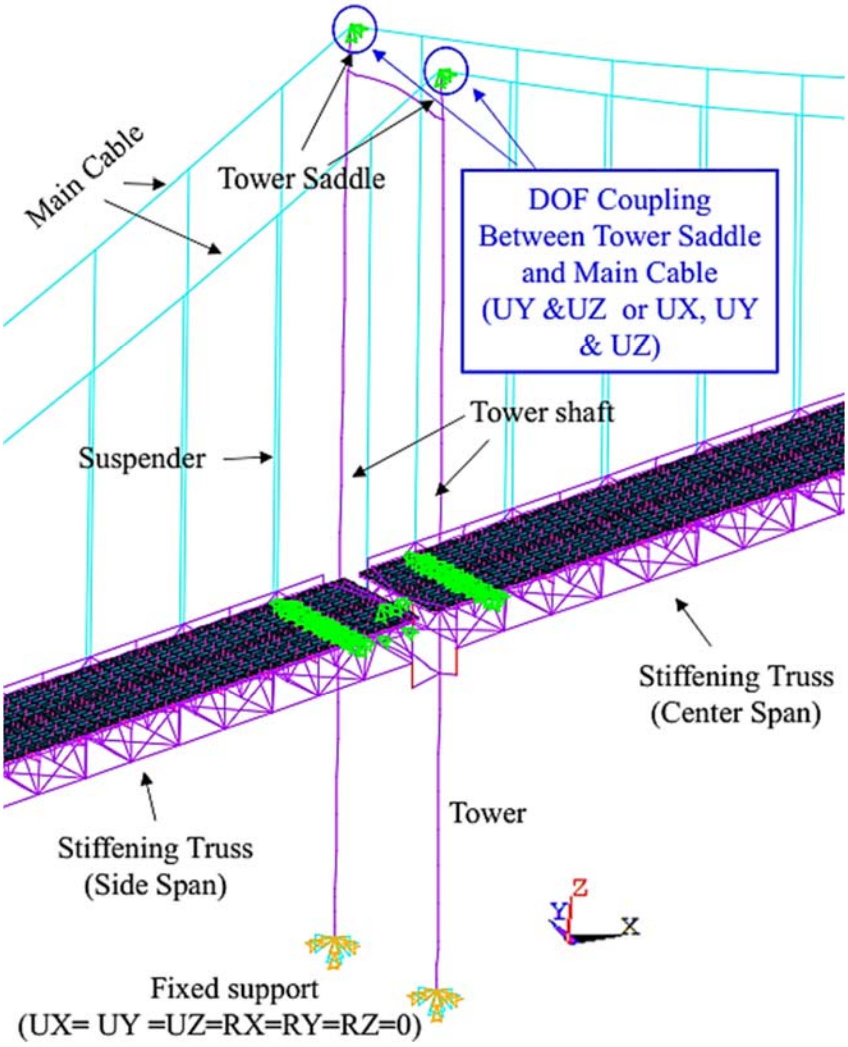

Source: FHWA.

(b) Boundary conditions around tower.

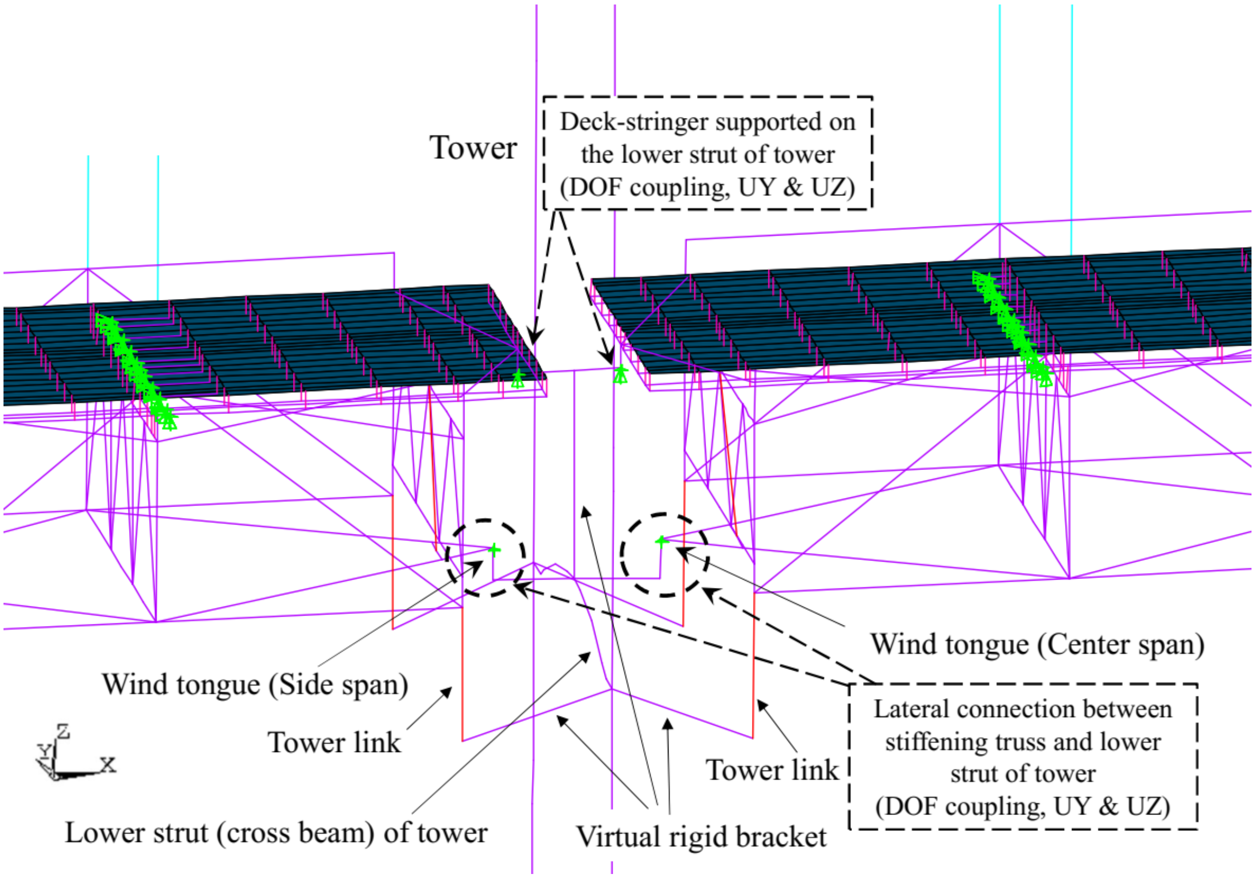

Source: FHWA.

(c) Internal connection between stiffening trusses and lower strut of tower.

Figure 44. Illustrations. Boundary conditions and internal connections of the implicit model.

Although the bridge had 0.75-inch wide interior expansion joints in the stringers and concrete decks between every three panels of the stiffening truss, they were not modeled in the implicit model, considering the fact that the bridge behavior will be hardly affected by these expansion joints under dead and live loads. Except for the rigid structural components, such as saddles, all the other elements in the implicit model were modeled by linear elastic material models. Overall, the entire model consisted of 23,358 nodes and 36,231 elements, including 294 link elements, 14,222 beam elements, 11,200 shell elements, 2,541 mass elements and 7,974 multipoint constraint elements. A summary of component modeling and element types are shown in Table 15.

Table 15. Elements types in the implicit model of the Delaware Memorial Bridge.

Structural Members	Element Type
Main Cables, Suspenders and Tower Links	LINK180
Towers, Stiffening Trusses and Stringers	BEAM188
Deck	SHELL181
Miscellaneous Connections	MPC184
Saddles, Brackets and other Stiff Members	BEAM188
Non-structural Elements (Inspection Walk, Hand Ropes, Light Poles and others)	MASS21

Explicit Model

An explicit 3-D finite element model of the 2nd structure of Delaware Memorial Bridge was developed using LS-DYNA®, as shown in Figure 45. The basic geometry of the explicit model was the same as that of the implicit model. The element types and material models used for different structural and non-structural components are summarized in Table 16. Overall, the explicit model had 25,898 nodes, 19,928 beam elements, 11,200 shell elements, 6,649 nodal rigid bodies, 2,541 mass elements and 100 rigid elements. Details about the material nonlinearity for each structural component, modeling for some special structural components and key connections are introduced in the following sub-sections.

Source: FHWA.

(a) Elevation view.

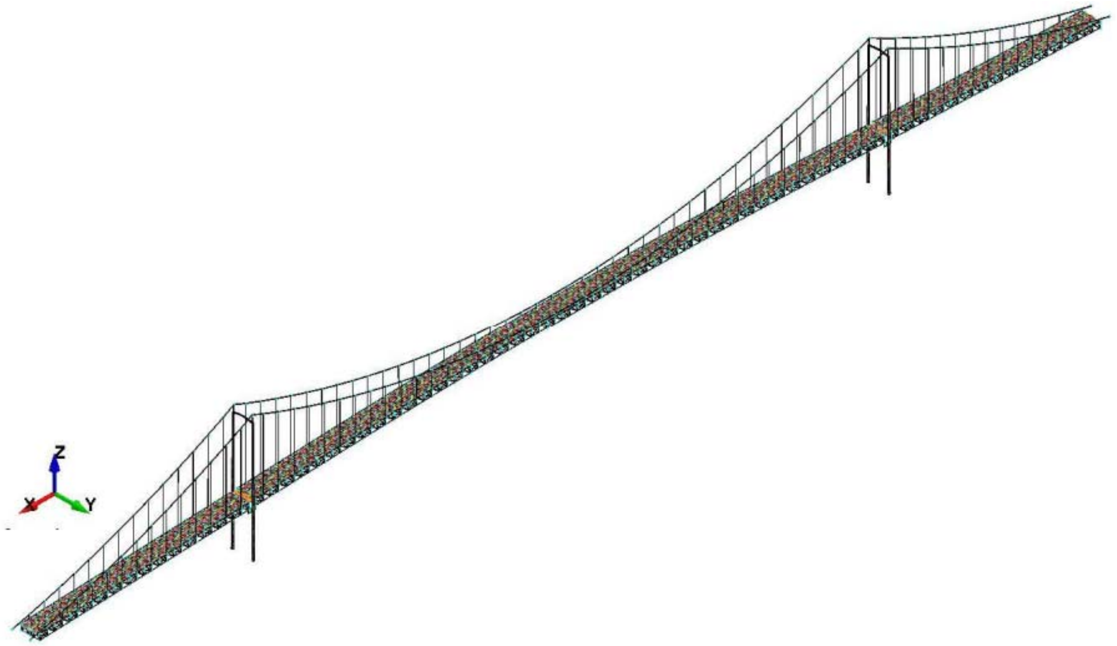

Source: FHWA.

(b) Isometric view.

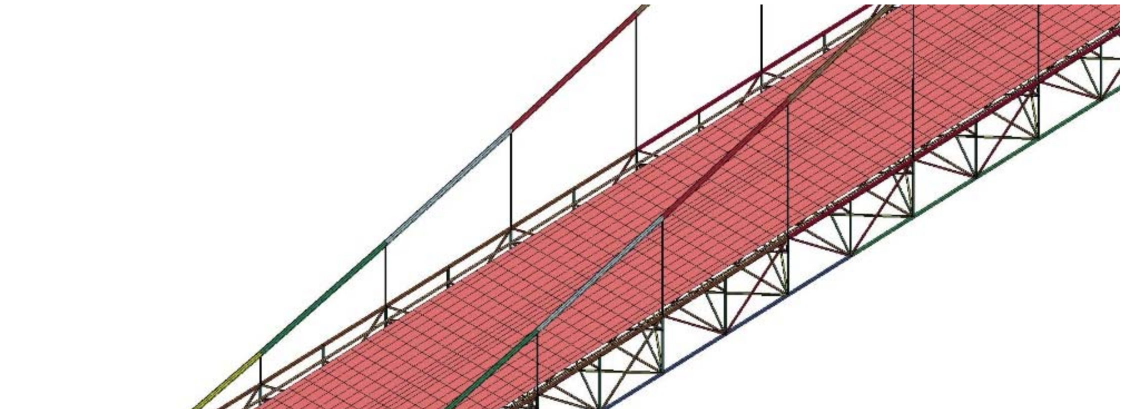

Source: FHWA.

(c) Suspended structure near a bridge abutment.

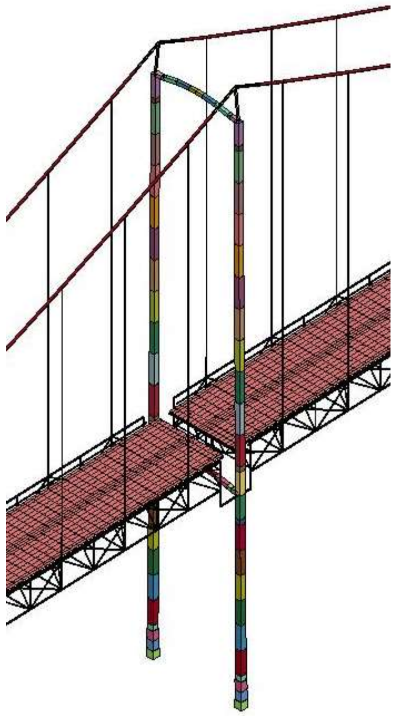

Source: FHWA.

(d) Tower.

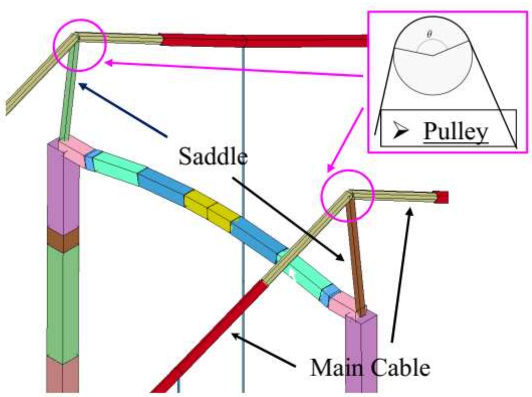

Source: FHWA.

(e) Pulley elements.

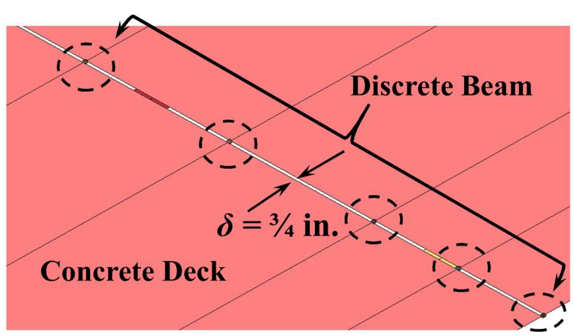

Source: FHWA.

(f) Interior Expansion Joints (IEJ) between deck panels.

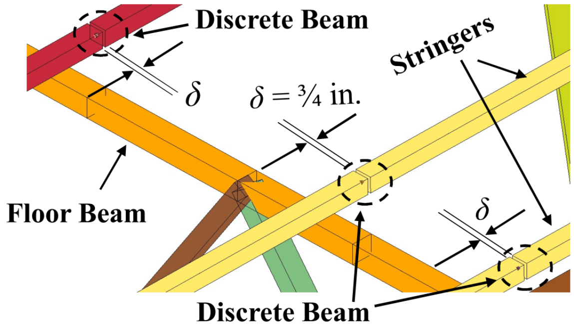

Source: FHWA.

(g) IEJ between stringers.

Figure 45. Illustrations. The explicit model of the Delaware Memorial Bridge.

Table 16. Element types and material models for the explicit model of the Delaware Memorial Bridge.

Structural Members	Element Type	Material Model
Main Cables (near tower saddles)	Cable	*MAT_CABLE_DISCRETE_BEAM(*MAT_071)
Main Cables (others)	Truss	*MAT_PLASTIC_KINEMATIC(*MAT_003)
Suspenders	Truss	*MAT_PLASTIC_KINEMATIC(*MAT_003)
Towers, Stiffening Trusses and Stringers	Belytschko-Schwer Resultant Beam	*MAT_ELASTIC(*MAT_001) *MAT_SIMPLIFIED_JOHNSON_COOK(*MAT_098)
Tower Saddles, Brackets and other Stiff Members	Belytschko-Schwer Resultant Beam	*MAT_RIGID(*MAT_020)
Deck	Shell	*MAT_PLASTICITY_COMPRESSION_TENSION(*MAT_124)
Non-structural Components	Mass	N.A.
Connections between Main Cables and Tower Saddles	Pulley with Friction	N.A.
Connections between Concrete Deck and Steel Girders	N.A.	*CONSTRAINED_NODAL_RIGID_BODY
Connections at Internal Expansion Joint	Discrete Beam	*MAT_NONLINEAR_ELASTIC_DISCRETE_BEAM(*MAT_067)

Component Modeling

Main Cables

Each of main cables consists of 9,196 No. 6 U.S. gauge galvanized cold-drawn steel wires, each wire being 0.196 inches in diameter. The cables were modeled by line type elements (i.e., truss or cable elements) with properties equivalent to the bundle of wires. Only one element was used to model the portion of the main cable between each two adjacent suspenders. A total of 152 elements were used to model the two main cables.

Two types of elements were used to model the main cables, see Figure 46. Most of main cable segments were modeled by a resultant truss element with the nonlinear material type *MAT_PLASTIC_KINEMATIC (*MAT_003), which can simulate both the plastic kinematic and failure behavior of cable materials. Pulley elements were used to simulate potential slipping of the main cables over tower saddles. However, since pulley elements are not compatible with truss elements with the material type *MAT_003, a portion of the main cables element near the tower saddle was modeled by a cable element with the material type *MAT_CABLE_DISCRETE_BEAM (*MAT_071), which is compatible with the pulley element. It should be noted that the material model *MAT_ 071 is only applicable for linear/nonlinear elastic cables, unlike the other material model, which could account for material inelasticity. However, since this segment of the main cable is short, its effect on the overall main cable and the whole bridge was deemed negligible.

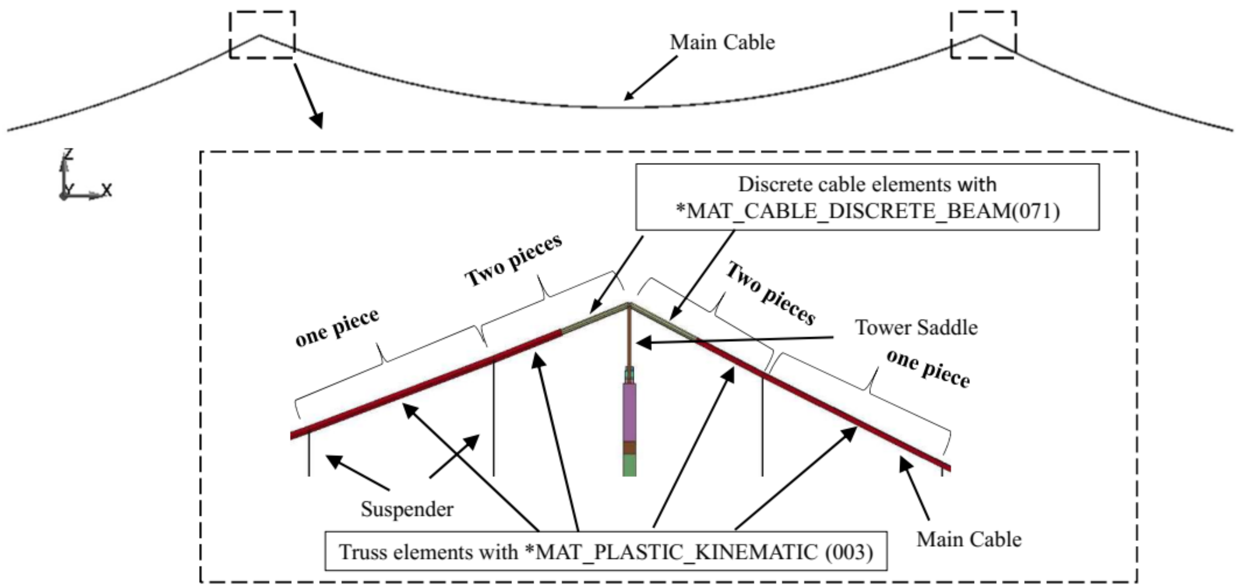

Source: FHWA.

Figure 46. Illustration. Main cable in the explicit model.

Cable Slippage

The main cable can slip over the saddle when the friction force between the cable and saddle is overcome by the unbalanced force across the saddle. Slip is important to model because this type of behavior can occur under pushdown analysis or after the bridge suffers significant damage, such as the loss of a certain number of suspenders. In order to simulate such behavior, pulley elements (*ELEMENT_BEAM_PULLEY) were added between the tower saddles and the main cable elements near the saddle. The Coulomb friction model was used to simulate friction between the main cable and tower saddle. The input parameters of the pulley are shown in Table 17, in which FD is the dynamic friction coefficient and FS is the static friction coefficient, LMIN is the minimum length, and DC is the decay constant to allow a smooth transition between the static and dynamic friction parts of the response. With this modeling option, the explicit model of the bridge was able to simulate the bridge behavior well without and with slipping of the main cable. The values in Table 17 were based on research in Takena et al. (1992), who investigated the friction between main cables and tower saddles in several existing long-span suspension bridges with characteristics similar to the 2nd structure of the Delaware Memorial Bridge. They reported the friction coefficient to be mainly in the range of 0.15 ~ 0.30. Hence, the median values of 0.21 and 0.20 were taken for the static and dynamic friction coefficients, respectively, in this research.

Table 17. Parameters for pulley elements.

FD	FS	LMIN	DC
0.20	0.21	0.0	1.0

Suspenders

There are 138 suspenders in total in the 2nd structure of the Delaware Memorial Bridge. These suspenders are divided into two types based on their equivalent diameter of four steel cables: 0.301 feet (Type-I) and 0.325 feet (Type-II). In each cable plane, 11 Type-II suspenders are located in the middle of the center span. All remaining suspenders are Type-I. Depending on the length of suspenders, each suspender was modeled by 2 to 10 truss elements.

Suspended Structure

The top and bottom chords, vertical and diagonal members of the stiffening trusses, the floor trusses and the bottom lateral bracing were modeled by 3-D beam elements (with element formulation 3, i.e., Belytschko-Schwer Resultant Beam). The concrete deck and the stringers underneath were modeled by shell and beam elements, respectively, as shown in Figure 45(f) and (g). The constraint *CONSTRAINED_NODAL_RIGID_BODY was used to connect the nodes of the stringers and the corresponding nodes of the deck to simulate the composite action between them.

Interior Expansion Joints (IEJ)

Stringers and deck have ¾ inch interior expansion joint (IEJ) after every three truss panels (they are continuous across these three panels) along the longitudinal direction of the bridge to decrease the adverse effects of temperature changes on the deck, see Figure 45(f) and (g). The stringers are riveted to the floor beams at each IEJ. Within these three truss panel points, stringers can slide freely and longitudinally on the top of the floor beams. In the explicit model, IEJs were modeled as ¾ inch gaps, both in the concrete deck and stringers. Additionally, discrete beam elements were added to the nodes on two sides of the gap to simulate both free-open and close-contact behaviors. It should be noted that these IEJs were not modeled in the implicit model.

Towers

All the tower members, including tower shafts and tower struts, were modeled by 3-D beam elements. The tower shafts have a straight tapered box section decreasing from base to top. The tower struts have a curved tapered box section which decreases from the tower shafts to the center of the bridge in the transverse direction of the bridge. In both the implicit and explicit models, they were divided into multiple prismatic elements with different section properties. As shown in Figure 45(d) and (e), each tower shaft was modeled by 26 elements and each tower strut was modeled by 10 elements.

Miscellaneous Members

The steel tower saddles were modeled by rigid beam elements. To simplify the analysis, each saddle was modeled by only one beam element. Non-structural members, such as inspection walks in the stiffening trusses, cat-walks on the main cables, traffic gantries and light poles, were modeled by mass elements, similar to that in the implicit model.

Material Model

Main Cable and Suspenders

The main cables and suspenders are wire bundles, composed of multiple galvanized steel wires. For an individual steel wire, the minimum yield and the minimum ultimate strengths are 160 ksi and 225 ksi, respectively. The typical stress-strain curve for a single new bridge wire (Mayrbaurl and Camo 2004) is shown in Figure 47. It was assumed that all wires in a wire bundle follow the same stress-strain diagram, and that the stresses in all wires were the same at any specific value of strain. Moreover, in order to simplify the analysis, the stress-strain curve was simplified into the bilinear curve shown in Figure 48. Thus, the nonlinear material model *MAT_PLASTIC_KINEMATIC (*MAT_003) with the parameters in Table 18 was used for the majority of the main cable segments and all suspenders.

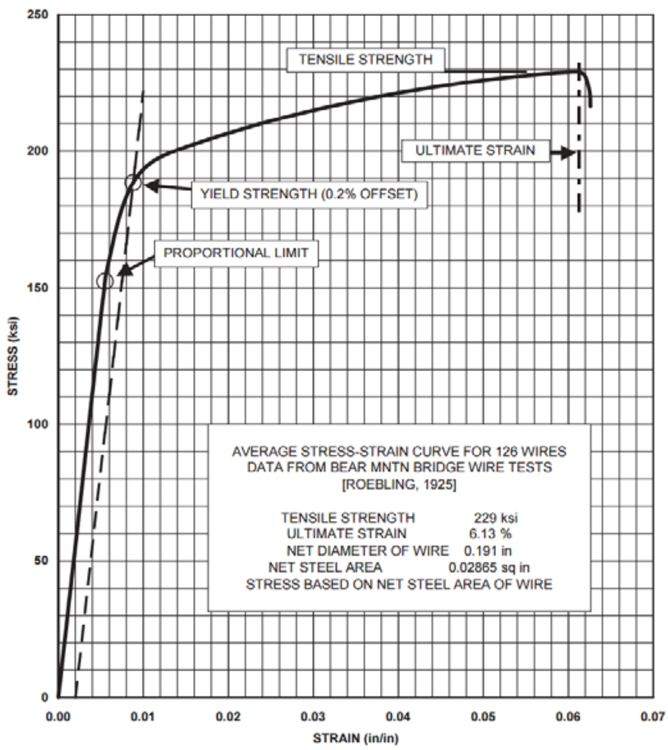

Source: The National Academies Press.

Figure 47. Graph. Typical stress-strain curve for bridge wire.

Table 18. Parameters of *MAT_003 for main cables and suspenders.

SIGY(ksi)	***E***$_t$ (ksi)	***E*** (ksi)	ε_u
160	1,197	28,000 (Main cable) 20,000 (Suspender)	6.0% (Main cable) 6.2% (Suspender)

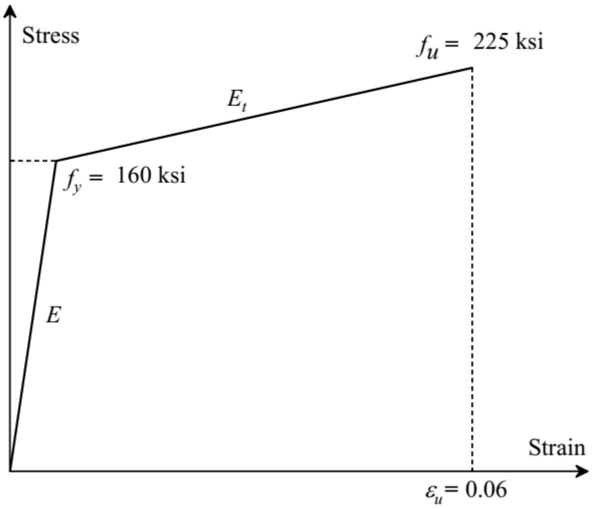

Source: FHWA.

Figure 48. Graph. Typical stress-strain curve for main cables and suspenders (*MAT_003).

For the main cable segments in the vicinity of the tower saddles, which were modeled by discrete cable elements, a simplified multilinear stress-strain curve was used in the material model *MAT_CABLE_DISCRETE_BEAM (*MAT_071), as shown in Figure 49. The Young's modulus in the linear elastic range was 28,000 ksi. The proportional limit was 140 ksi, and the yield strength was 160 ksi. The ultimate strain was set at 0.06 corresponding to the ultimate strength of 225 ksi.

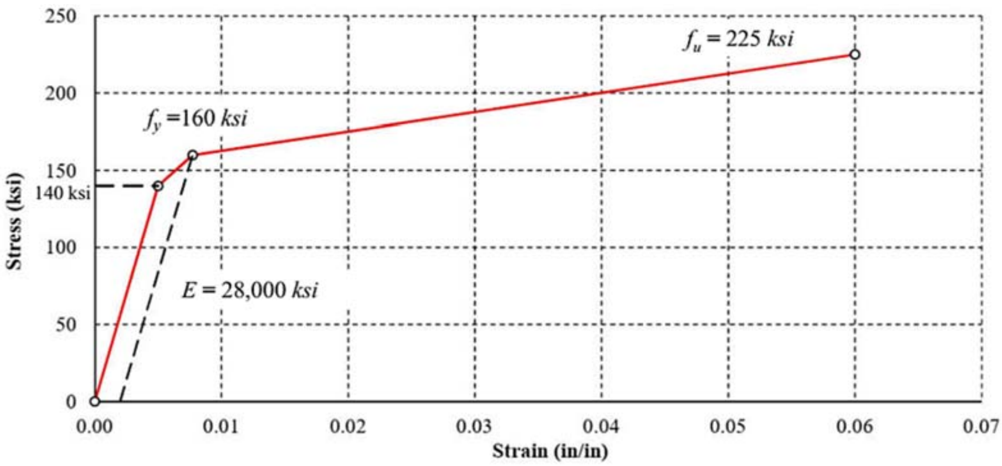

Source: FHWA.

Figure 49. Graph. Stress-strain curve for the main cable in the vicinity of the tower saddles (*MAT_071).

Stiffening Trusses, Towers and Stringers

In the Delaware Memorial Bridge, the suspended structure, steel towers and all other steel structural member were built of ASTM A36 carbon steel. The minimum yield strength of this material is 36.0 ksi, the minimum ultimate strength is 58.0 ksi, and the modulus of elasticity is 29,000 ksi. In the explicit model, the suspended structures and towers were modeled by 3-D resultant beam elements (ELFORM =2 in *SECTION_BEAM card). To simulate failure, the nonlinear material model *MAT_SIMPLIFIED_JOHNSON_COOK (*MAT_098) was used. In material model *MAT_098, the flow stress is expressed as,

$$\sigma_y = \left(A + B\bar{\varepsilon}^{p^n}\right)(1 + C \ln \dot{\varepsilon}^*) \tag{13}$$

where, A, B, C and n are input constants, $\bar{\varepsilon}^p$ is the effective plastic strain, $\dot{\varepsilon}^*$ is the normalized effective stain rate.

A set of parameters for characterizing A36 steel behavior were obtained through extensive simulation trails. As shown in Table 19, the selected PSFAIL is the effective plastic strain at failure and corresponds to an engineering failure strain of 0.20.

To demonstrate the behavior of the model with the selected parameters, a cantilever beam was loaded in tension and compression at three different strain rates (i.e., loading speeds): 0.0074/second (Test #1), 0.01444/second (Test #2) and 0.1300/second (Test #3). The corresponding stress-strain curves are plotted in Figure 50, which also shows the stress-strain curve used in SAP 2000®. It is observed that the stress-strain cure of *MAT_098 agrees well with that used in SAP 2000®, not only in the elastic range but also in the hardening range under both quasi-static loading and relatively faster loading. With PSFAIL = 0.158, the material failed at an approximate ultimate stain of 0.20 in tension and an ultimate strain of 0.168 in compression, and the ultimate strength varied within a narrow range of 58.2 ~ 60.9 ksi, which is close to 58.0 ksi used in SAP 2000®. It should be noted that there are relatively larger differences in the vicinity of yielding between the results of *MAT_098 and that used in SAP 2000®. Unlike the flat yielding plateau in the stress-strain curve used in SAP 2000®, there is no obvious yield plateau in the curves obtained from *MAT_098, and the stress-strain curves go directly into a long hardening range after the elastic range, although the increase in stress with strain is slow. Hence, the yielding point is not well defined and the yielding stress is roughly within a range of 40.0 ~ 45.0 ksi, which is larger than 36.0 ksi yielding stress in SAP 2000® by 11.1 to 25.0%.

Table 19. Parameters of *MAT_098 for steel A36.

A (*ksi*)	**B** (*ksi*)	**N**	**C**	$\dot{\varepsilon}_0$ (sec^{-1})	**PSFAIL**
36.25	39.50	0.328	0.0162	0.1	0.158

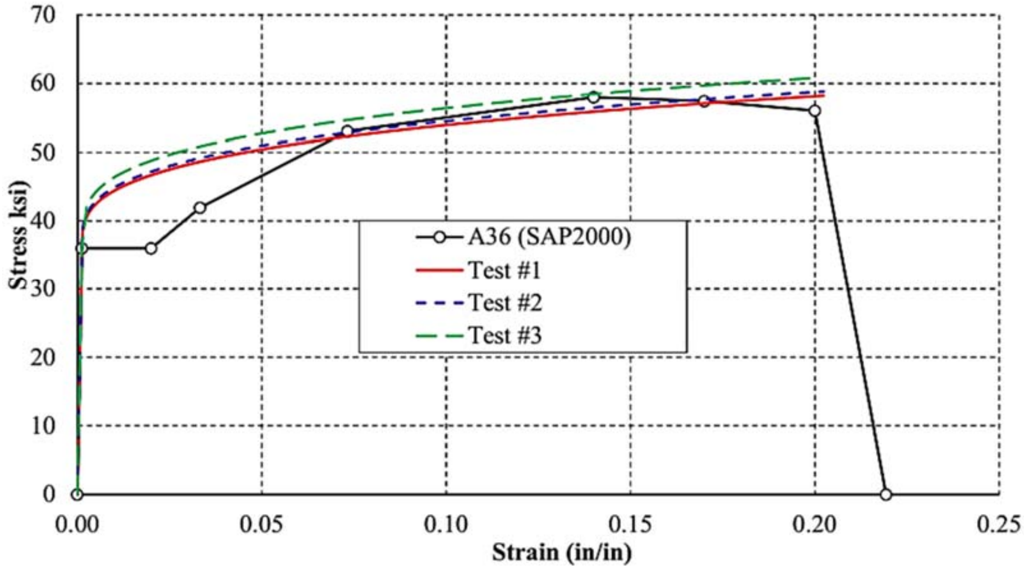

Source: FHWA.

(a) *MAT_098 for simulating A36 steel under tension.

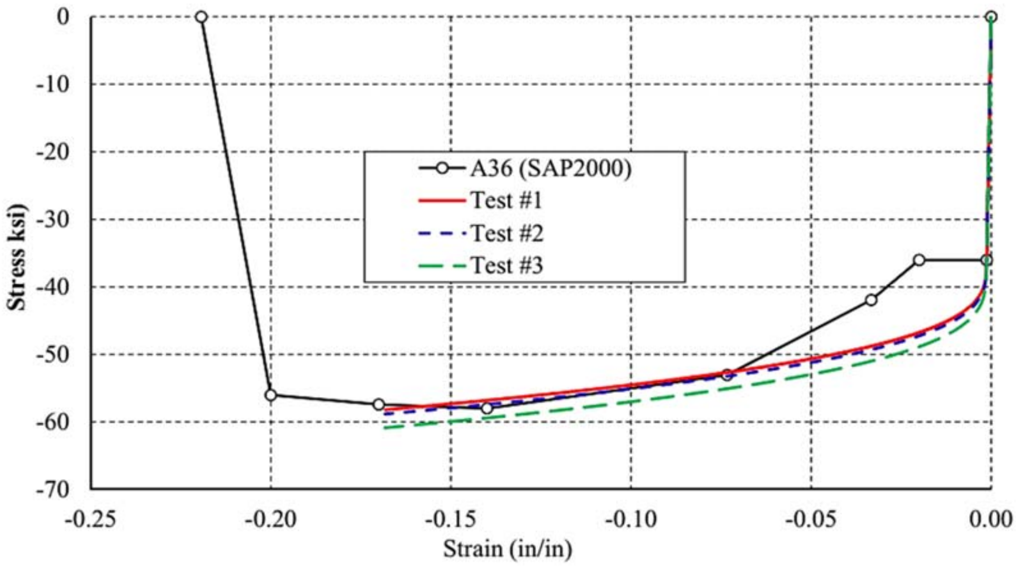

Source: FHWA.

(b) *MAT_098 for simulating A36 steel under compression.

Figure 50. Graphs. Stress-strain curves of *MAT_098 for A36 steel under quasi-static loading.

Buckling of beam member

Some members of the suspended stiffening trusses are prone to buckling when subjected to large compressive forces. For example, during the pushdown analysis, buckling was observed in some diagonal members of the stiffening trusses around the abutment support and near the lower strut of the towers. To model buckling behavior, a small initial imperfection (i.e., 1/500 of the member length) was added at mid-member length to structural members that could possibly be subjected to large compression, such as the top chords and some diagonal members of the stiffening trusses.

This approach has been validated by a simple case of a slender beam fixed at the left end and supported by a guided roller on the right end, as illustrated in Figure 51(a). Parameters of the beam are listed in Table 20. The beam was modeled by two equal-length elements using the Simplified Johnson Cook Model (*MAT_098) with the parameters in Table 19. A 0.05-feet initial imperfection was set at the middle (i.e., node 3) in the vertical direction. A prescribed displacement shown in Figure 51(b) was applied horizontally at the right end. The time histories of the axial forces of the beam elements are plotted in Figure 51(c). This figure shows that the model can very well capture buckling behavior during the loading. The corresponding buckling load is 227.07 kip, which is 3.5% larger than the theoretical value.

Table 20. Parameters of the beam in an example of buckling.

Length (*feet*)	**Area** (*feet*^{2})	**Moment of Inertia** (*feet*^{4})	**Yield stress** (ksi)	**Theoretical Buckling Strength** (kip)	**Result by simulation** (kip)	**Difference** (%)
25.0	0.1	8.309×10^{-4}	36.0	219.39	227.07	3.5%

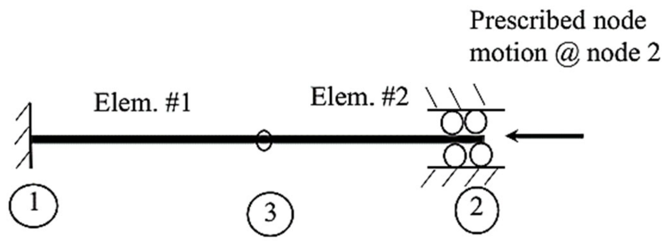

Source: FHWA.

(a) Beam Model.

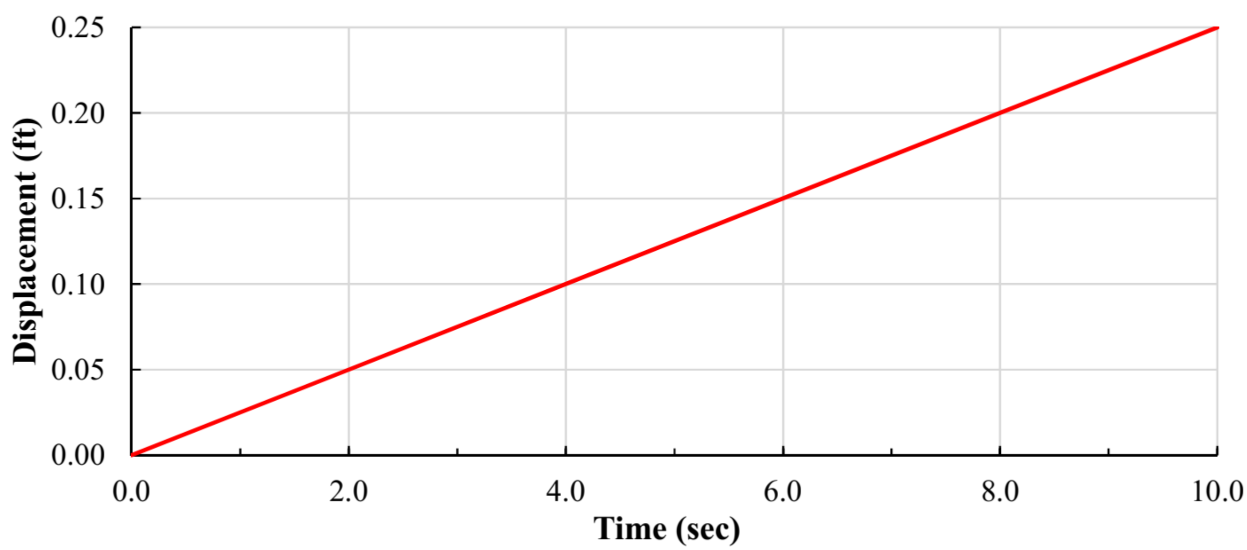

Source: FHWA.

(b) The prescribed displacement applied at Node 2.

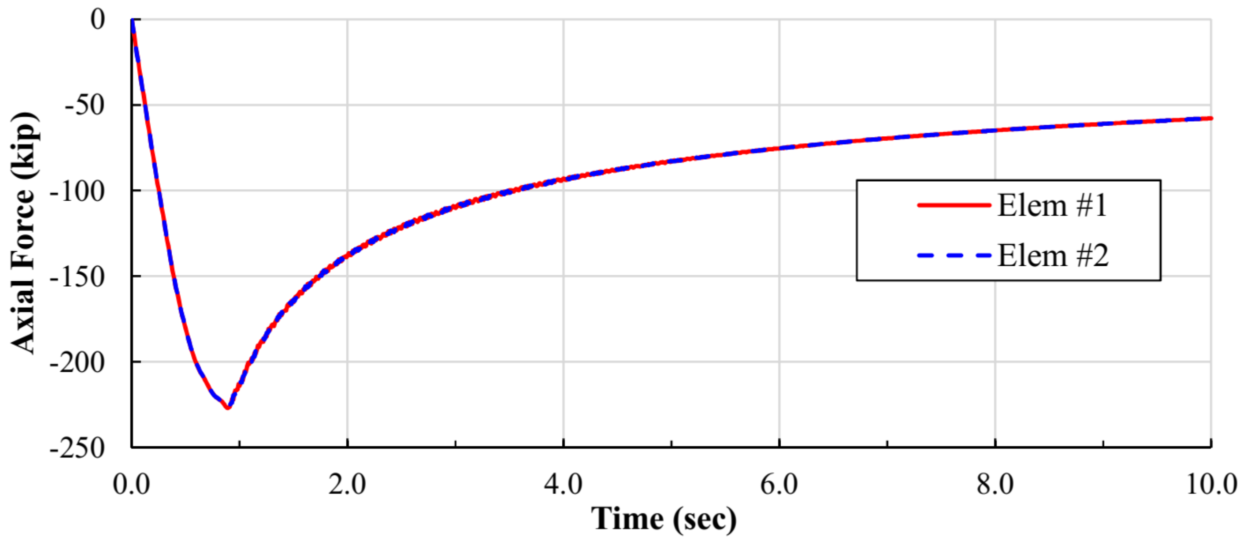

Source: FHWA.

(c) Time histories of axial forces of the beam elements.

Figure 51. Illustration and Graphs. Flexural buckling example.

Concrete Deck

The concrete deck was modeled by shell elements. Similar to that in the explicit model of the Cooper River Bridge, *MAT_PLASTICITY_COMPRESSION_TENSION (*MAT_124) was also used to simulate the nonlinear behavior of the concrete deck, such as cracking, crushing, reinforcement yielding, etc. The concrete deck in this bridge is 8 inches thick. However, other details such as strength of concrete, strength of reinforcement, rebar size and spacing, are not available. Moreover, the original concrete deck was replaced several times since the bridge was opened to traffic in 1968. Based on common design details of similar types of bridge decks, the strengths of concrete and reinforcement were assumed to be 4.0 ksi and 60.0 ksi, respectively. The rebars were assumed to be of #6 size with a 6-inch spacing in both longitudinal and transverse directions. The ultimate tensile strain of the deck was taken as 0.10. The stress-stain relationship used in *MAT_124 for this composite deck is shown in Figure 52.

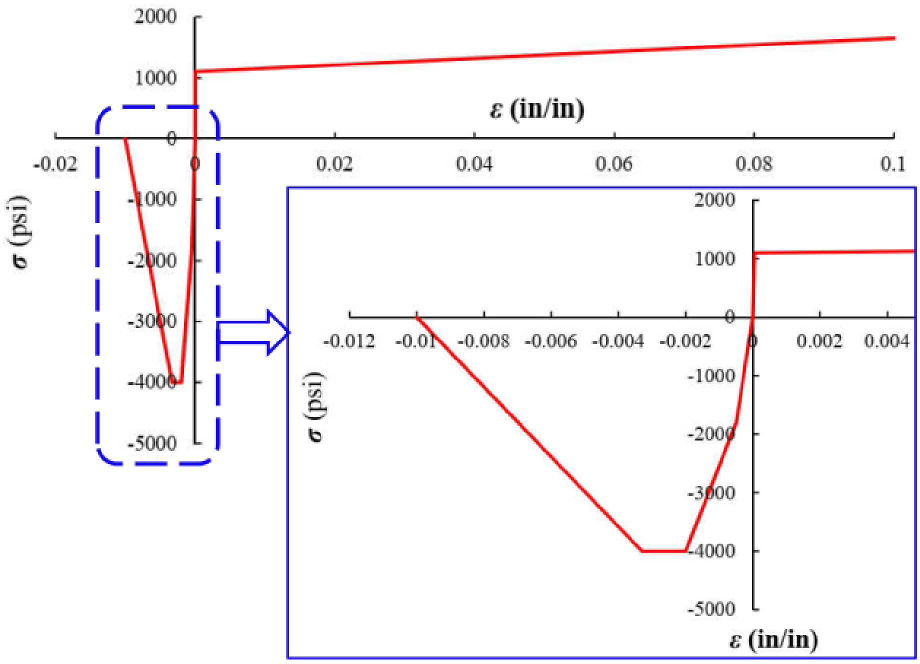

Source: FHWA.

Figure 52. Graph. Equivalent stress-strain relationship of deck elements.

Interior Expansion Joints (IEJ)

As shown in Figure 45(f) & (g), discrete beams were added at the IEJ between the node pairs of the concrete deck and stringer elements. In LS-DYNA®, the material model *MAT_NONLINEAR_ELASTIC_DISCRETE_BEAM (*MAT_067) is able to simulate an elastic resultant beam with highly nonlinear behavior through user-defined resultant force-displacement curves. Failure can be defined by force or displacement criteria in this model. Therefore, the discrete beams with *MAT_067 and force-displacement curves based the axial stiffness of the corresponding concrete deck strip or steel girder were used to simulate the compression-only gap behavior of the IEJ. One of such resultant force-displacement curves is shown in Figure 53. This figure is based on the axial stiffness of a strip of concrete deck near the discrete beam. It is noted that the number 0.0001, such as in (-0.0625, -0.0001), was used to replace zero in the curve, since force-displacement curve in *MAT_067 doesn't allow a zero slope.

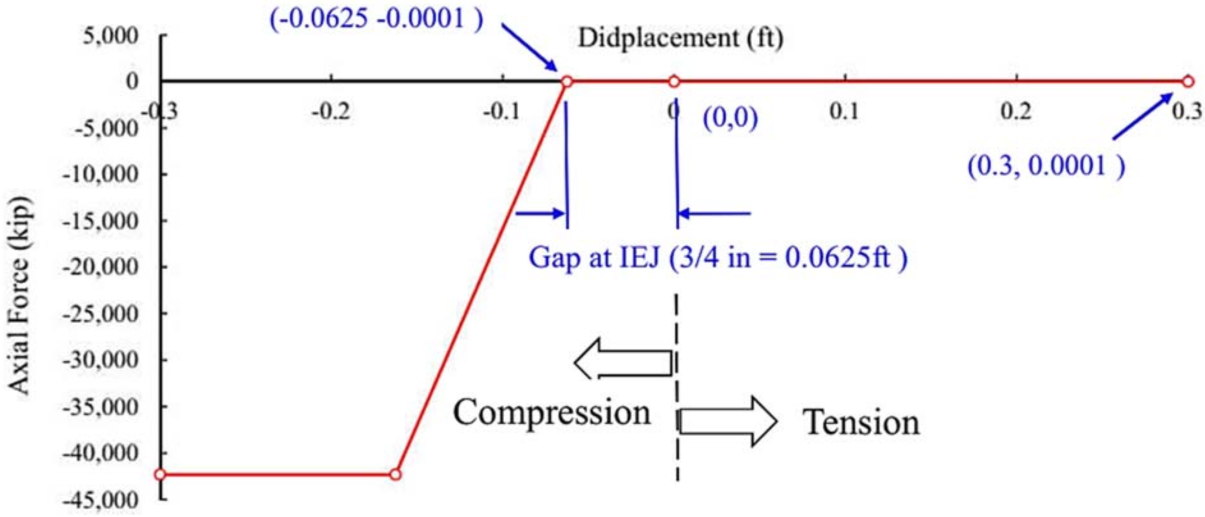

Source: FHWA.

Figure 53. Graph. A resultant force-displacement curve for the nonlinear discrete beam at IEJ.

Miscellaneous Members

Tower saddles and the bottom lateral bracing of the stiffening trusses around towers (i.e., wind tongues) were modeled by rigid material model *MAT_RIGID (*MAT_020). Similarly, virtual elements used to simplify the complex internal connections, for example, the brackets on towers to support the stiffening truss, were also modeled by *MAT_020.

Boundary Conditions and Internal Connections

The main cables are bent around steel spray saddles at the abutments and then they are anchored at the reinforced concrete anchorages. To simplify the analysis, the physical spray saddles and anchorages were not modeled and the main cables were just pin connected to the ground near the abutments.

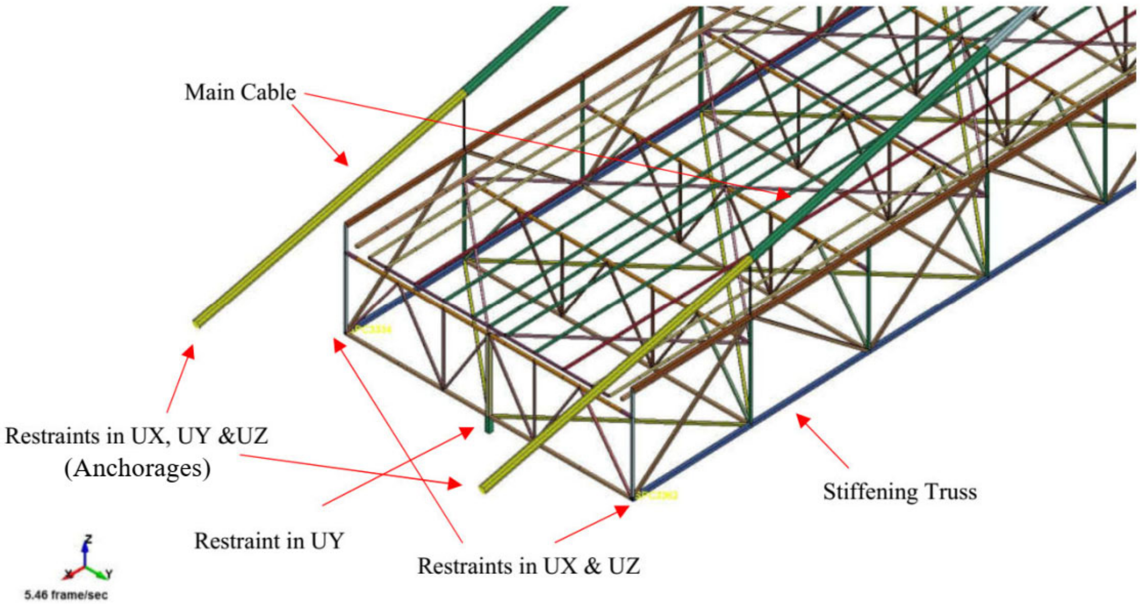

Source: FHWA.

Figure 54. Illustration. Boundary conditions of the explicit model around anchorage.

Source: FHWA.

(a) View 1.

Source: FHWA.

(b) View 2.

Figure 55. Photos. Connection between stiffening trusses and tower at low struts in the bridge.

At the lower strut of the towers, the stiffening trusses are disconnected and vertically supported by tower links, see Figure 55. The ends of bottom lateral bracings (i.e., wind tongues) are strengthened by large sections and connected to brackets on the lower tower strut so that they can transfer the transverse loads acting on the suspended structure, such as wind load and seismic load, to the bridge towers. At the lower tower struts, tooth-type expansion joints are provided to reduce temperature effects on the side spans and the center span. Such expansion joints and the tower shafts together restrain the translation of the deck and stringers in the transverse direction around the towers. Moreover, the stringers and decks are disconnected here and are simply supported on the top of the tower struts vertically. In the transverse direction, the stringers are connected together by strong transverse beam at each span.

All of the above-mentioned internal connections between the suspended structure and the tower were modeled as shown in Figure 56. The tower links were modeled by truss elements. Brackets on the tower shafts were modeled as rigid beam elements with negligible mass. Nodal rigid links were used to connect all the stringer elements together at the end transverse beam in the bridge. Planar joints *CONSTRAINED_JOINT_PLANAR were used to model the connection between stringer-deck system and the tower, and the connection between the wind tongues and the lower strut of the towers.

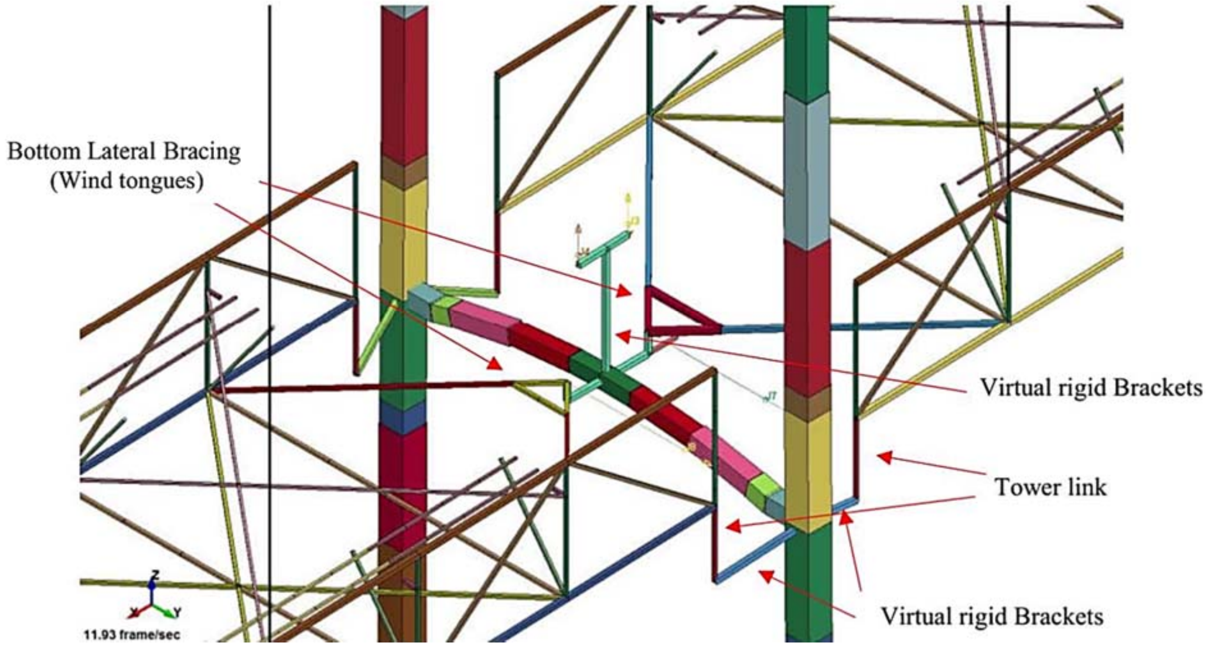

Source: FHWA.

Figure 56. Illustration. Connection between stiffening trusses and tower at low strut in the explicit model.

Accuracy of the FE Models

In order to ensure accuracy of both implicit and explicit models, dead load analysis was conducted on the two models separately, and then the results such as vertical displacement, main cable forces, suspender forces, etc. were compared. These results were also compared with results obtained from the implicit model provided by the bridge's design firm (HNTB 2016). For a better illustration, the main cables and suspenders are named, and the details are shown in Figure 57.

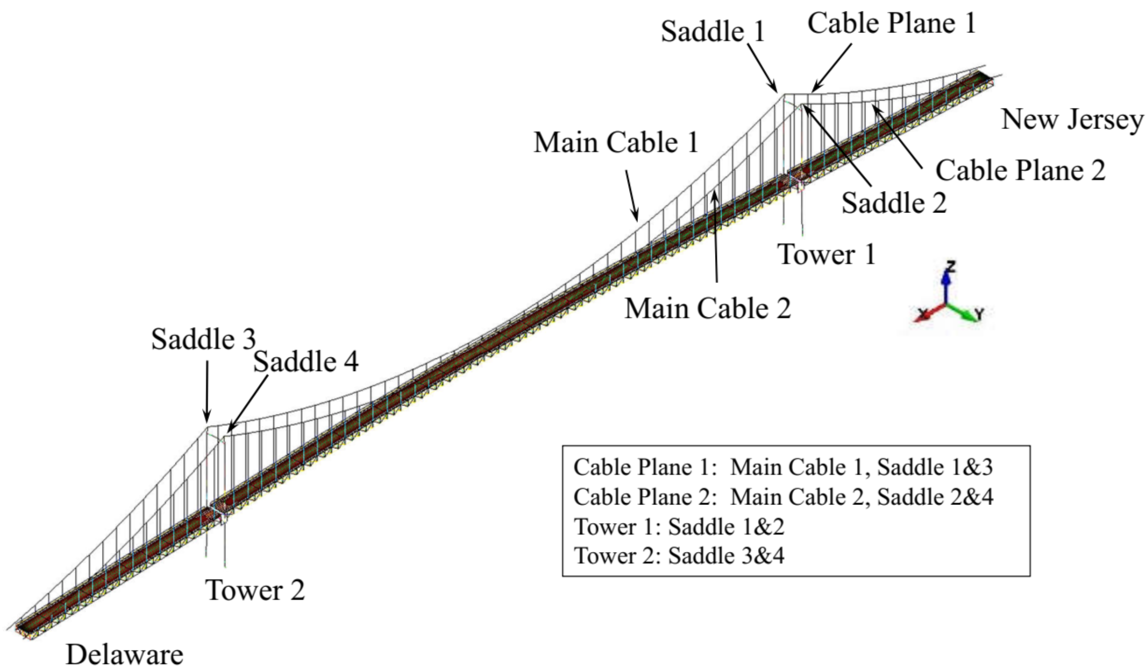

Source: FHWA.

(a) Cable Planes 1&2.

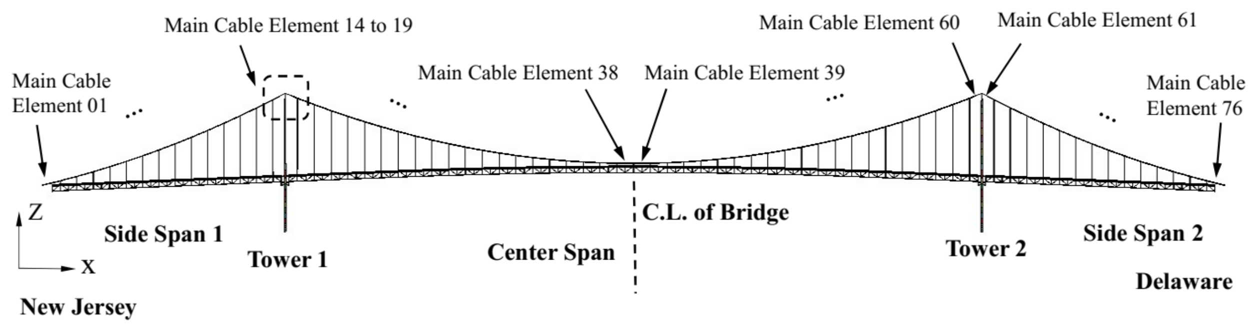

Source: FHWA.

(b) Main Cable Element IDs of Main Cable 1 in Cable Plane 1.

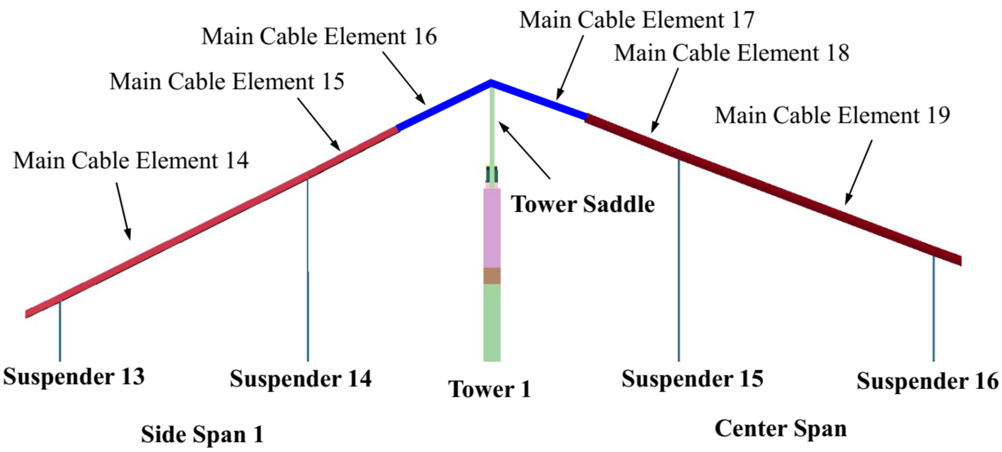

Source: FHWA.

(c) Main Cable Elements around Tower 1.

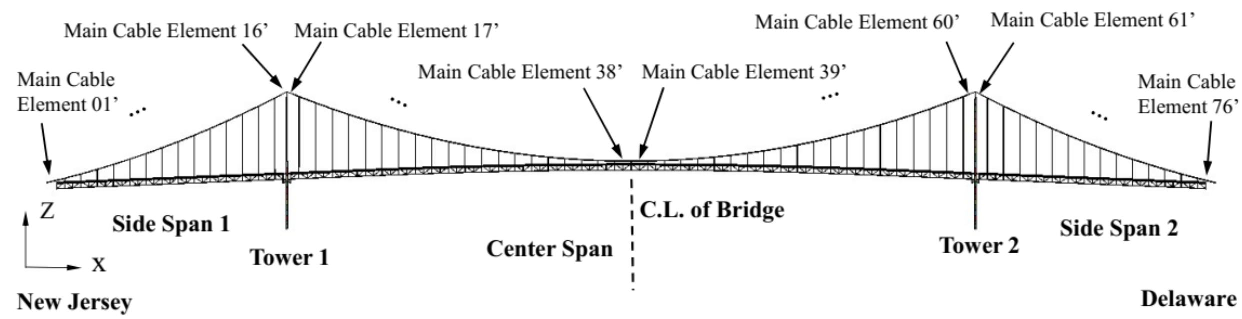

Source: FHWA.

(d) Main Cable Element IDs of Main Cable 2 in Cable Plane 2.

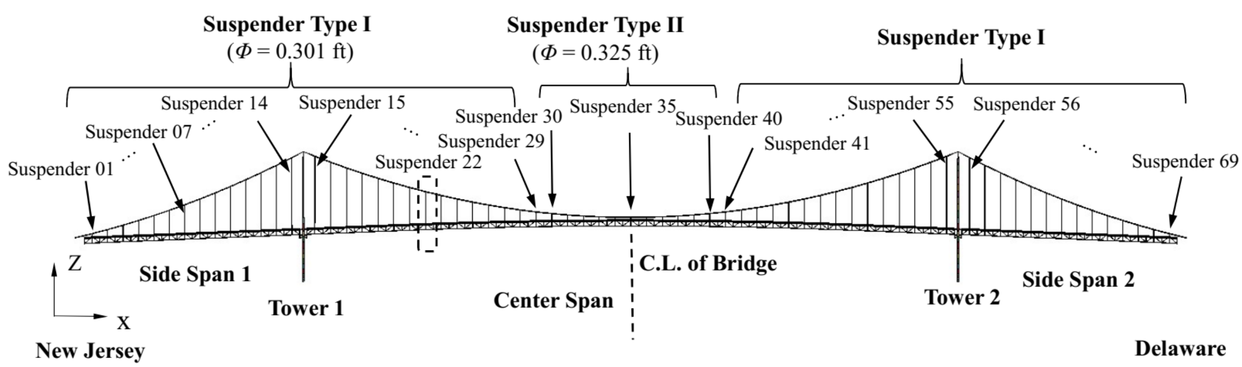

Source: FHWA.

(e) Suspenders in Cable Plane 1.

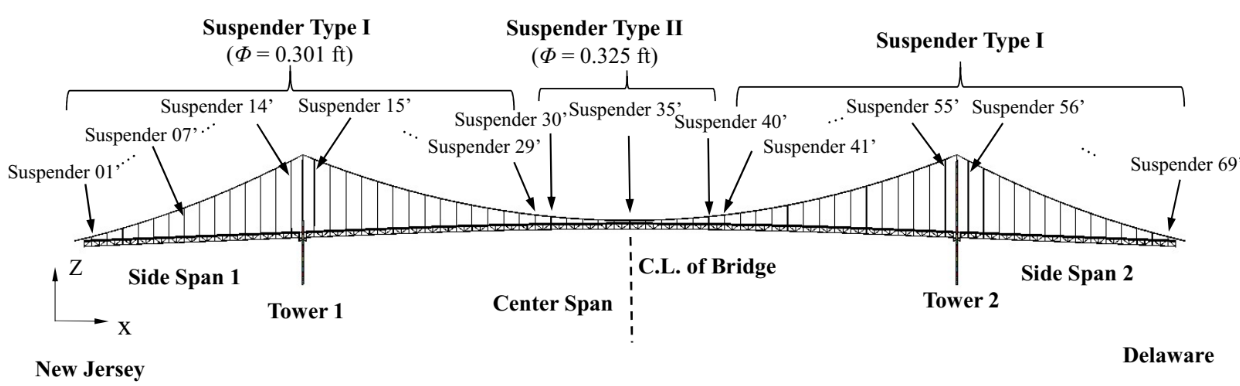

Source: FHWA.

(f) Suspenders in Cable Plane 2.

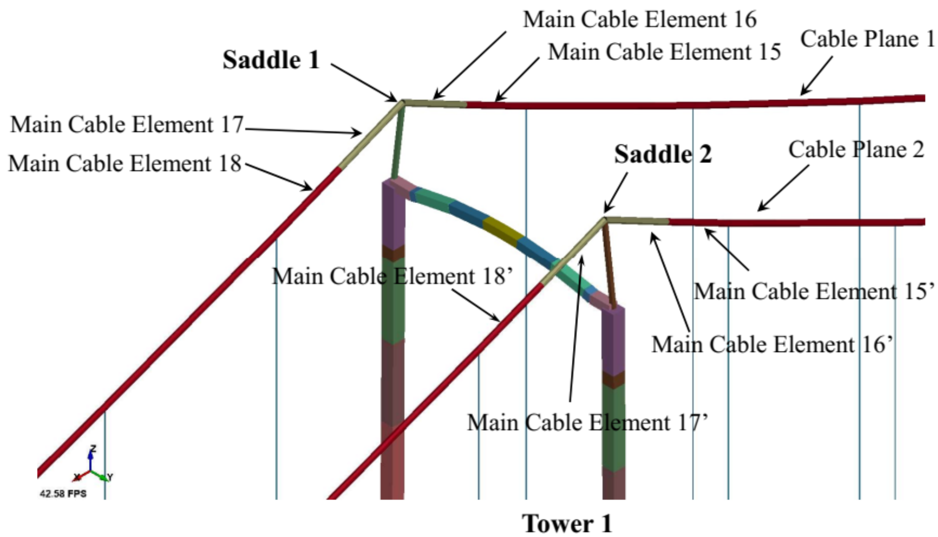

Source: FHWA.

(g) Saddles on top of Tower 1.

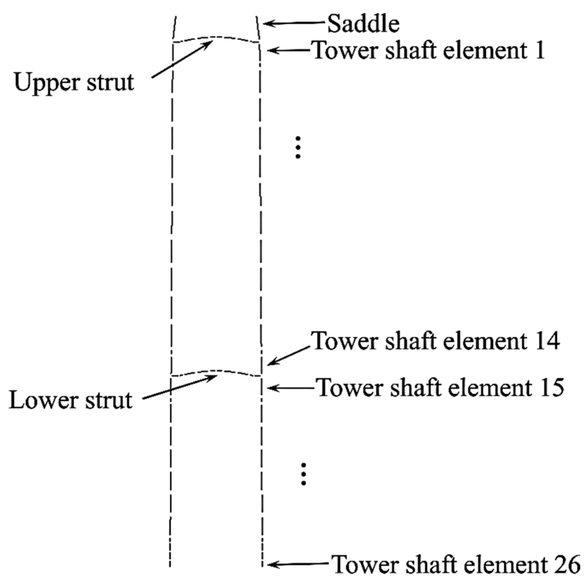

Source: FHWA.

(h) Tower shaft of Tower 1.

Figure 57. Illustrations. Naming scheme of structural components in the suspension bridge.

Vertical Displacements

The vertical displacements along the top chord members of the stiffening trusses of the bridge under dead load are shown in Figure 58 and Figure 59. For a better illustration, the upward deflection with respect to the designed geometric profile is defined as positive (i.e., +Z direction). Accordingly, the downward deflection (i.e., -Z direction) is negative. In the implicit model, both the side spans and the center span deflect downward gradually near the towers. The maximum positive displacement is 0.03 feet in the middle of the center span, and the maximum negative displacement is -0.11 feet around the two towers. In the explicit model, the side spans and the center span deflect upwards due to the pretensions in the main cables and suspenders. The maximum positive displacement is 0.35 feet in the middle of the center span, the maximum negative displacement is -0.04 feet around the two towers, similar to that in the implicit model. The difference in the vertical displacement of the two models is mainly attributed to the pulley elements used in the explicit model, which were not modeled in the implicit model. Tension forces in the main cables can change significantly, which in turn change the vertical deflection. However, even with such differences, deviations between overall dead-load deflection responses from the two models are quite small compared to the potential deformations that could occur under pushdown loading.

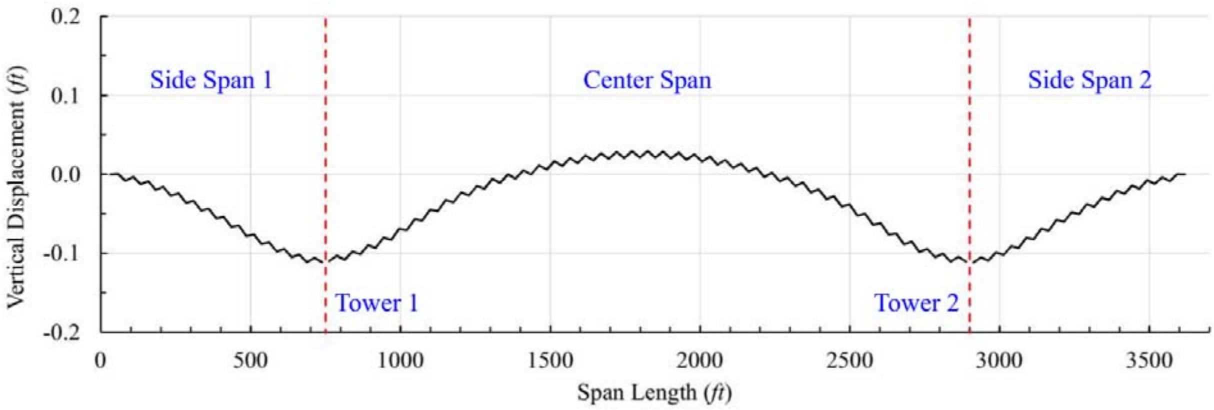

Source: FHWA.

Figure 58. Graph. Vertical displacement of the bridge under dead load by the implicit model.

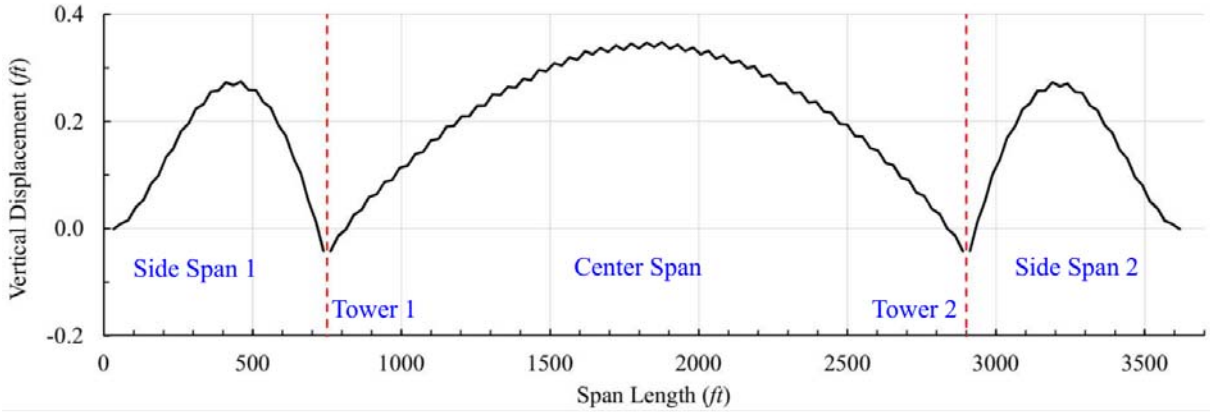

Source: FHWA.

Figure 59. Graph. Vertical displacement of the bridge under dead load by the explicit model.

Tension in Main Cables

The tension values along the main cable obtained from both explicit and implicit models are shown in Figure 60. This figure also shows the results from another implicit model provided by HNTB (2016). Because of the symmetry between the two cable planes of the bridge, only the results for a single cable plane are shown here. It is observed from Figure 60 that the tension along the main cable increased gradually from the anchorages to the towers at the side spans. After passing the tower saddles, the tension decreases gradually from the towers to the center of the bridge. The maximum tension, which was 21,534.1 kips in the implicit model and 21,554.2 kips in the explicit model occurs in the side span just next to the tower. The minimum tension, which was 19,166.6 kips in the implicit model and 19,182.7 kip in the explicit model, occurs in the middle of the center span. The maximum and minimum values of tension in the main cable from HNTB's model are 21,539.4 kip and 19,161.8 kip, respectively. Figure 60 shows that the results from the two models agree well with those HNTB's model, the differences are -0.07% ~ 0.12% for the explicit model and -0.05% ~ 0.04% for the implicit model.

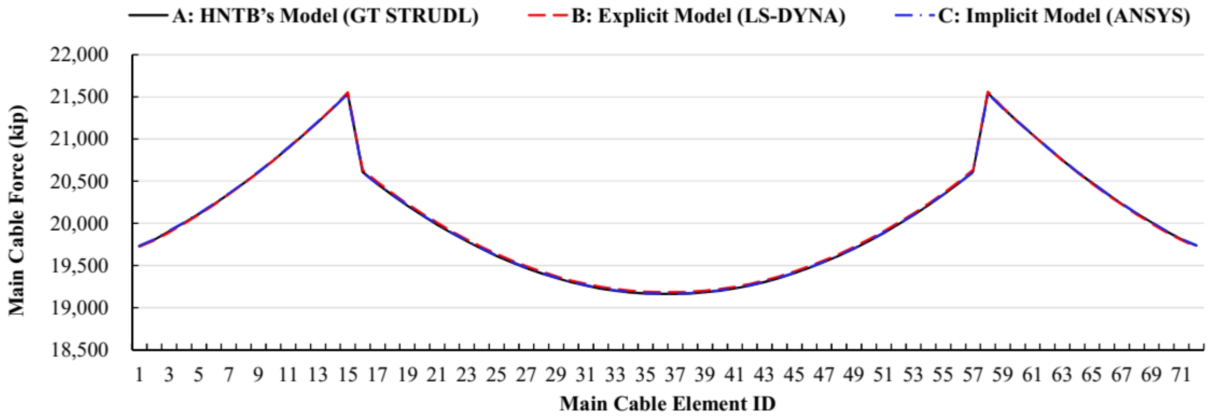

Source: FHWA.

(a) Main cable forces.

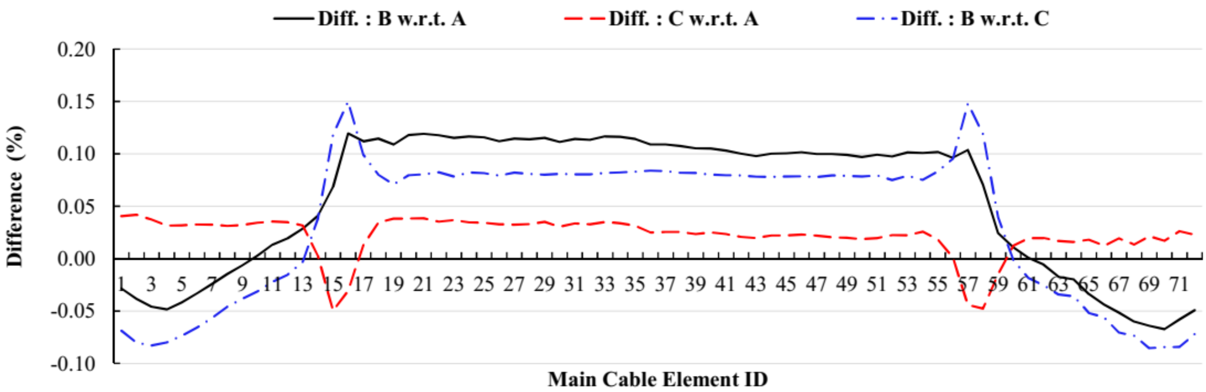

Source: FHWA.

(b) Differences of main cable forces between the three models.

Figure 60. Graphs. Comparison of main cable forces for the bridge under dead load.

Tension in Suspenders

A plot of the tension values in the suspenders is shown in Figure 61. Due to the symmetry of the bridge, only the 69 suspenders in Cable Plane 1 are presented in this figure. It is observed that a majority of results from the two models are very consistent with those from HNTB's model, and the maximum difference with respect to HNTB's model is 3.35% for the implicit model and 6.38% for the explicit model, except for two suspenders around the bridge abutments (Suspender 1 & 69) and four suspenders around the towers (Suspender 14, 15, 55 & 56). For suspenders around the bridge abutments, the differences with respect to HNTB's model are quite large, i.e. 26.3% for the explicit model and 23.3% for the implicit model. These differences are mainly attributed to differences in bridge modeling. In the implicit and explicit models in this research, both decks and stringers on the suspended stiffening truss were modeled. However, they were not included in HNTB's model and their effect was represented only by equivalent masses added onto the stiffening truss.

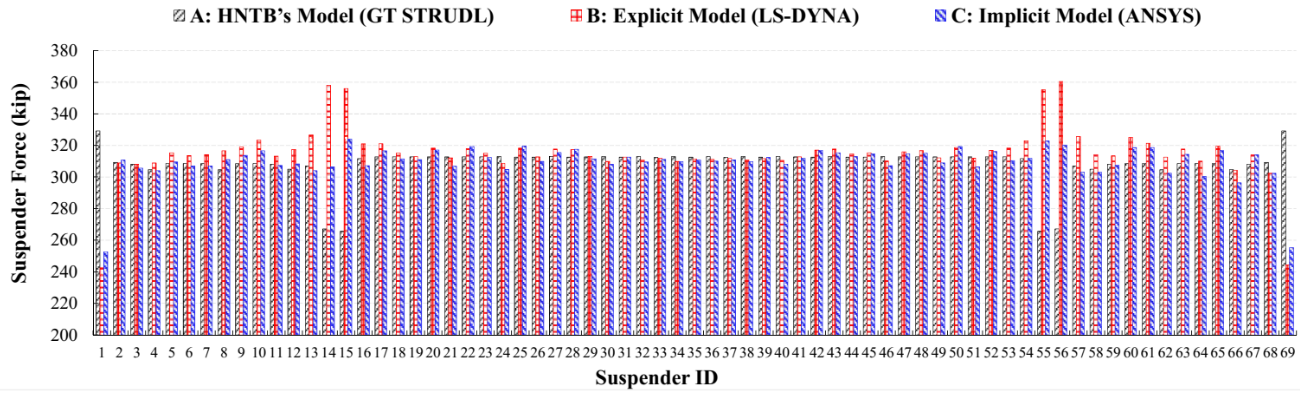

Source: FHWA.

(a) Suspender forces.

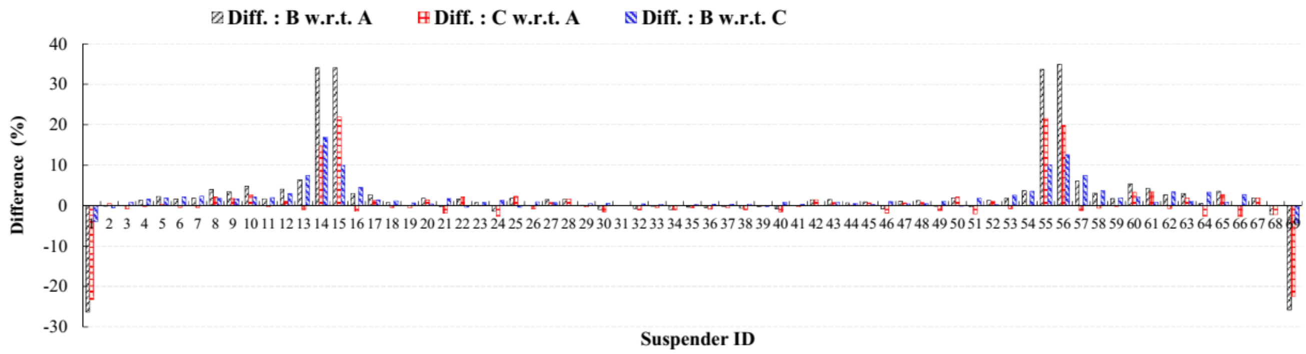

Source: FHWA.

(b) Differences of suspender forces between the three models.

Figure 61. Graphs. Comparison of suspender forces for the bridge under dead load.

Compression in Tower Shaft

The tower shaft was modeled by 26 beam elements in both implicit and explicit models. The axial compression forces in the tower shaft elements are shown in Figure 62. Considering the symmetry of the tower, only the axial forces in one shaft are presented. Since the results from HNTB's implicit model are not available, only the results from the explicit and implicit models are compared. The compression in the tower shaft increases gradually from top to bottom. The minimum compression is 17,695.1 kip in the implicit model and 17,738.4 kip in the explicit model. Both occurred at the top of the tower. The maximum compression of 21,992.1 kip in the implicit model and 22,066.5 kip in the explicit model occurred at the tower base. The results from the explicit and implicit models show a very good agreement, and the maximum difference is only 0.54% at the 2nd segment of the tower shaft.

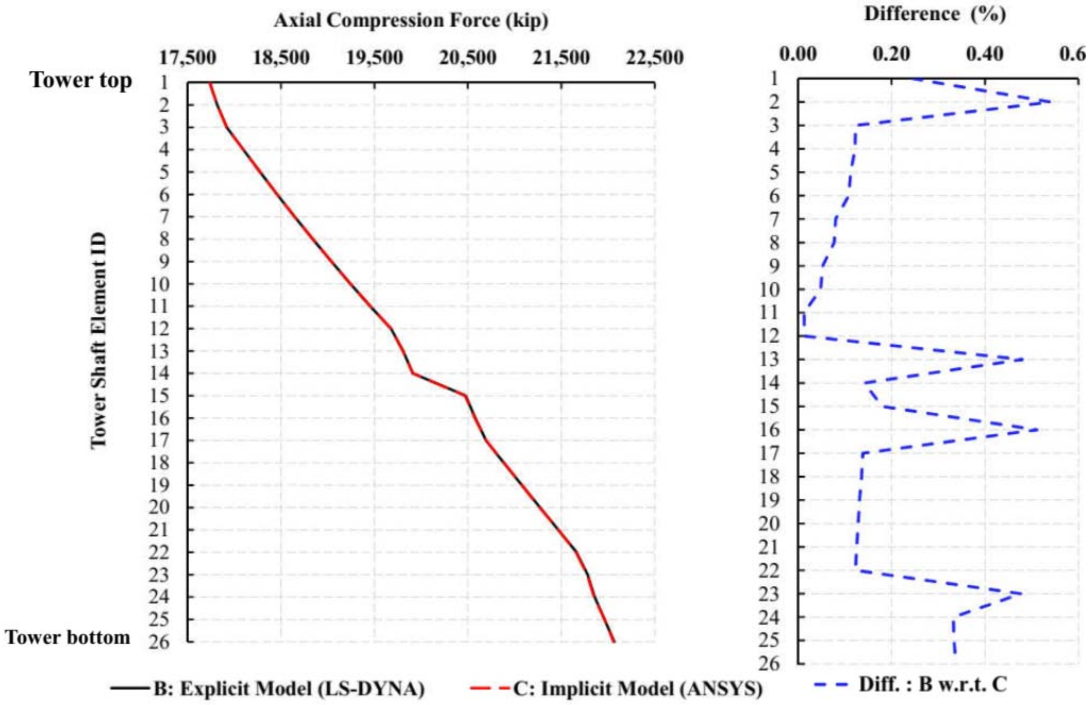

Source: FHWA.

Figure 62. Graph. Comparison of axial compressions in tower shaft for the bridge under dead load.

Modal Analysis

The first ten global modes of the bridge obtained from the implicit and explicit models are plotted in Figure 63. Due to differences in the modeling effort, there are some discrepancies in these mode shapes. Nevertheless, overall there is a good agreement between the mode shapes obtained from both models. The corresponding natural frequencies are listed in Table 21. The maximum difference was approximately -17.6% in the 1st mode, which is primarily due to the interior expansion joints (IEJ) in the stringers and decks, which were modeled in the explicit model but not in the implicit model.

Overall, the multiple successful comparisons shown above provide confidence in the modeling process.

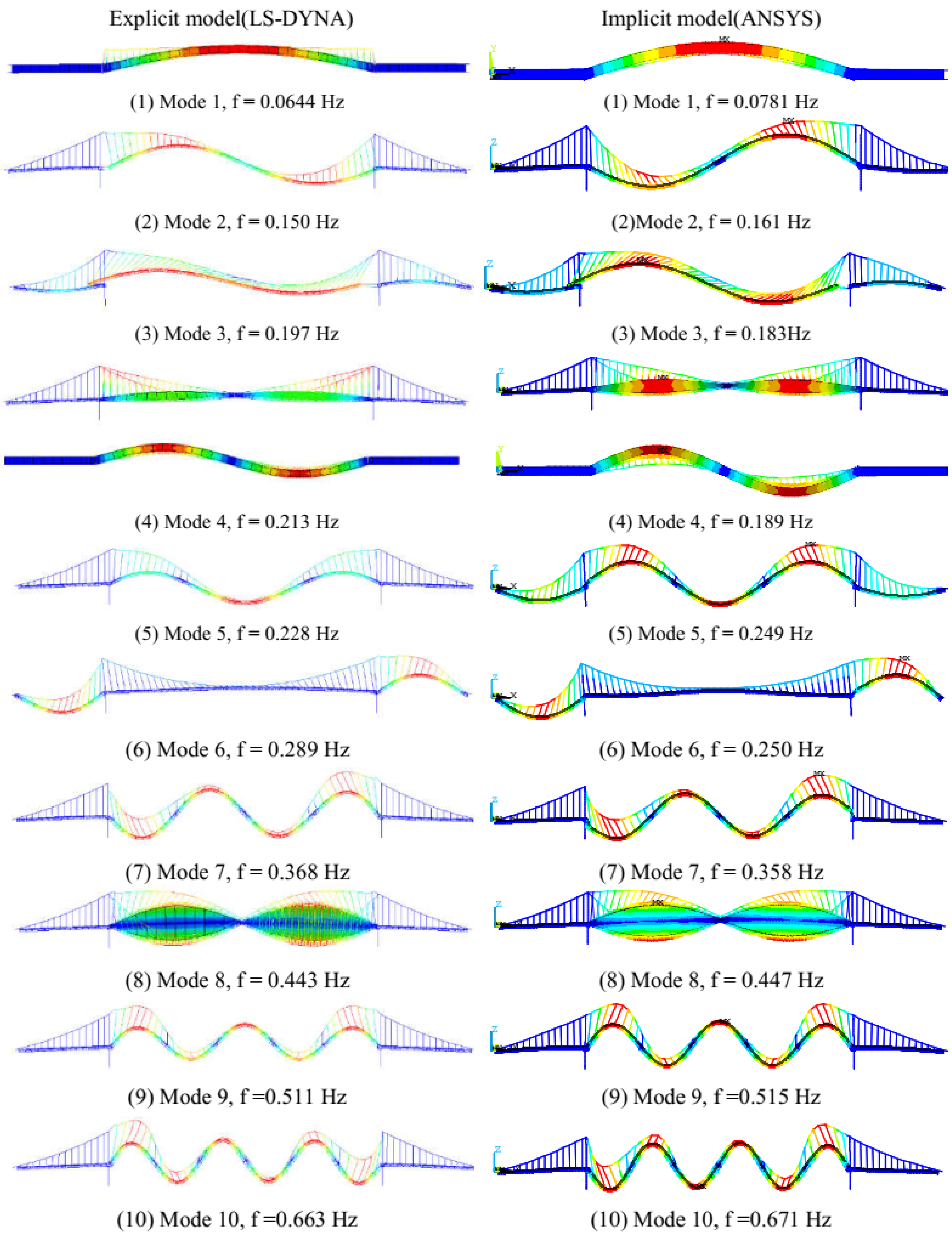

Source: FHWA.

Figure 63. Illustrations. First ten global mode shapes of the Delaware Memorial Bridge.

Table 21. Natural frequencies of the Delaware Memorial Bridge.

Mode No.	Mode Type	Explicit Model Frequency (Hz)	Implicit Model Frequency (Hz)	Difference (%)
1	1st Symmetric transverse bending	0.0644	0.0781	-17.6
2	1st asymmetric vertical bending	0.150	0.161	-6.9
3	Longitudinal floating of stiffening trusses	0.197	0.183	8.0
4	1st asymmetric transverse bending	0.213	0.189	12.5
5	1st symmetric vertical bending	0.228	0.249	-8.5
6	1st asymmetric vertical bending (side spans)	0.289	0.250	15.5
7	2nd asymmetric vertical bending	0.368	0.358	2.8
8	1st asymmetric torsion	0.443	0.447	-0.8
9	2nd symmetric vertical bending	0.511	0.515	-0.85
10	3nd asymmetric vertical bending	0.663	0.671	-1.1

SUMMARY

Three long-span bridges selected in this research for evaluation were introduced. The FE models of these bridges were presented in detail, including modeling of key structural members, internal connections and boundary conditions, material models, etc. Both implicit and explicit models were developed for each bridge. Dead load analysis and modal analysis were conducted using these FE models and a comparison between both models were performed for each bridge. The results showed an excellent agreement between both model types, providing confidence in the explicit models in particular. These are used to investigate the dynamic behavior of the three bridges subjected to single/multiple member failure in the following chapters.

CHAPTER 4. BRIDGE BEHAVIOR UNDER MEMBER LOSS EVENT

INTRODUCTION

Compared to short-to-medium span bridges, long-span cable-supported bridges, such as cable-stayed, tied-arch, and suspension bridges, are flexible structures that can be damaged by excessive vibrations during extreme hazard events, such as wind, corrosion-induced member loss, traffic accidents, etc. Among all structural members in such bridges, cables, hangers and suspenders are the most vulnerable elements. These slender elements could be damaged or may break during intentional or unintentional hazards. Hence, simulations were performed in this chapter by sudden removal of cables, hangers or suspenders to investigate the effects of member loss events on the safety and stability of three types of long-span cable supported bridges. The member removal processes were simulated in the explicit models of the bridges in LS-DYNA® with the command *DEFINE_ELEMENT_DEATH, which deletes the lost elements over an integration time step.

DEMONSTRATION OF MEMBER LOSS EFFECTS ON AN IDEALIZED SYSTEM

The dynamic response associated with a member-loss event is demonstrated through a single degree of freedom (SDOF) mass-spring system subjected to sudden loss of a support as shown in Figure 64. This example has an explicit theoretical solution. Here, the stiffness of the springs is equal to 3426.09 lbf/feet (50 kN/m) and the mass M is equal to 220.462 lb (100 kg).

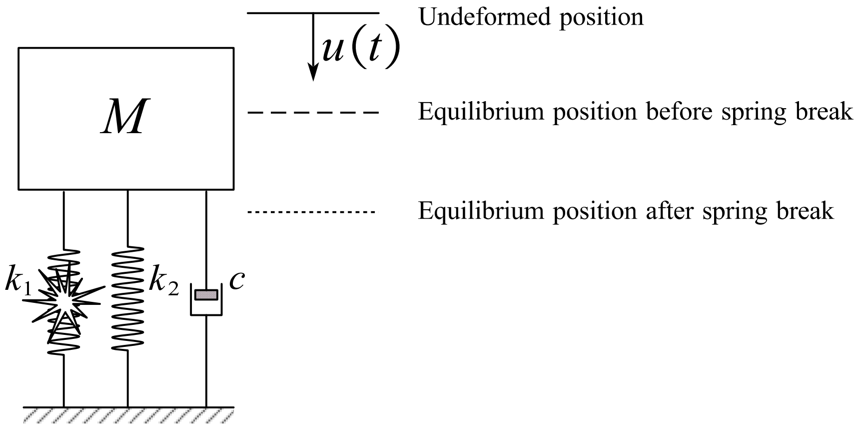

Source: FHWA.

Figure 64. Illustration. A single-degree-of-freedom mass-spring system.

The system was in equilibrium initially when the spring k_1 was removed suddenly, which caused the mass to vibrate freely. The displacement time history was measured from the undeformed position. The initial condition for the mass could be expressed as $u(0) = Mg/(k_1+k_2)$ and $u'(0) = 0$. The theoretical solution of displacement time history the loss of spring k_1 was calculated from Equation (14), which is available in Chopra (2012).

$$u(t) = \left(\frac{Mg}{k_1+k_2} - \frac{Mg}{k_2}\right) e^{-\xi\omega_n t}\left(\cos\omega_D t + \frac{\xi}{\sqrt{1-\xi^2}}\sin\omega_D t\right) + \frac{Mg}{k_2} \tag{14}$$

in which, M is the mass, g is acceleration of gravity, k_1 and k_2 are the stiffness of the springs, ξ is the damping ratio, ω_n is the undamped natural frequency of the SDOF system, and ω_D is the damped natural frequency.

In LS-DYNA®, the mass was modeled by a mass element and the springs were modeled by discrete beam elements with *MAT_LINEAR_ELASTIC_DISCRETE_BEAM (*MAT_066). Different damping effects were considered by varying the damping constant parameter D_s for *DAMPING_GLOBAL. Comparisons between displacement time histories from Equation (14) and that from LS-DYNA® for different values of damping ratios are shown in Figure 65. As expected, both solutions match well.

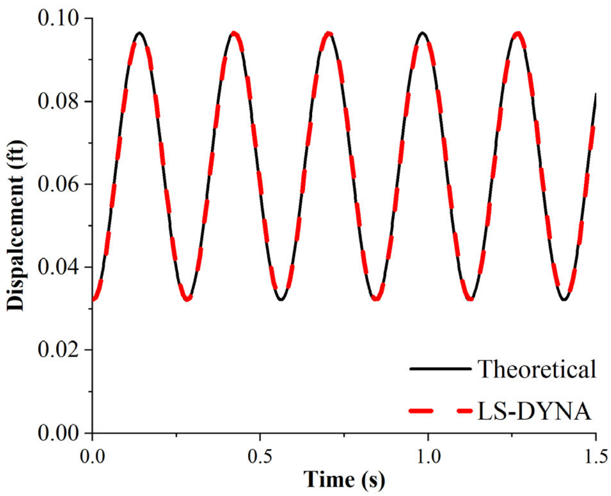

Source: FHWA.

(a) Damping Ratio = 0.00.

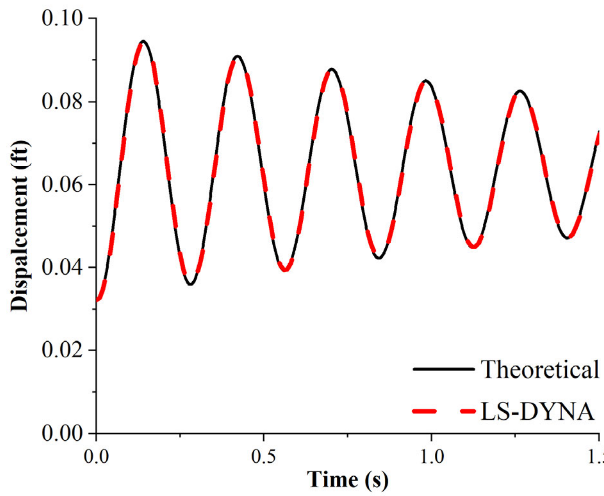

Source: FHWA.

(b) Damping Ratio = 0.05.

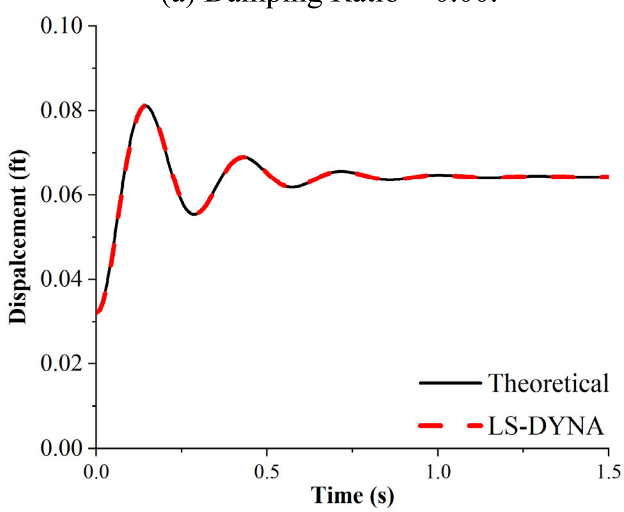

Source: FHWA.

(c) Damping Ratio = 0.20.

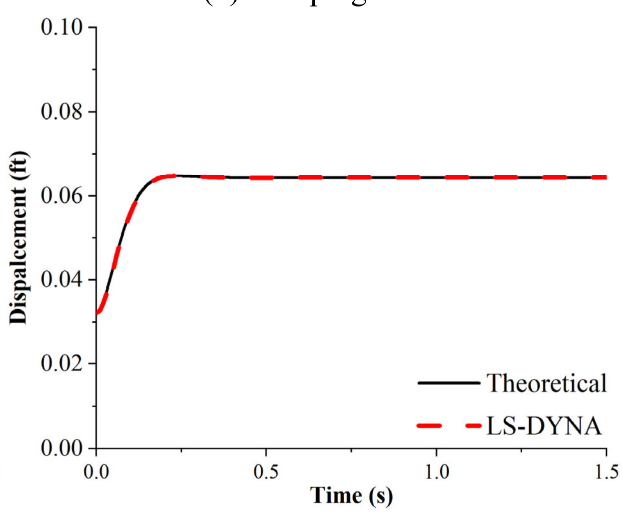

Source: FHWA.

(d) Damping Ratio = 0.80.

Figure 65. Graphs. Comparison of dynamic responses of SDOF system.

In the remainder of this Chapter, a detailed investigation of the behavior of each of the three bridges under sudden cable, suspender or hanger loss was carried out for different live load scenarios. This is presented in detail for each bridge.

CABLE-STAYED BRIDGE

Typical Design Live Load Patterns

Bridges are usually designed for different live load configurations, which govern the limit states of different members of a bridge. Figure 66 shows 13 possible design live load patterns for this bridge. Based the symmetric properties of the bridge and the applied loads, four live load patterns were selected to perform member removal and redundancy analyses. The selected four live load patterns are LL01, LL04, LL05 and LL08 in Figure 66.

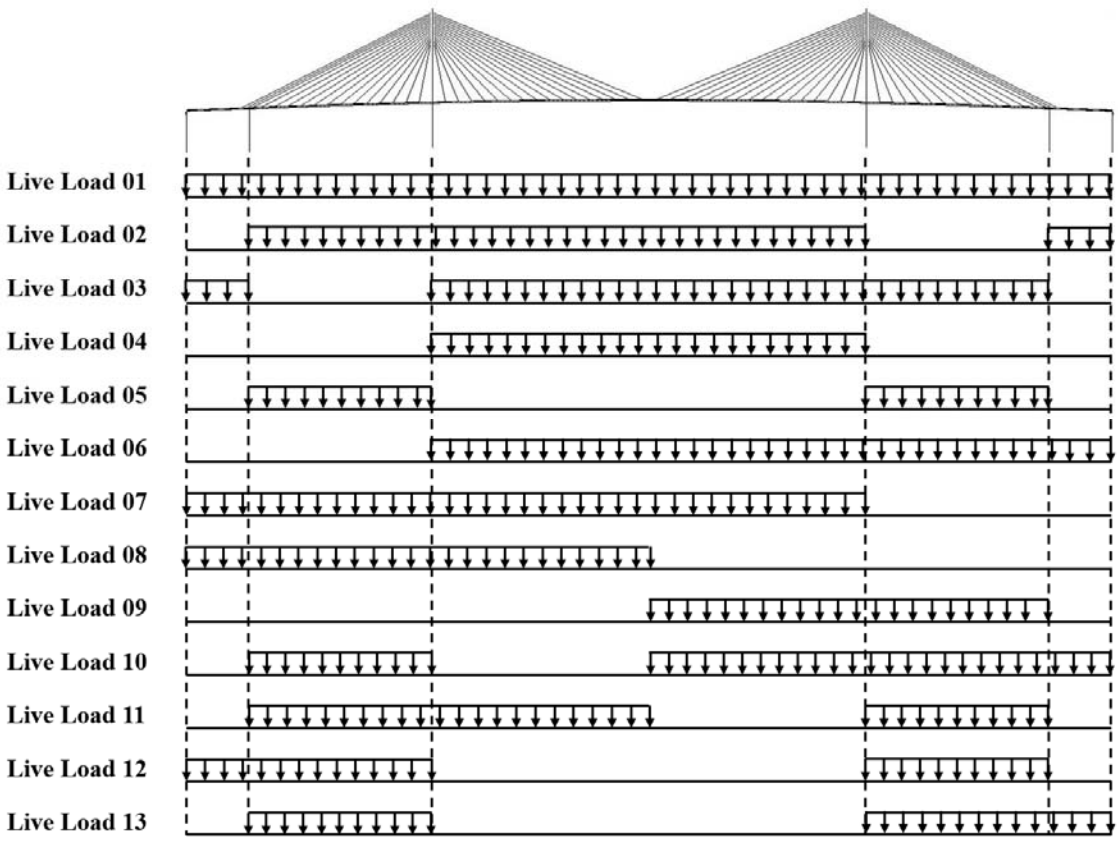

Source: FHWA.

Figure 66. Illustration. Typical design live load patterns.

Live Load Analysis

Live load was applied after the bridge reached its equilibrium state under dead load, which was applied in Stage 1 (0 to 8 seconds) and Stage 2 (8 to 20 seconds) as discussed in Chapter 3. Live load is applied in Stage 3 (20 to 30 seconds) as discussed next. The overall dead load and live load curves are shown in Figure 67.

Stages 1 and 2 (0 to 20 seconds): These stages entail application of dead load as discussed earlier in Chapter 3.

Stage 3 (20 to 30 seconds): After completion of Stages 1 and 2, live load is applied from 20 to 30 seconds. This stage is also accompanied by large global damping (e.g., 80% of critical damping) to prevent any spurious failure mode due to sudden large vibrations when the live loads are applied.

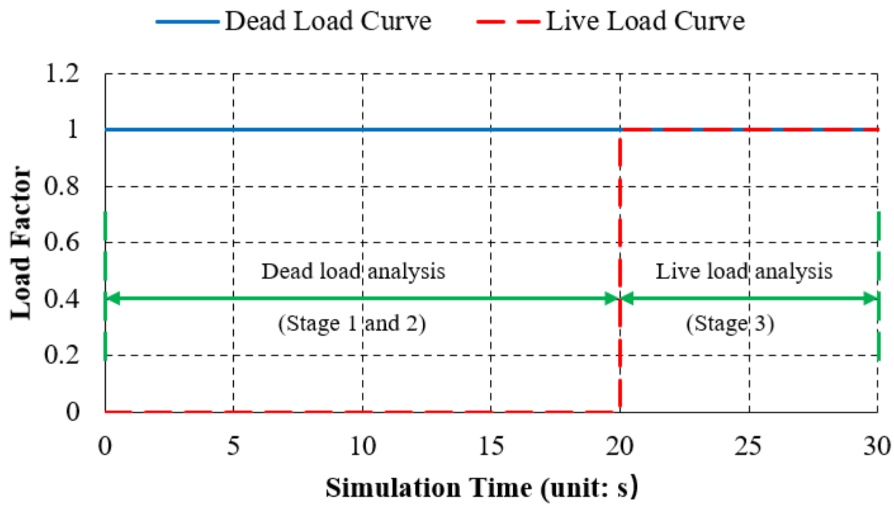

Source: FHWA.

Figure 67. Graph. Dead load and live load curves during live load analysis.

The bridge's responses under the dead load plus the selected four live load patterns LL01, LL04, LL05 and LL08 (denoted as combinations COMB01, COMB04, COMB05 and COMB08, respectively) are introduced in the following subsections. Due to similarity of the results between the two planes of the bridge, only the results of the south plane are presented.

Vertical Displacements

The vertical deflections along the main girder in the south plane under the four load combinations are shown in Figure 68. The deflection is measured from the initial fabrication camber position of the girder. Under COMB01, when the live load is applied on all spans of the bridge, the maximum vertical downward displacement in the center span increases by approximately 1.9 feet compared to that for dead load (DL) only. However, the vertical displacement in the side span for the combination COMB01 remains similar to that for DL only. Under COMB04 with the live load being applied only in the center span, the maximum vertical downward displacement in the center span increases by approximately 2.6 feet over that from DL only, while the side span undergoes an upward displacement of up to 1.1 feet. Under COMB05, with the live load being applied only in the two side spans, while the maximum vertical downward displacement in the center span decreases by approximately 0.7 feet compared that for DL, the side span undergoes an additional downward displacement of 0.7 feet. Under COMB08, where the live load is applied only on the left half of the span of the bridge, the displacements in the loaded half span part is almost similar to that under COMB01, where the displacements in the remaining right half span without live load is similar to that for DL only.

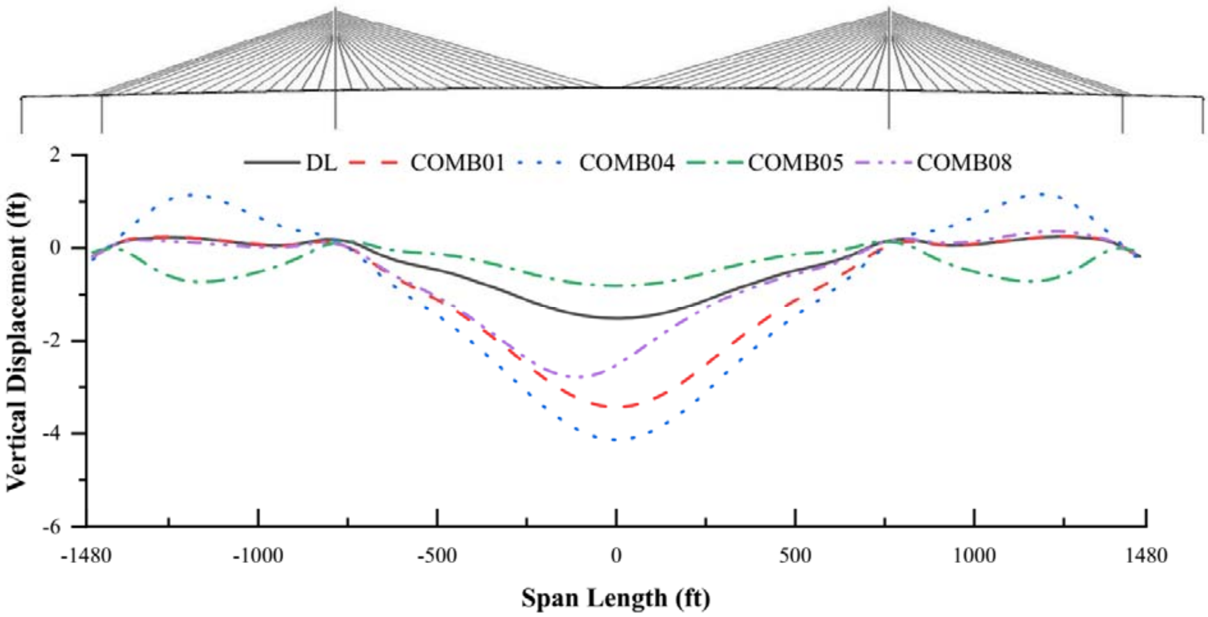

Source: FHWA.

Figure 68. Graph. Girder vertical deflection under the selected four load combinations.

Cable Stresses

The stresses in the stay cables of the bridge for the four load combinations are shown in Figure 69 to Figure 72. For comparison, cable stresses under dead load (DL) are also presented in these figures. Under COMB01, stresses in different cables increased in the range of 8.9 ksi to 15.5 ksi with respect to those under DL. Under COMB04, while stresses in different cables in the center span increased in the range of 12.6 ksi to 15.6 ksi with respect to DL, stress in the longest cable in the side span increased by approximately 25 ksi and stresses in other cables in the side span remained close to that for DL. Under COMB05, stresses in different cables in the center of the side span increased in the range of 12.8 ksi to 18.3 ksi over those for DL. However, the stress in the longest cable in the side span decreased in the range of 9.3 ksi to 11.6 ksi compared to DL. Cable stresses in the center span in this case remained close to those for DL. Under COMB08, stresses in different cables in half of the span with live load were similar to those for COMB01, and cable stresses for the other half without the live load were close to those for DL.

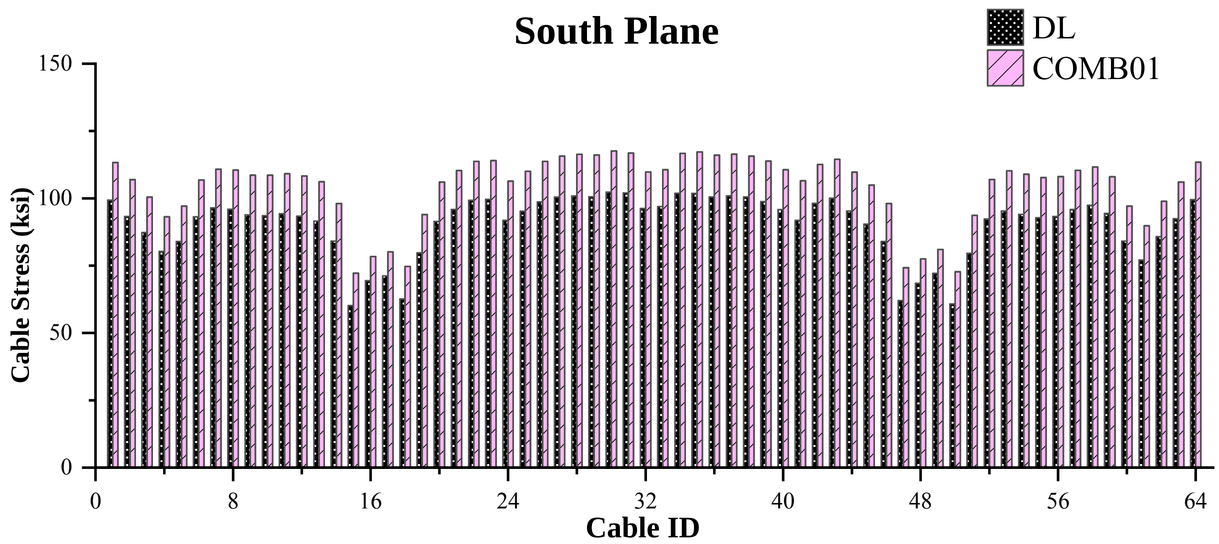

Source: FHWA.

Figure 69. Graph. Cable stresses under dead load and COMB01.

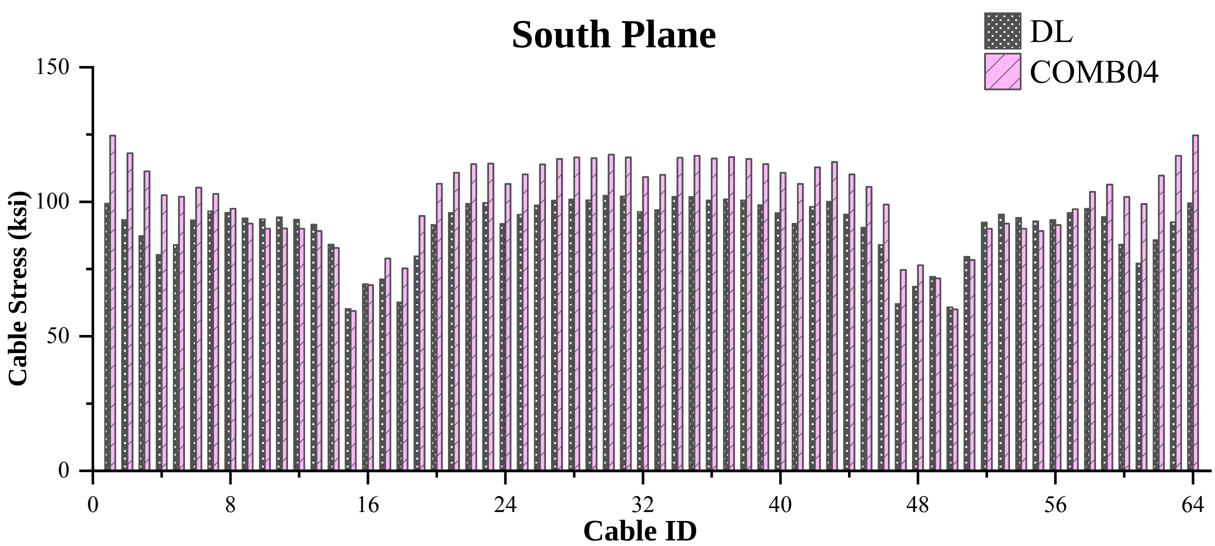

Source: FHWA.

Figure 70. Graph. Cable stresses under dead load and COMB04.

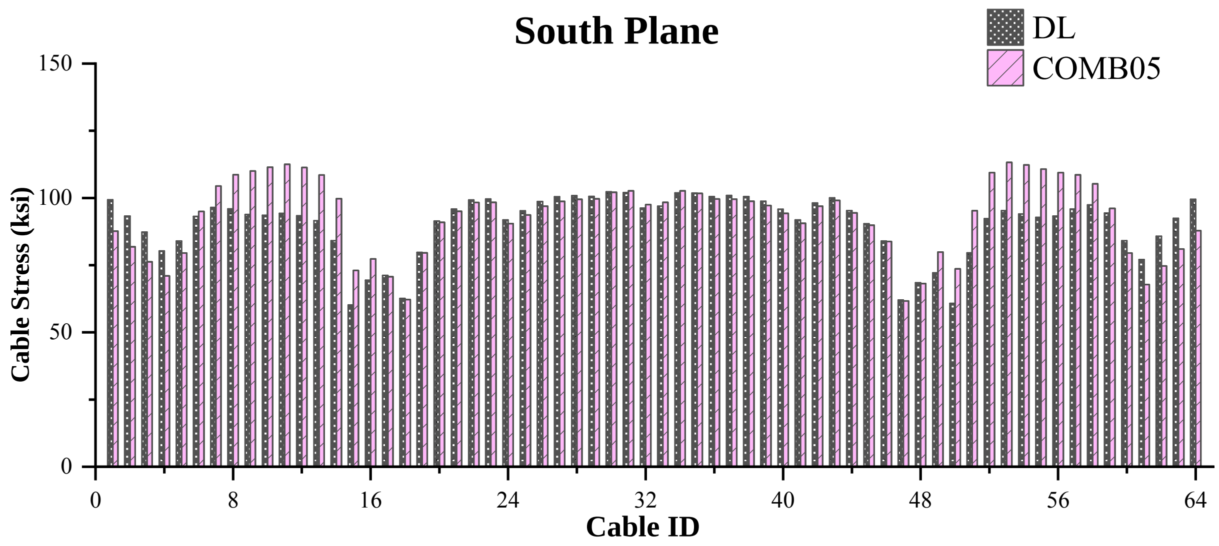

Source: FHWA.

Figure 71. Graph. Cable stresses under dead load and COMB05.

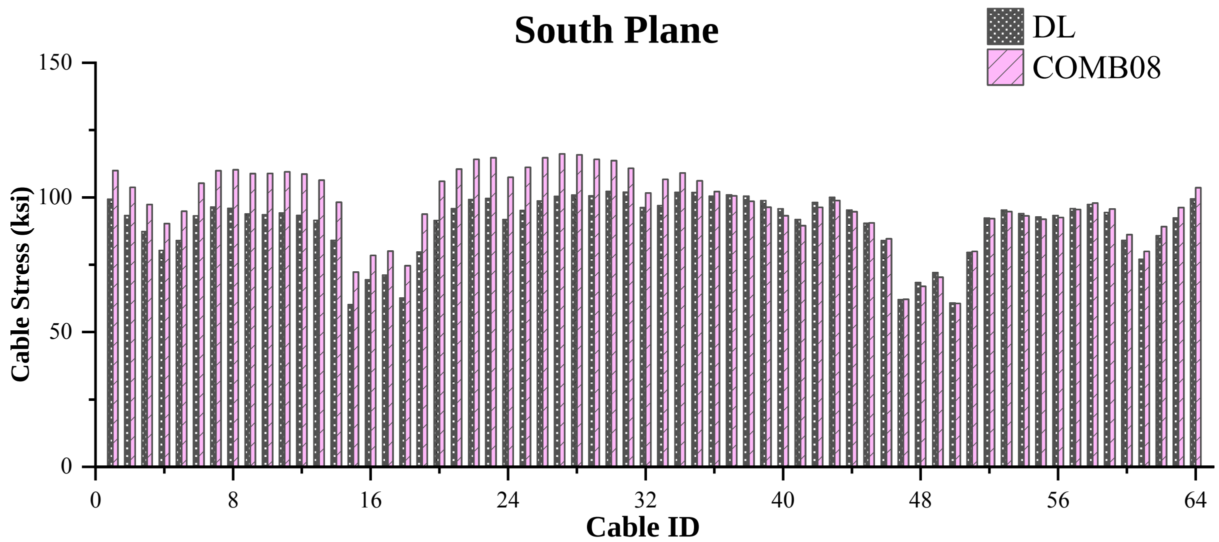

Source: FHWA.

Figure 72. Graph. Cable stresses under dead load and COMB08.

Behavior of the Bridge under Single Cable Loss Event

Based on geometric symmetry of the bridge and applied loading, 32 cable loss scenarios were considered for the four loading configurations. In each cable loss scenario, the cable in question was suddenly removed. The cable ID information is shown in Figure 73. The cable ID increases from left (west side) to right (east side). The longest cable at the left (west) side span is labeled as S.01(N.01); the shortest cable at the left (west) side span is labeled as S.16 (N.16); the shortest cable in the main span attached to the west pylon is labeled as S.17 (N.17); the longest cable in the main span attached to the west pylon is labeled as S.32 (N.32); the longest cable in the main span attached to the east pylon is labeled as S.33 (N.33) and the longest cable in right (east) side span is labeled as S.64 (No.64). Here "S (or N)" represents South Plane (or North Plane). For cable removal analysis cases under COMB01, COMB04 and COMB05, the removed cables S.01 to S.32 are all located in South Plane and attached to the west pylon. For cable removal analysis under COMB08, additional 32 cable removal scenarios were considered on cables S.33 to S.64, which are in South Plane and attached to the east pylon.

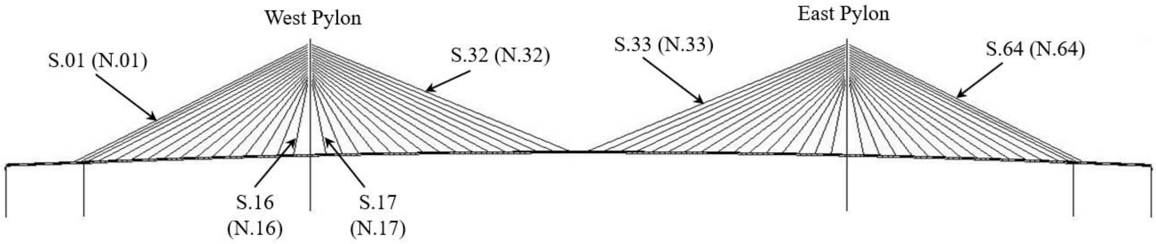

Source: FHWA.

Figure 73. Illustration. Cable ID designation.

Simulation Stages and Damping Effect

Member removal analysis was conducted through the following steps.

Stages 1-3: Application of dead and live loads until a simulation time of 30 seconds, as discussed earlier.

Stage 4: From 30 to 35 seconds. The large global damping is adjusted back to a normal value once the vibrations due to load application subside. The 'normal' damping ratio is taken as 2% of critical damping, which is a representative value for long-span cable-stayed bridges (Narita and Yokoyama, 1991).

Stage 5: From 35 to 45 seconds. After the structure reaches its steady-state under normal damping in Stage 4, a single cable is removed at 35 seconds, which triggers vibration of the bridge. This stage lasts for 10 seconds, which is long enough to capture the peak response due to a sudden cable loss.

Stage 6: From 45 to 65 seconds, after the bridge vibrates for 10 seconds due to cable loss in Stage 5, the global damping is increased back again to a large value (i.e., approximately 80% of critical damping) to damp out the vibrations rapidly so that the response can reach a new steady state. Experience has shown that this duration is sufficient for the bridge to reach a new steady state following the loss of a cable.

The overall simulation stages and damping curve during single cable removal analysis are shown in Figure 74.

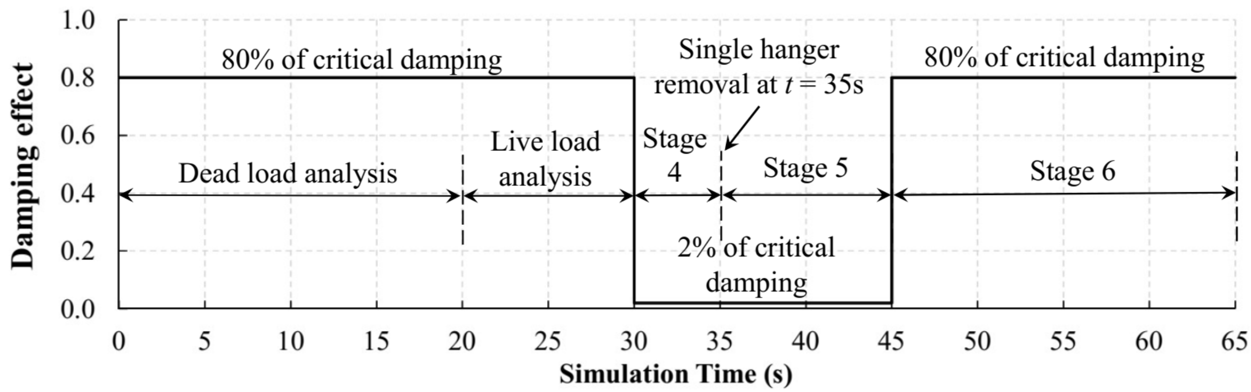

Source: FHWA.

Figure 74. Graph. Simulation stages and damping curve for single cable removal analysis.

The typical structural response under a single member loss event could be categorized into three phases, as illustrated in Figure 75. The steady-state response of the intact bridge is denoted as S_{intact}. Following the loss of a cable, the structural response achieves a peak value, which is denoted as S_{damage_peak}. Following this, the amplitude of vibration is damped out to a new steady-state value of S_{damage_steady}. Based on these response quantities, the behavior of the bridge during a cable loss event can be evaluated by the following four indexes: demand capacity ratio (DCR), dynamic increase factor (DIF), static increase factor (SIF) and dynamic amplification factor (DAF). Definitions of these indexes and results under different cable loss scenarios are presented in the following subsections.

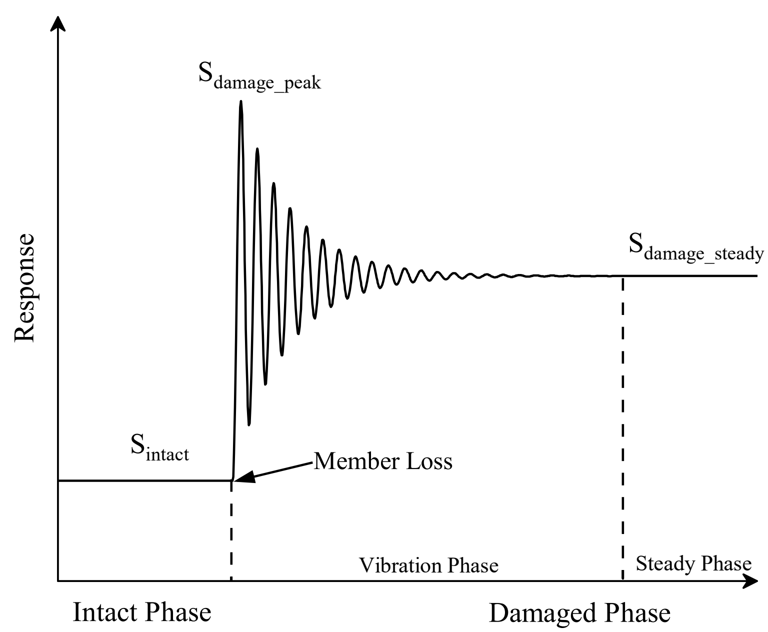

Source: FHWA.

Figure 75. Illustration. Typical structure response under single member loss.

Demand Capacity Ratio (DCR)

Three demand to capacity ratios (DCRs) were computed as defined by Equation (15) below,

$$DCR_{intact} = \frac{\sigma_{intact}}{\sigma_y};\ DCR_{damage\_peak} = \frac{\sigma_{damage\_peak}}{\sigma_y};\ DCR_{damage\_steady} = \frac{\sigma_{damage\_steady}}{\sigma_y} \quad (15)$$

where σ_{intact} = stress corresponding to dead and live loads on the bridge in the intact condition (without member loss), σ_{damage_peak} = peak stress following the sudden removal of a member and σ_{damage_steady} = steady-state stress after sudden removal of a member and σ_y = the yield stress shown in Figure 16 and Table 5. For cables, the above stresses were calculated from the axial forces divided by the cross-sectional area of the cables.

For each cable loss scenario, the demand capacity ratios were calculated for each member of the bridge and then the maximum value of DCR was identified for each type of structural components. This process was repeated for sudden loss of different cables to obtain the envelope of DCR. This envelope for COMB01 due to 32 single cable loss scenarios is shown in Figure 77. The DCR envelopes for the other 3 load combinations discussed previously were similar to that for the load combination COMB01 and are not presented in this report.

The cables lost suddenly in the 32 scenarios were all located in South Plane, attached to the west pylon and designated S.01 to S.32. As shown in Figure 76, cables in the bridge are categorized into 4 zones: (1) Zone 1 with cables N.01 to N.32 connected to the west pylon in North Plane, (2) Zone 2 with cables N.33 to N.64 connected to the east pylon in North Plane, (3) Zone 3 with cables S.01 to S.32 connected to the west pylon in South Plane (i.e., cable removal zone), and (4) Zone 4 with cables S.33 to S.64 connected to the east pylon in South Plane.

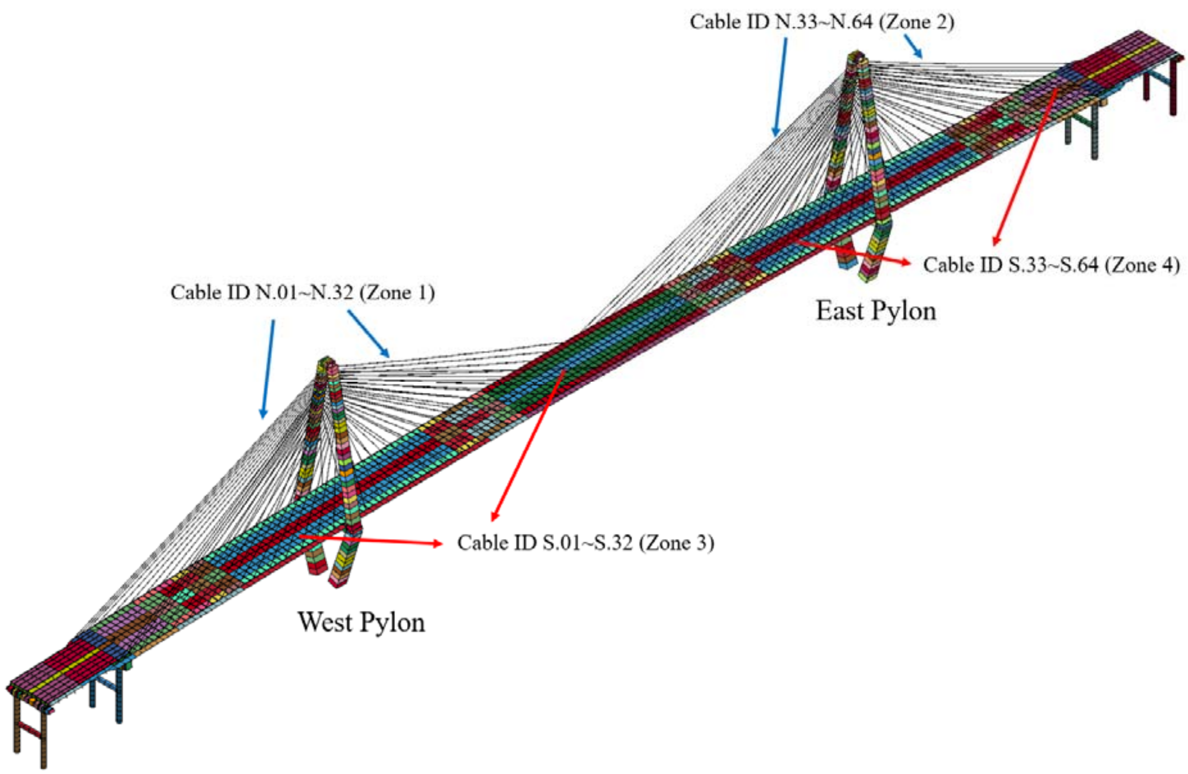

Source: FHWA.

Figure 76. Illustration. Cable ID designation categorized into 4 zones.

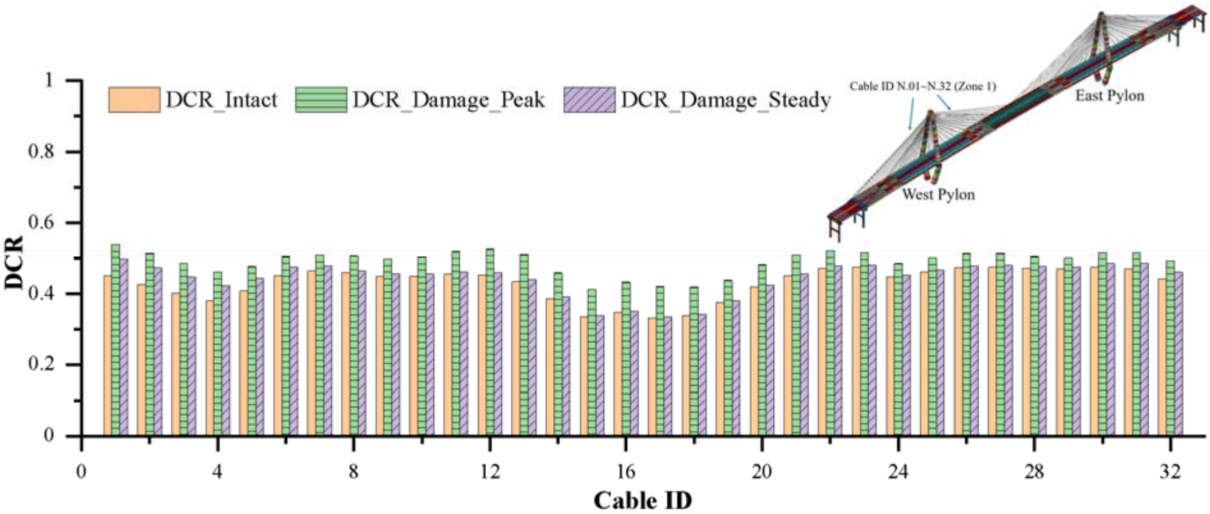

Source: FHWA.

(a) Envelope of DCR for cable stress in Zone 1.

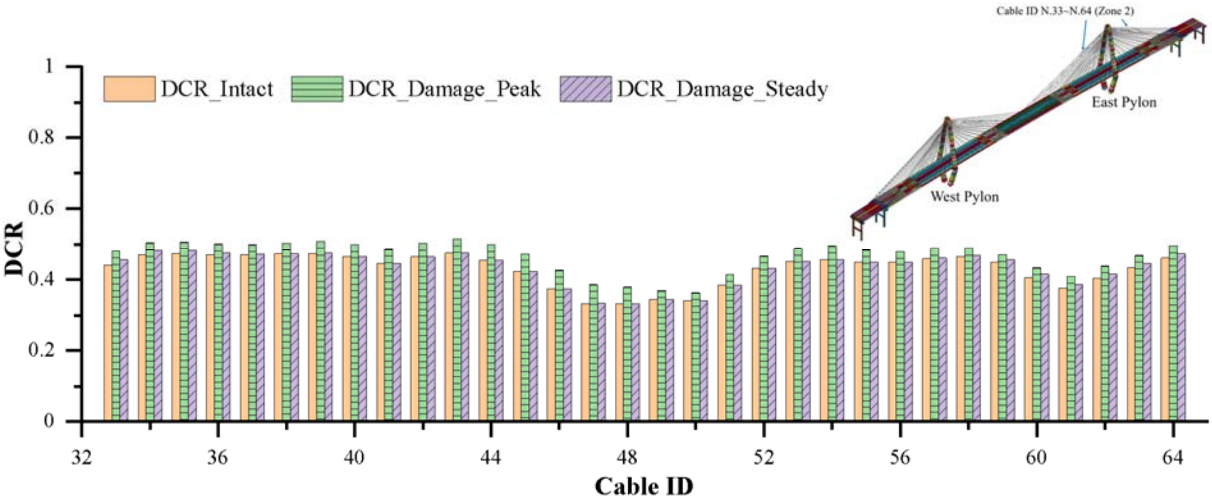

Source: FHWA.

(b) Envelope of DCR for cable stress in Zone 2.

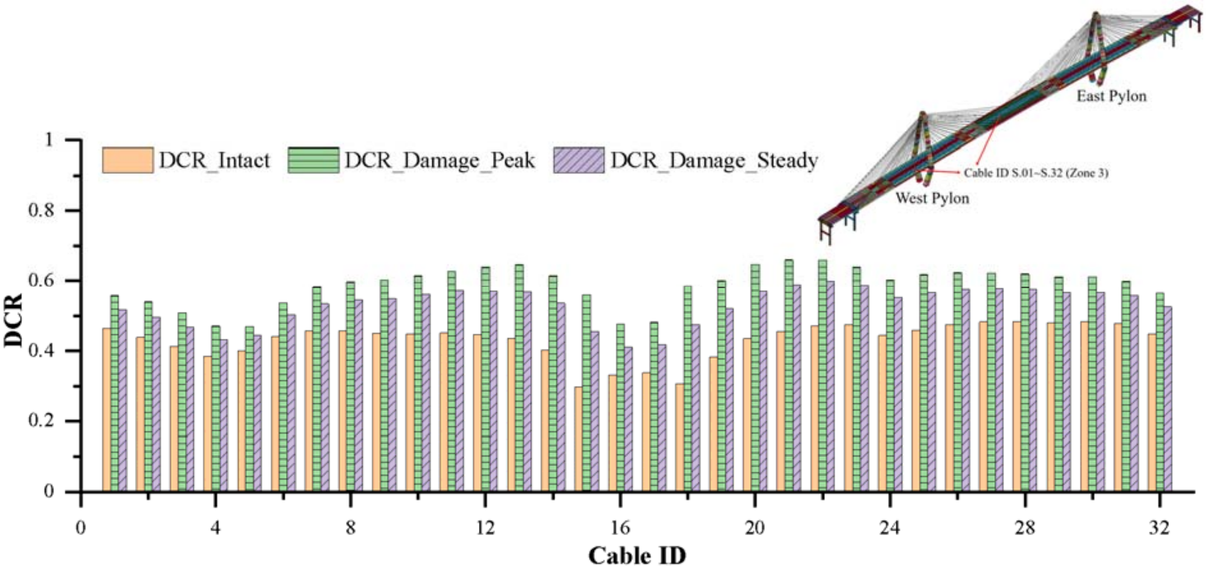

Source: FHWA.

(c) Envelope of DCR for cable stress in Zone 3.

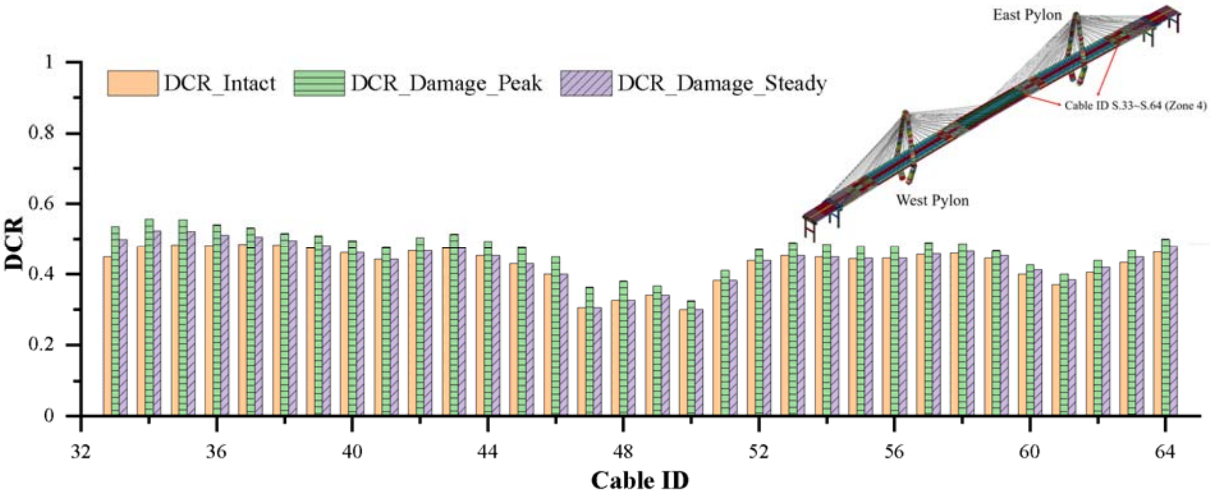

Source: FHWA.

(d) Envelope of DCR for cable stress in Zone 4.

Figure 77. Graphs. Envelope of DCR for cable stress under COMB01 due to representative cable loss cases.

Bar charts in Figure 77 show DCR_{intact}, DCR_{damage_peak} and DCR_{damage_steady} following sudden loss of a cable for Zone 1 through 4. As shown in Figure 77, most cables in the intact bridge had a DCR of approximately 0.45, except for DCRs of approximately 0.35 for the cables near pylons (i.e., cables 15-18 and 47-50 in both South Plane and North Plane). Since all suddenly removed cables S.01 to S.32 were located in South Plane and were attached to the west pylon, the envelope of DCR_{damage_peak} showed different trends in different zones. For cables in Zone 1, the envelope DCR_{damage_peak} increased by 0.03 ~ 0.09 with respect to DCR_{intact}. For cables in Zone 2, the envelope

DCR_{damage_peak} increased by 0.02 ~ 0.05 with respect to DCR_{intact}. For cables in Zone 3, which was the cable loss zone, the envelope DCR_{damage_peak} increased by 0.07 ~ 0.28 with respect to DCR_{intact}. For cables in Zone 4, the envelope DCR_{damage_peak} increased by 0.02 ~ 0.08 with respect to DCR_{intact}. Typically, the value of DCR_{damage_peak} for cable S.18 increased to 0.58 from a value of DCR_{intact} = 0.31 and the maximum value of DCR_{damage_peak} occurred in cables S.21 and S.22 with a value up to 0.66 due to a single cable loss.

After the vibration caused by the loss of a single cable dissipated, the damaged bridge reached its new steady state and there was a residual increased stress in the remaining cables. In the damaged state, the envelope of DCR_{damage_steady} calculated from the steady-state stress also showed different trends in different zones. For most cables in Zone 1, Zone 2 and Zone 4, the stress level in the damaged bridge returned to the level of the intact bridge, which indicates that a single cable loss event in one zone has limited effect on cables in the other zones. For some long cables in the Zone 1 (cables N.01 to N.04) and Zone 4 (cables S.33 and S35), the envelope of DCR_{damage_steady} increased by approximately 0.05 from the intact state DCR_{intact}. However, for cables in Zone 3, which was the cable loss zone, the envelope of DCR_{damage_steady} increased by 0.04 ~ 0.17 from the intact state DCR_{intact}. Particularly, the DCR in cable S.18 increased from 0.31 during the intact state to 0.58 for the peak vibration state and then reduced to 0.47 in the damaged steady-state. The maximum DCR_{damage_steady} in the damaged steady-state occurred in cable S.22 with a value of 0.60.

Dynamic Increase Factor (DIF) and Static Increase Factor (SIF)

The dynamic increase factor (DIF) and the static increase factor (SIF) are defined by Equation (16) and Equation (17), respectively. Here, DIF represents the dynamic increase effect, whereas SIF represents the static increase effects due to a cable loss event. The ratio of DIF to SIF represents the dynamic effect due to cable loss, which is introduced as the dynamic amplification factor in the next section.

$$DIF = \frac{S_{damage\_peak}}{S_{intact}} \tag{16}$$

$$SIF = \frac{S_{damage\_steady}}{S_{intact}} \tag{17}$$

In the equations above, *S* represents structural quantities such as stresses in cables or structural steel members or peak value of deck displacement. The envelopes of DIF and SIF for stress in a single cable for the bridge under COMB01 due to each of the 32 representative single cable loss events are shown in Figure 78. The DIF and SIF results under other load combinations showed similar trends as those under COMB01 and are not presented in this report.

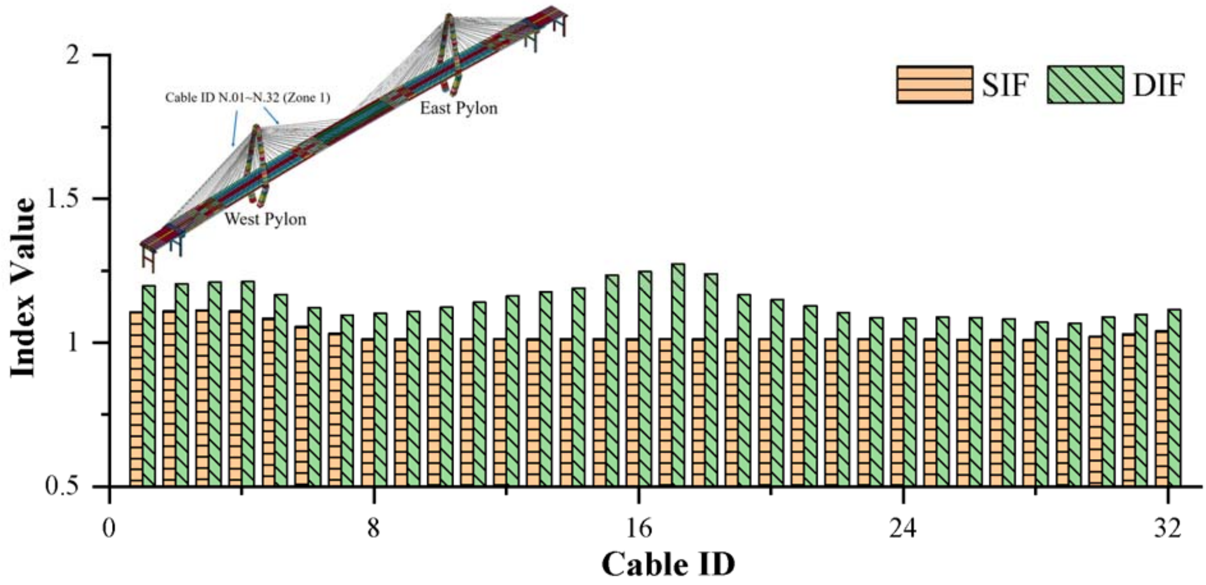

Source: FHWA.

(a) Envelope of DIF and SIF for cable stress in Zone 1.

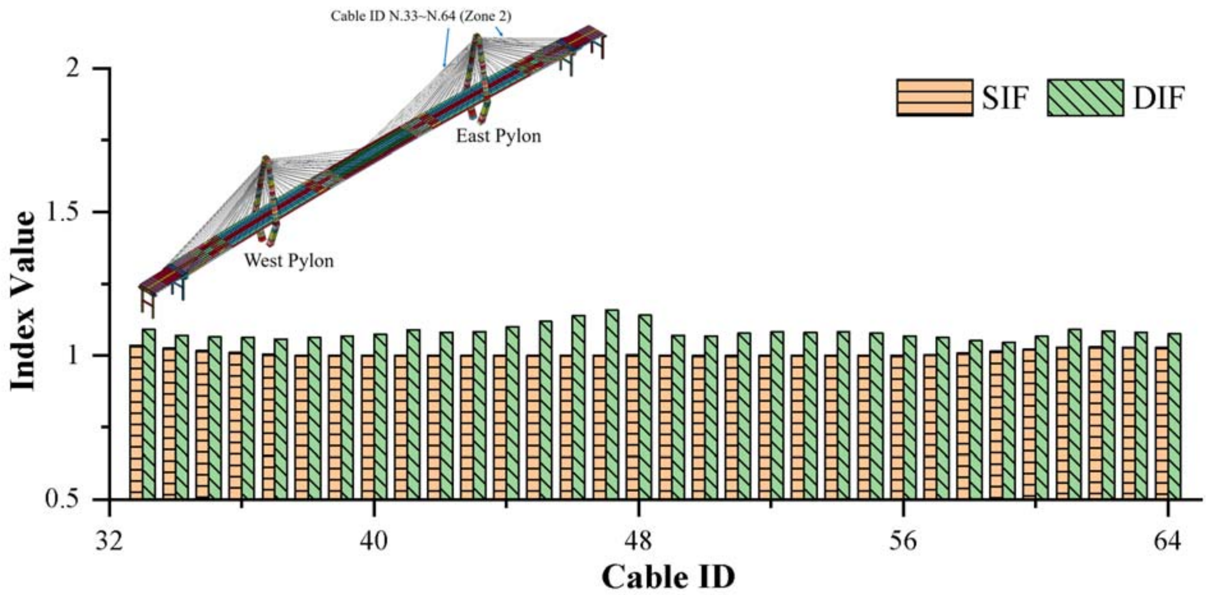

Source: FHWA.

(b) Envelope of DIF and SIF for cable stress in Zone 2.

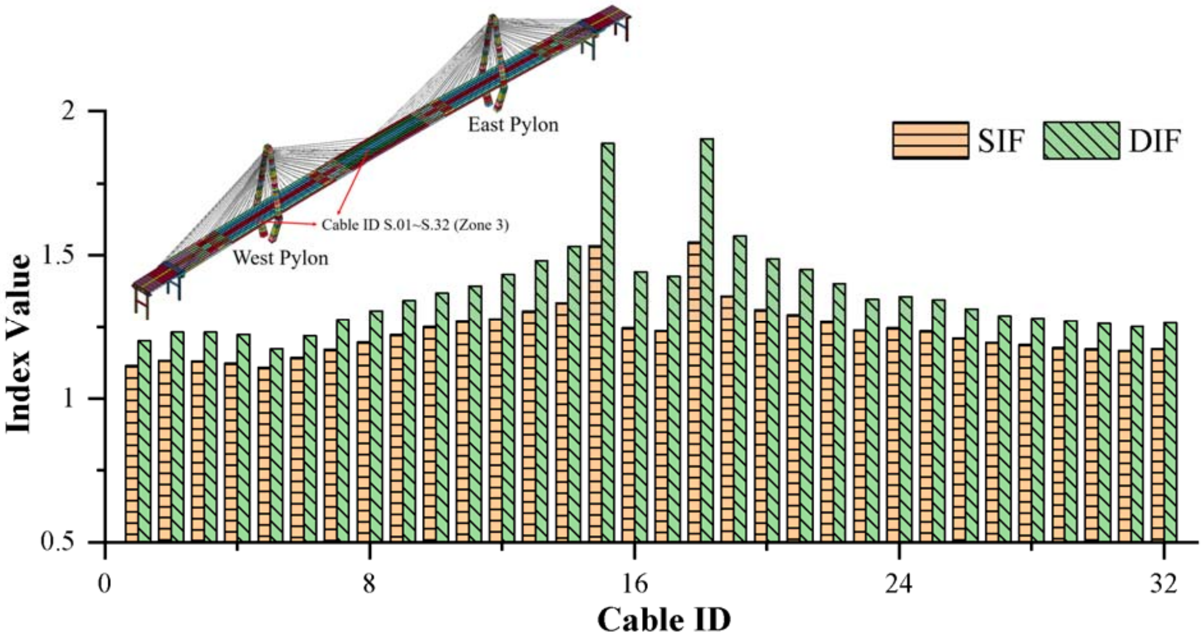

Source: FHWA.

(c) Envelope of DIF and SIF for cable stress in Zone 3.

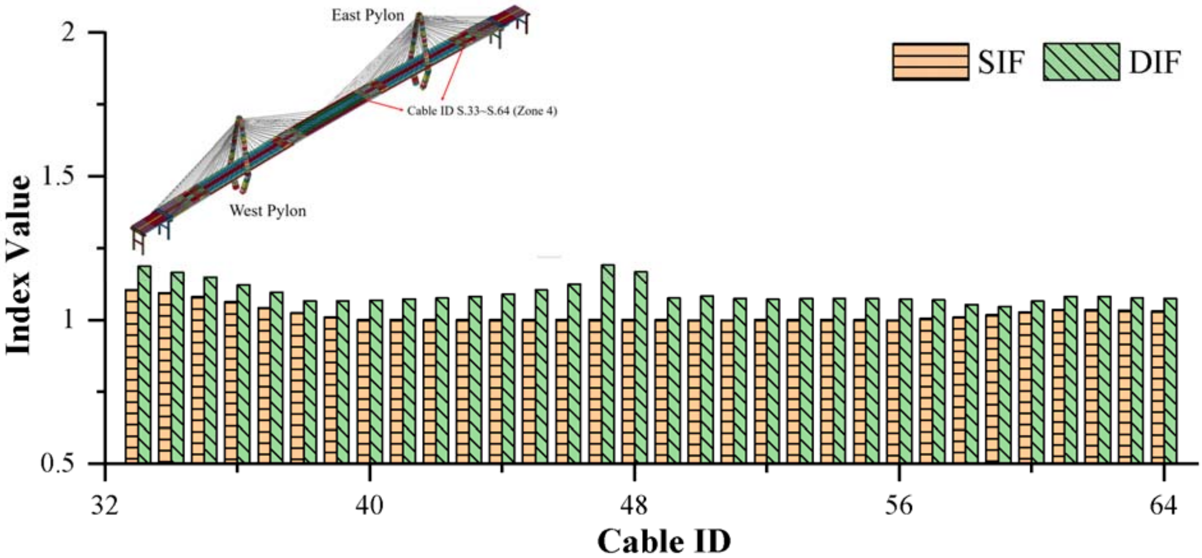

Source: FHWA.

(d) Envelope of DIF and SIF for cable stress in Zone 4.

Figure 78. Graphs. Envelope of DIF and SIF for cable stress under COMB01 due to representative cable loss cases.

It is observed from bar charts in Figure 78 that the envelope of SIF in Zone 1, 2 and 4 was close to 1, which indicates that single cable loss in a zone had a negligible effect on cables in other zones (cables in the other plane or attached to the pylon without cable loss). Cables N.01 to N.06 in Zone 1 and cables S.33 to S.36 in Zone 4 had slightly larger SIF values around 1.10. Cable N.01 to N.06 in Zone 1 are the longest cables attached to the west pylon with cable loss and were likely influenced by sudden cable loss in South Plane (also connected to the same pylon) due to deflection of the pylon. Cables S.33 to S.36 in Zone 4 are the longest cables in the cable loss plane, but attached to the east pylon and were influenced by the loss of cables anchored in the center span, such as cable S.32, because of deflection of the edge girder in the main span. The SIF values in Zone 3 (the cable loss zone) ranged from 1.11 to 1.55. The highest SIF values occurred in cables S.15 and S.18, which are the two cables closest to the west pylon. The stresses in these two cables were the lowest in the intact bridge with DCR_{intact} = 0.30. Larger SIF values in these cables were caused by the loss of the adjacent cables, such as S.14 or S.19, which caused transfer of large forces into these cables.

The trend of DIF in Figure 78 is similar to that of SIF. It is observed that the envelope of DIF in Zone 1 ranged from 1.07 to 1.27, whereas the envelope of DIF in Zone 2 ranged from 1.05 to 1.16. The envelope of DIF in Zone 4 ranged from 1.05 to 1.19, and the envelope of DIF in Zone 3 (the cable loss zone) ranged from 1.17 to 1.90. The largest value of DIF occurred in cables S.15 and S.18, similar to that for SIF.

Dynamic Amplification Factor (DAF)

Dynamic amplification factor is usually defined as a ratio between the dynamic response to the static response, when a dynamic load is applied on a structure and can be calculated by Equation (18) (Chopra 2012). Some researchers (Wolff and Starossek 2010) also proposed Equation (19) to calculate DAF for cable supported structures under sudden cable loss. However, DAF calculated by Equation (19) sometimes results in meaningless results. For example, when responses of the damaged bridge (S_{damage_steady}) and the intact bridge (S_{intact}) are quite close when the lost member is far, the denominator in Equation (19) may be close to zero. In this situation, a slightly larger value of peak response (S_{damage_peak}) will make the calculated DAF unrealistically large. Hence, Equation (18) has been used to calculate the DAF.

$$DAF = \frac{S_{dynamic}}{S_{static}} = \frac{S_{damage\_peak}}{S_{damage\_steady}} \tag{18}$$

$$DAF = \frac{S_{damage\_peak} - S_{intact}}{S_{damage\_steady} - S_{intact}} \tag{19}$$

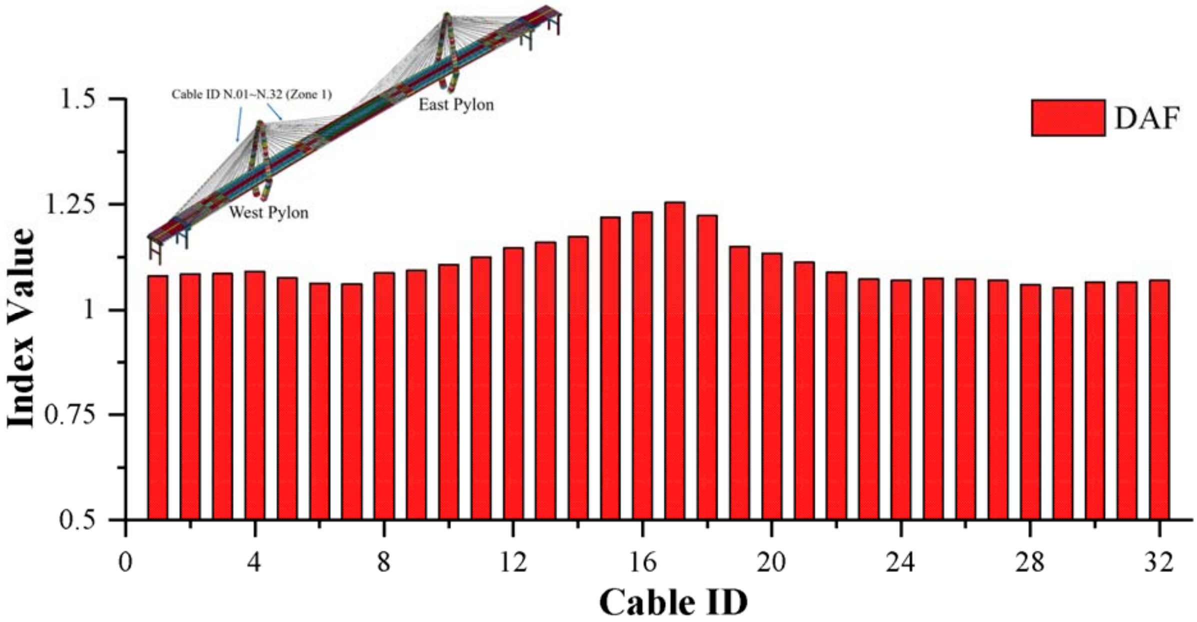

Source: FHWA.

(a) Envelope of DAF for cable stress in Zone 1.

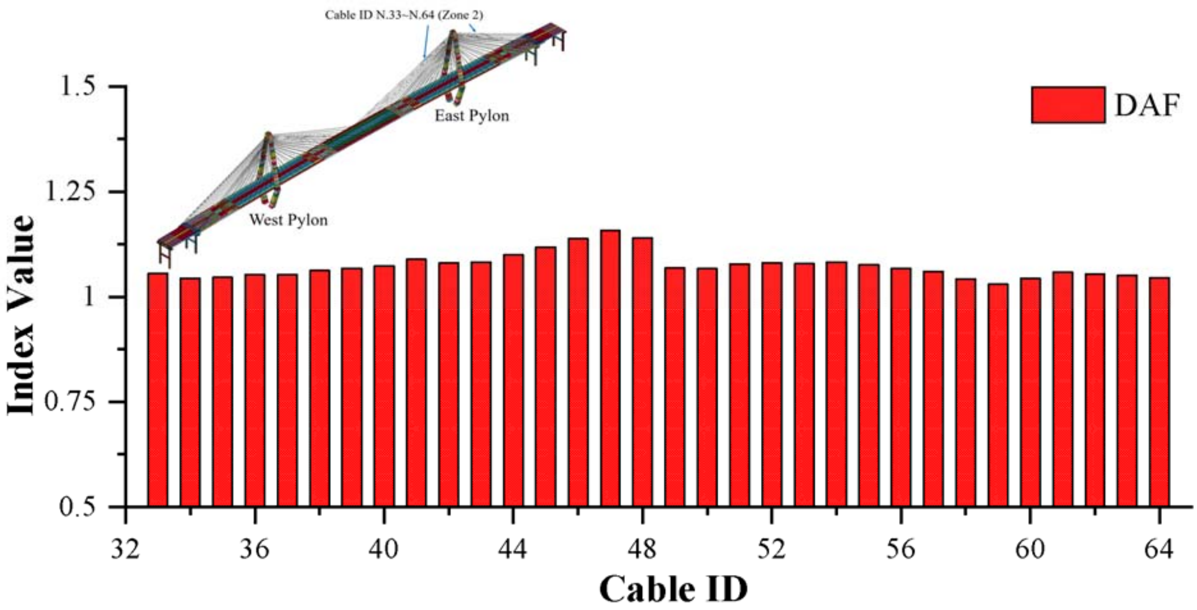

Source: FHWA.

(b) Envelope of DAF for cable stress in Zone 2.

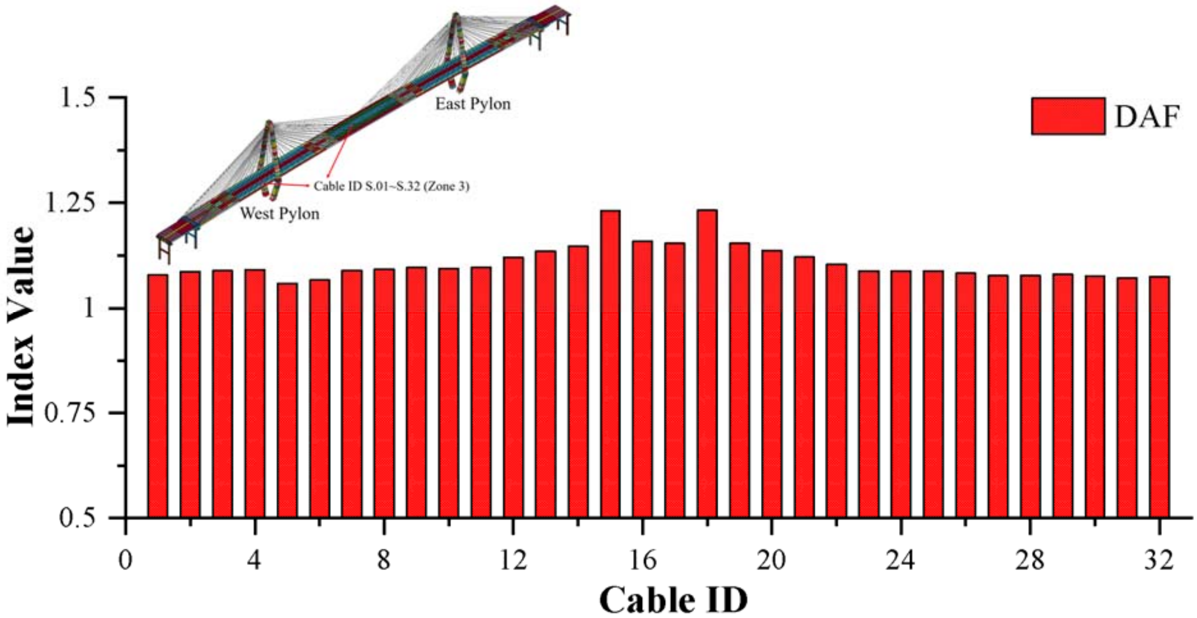

Source: FHWA.

(c) Envelope of DAF for cable stress in Zone 3.

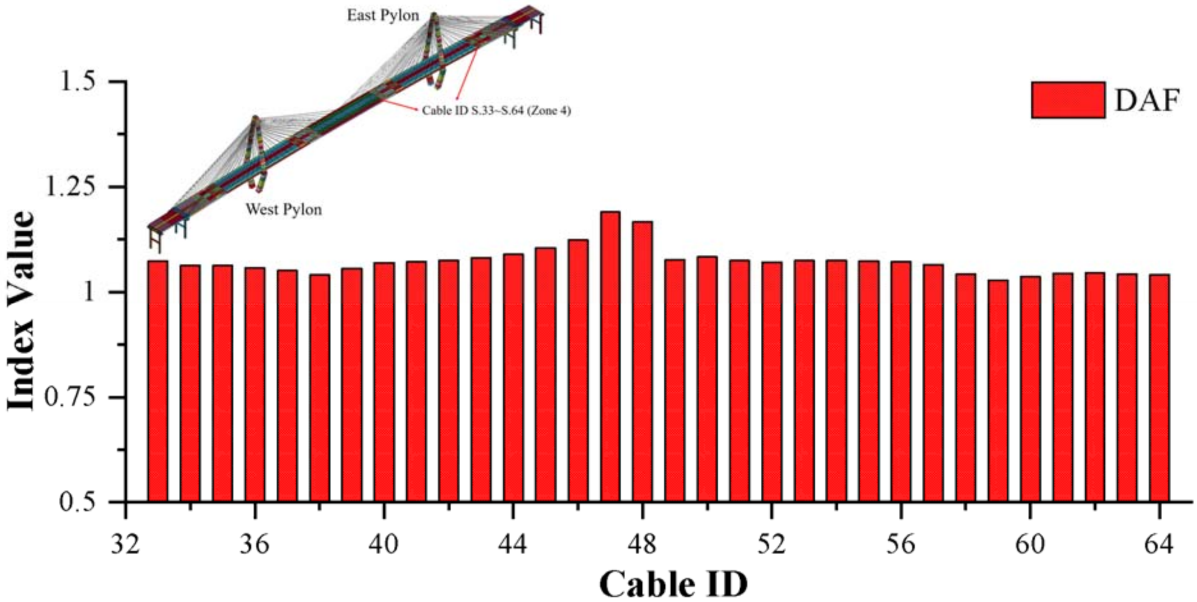

Source: FHWA.

(d) Envelope of DAF for cable stress in Zone 4.

Figure 79. Graphs. Envelope of DAF for cable stress under COMB01 due to representative cable loss cases.

It is observed from Figure 79 that overall, DAF had a similar trend in all four zones of cables. Based on 32 representative cable loss cases, the envelope of DAF in the four zones ranged from 1.05 to 1.25, 1.03 to 1.15, 1.06 to 1.23 and 1.03 to 1.19, respectively. The DAF values were slightly larger in Zone 1 and 3 in comparison to those in Zone 2 and 4, since the cables in Zone 1 and 3 are attached to the same pylon from which cables are removed. Additionally, the DAF was slightly larger in the cables near the bridge pylons in all four Zones.

Time-history Responses during Single Cable Removal

It is clear that DCR for cable stresses due to single cable loss were below 1.0 in all four zones, which indicates the bridge remained elastic under each single cable loss case. Additionally, the SIF in Zone 1, 2 and 4, which are the non-cable-removal zones, were close to 1. This indicates that single cable loss had a generally limited effect on bridge behavior. An example case of single cable removal is illustrated in this section. The selected representative case is the removal of cable S.19 under COMB01. Loss of this cable resulted in the largest DIF in its adjacent cable S.18.

The time history of maximum vertical displacement in the entire bridge deck and at the location of S.19 loss are shown in Figure 80. The maximum vertical displacement in the entire bridge deck remained almost the same as the intact bridge after loss of cable S.19. However, the maximum localized vertical displacement at the location of cable S.19 increased from a static value of 0.59 feet to a peak value of 1.17 feet due to vibration induced by the sudden loss of cable S.19 and then stabilized to a new steady-state value of 0.97 feet in the damaged condition.

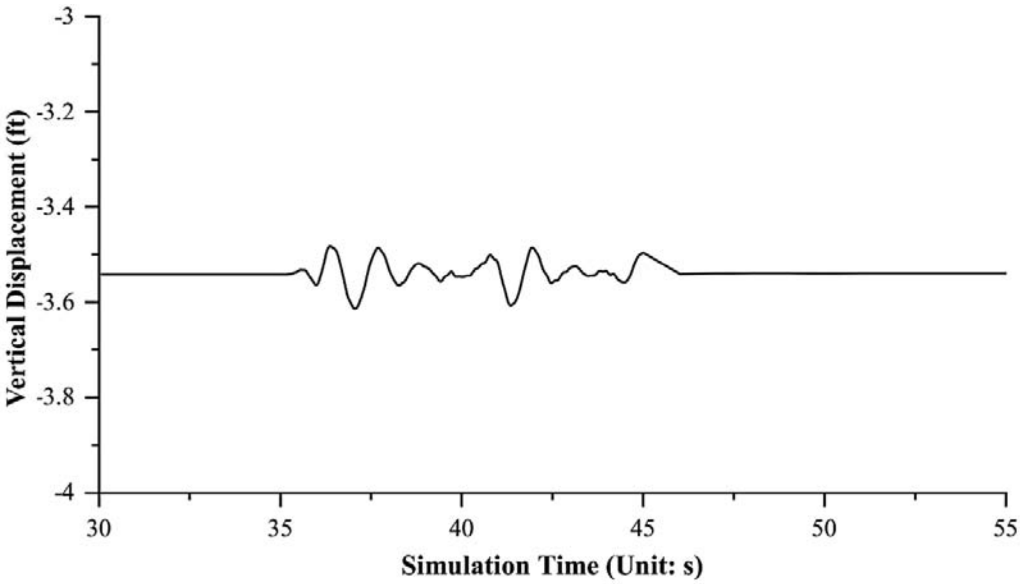

Source: FHWA.

(a) Maximum vertical displacement at the whole bridge deck.

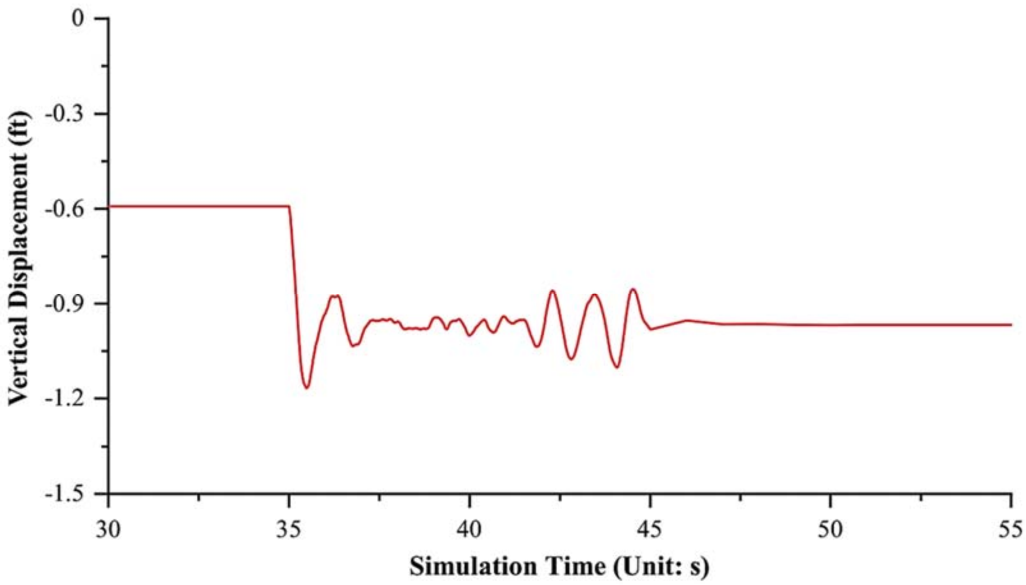

Source: FHWA.

(b) Maximum vertical displacement at S.19 loss area.

Figure 80. Graphs. Time history of maximum vertical displacements during S.19 loss under COMB01.

The time histories of cable stress in the adjacent cables during the loss of cable S.19 are shown in Figure 81. It is observed that the change in cable stress in North Plane was very small due to loss of cable S.19. However, loss of cable S.19 had a much larger effect on the adjacent cables in South Plane, particularly in the adjacent cable S.18.

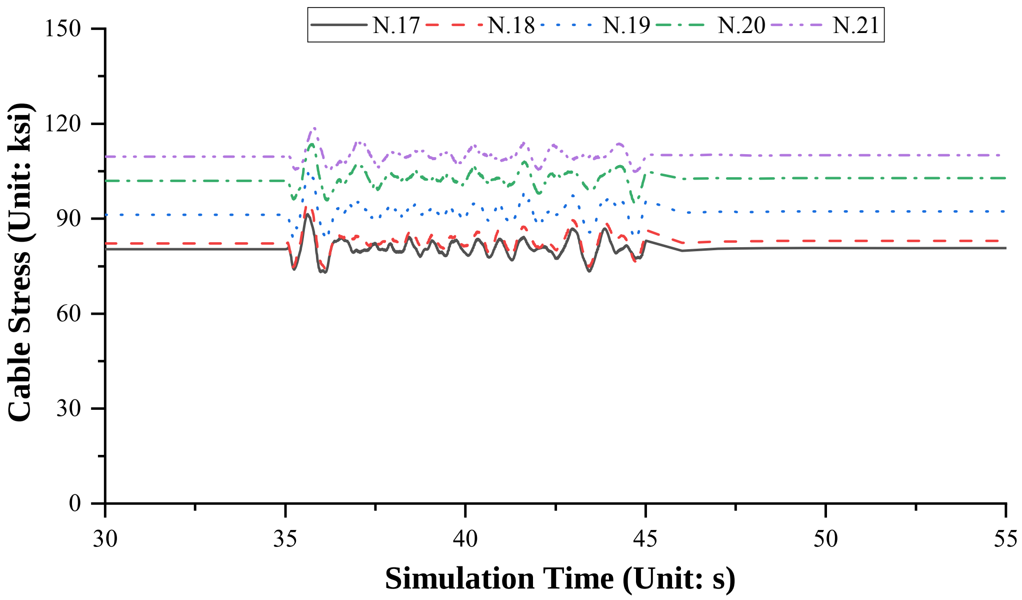

Source: FHWA.

(a) Stress time history in cables near S.19 in North Plane.

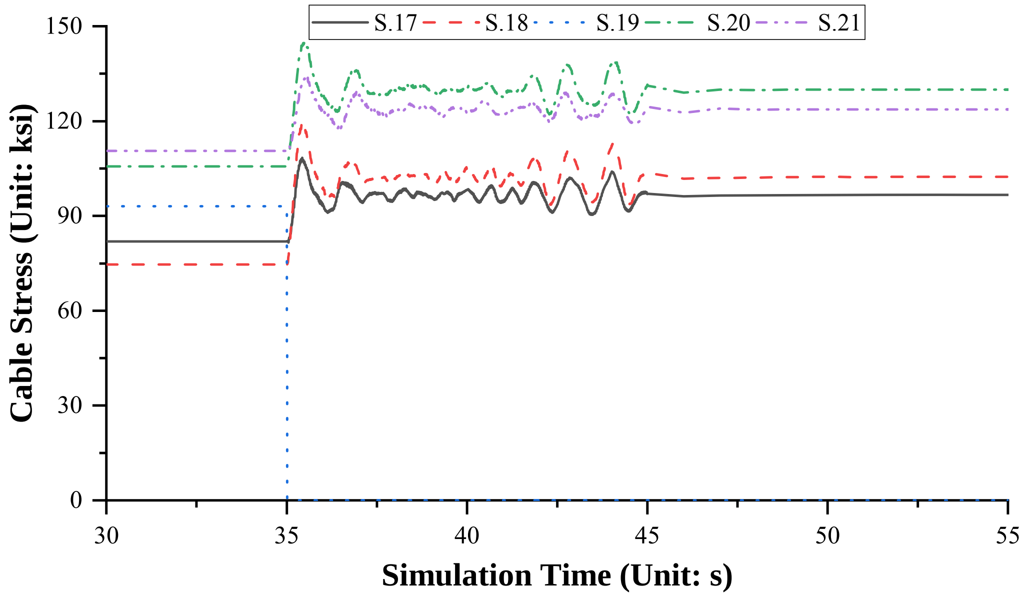

Source: FHWA.

(b) Stress time history in cables near S.19 in South Plane.

Figure 81. Graphs. Time history of cable stress in adjacent cables during S.19 loss under COMB01

Behavior of the Bridge under Multiple Cable Loss Events

Potential progressive collapse behavior of the bridge was analyzed under COMB01, which is used as a representative load case. Similar to the process used for single cable removal analysis, the global damping constant was reduced to 2% of critical damping before the first cable was removed. The damping constant was then increased to a large value (80% of the critical damping) after a simulation time of 10 seconds (about four times the period of the first vibration mode), which is long enough to capture the peak response following the sudden loss of the first cable. Once the bridge reached its new steady state, the global damping constant was reduced to 2% of critical damping once again prior to removing the second cable. This process was repeated for subsequent cable loss scenarios. The live load applied on the bridge was assumed constant during the whole cable loss event. Two multiple cable loss scenarios were considered, which represent failure sequences in different parts of the bridge as shown in Table 22. The first, termed Cable Loss Scenario 1 (CLS 1) is demonstrated in Figure 82, while the second, designated CLS 2 is shown in Figure 86.

Table 22. Cable loss scenarios of cable stayed bridge.

Scenario Name	Lost Cable No.
Cable Loss Scenario 1 (CLS 1) – See Figure 82	S.17→S.18→S.19→S.20
Cable Loss Scenario 2 (CLS 2) – see Figure 86	S.32→S.31→……→S.24→S.23

Three limit states were established in order to evaluate the level of damage to the bridge: functionality limit state, member failure limit state and ultimate limit state. The functionality limit state is defined as the damage level when tension cracks occurred in 10% of the deck area or the deflections due to dead load reached the limit of L/400 (JSCE 2007b). The member failure limit state is defined as the damage level when a main structural member reached its yield point. The ultimate limit state is defined as the damage level when fracture occurred in a main structural member or the entire bridge completely collapsed.

Progressive Collapse Behavior and Failure Modes during Cable Loss Scenario 1

The main edge girder deformation in the center span due to CLS 1 is shown in Figure 83.

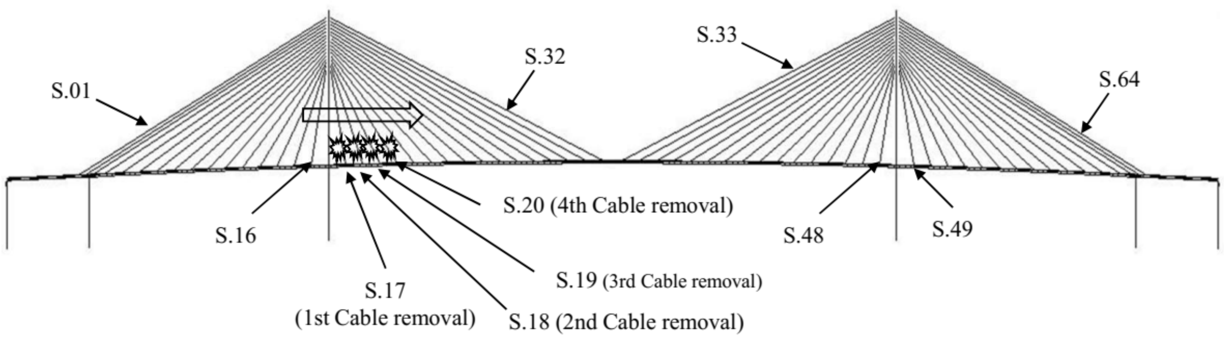

Source: FHWA.

Figure 82. Illustration. Cable removal pattern in CLS 1.

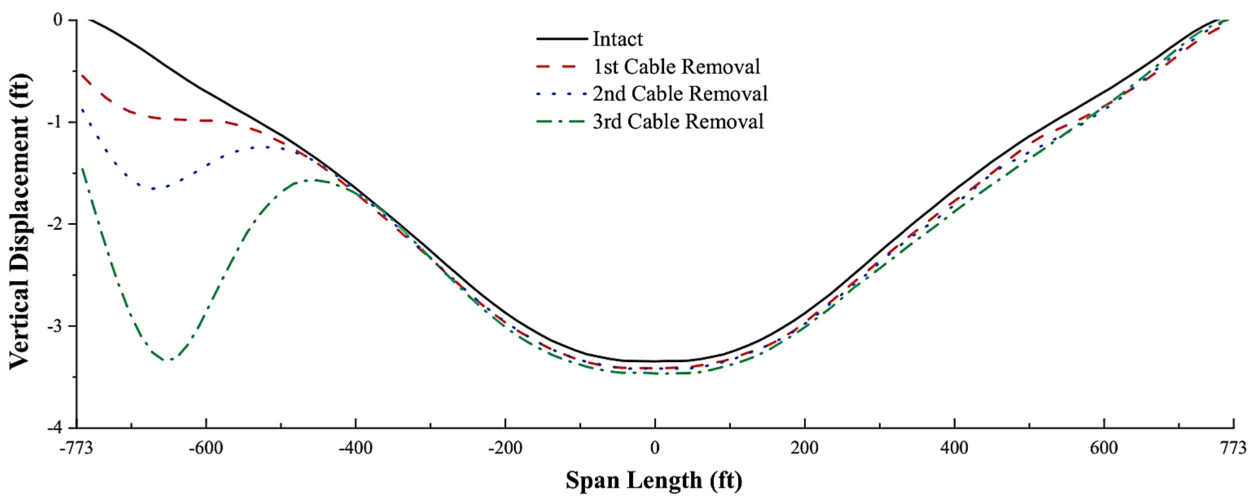

Source: FHWA.

Figure 83. Graph. Vertical displacements due to different cable removal in CLS 1.

Removal of First and Second Cables

Cable S.17 was the first cable removed at 35 seconds. The bridge's response reached steady-state behavior at 65 seconds. Following this, the second cable, cable S.18, was removed. The maximum vertical displacements along the edge girder in the center span during loss of cables S.17 and S.18 are shown by the red dash and blue dot lines in Figure 83, respectively. The overall deformation after the loss of cable S.17 was almost the same as that of the intact bridge. However, close to the lost cable, the deformation increased by approximately 0.5 feet. After the loss of cable S.18, the deformation in the cable loss zone increased by another 0.5 feet. The structural steel and stayed cables remained elastic due to these two cables loss events.

First Member Failure Limit State after the Third Cable Loss

The third cable (cable S.19) was removed at 95 seconds. During the vibration of the bridge due to the loss of this cable, localized deflection increased suddenly to more than 3 feet in the cable loss region, which was the largest deformation along the girder, as shown in Figure 83. The maximum stress in the main edge girder was around 22 ksi before the loss of the third cable. After the cable loss event, the stress in main girder in the cable loss region increased to more than 50 ksi and reached its yield strength, as shown in Figure 84.

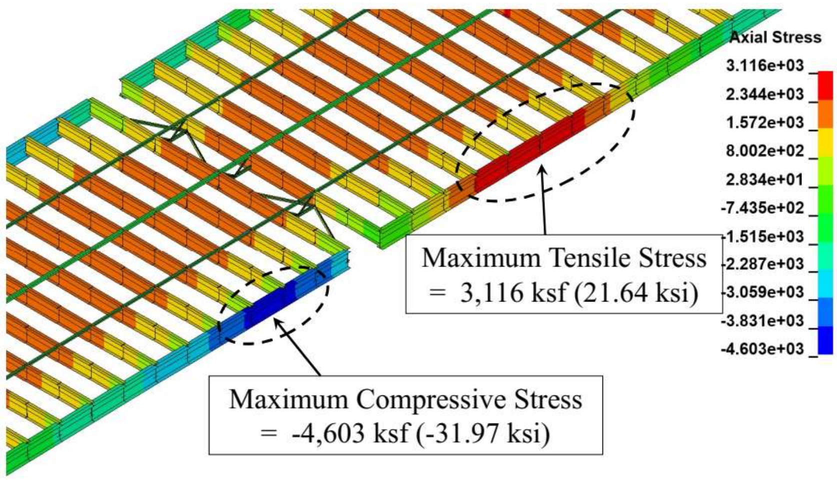

Source: FHWA.

(a) Before cable loss.

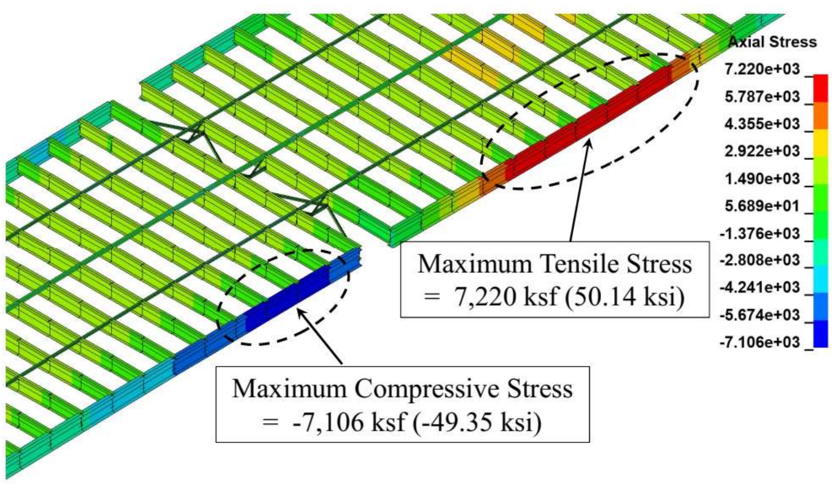

Source: FHWA.

(b) After cable loss.

Figure 84. Illustrations. Beam stress contour due to 3rd cable loss (unit: ksf).

Ultimate Limit State after the Loss of the Fourth Cable

The 4th cable (cable S.20) was removed at 125 seconds. During the vibration of the bridge due to sudden loss of this cable, two cables in the opposite plane (cables N.18 and N.19) reached their fracture strength. The lateral bearings also reached their ultimate deformation and suffered failure. The superstructure in the cable loss region collapsed and was supported by the pylon transverse beam only, as shown in Figure 85. The maximum vertical displacement in the cable loss region exceeded 55 feet and the bridge reached its ultimate limit state.

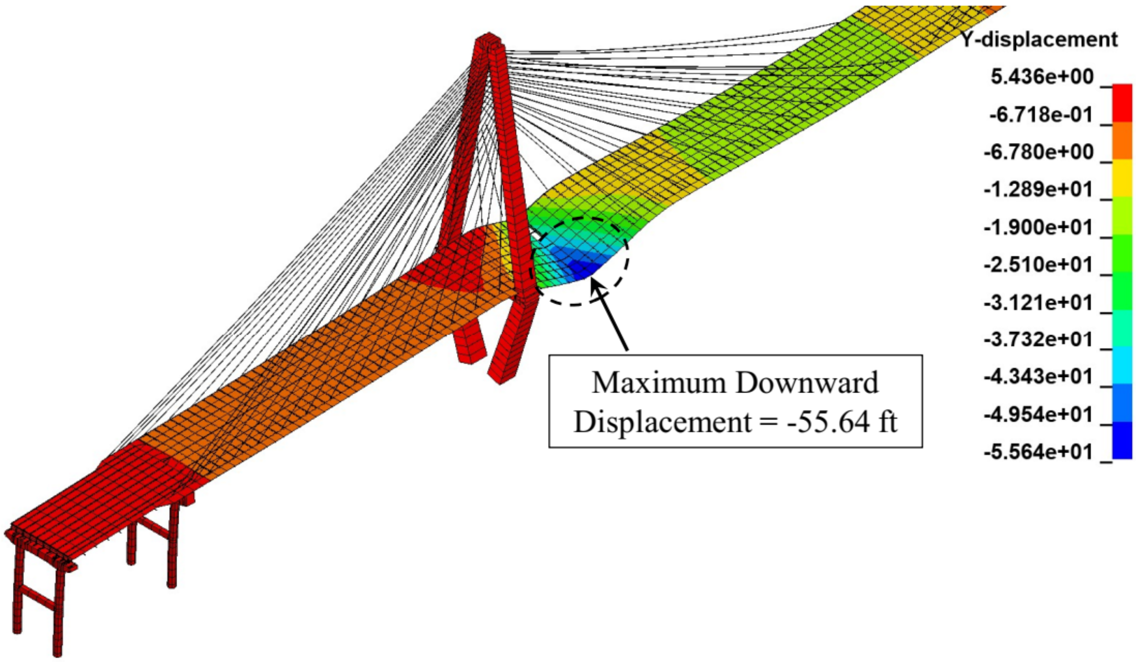

Source: FHWA.

Figure 85. Illustration. Ultimate limit state after 4th cable loss (unit: feet).

Progressive Collapse Behavior and Failure Modes during Cable Loss Scenario 2

The CLS 2 process is illustrated in Figure 86. The main edge girder deformation in the center span during the cable removal process is shown in Figure 87. In this cable loss scenario, the displacements at the edge girder increased gradually as the cables were removed one by one until the 10th cable was removed. The displacements increased suddenly after the loss of the 10th cable, indicating the collapse of the bridge.

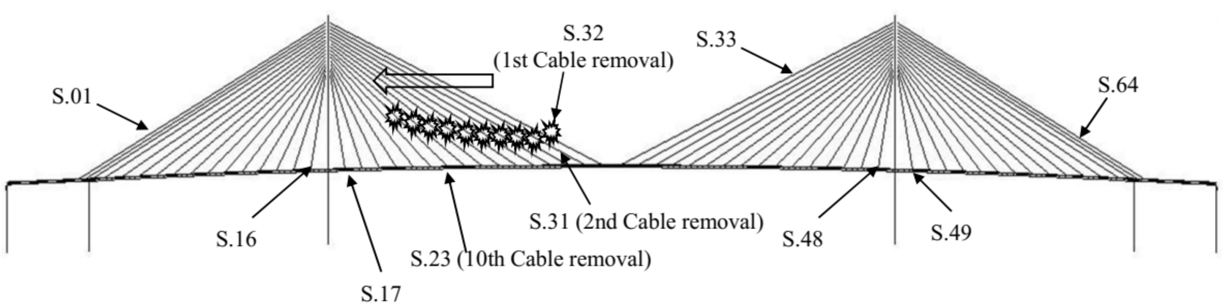

Source: FHWA.

Figure 86. Illustration. Cable removal pattern in CLS 2.

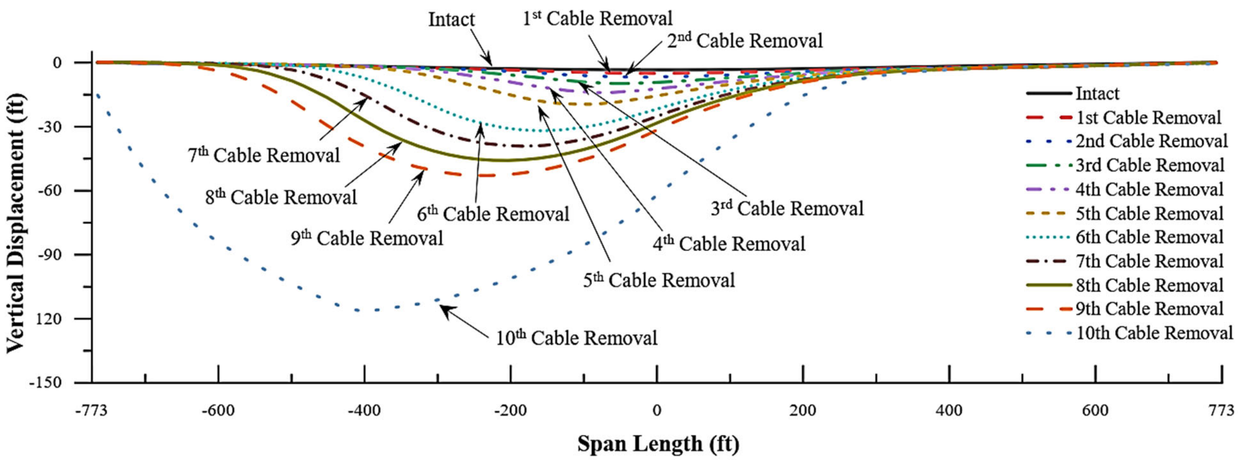

Source: FHWA.

Figure 87. Graph. Vertical displacements due to different cable removal in CLS 2.

First Cable Loss and Second Cable Loss

The first cable (cable S.32) was removed at 35 seconds and the bridge response reached steady-state conditions at 55 seconds. Following this, the second cable, cable S.31, was removed at 65 seconds. The maximum vertical displacement time history for the first two cables' removal is shown in Figure 88. As a result of the loss of the first cable, the downward displacement reached a peak of 5.0 feet during the vibration of the bridge, which then became 4.5 feet at the steady-state. The maximum downward displacement reached 6.7 feet during the vibration of the bridge due to loss of the second cable. At this point, the bridge exceeded its functionality limit state (i.e., L/400 = 5.37 feet).

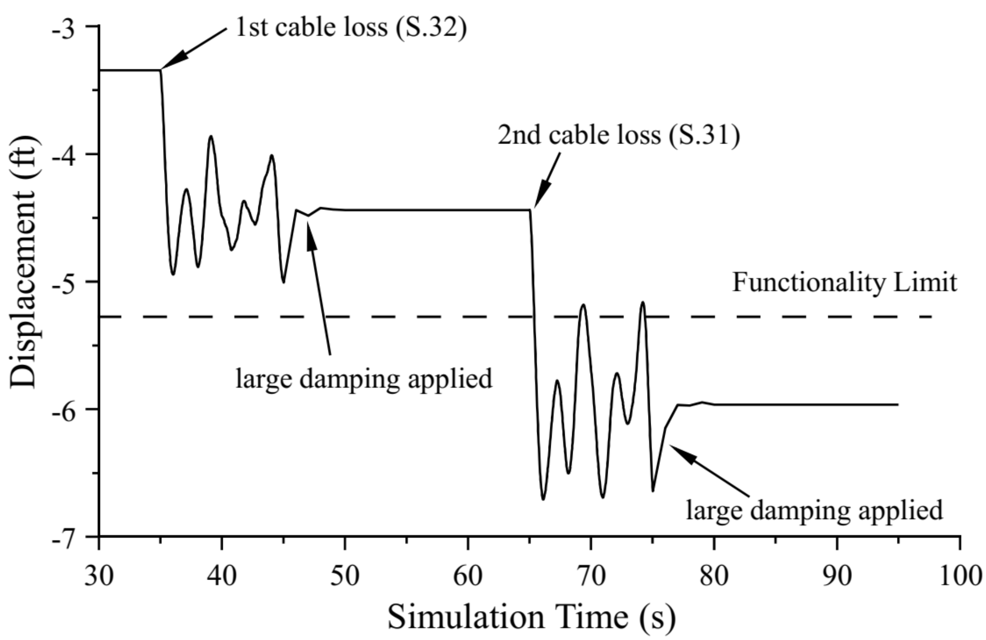

Source: FHWA.

Figure 88. Graph. Vertical displacement time history due to first two cables loss.

Member Failure Limit State Reached after the Third Cable Loss

The third cable (cable S.30) was removed at 95 seconds. The maximum stress in the main edge girder was 42.2 ksi before the third cable was removed. After its removal, the stress in the main girder in the cable loss region reached its yield strength, as shown in Figure 89.

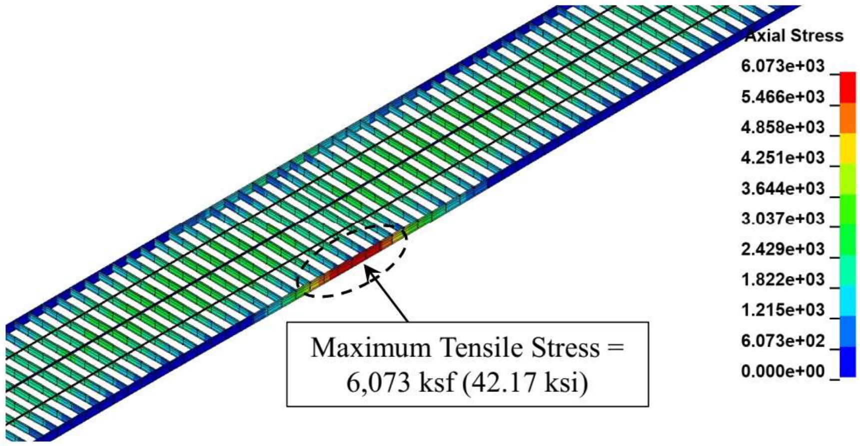

Source: FHWA.

(a) Before cable loss.

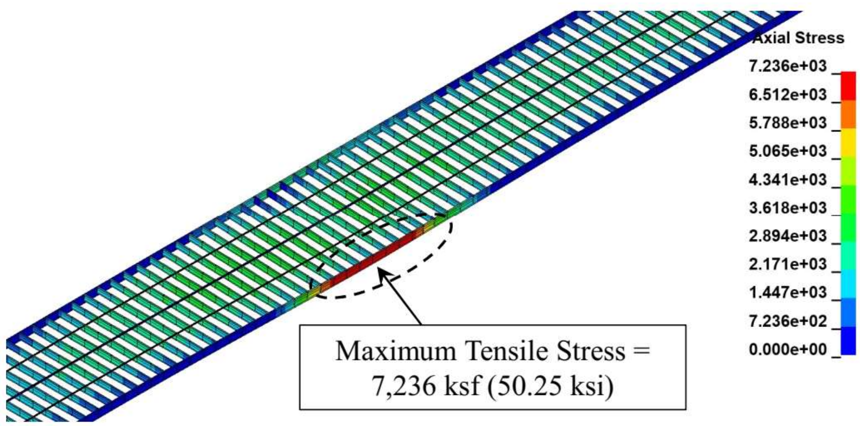

Source: FHWA.

(b) After cable loss.

Figure 89. Illustrations. Stress contour of girders due to 2nd cable loss (unit: ksf).

Serious Damage State after Loss of the Fifth Cable

Unlike CLS 1, the bridge showed ductile behavior during the cable removal process in this cable loss scenario. The 5th cable (cable S.28) was removed at 155 seconds. The vertical deformed shape after the 5th cables loss is shown in Figure 90. It was observed that the bridge suffered large downward displacement near the cable loss location in this stage. In addition, main structural members, such as girders and adjacent stayed cables (cable S.27), reached their yield strength. The bridge was seriously damaged and was close to its ultimate limit state after loss of the 5th cable.

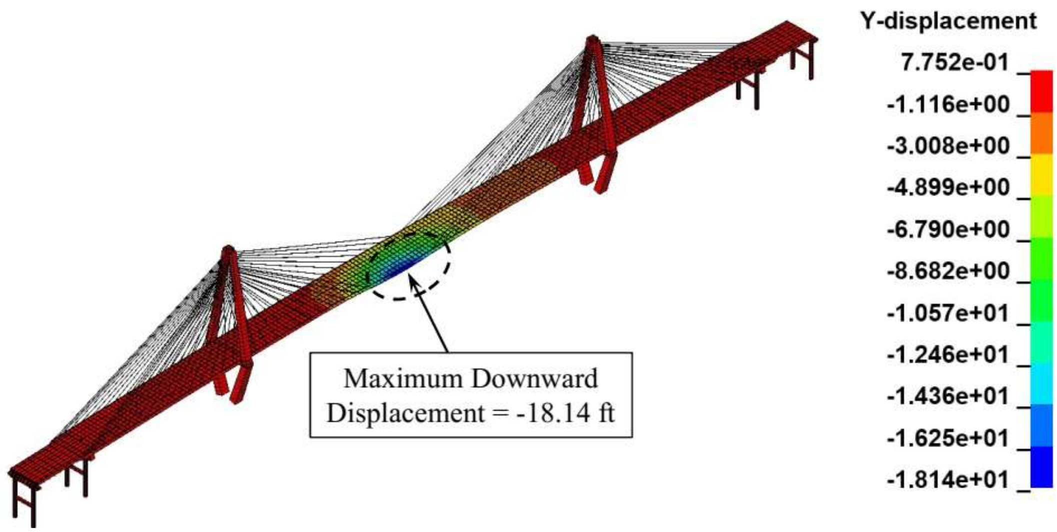

Source: FHWA.

Figure 90. Illustration. Vertical deflection due to 5th cable loss (unit: feet).

Ultimate Limit State after the Tenth Cable Loss

The tenth cable (cable S.23) was removed at 305 seconds. The adjacent cable (cable S.22) ruptured as a result. This was followed by rupture of cables S.21, S.20 and so on, thereby triggering an unzipping type progressive collapse of the bridge. The ultimate limit state of the bridge was then reached as shown in Figure 91.

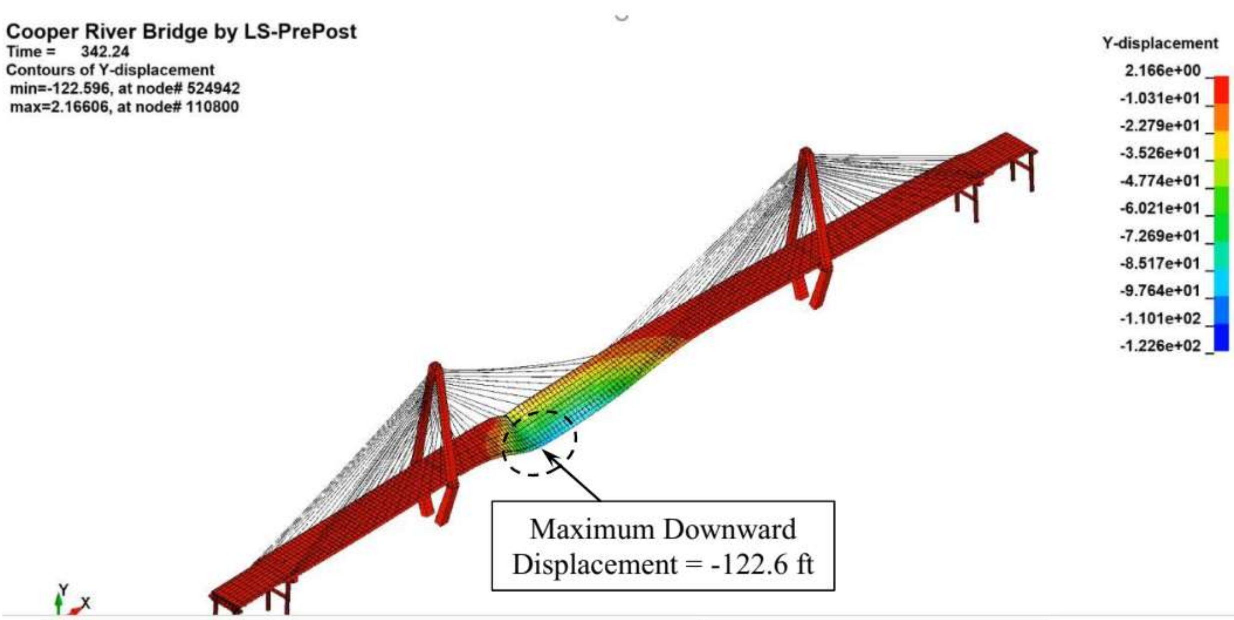

Source: FHWA.

Figure 91. Illustration. Ultimate limit state after 10th cable loss (unit: feet).

TIED-ARCH BRIDGE

Live Load on the Tied-Arch Bridge

Unlike the cable-stayed bridge which had multiple live load pattern, the tied-arch bridge, being a single span structure, has only one live load pattern in longitudinal direction, i.e. the entire span is loaded with live load. According to AASHTO (2014), bridge live load is a combination of lane load and standard truck load. Thus, a uniformly distributed design lane load of 0.64 kip/feet plus a standard design truck were applied on each of the loaded vehicle lanes. The truck loads were applied at the center of the bridge in the longitudinal direction and a dynamic load allowance of 33% was applied. In the transverse direction, the bridge has four vehicular lanes plus one shared use path for pedestrian and bicycles. Thus, four live-load cases with different numbers of vehicle lanes loaded were considered, i.e., 1 lane loaded, 2 lanes loaded, 3 lanes loaded and 4 lanes loaded. For the case with only one vehicle lane loaded with live load, each lane was loaded separately and the envelope of all the loaded lanes was considered as the response of this case. A similar approach was used when two and three lanes were loaded simultaneously. When different numbers of vehicle lane were loaded, multiple presence factors were considered based on Table 23. In addition to the vehicle live load, another 0.075 ksf pedestrian load was applied on the shared use path on the west side of the bridge. The overall live load analysis cases are summarized in Table 24.

Table 23. Multiple presence factors.

Number of loaded lanes	Multiple presence factors
1	1.20
2	1.00
3	0.85
>3	0.65

Table 24. Live load analysis cases.

Load Case	Information
COMB01	Envelope of {DL + 1 vehicle lane loaded + pedestrian load}
COMB02	Envelope of {DL + 2 vehicle lanes loaded + pedestrian load}
COMB03	Envelope of {DL + 3 vehicle lanes loaded + pedestrian load}
COMB04	DL + 4 vehicle lanes loaded + pedestrian load

Live Load Analysis

As done for the cable-stayed bridge, live load was applied after the bridge reached its the equilibrium state under dead load, which was applied in three stages (0 to 40 seconds) as discussed in Chapter 3. Live load was applied in Stage 4 (40 to 50 seconds) as discussed next.

Stages 1-3 (0 to 40 seconds): Application of dead load as discussed earlier in Chapter 3.

Stage 4 (40 to 50 seconds): Live load was applied at the beginning of this stage. Large global damping (i.e., 80% of critical damping) was employed to prevent premature failure of the bridge due to large vibration associated with sudden application of the load.

The bridge's responses under the four load cases (COMB01, COMB02, COMB03 and COMB04) are introduced in the following subsections. Due to similarity of the results between the two planes, only the results for the west plane are presented.

Vertical Displacements

The vertical deflections along the main girder and arch in West Plane under the four load cases (COMB01, COMB02, COMB03 and COMB04) are shown in Figure 92 and Figure 93, respectively. For comparison, deflections under dead load (DL) are also presented in the figures. The deflections were measured from the initial fabrication camber position.

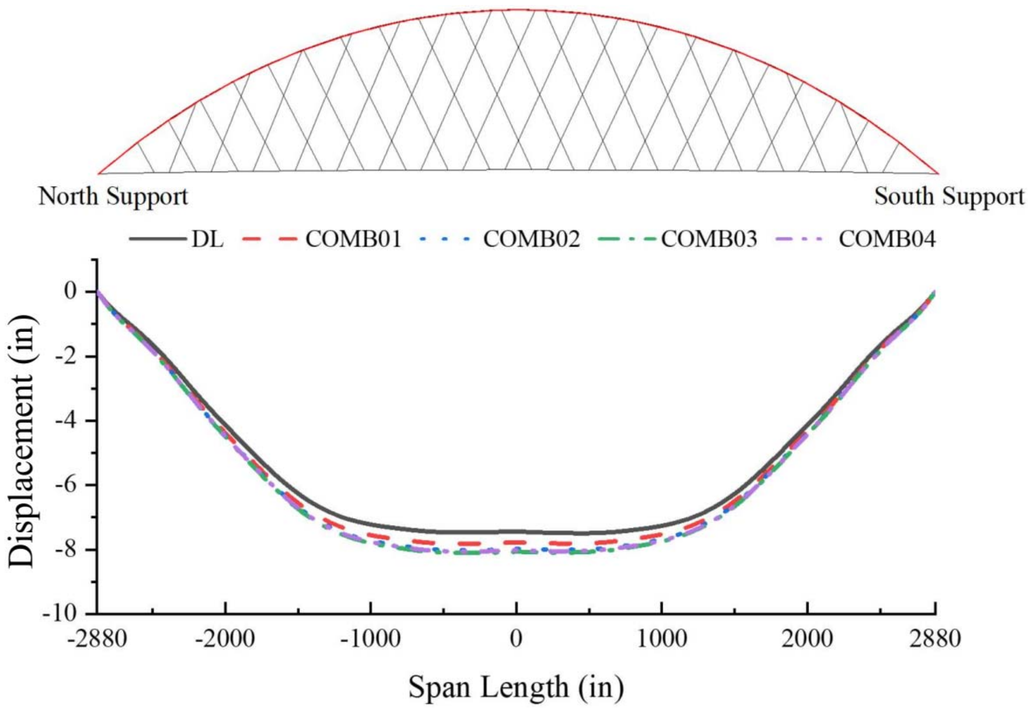

Source: FHWA.

Figure 92. Graph. Arch vertical deflection under the four load cases.

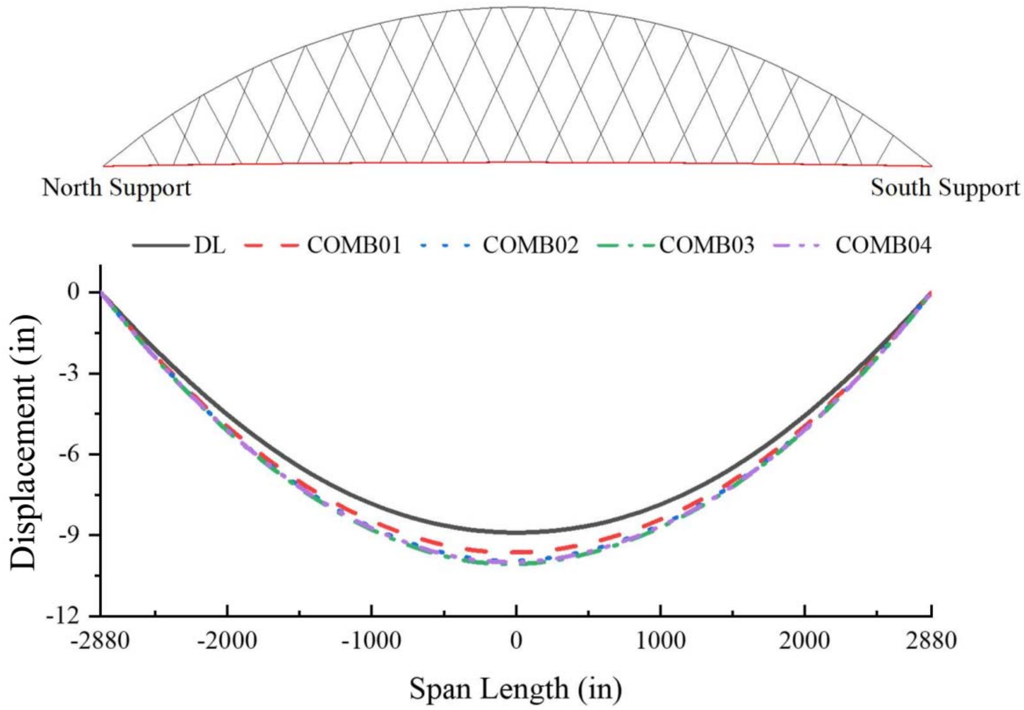

Source: FHWA.

Figure 93. Graph. Girder vertical deflection under the four load cases.

As shown in Figure 92 and Figure 93, the live load effects were much smaller than the dead load effect for the selected tied-arch bridge. Under COMB01, the maximum vertical downward displacement on the arch was 7.8 inches and the maximum vertical downward displacement on the girder was 9.6 inches. In comparison with the bridge under DL, these maximum downward displacements increased by 0.3 inches and 0.7 inches, respectively. The deflection under COMB02, COMB03 and COMB04 were almost the same. The maximum vertical downward displacement on the arch was 8.1 inches and the maximum vertical downward displacement on the girder was 10.0 inches. In comparison with the bridge under DL, these maximum downward displacements increased by 0.6 inches and 1.1 inches, respectively.

Hanger Stresses

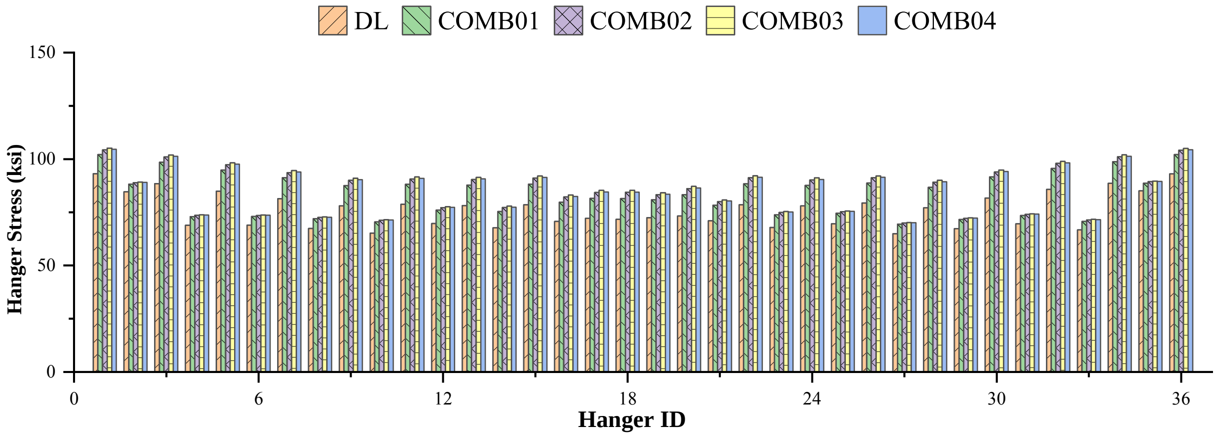

Source: FHWA.

Figure 94. Graph. Hanger stress under the four load cases.

The stresses in the hangers of the bridge for the four load cases (COMB01, COMB02, COMB03 and COMB04) are shown in Figure 94. For comparison, hanger stresses under DL are also presented in the figure. Under COMB01, stresses in different hangers increased in the range of 3.6 ksi to 10.1 ksi with respect to DL. Under COMB02, stresses in different hangers increased in the range of 4.3 ksi to 12.9 ksi with respect to DL. Under COMB03, stresses in different hangers increased in the range of 4.5 ksi to 13.9 ksi with respect to DL. Under COMB04, stresses in different hangers increased in the range of 4.6 ksi to 13.9 ksi with respect to DL. The hangers most affected by the live load were those with the largest stresses under DL including W01, W03, W05, W32, W34, and W36. Since COMB04 caused the highest demands, it is used for the subsequent member removal analyses.

Behavior of the Bridge under Single Hanger Loss Event

Based on geometric symmetry of the bridge and loading, 36 hanger loss scenarios were considered. The hanger ID information is shown in Figure 95. The hanger ID increases from left (North Side) to right (South Side) at the girder level. The shortest hanger on the left (North) side is labeled as W.01 (E.01); the shortest cable at the right (South) side is labeled as W.36 (E.36). Here "W (or E)" represents the West Plane (or East Plane). In the subsequent member removal analyses, the removed hangers are all located in West Plane, i.e. W.01 to W.36.

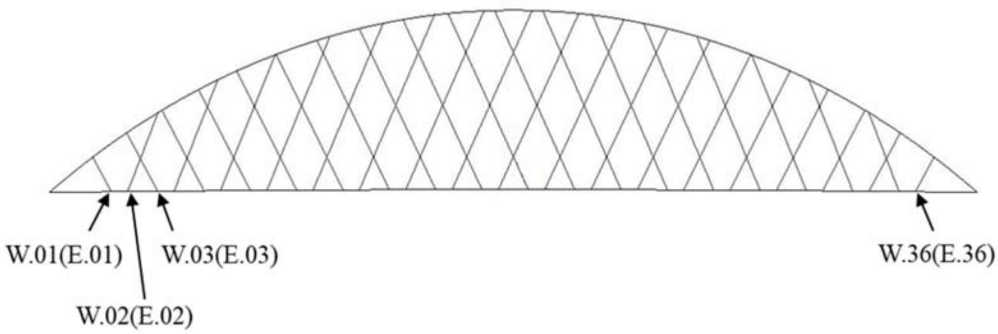

Source: FHWA.

Figure 95. Illustration. Hanger ID designation.

Simulation Stages and Damping Effect

Member removal analysis was conducted through the following steps.

Stages 1-4: Application of dead and live load effects for a simulation time of 40 seconds, as discussed earlier.

Stage 5 (50 to 55 seconds): The large global damping was adjusted back to its normal value of 2% after the vibrations died down.

Stage 6 (55 to 65 seconds): After the structure reached steady-state, a single hanger was removed at 55 seconds, which triggered dynamic vibration of the bridge. This stage lasted for 10 seconds, which was deemed long enough to capture the peak bridge's response due to a hanger loss.

Stage 7 (65 to 75 seconds): After the bridge vibrated for 10 seconds due to hanger loss in Stage 6, the global damping was increased back again to a large value (80% of critical damping) to damp out the vibration. This duration was deemed sufficient for the bridge's response to reach its steady-state condition in the damaged condition.

The overall simulation stages and damping curve during single hanger removal analysis are shown in Figure 96.

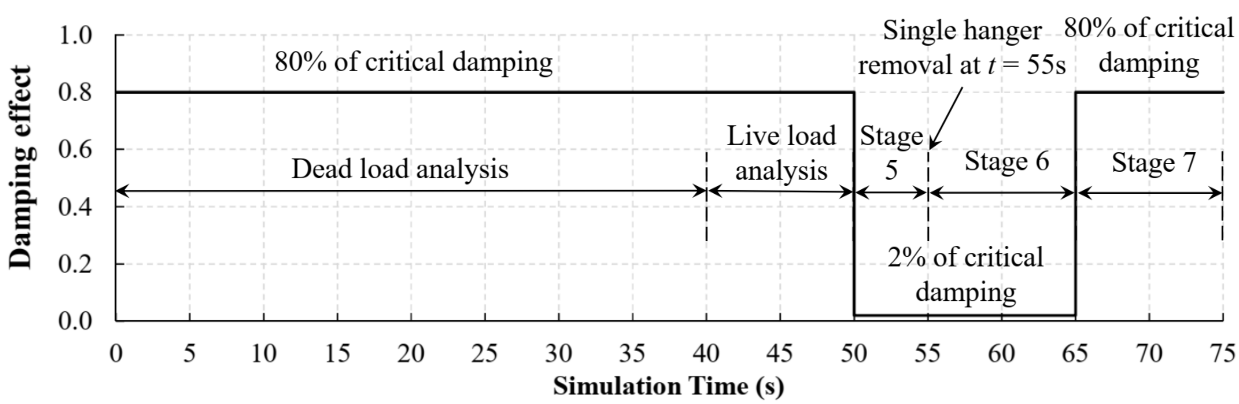

Source: FHWA.

Figure 96. Graph. Simulation stages and damping curve for single hanger removal analysis.

Demand Capacity Ratio (DCR)

For each hanger loss scenario, the demand capacity ratios were calculated for each member using Equation (15) to identify the maximum value of DCR. The envelope of DCR for hanger stress under dead and live loads due to the 36 representative hanger loss cases is shown in Figure 97.

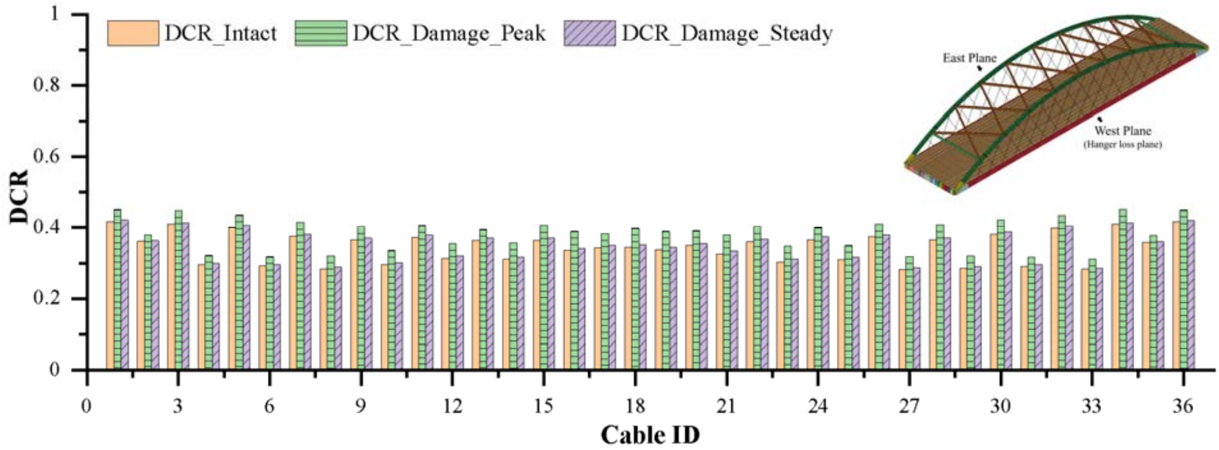

Source: FHWA.

(a) Envelope of DCR for hanger stress in East Plane.

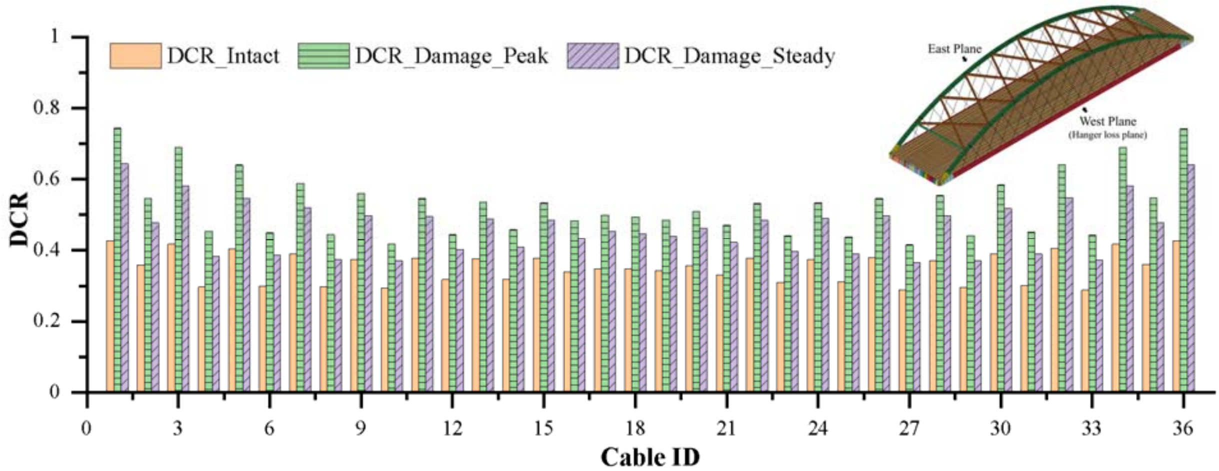

Source: FHWA.

(b) Envelope of DCR for hanger stress in West Plane (Hanger Loss Plane).

Figure 97. Graphs. Envelope of DCR for hanger stress due to representative single hanger loss cases

The DCR of the intact state (DCR_{intact}), peak response in the damaged state (DCR_{damage_peak}) and steady-state response in the damaged state (DCR_{damage_steady}) are shown as bar charts for each cable loss case in Figure 97. As shown in Figure 97, hangers had DCR_{intact} in the range of 0.28 to 0.42. The hangers labeled with odd numbers near the left support (e.g., hangers 01, 03, 05, 07 and 09 in Figure 95) and even numbers near the right support (e.g., hangers 28, 30, 32, 34 and 36 in Figure 95) had relatively higher DCR values than the other hangers. The envelope of DCR_{damage_peak} calculated from the peak stress due to sudden hanger loss shows different trends in either plane. For cables in the hanger loss plane (West Plane), the envelope of DCR_{damage_peak} increased by 0.13 ~ 0.32 with respect to DCR_{intact}. However, the envelope of DCR_{damage_peak} for cables in the other plane (East Plane) increased by 0.02 ~ 0.05 with respect to DCR_{intact}. The largest effect occurred for W.01 and W.36, where DCR_{damage_peak} increased to 0.74 from the intact state (DCR_{intact} = 0.43).

Once the vibrations due to sudden hanger loss dissipated, the damaged bridge reached its new steady equilibrium state and there were residual increased stresses in the remaining hangers. In the damaged state, the envelope of DCR_{damage_steady} for hangers in the hanger loss plane in the damaged steady-state increased by 0.084 ~ 0.21 with respect to their intact state DCR_{intact}. However, for hangers in the other plane, the stress level in the hangers of the damaged bridge returned to their intact state value. The DCR of the most critical hangers (W.01 and W.36) leveled off at 0.64 in the damaged steady-state.

Dynamic Increase Factor (DIF) and Static Increase Factor (SIF)

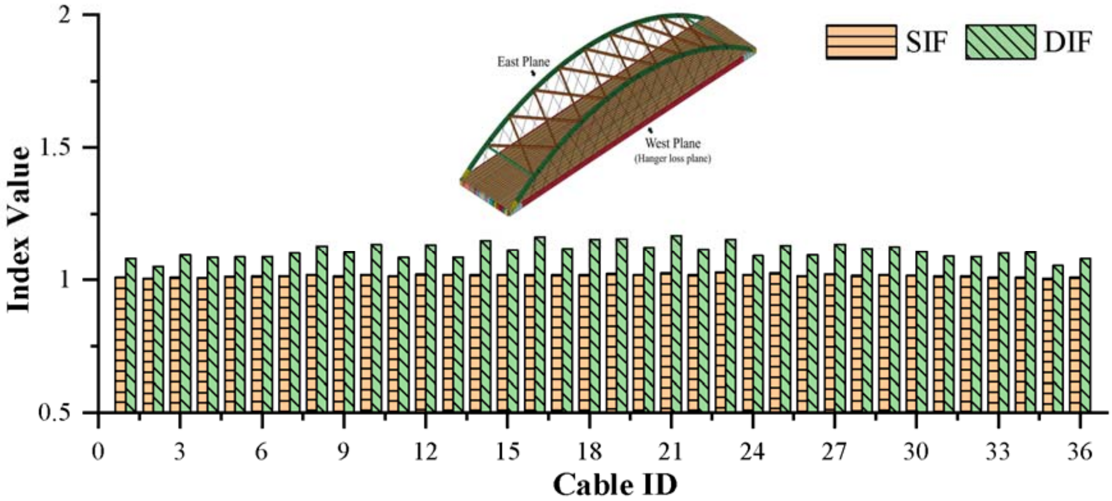

Source: FHWA.

(a) Envelope of DIF and SIF for hanger stress in East Plane.

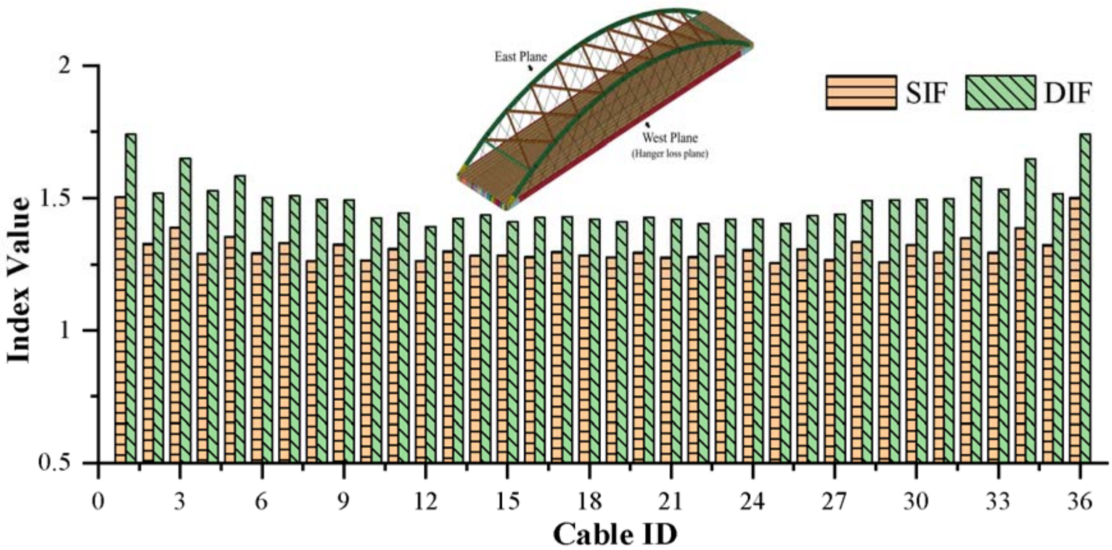

Source: FHWA.

(b) Envelope of DIF and SIF for hanger stress in West Plane (Hanger Loss Plane).

Figure 98. Graphs. Envelope of DIF and SIF for hanger stress due to representative hanger loss cases.

Figure 98 shows the envelope of SIF in East Plane. It is observed that the SIF values in East Plane were close to 1, which indicates that hanger loss in one plane had limited effect on hangers in the other plane. The SIF values in West Plane (i.e., the hanger loss plane) ranged from 1.26 to 1.51. The largest SIF values were observed in hangers W.01 and W.36, which are the two end hangers.

It is further observed from Figure 98 that the envelope of DIF in East Plane ranged from 1.05 to 1.14, whereas the envelope of DIF in West Plane ranged from 1.39 to 1.74. The largest value of DIF was observed in hangers W.01 and W.36, similar to the case of SIF.

Dynamic Amplification Factor (DAF)

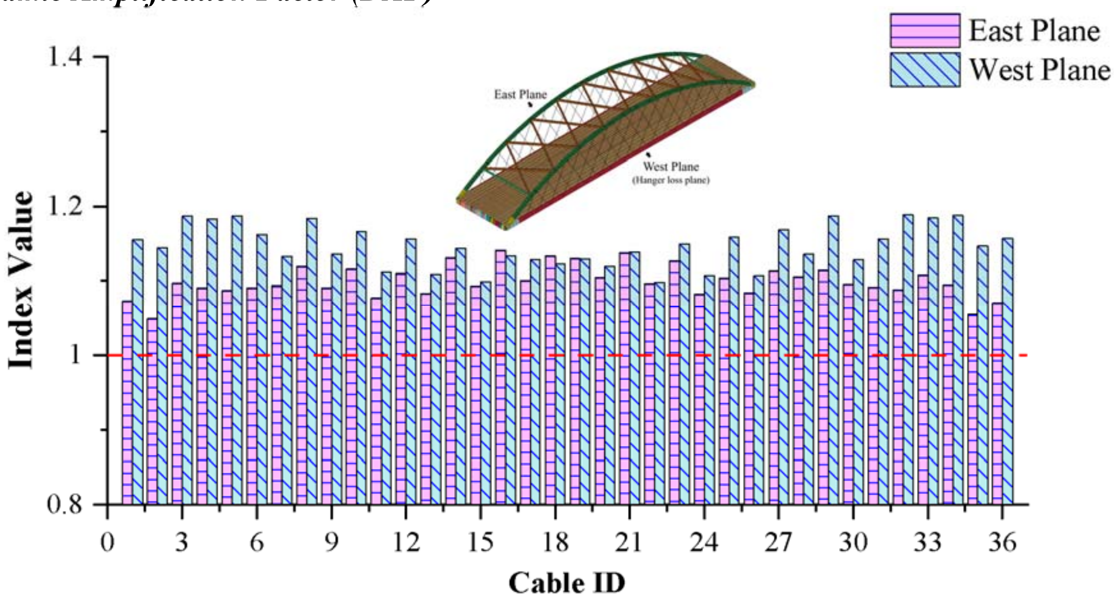

Source: FHWA.

Figure 99. Graph. Envelope of DAF for hanger stress due to representative hanger loss cases.

Figure 99 shows the envelope of DAF in East Plane for 36 representative hanger loss cases. It is observed that DAF values ranged from 1.05 to 1.15. The envelope of DAF values in West Plane ranged from 1.09 to 1.19. Overall, the dynamic amplification factors of hanger stresses in West Plane (i.e., hanger loss plane) were slightly larger than those in East Plane. In addition to this, the DAFs in the hangers close to the center in East Plane are higher than those for other hangers in this plane.

Bridge Behavior under Multiple Hanger Loss Event

Similar to the cable-stayed bridge, progressive collapse behavior was investigated by successively removing hangers until failure occurred as shown in Figure 100. After the bridge response reached steady state under the applied dead and live loads, the global damping constant was reduced to 2% of critical damping before the first hanger was removed. The damping constant was then increased to a large value (80% of the critical damping) after a simulation time of 10 seconds (about 12 times of the period of the first mode), which is long enough to capture the peak response following the sudden loss of the first hanger. The global damping constant was then reduced to 2% of critical damping constant again just before removal of the next hanger. This process was repeated during sequential removal of hangers until the bridge became severely damaged. The live load was assumed to remain in its location during the simulation process.

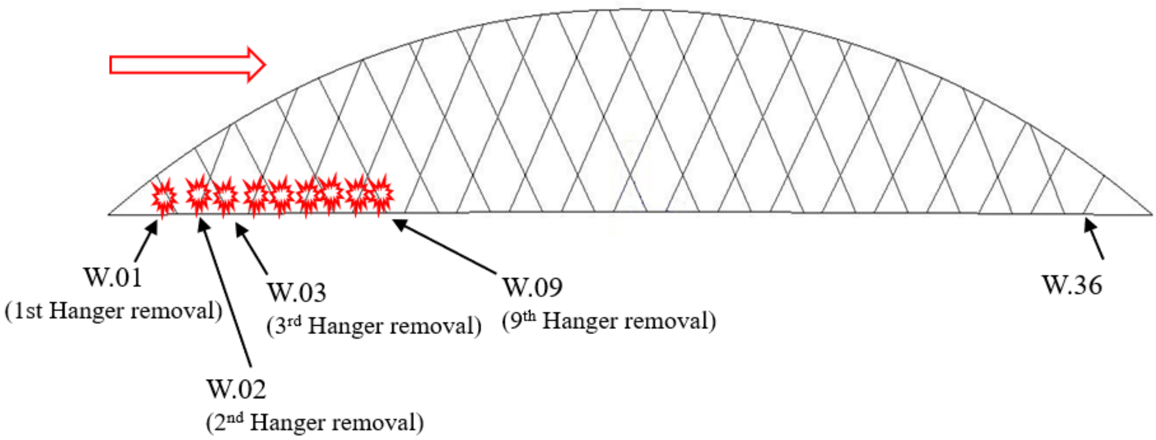

Source: FHWA.

Figure 100. Illustration. Hanger removal pattern.

Two limit states were established in order to evaluate the level of damage to the bridge, i.e., functionality limit state and member failure limit state. The functionality limit state is defined as the damage level when more that 10% of the deck elements develop tension cracks or the deflection at mid span reaches L/600 (JSCE 2007b). The member failure limit state was defined as the damage level when a main structural member reached the yield strength.

Removal of the 1st and 2nd Hangers

The first hanger (hanger W.01) was removed at 55 seconds and the bridge response reached the steady state at 75 seconds. Following this, the second hanger (hanger W.02) was removed. The maximum vertical displacements along the edge girder in the hanger loss plane are shown in Figure 101. Similarly, the maximum vertical displacements along the arch in the hanger loss plane are shown in Figure 102.

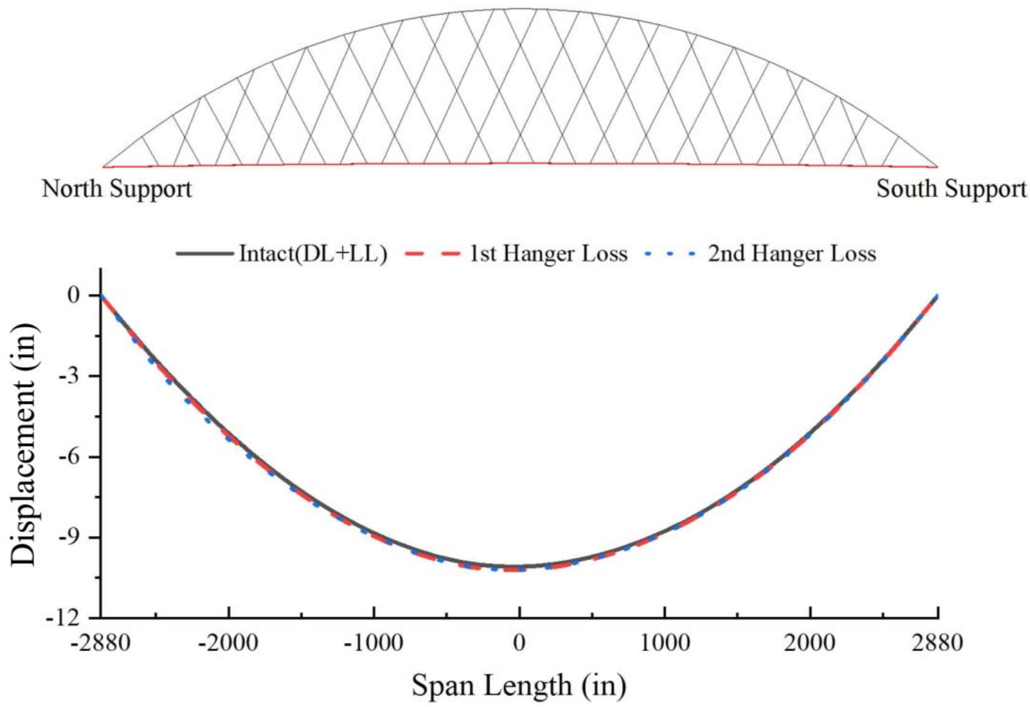

Source: FHWA.

Figure 101. Graph. Vertical deflection of girder in West Plane due to 1st and 2nd hanger loss.

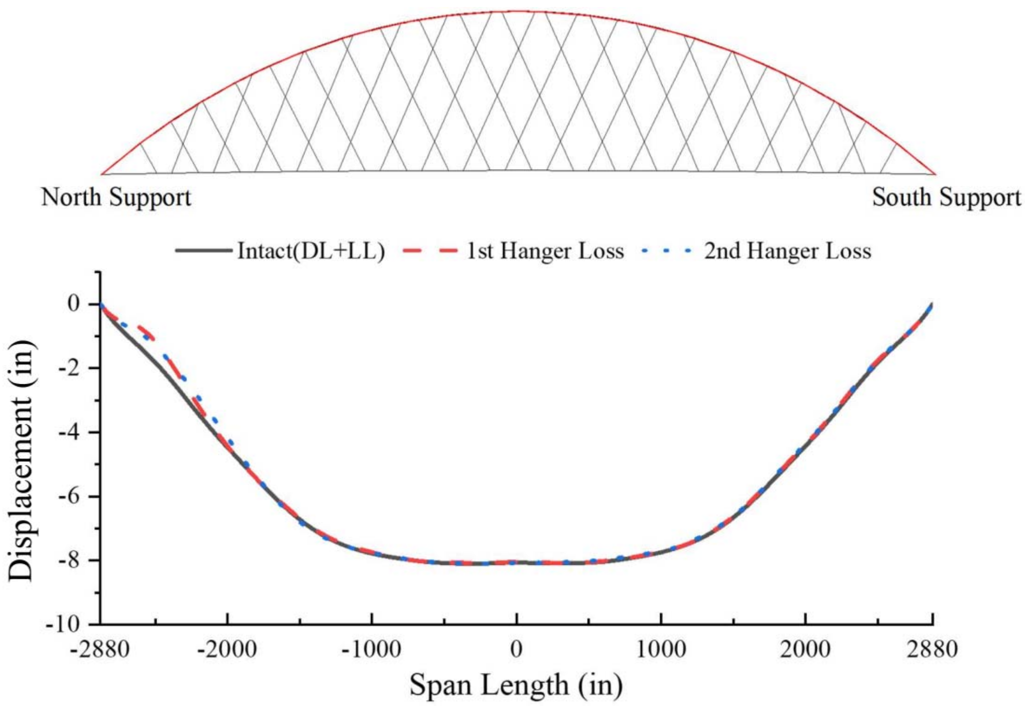

Source: FHWA.

Figure 102. Graph. Vertical deflection of arch in West Plane due to 1st and 2nd hanger loss.

As shown in Figure 101 and Figure 102, the overall deformation profiles after the loss of hangers W.01 and W.02 are almost the same as that of the intact bridge, since the lost hangers W.01 and W.02 are close to the pinned support. However, in the vicinity of the lost hangers, the girder deflected downward by approximately 0.2 inches and the arch deflected upward by approximately 0.7 inches. The structural steel and hangers remained elastic due to the loss of these two hangers.

Member Failure Limit State after Removal of the 3rd Hanger

The 3rd hanger (hanger W.03) was removed at 115 seconds. During the vibration of the bridge due to the loss of this hanger, the downward deflection of the girder increased by 0.7 inches, as shown in Figure 103. However, the arch moved upward suddenly by more than 3 inches, as shown in Figure 104.

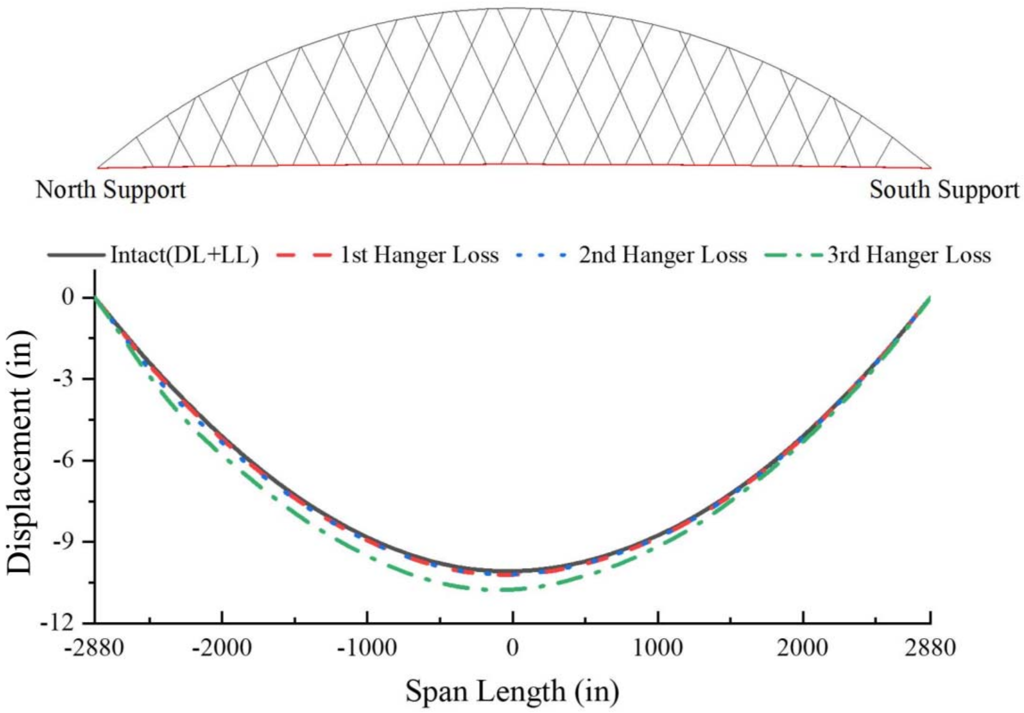

Source: FHWA.

Figure 103. Graph. Vertical deflection of girder in West Plane due to 3rd hanger loss.

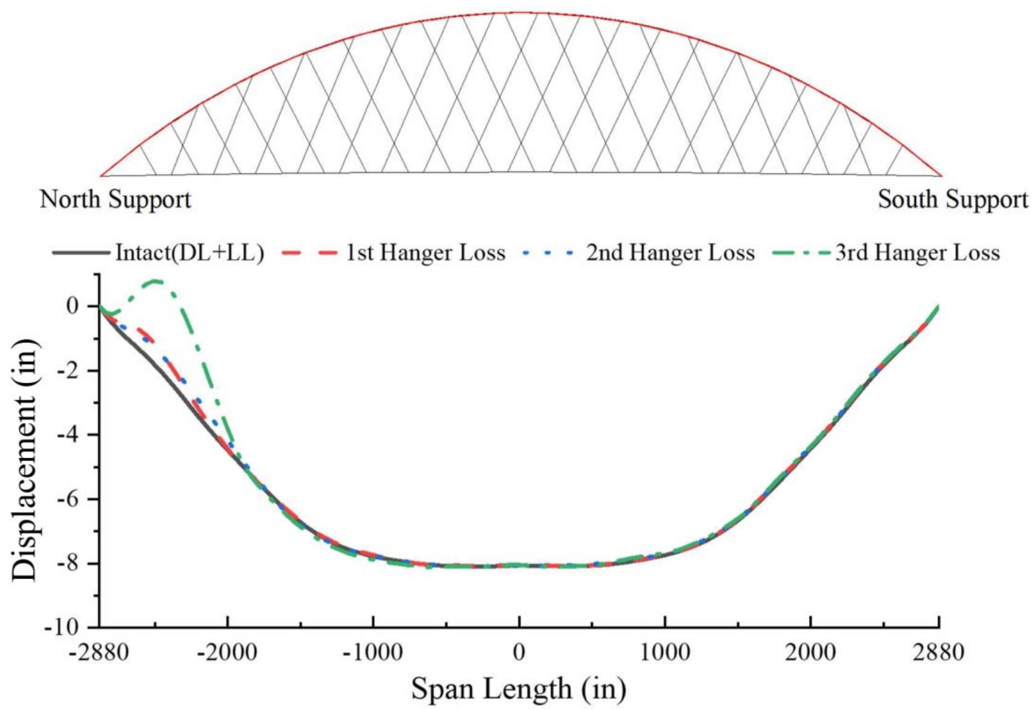

Source: FHWA.

Figure 104. Graph. Vertical deflection of arch in West Plane due to 3rd hanger loss.

The stress time history in hanger W.05 due to the 3rd hanger loss (hanger W.03) is shown in Figure 105. The stress in hanger W.05 was 124.6 ksi before the loss of the third hanger. After the hanger loss event, the stress in hanger W.05 increased suddenly to more than 243 ksi and reached the yield strength. After the bridge vibration damped out and reached a new steady state, the stress in W.05 dropped below the yield strength reaching a value of 196.3 ksi. However, the hanger had experienced irreversible plastic strain. In addition, due to the 3rd hanger loss (hanger W.03), the main arch member near the support also reached the yield strength, as shown in Figure 106.

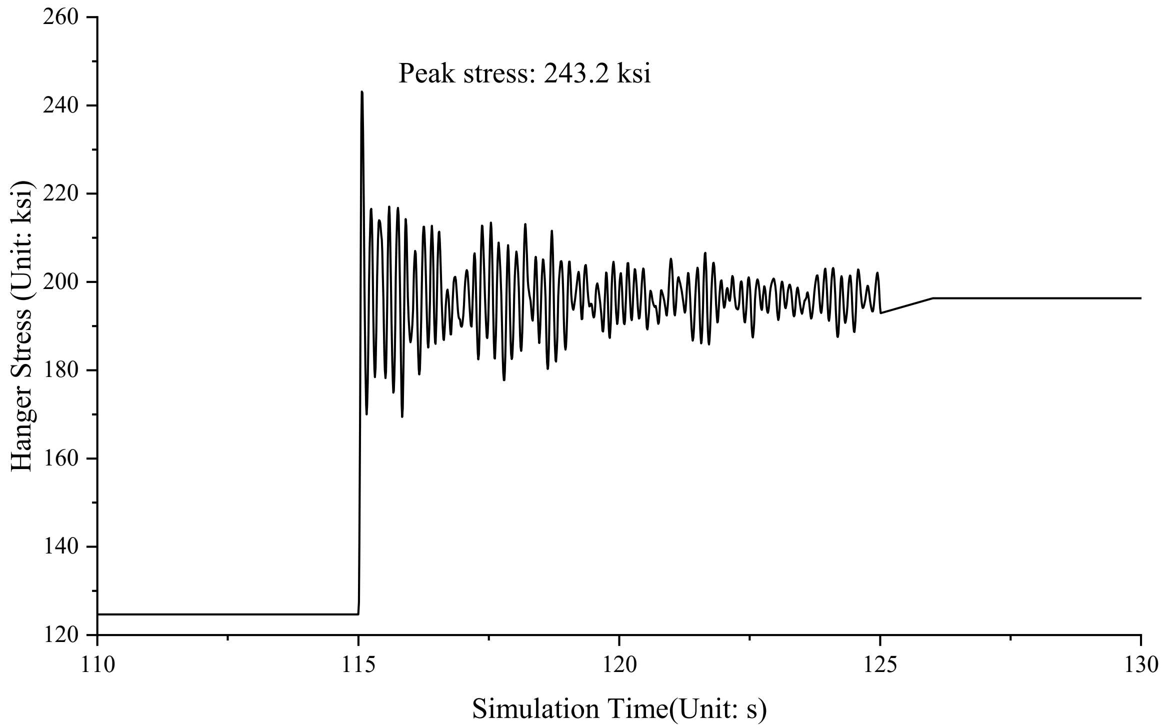

Source: FHWA.

Figure 105. Graph. W.05 Hanger stress time history due to 3rd hanger loss.

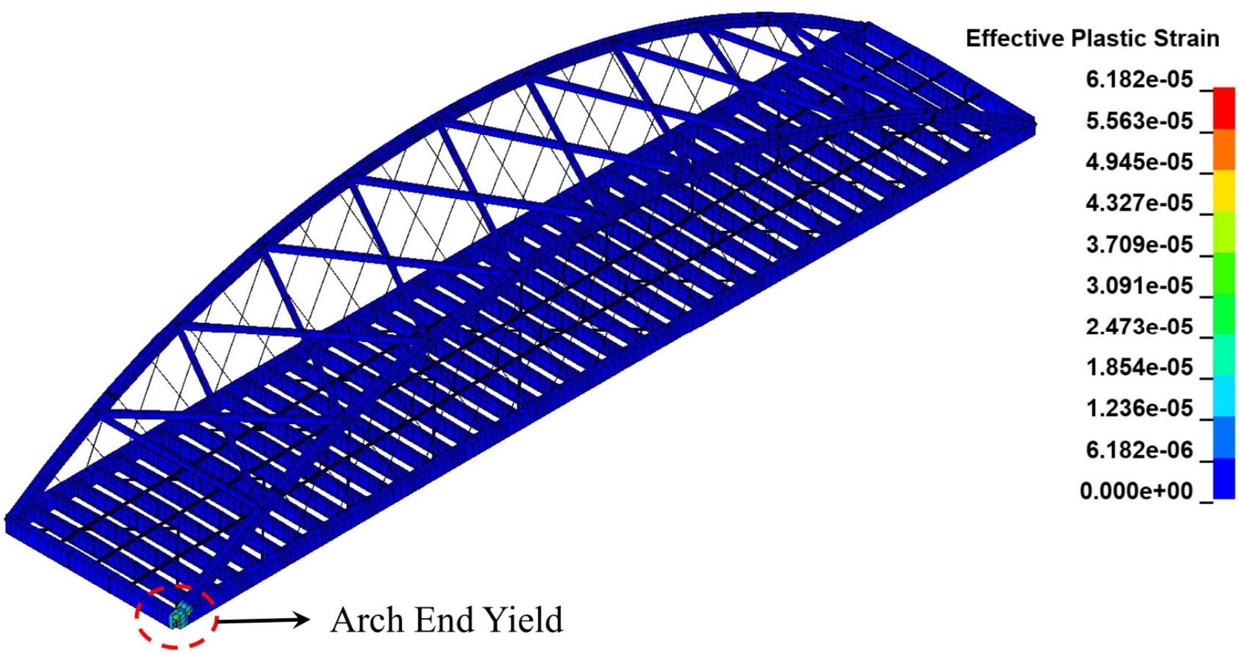

Source: FHWA.

Figure 106. Illustration. Effective plastic strain contour due to 3rd hanger loss.

Functionality Limit State and Severe Damage after Removal of the 9th Hanger

The deformations of girder and arch in West Plane (hanger loss plane) due to multiple hanger loss are shown in Figure 107 and Figure 108, respectively. Since loss of hangers slanted backwards, such as W.01, W.03, W.05, had a much larger effect than loss of hangers slanted forward, such as W.02, W.04, W.06, the deformations due to loss of hangers slanted backwards are only shown here. More hangers and arch members reached their yield strengths as additional hangers were removed. As a result, the bridge suffered progressively larger deformations. The deflection functionality limit state (i.e., L/600 = 18.5 inches) was reached after loss of the 9th hanger, where the maximum deflection was 24.6 inches at the center, as shown in Figure 107. Simultaneously, the main arch suffered large deflections in the vicinity of the removed hangers (deflecting upwards by more than 22 inches) while deflecting downward by more than 15 inches elsewhere. The effective plastic strain in the arch member is shown in Figure 109. Clearly, the arch was on the verge of inelastic buckling.

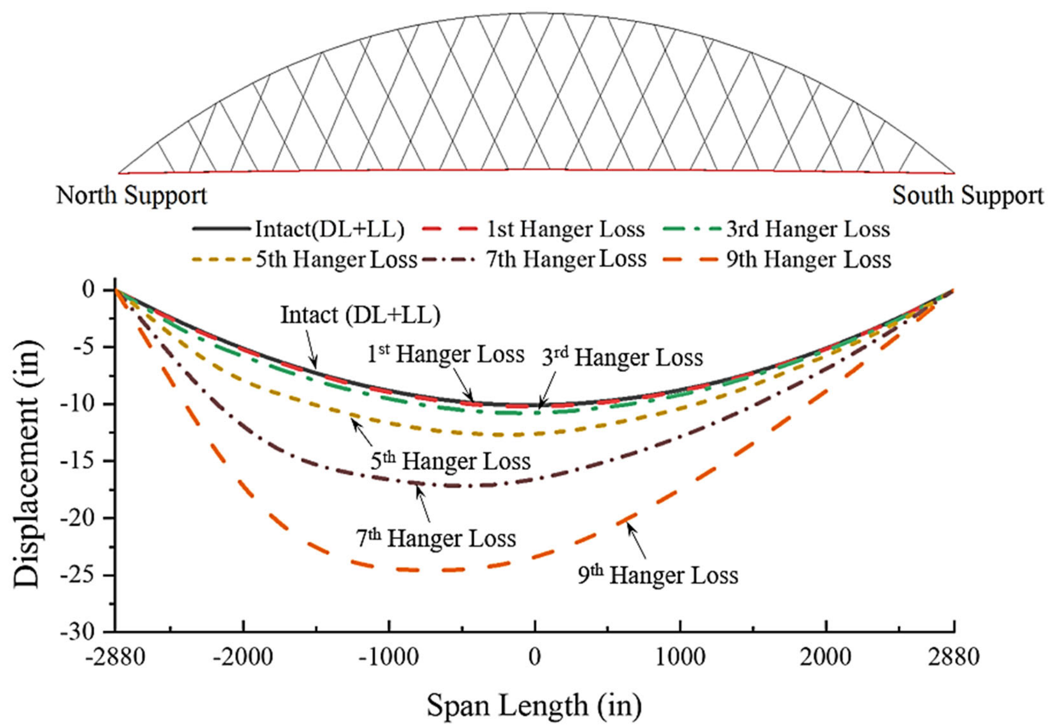

Source: FHWA.

Figure 107. Graph. Vertical deflection of girder in West Plane due to multiple hanger losses.

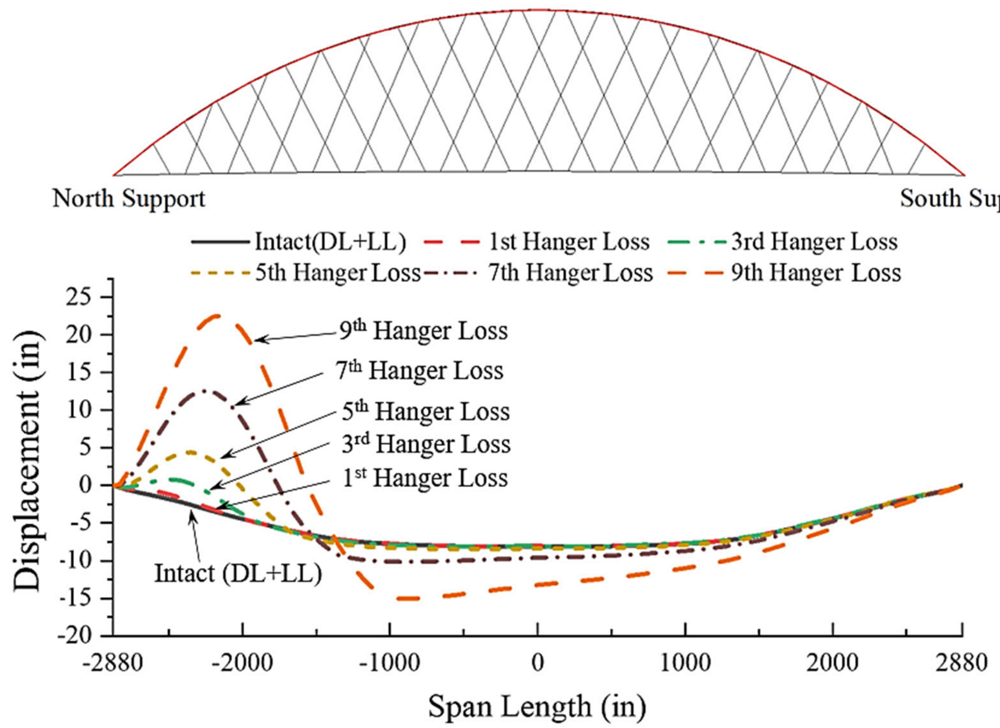

Source: FHWA.

Figure 108. Graph. Vertical deflection of arch in West Plane due to multiple hanger losses.

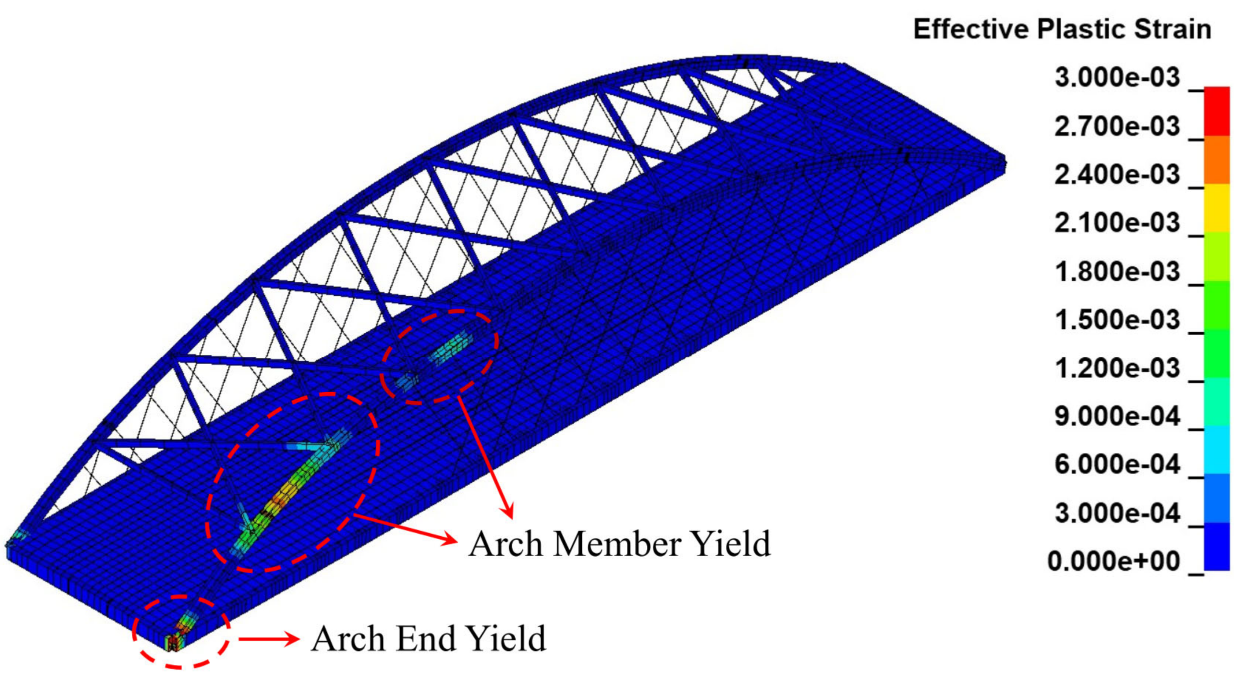

Source: FHWA.

Figure 109. Illustration. Effective plastic strain contour due to 9th hanger loss.

SUSPENSION BRIDGE

Live Load Patterns

The 2nd structure of the Delaware Memorial Bridge was designed in accordance with 1961 AASHO Specifications (AASHO 1961). The design live loads for the stiffening trusses, cables and towers were selected as 2.25 kip/feet, based on the assumption that each of the four lanes was loaded by 20-ton trucks spaced 71 feet apart or 15-ton trucks spaced 53 feet apart. Since the distribution of live load on the bridge is a crucial factor, three live load patterns illustrated in Figure 110 were selected to investigate the effects of suspender removal: (i) live load pattern 1 (LL1) with the design live load distributed on all three spans, (ii) live load pattern 2 (LL2) with the design live load distributed on the two side spans only, and (iii) live load pattern 3 (LL3) with the design live load distributed on the center span only.

Source: FHWA.

Figure 110. Illustration. Live load patterns.

Simulation Steps

The stimulation procedure was divided into the following stages:

Stage 1: Dead load analysis. The explicit model of the suspension bridge was built to represent the final geometrical configuration of the bridge after construction as per the design drawings with initial pretensions of the main cables and suspenders in equilibrium with the design dead load on the bridge. No attempt was made to simulate the construction stages. In this step, it was crucial to obtain the appropriate initial pretensions in the main cables and suspenders first, then geometrical nonlinear analysis was performed to establish the deformed configuration under dead load, which had to match the final geometrical configuration. Results for this stage were presented in Chapter 3.

Stage 2: Live load analysis. After the equilibrium of the bridge under dead load was reached, the live loads shown in Figure 110 were applied on the bridge to obtain the deformed equilibrium configuration of the bridge under the different dead and live load combinations. After obtaining the appropriate initial pretensions in the main cables and suspenders, simulation Stage 1 and 2 were combined together as a single stage to reduce the simulation time. Therefore, the dead and live loads were applied simultaneously on the intact bridge in the initial stage of the suspender removal analysis. Specifically, dead load, live load and initial pretensions of the main cables and suspenders were applied on the bridge within the first 2 seconds of the simulation using a linear ramp curve as shown in Figure 111(a). A over global damping (i.e., damping ratio ζ = 400%) was used to reduce the excessive dynamic responses induced by the rapid buildup of the loads. Once the response of the bridge reached equilibrium, the global damping was reduced to an estimated critical damping of the bridge (e.g., ζ = 100%) to let the bridge reach its steady state. Then, the global damping was reduced further to ζ = 2% to simulate suspender removal.

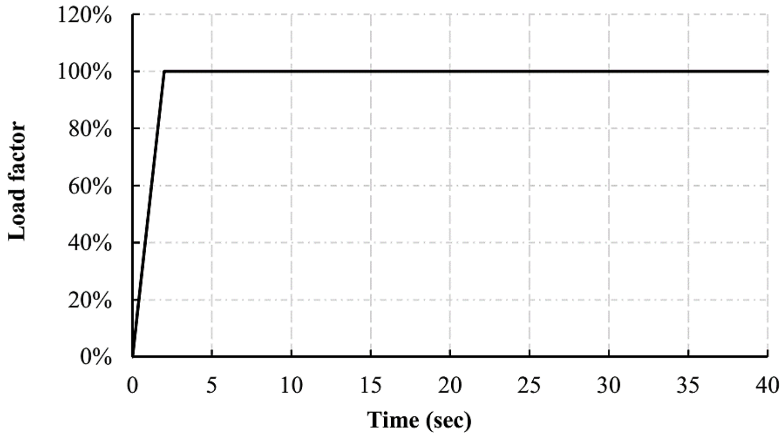

Source: FHWA.

(a) Linear ramp loading curve.

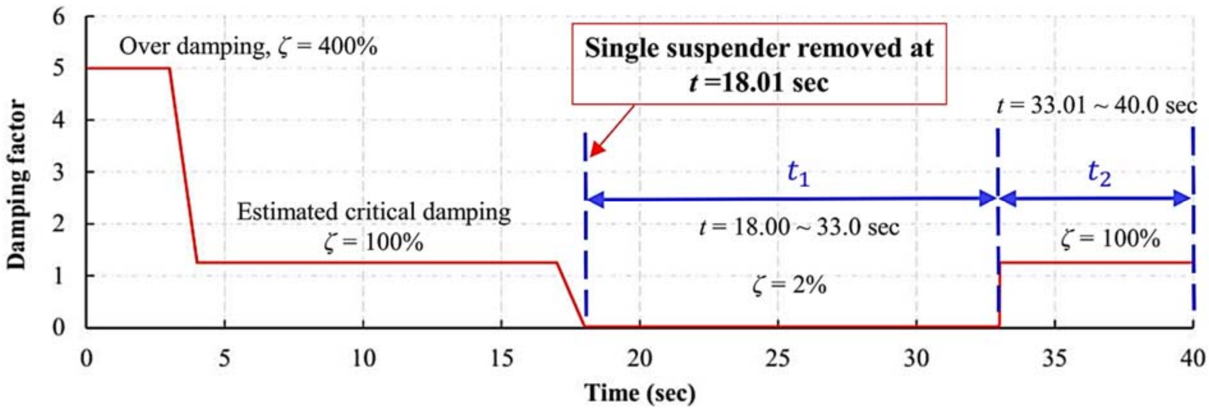

Source: FHWA.

(b) Damping curve for single suspender removal analysis.

Figure 111. Graphs. Loading curve and damping curve in single suspender removal analysis.

Stage 3: Suspender removal analysis. After reaching the steady state in Stage 2, one suspender was removed suddenly at 18.01 seconds from the intact bridge to simulate a sudden member loss event, as shown in Figure 111(b). This triggered dynamic vibration of the bridge, particularly near the location of the removed suspender. A simulation duration of 15 seconds was allowed to capture the dynamic response of the bridge, as shown in Figure 111(b). During this simulation period, the global damping was maintained at ζ = 2%. Following this, the global damping was increased to ζ = 100% for a simulation duration of approximately 7 seconds to damp out vibration of the bridge, so that the bridge response could reach a new steady state in the damaged condition and be ready for removal of the second suspender.

Live Load Analysis

Three load combinations were considered, denoted by COMB1, COMB2, and COMB3 (i.e., dead load with live load patterns LL1~3). The results of suspender removal analyses for each of these three cases are presented next.

Vertical Displacement

The vertical displacements of the suspension bridge under the three load combinations are plotted in Figure 112, Figure 113 and Figure 114. It should be noted that only the displacements of stiffening trusses are shown for a better comparison. The maximum of the vertical displacements of the side spans and the center span are also summarized in Table 25 and compared with the results of the bridge under the dead load (DL) only. As defined in the dead load analysis in Chapter 3, the upward deflection (+Z direction) is positive, and the downward deflection (-Z direction) is negative. Under DL and the applied pretensions in the main cables and suspenders, the balanced positions of the stiffening trusses agreed well with their as-designed positions, in spite of some negligible errors (see Chapter 3 for more details).

Under COMB1, the entire bridge deflected downward. The maximum displacement in the middle of the center span was -1.41 feet and it was -0.72 feet in the middle of each side span. In comparison with the bridge under DL, these maximum negative displacements increased by 1.76 feet in the center span and 1.00 feet in two side spans.

Under COMB2, the two side spans deflected downward, while the center span moved upward. The maximum vertical displacement in the middle of each side span was is -0.74 feet, i.e., it increased 1.02 feet compared to that for the dead load. Hence, vertical displacement in the side spans was close to that for COMB1. The maximum vertical displacement in the middle of the center span was 0.39 feet, i.e., it increased by only 0.05 feet compared to that of the bridge under DL.

Under COMB3, the center span deflected downward, while the side spans deflected upward. The maximum vertical displacement in the middle of the center span was -1.41feet, the same as that under COMB1. However, the maximum vertical displacement in the middle of each side span was 0.31 feet, i.e., it increased by only 0.04 feet compared to that of the bridge under DL.

Table 25. Maximum vertical displacement of intact bridge under various load combinations.

Load Case	Side Span (feet)	Main Span (feet)
DL (Dead Load only)	0.274	0.348
COMB1 (DL+LL1)	-0.724	-1.408
COMB2 (DL+LL2)	-0.742	0.393
COMB3 (DL+LL3)	0.311	-1.408

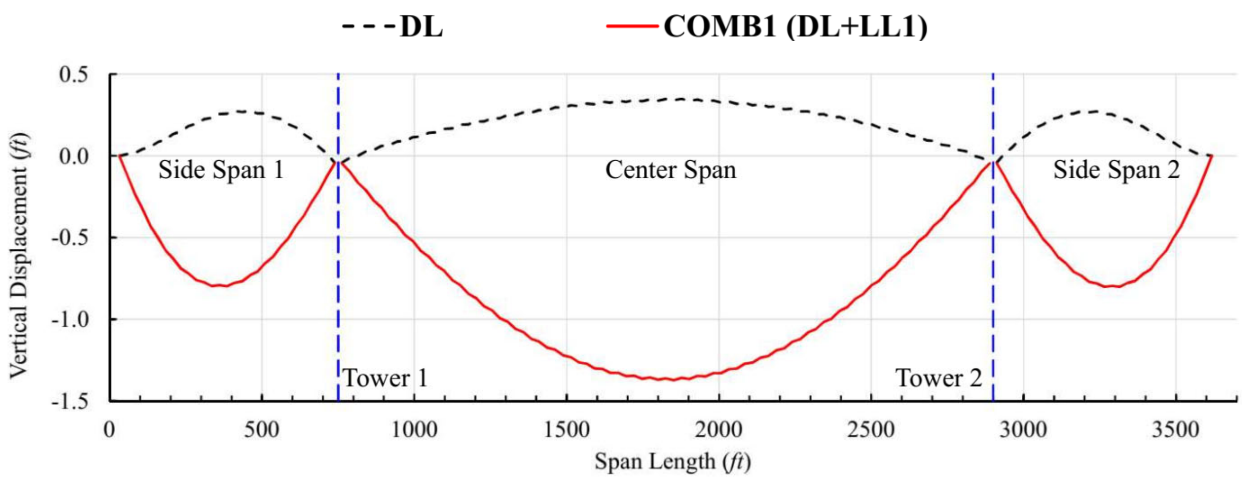

Source: FHWA.

Figure 112. Graph. Vertical displacement of intact bridge under COMB1.

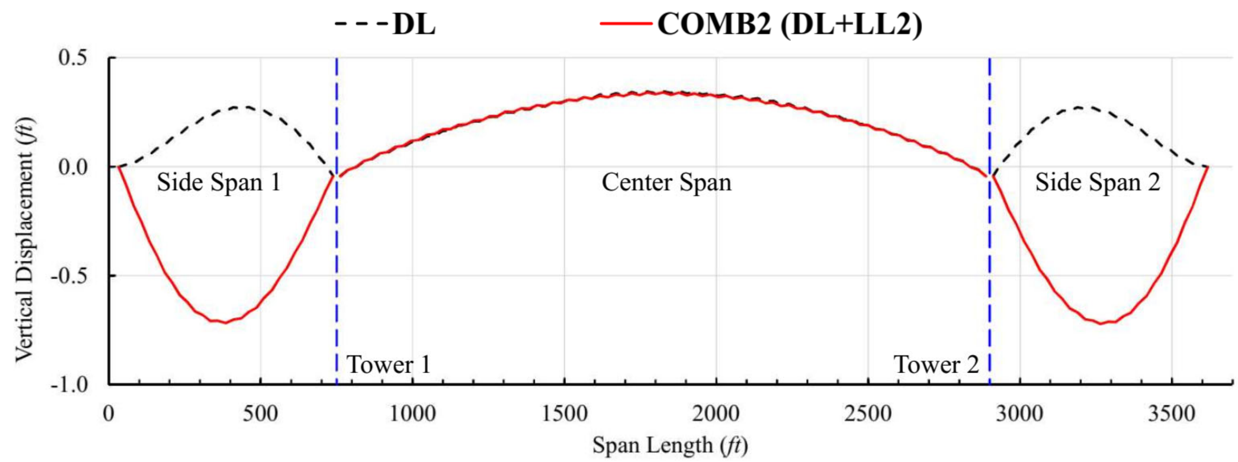

Source: FHWA.

Figure 113. Graph. Vertical displacement of intact bridge under COMB2.

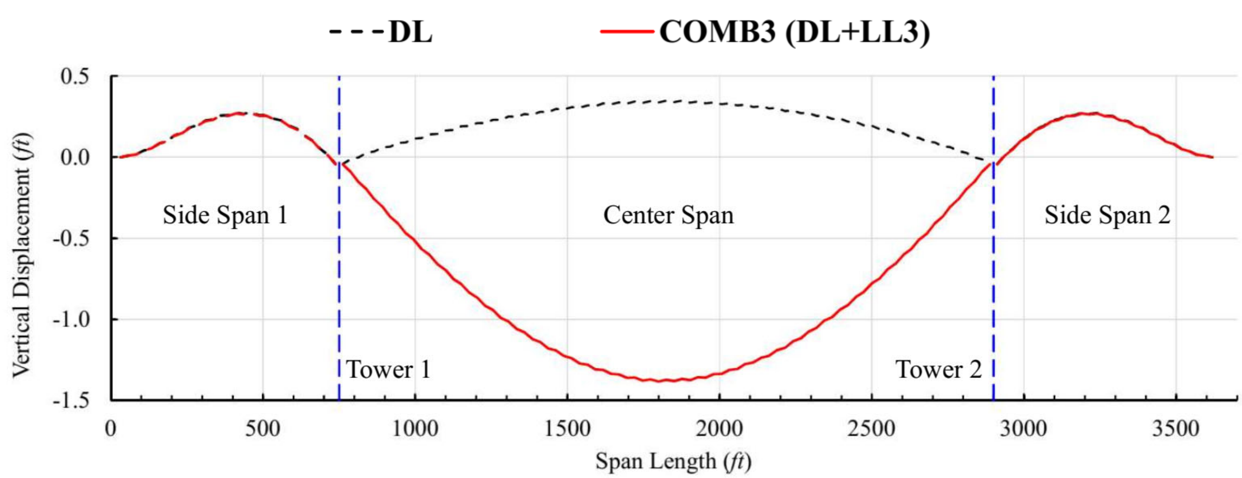

Source: FHWA.

Figure 114. Graph. Vertical displacement of intact bridge under COMB3.

Main Cable Force

The forces in a main cable under the three load combinations along with those under dead load only are plotted in Figure 115. Because of the symmetry of the bridge and the applied loads, the tension forces in the two main cables are symmetrical about the longitudinal center line of the bridge. Hence, only the results of a single main cable (i.e., Main Cable 1) are presented in this figure. It should also be noted that the cable tension forces under all the four load cases were also symmetrical with respect to the transverse centerline of the bridge. The cable tension forces were almost the same on both sides of the towers (i.e., main cable elements 15 and 16, 17 and 18, 59 and 60, 61 and 62), unlike the "spike" in main cable forces shown in Figure 60. Chapter 3 introduces the naming scheme of main cable segments (see Figure 57(b)). Additionally, under dead load (DL), the maximum tension of Main Cable 1 was 21,564.8 kips in each side span shown in Figure 115, and it was slightly larger than the average force of 21,554.2 kips in Figure 60.

Under COMB1, the tension along the entire main cable increased significantly, by 7.05% ~ 7.43% in each side span and by 14.78% ~ 14.96% in the center span, in comparison with DL. The maximum tension was 23,710.3 kips in cable segments 17 and 60, which are adjacent to the towers in the center span, and the minimum tension was 21,127.4 kips in cable segments 01 and 78, which are near the anchor points in the side spans.

Under COMB2, the tension in the main cable in both side spans increased by approximately 7.04% ~ 7.44% in comparison with that under DL, similar to COMB1. However, the tension in the main cable in the center span mostly remained unchanged, decreasing by 0.01% ~ 0.03% with respect to that for DL. The maximum tension was 23,159.6 kips in main cable segments 16 and 61, which are adjacent to the towers in the two side spans. The minimum cable tension was 19,182.5kips in the middle of the center span, approximately 0.02% less than that for DL.

Under COMB3, the tension in the main cable in the center span increased significantly by 14.79% ~ 14.98% in comparison with that under DL, similar to COMB1. However, the tension in the main cable in the side spans remained almost unchanged, decreasing only by 0.01% ~ 0.03% with respect to DL. The maximum cable tension was 23,711.0 kips in main cable segments 17 and 60 in the center span, and the minimum tension was 19,721.3 kips in cable segments 01 and 78 near the anchor points.

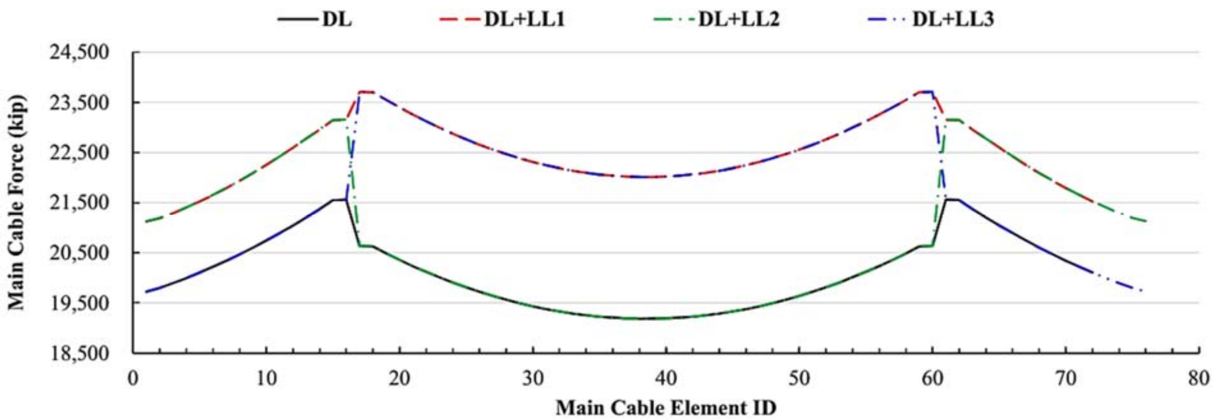

Source: FHWA.

Figure 115. Graph. Main cable forces of bridge under dead load and COMB1 through COMB3.

Suspender Forces

Forces in the suspenders in Cable Plane 1 of the bridge under the three load combinations are plotted in Figure 116, Figure 117 and Figure 118, respectively, along with those for dead load (DL). Under COMB1, most of the suspender forces were approximately within the range of 340 ~ 380 kips, increasing by 0.89% ~ 18.97%, depending on their locations, in comparison with those for DL. However, the tensions in suspenders 01 and 69 near the anchorages in the side spans decreased by approximately 11.19%. The maximum tension was 381.4 kips in suspenders 15 and 55, which are adjacent to the towers in the center span. The minimum tension was 215.5 kip in suspenders 01 and 69 near the anchorages.

Under COMB2, suspender forces in the side spans were approximately within the range of 335 ~ 375 kips, increasing by 1.37% ~ 11.51% in comparison with those for DL. Tension in suspenders 01 and 69 decreased by approximately 11.00%, similar to COMB1. However, suspenders in the center span were hardly affected and the suspender forces fluctuated slightly in the range of -0.38% to 0.15% with respect to those for DL. The maximum tension was 374.4 kips in suspenders 10 and 60.

Under COMB3, suspender forces in the center span were approximately in the range of 365 ~ 380 kips, increasing by 7.54% ~ 19.65% with respect to DL. However, forces in the suspenders in the side spans were hardly affected and the suspender forces fluctuated slightly in the range of -0.51% ~ 0.09% with respect to those for DL. The maximum suspender tension was 382.4 kips in suspenders 15 and 55.

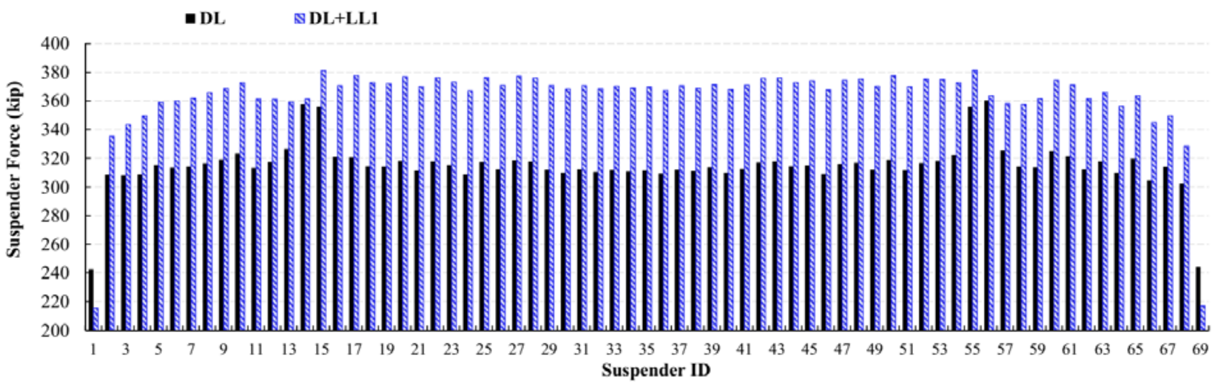

Source: FHWA.

Figure 116. Graph. Suspender forces of bridge under dead load and COMB1.

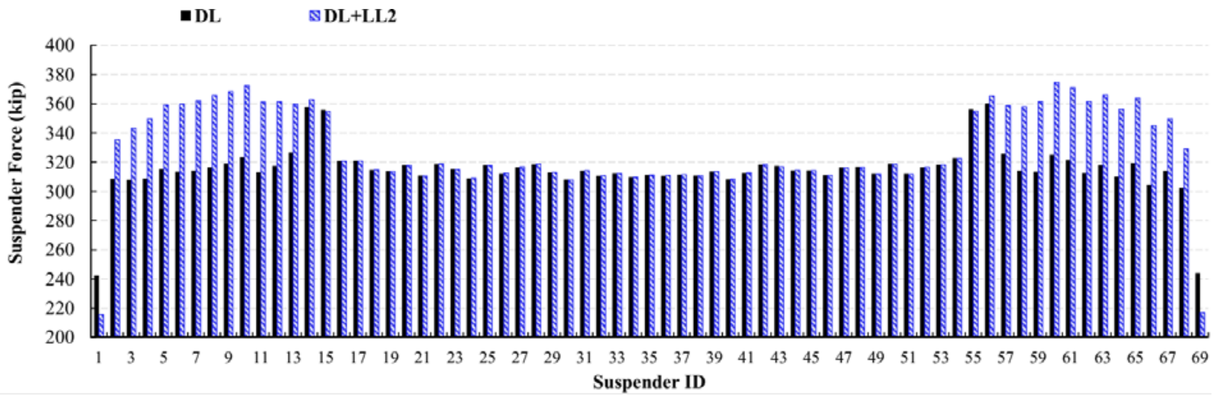

Source: FHWA.

Figure 117. Graph. Suspender forces of bridge under dead load and COMB2.

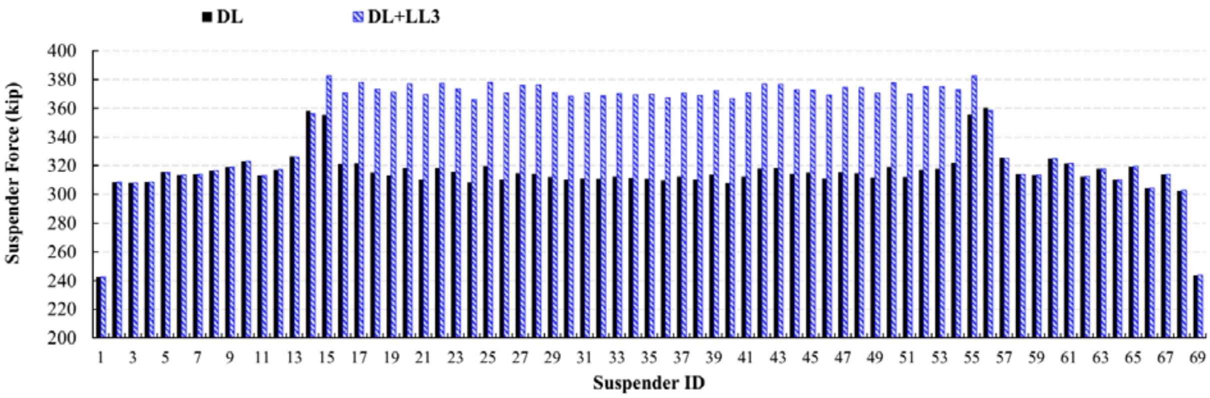

Source: FHWA

Figure 118. Graph. Suspender forces of bridge under dead load and COMB3.

Behavior of the Bridge under Single Suspender Loss Events

Due to symmetries of the bridge and the loads applied, 35 single-suspender loss scenarios were simulated for the suspension bridge under each live load pattern. During each suspender loss scenario, a single suspender was removed suddenly at 18.01 seconds when the bridge was in its steady-state under dead and live loads. As illustrated in Figure 119, the member removal simulations were conducted on suspenders 01 through 35 in Cable Plane 1 to take advantage of the symmetry of the bridge.

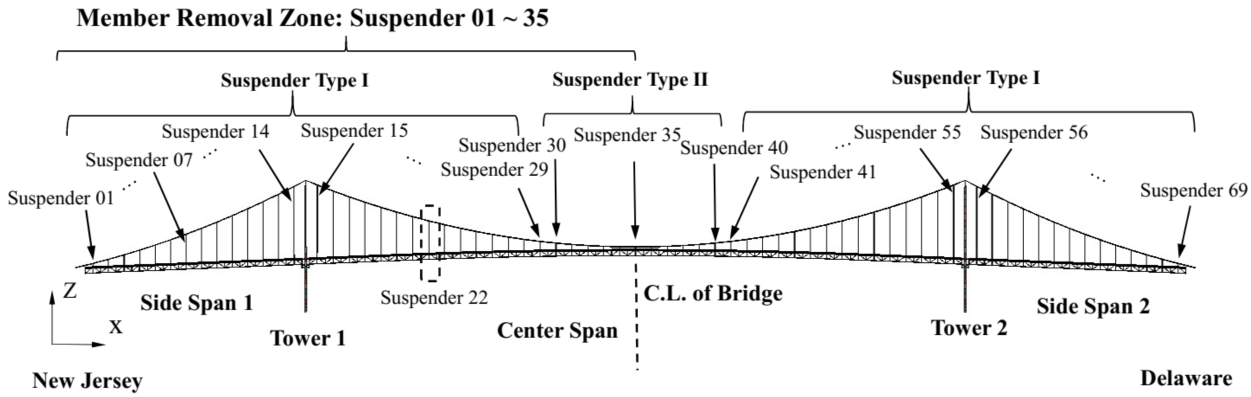

Source: FHWA.

Figure 119. Illustration. Sudden suspender removal Scenarios.

Example Case of Single Suspender Removal

The simulation results show that the entire bridge was only affected slightly by single suspender removals, while the structural members in the vicinity of the removed suspender were affected significantly. To illustrate this effect, removal of suspender 22 under COMB1 is discussed as a representative case.

The vertical displacement of the entire bridge after it had reached steady state subsequent to the removal of suspender 22 is plotted in Figure 120. The maximum downward displacement was -1.421 feet. For the intact bridge under COMB1, this displacement was -1.408 feet, as shown in Table 25. Therefore, the maximum downward displacement inceased only 0.013 feet, i.e., by 0.92% with respect to that for the intact bridge.

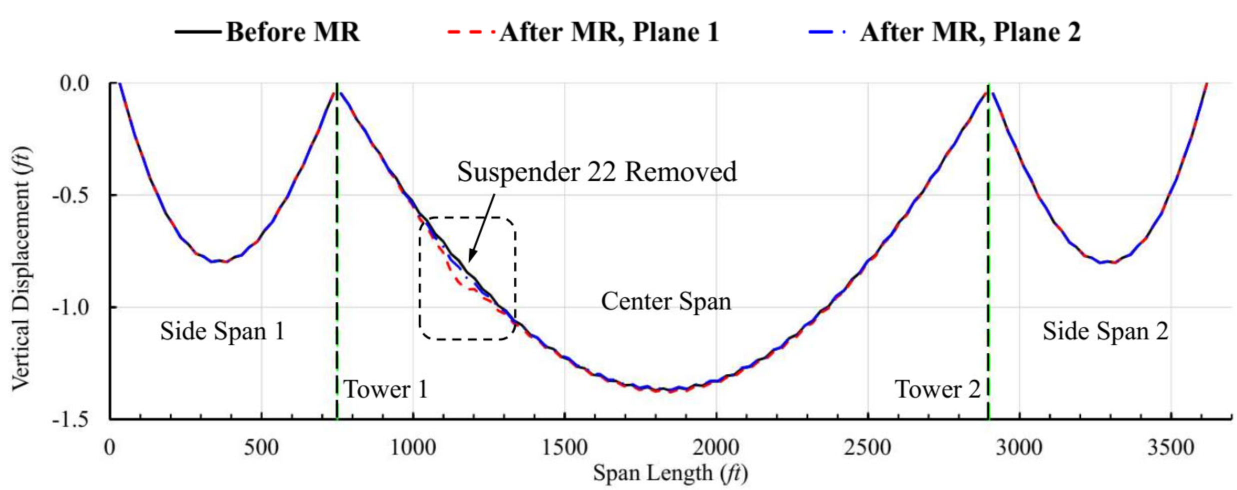

Source: FHWA.

(a) Entire bridge.

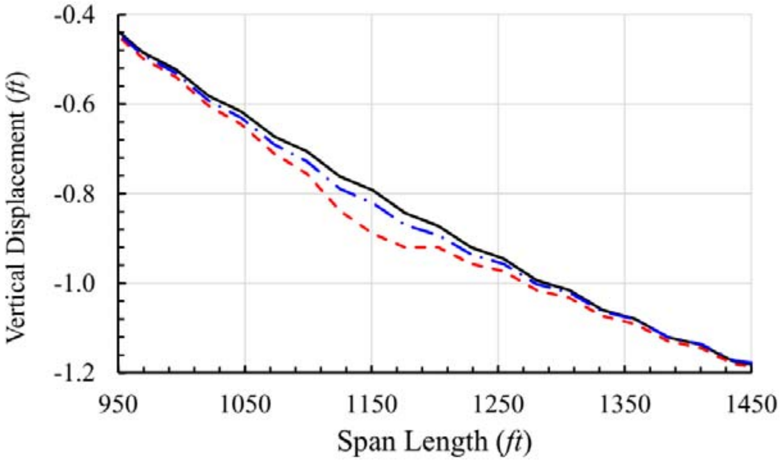

Source: FHWA.

(b) Close-up view of vertical displacement near suspender 22.

Figure 120. Graphs. Vertical displacement of entire bridge under COMB1 after removal of suspender 22.

In order to investigate the localized effect of suspender removal, the vertical displacement time history of Node 190, where the top chord meets suspender 22 (i.e., the lower-end node of suspender 22) is plotted in Figure 121. The local displacement of the intact bridge was -0.79 feet. Due to the sudden loss of suspender 22 at 18.01 seconds, the area surrounding the suspender vibrated significantly and the local displacement reached its peak value of -0.937 feet at 21.594 seconds. After 40.0 seconds, the bridge went into a steady state completely, and the local displacement reached the new steady-state displacement of -0.889 feet, increasing by approximately 12.25% with respect to the intact bridge.

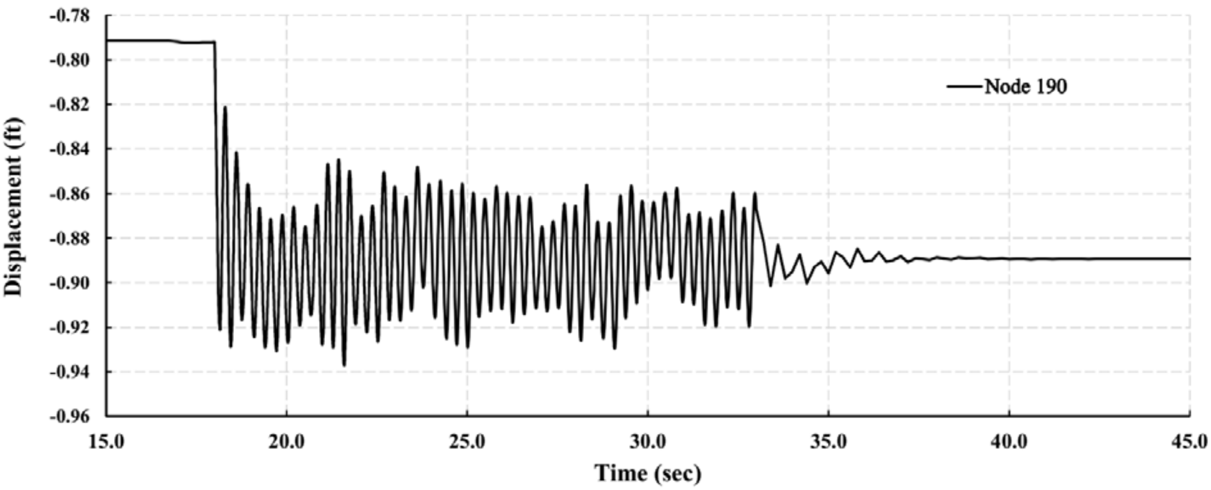

Source: FHWA.

Figure 121. Graph. Vertical-displacement time history of node 190 (lower end of suspender 22) during the removal of suspender 22.

The tension forces in the main cable segments, including the cable tension forces in the intact bridge, the peak dynamic cable tension forces of the damaged bridge during the removal of suspender 22 and the cable tension forces of the damaged bridge in its new steady-state, are replotted in Figure 122. It is observed from this figure that the main cable in the center span was substantially affected by the sudden removal of suspender 22, while the main cables in the side spans were hardly affected. In the center span, the effects of sudden suspender removal on cable segment forces decreased from the towers to the center of the bridge. The maximum effect was located at cable segment 17, which is adjacent to Tower 1 in Cable Plane 1. The peak dynamic cable tension force was 24,327.0 kips, increasing by approximately 2.57% with respect to that for the intact bridge. However, after the damaged bridge went into its steady state in the damaged condition, the cable tension forces became almost similar to those in the intact bridge. For the cable segments in Cable Plane 1, the differences were within 0.05%, except for cable segments 25 and 26 which were connected to the upper end of suspender 22. For cable segments in Cable Plane 2, the differences were even smaller, i.e., within 0.03% of those for the intact bridge. Hence, the overall effect of single suspender removal on the main cable tension forces was quite small.

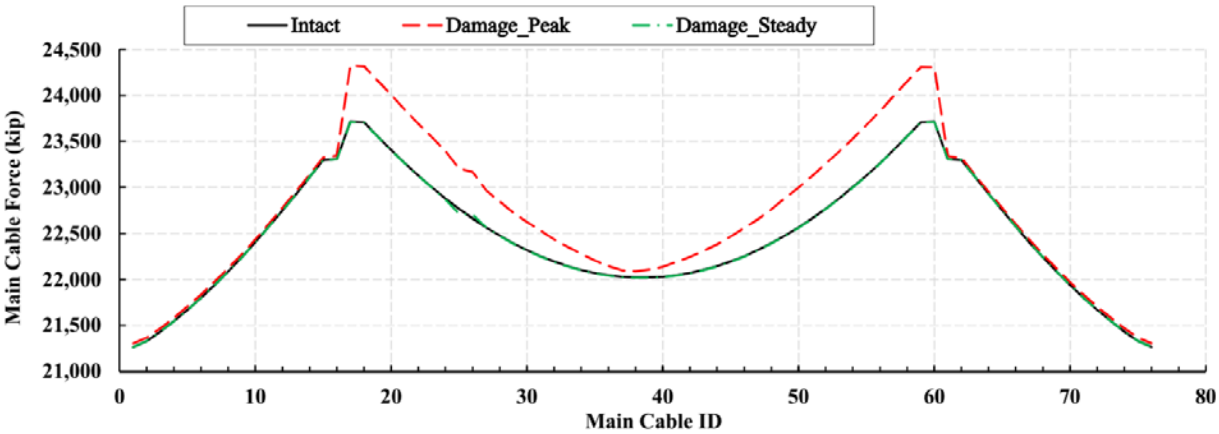

Source: FHWA.

(a) Main cable in Cable Plane 1.

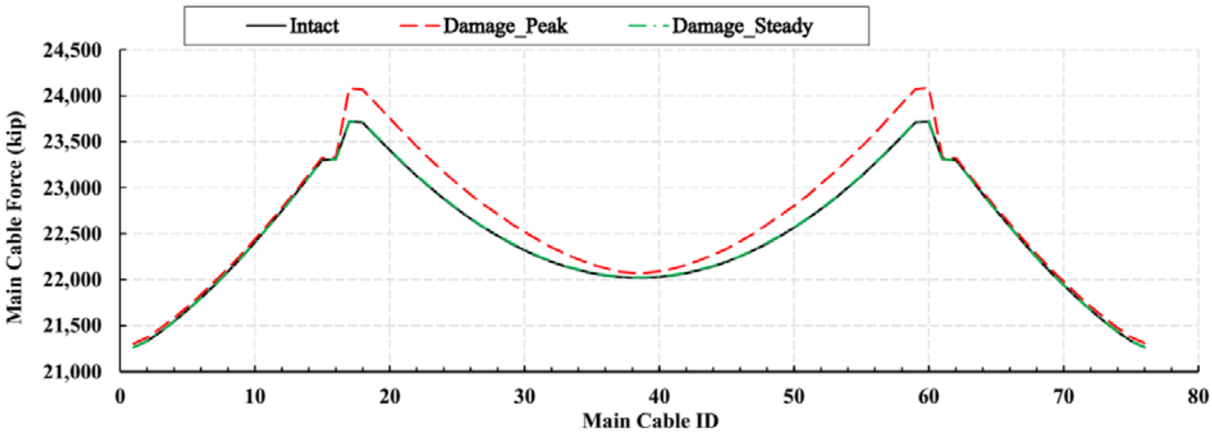

Source: FHWA.

(b) Main cable in Cable Plane 2.

Figure 122. Graphs. Tension in main cable due to loss of suspender 22.

To investigate the localized effects of sudden suspender loss on the main cable, cable segments 25 and 26, which are located on the left and right sides of the upper end of suspender 22, respectively, were examined. Their tension time histories are shown in Figure 123. After the sudden removal of suspender 22, these two cable segments started to vibrate. The peak values of the dynamic tension forces in these two segments were 23,206 kips and 23,168 kips, respectively, and increased by approximately 1.92% and 2.23%, respectively, with respect to those for the intact bridge. However, after the vibrations were damped out, the differences decreased to -0.22% and 0.18%, respectively. Hence, the localized effect of single suspender removal on the main cable was also very small, especially when the bridge went to the steady state in the damaged condition.

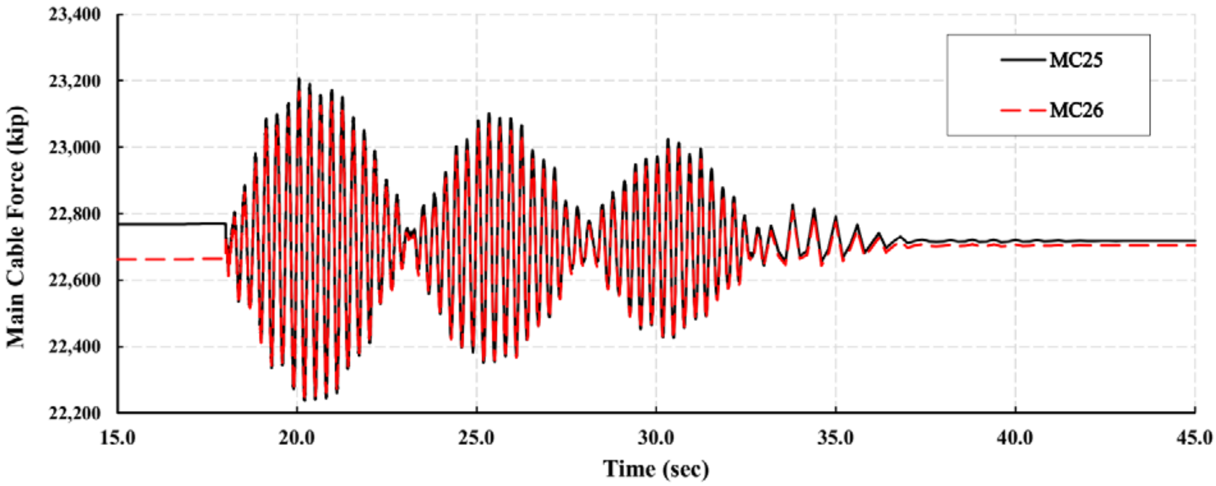

Source: FHWA.

Figure 123. Graph. Time histories of tensions of the adjacent main cable segments during the loss of suspender 22 under COMB1.

The effect of single suspender removal on other suspenders may be significant. However, the effect is limited to the adjacent suspenders in the same cable plane and decreases significantly with distance from the location of the lost suspender. In order to illustrate this, tension force time histories of six suspenders (suspenders 19 to 25) in the vicinity of suspender 22 are plotted in Figure 124. Due to the sudden removal of suspender 22, the tensions in suspenders 21 and 23 increased rapidly and significantly. The peaks of the dynamic tension forces were 746.8 kips and 752.2 kips, respectively, for suspenders 21 and 23, and their corresponding dynamic increase factor (DIF) were 2.02 and 2.01, respectively. After the dynamic vibration was damped out, steady-state tension forces in suspenders 21 and 23 were 529.2 kips and 544.7 kips, respectively, corresponding to SIF of 1.43 and 1.46, respectively. Although suspenders 19, 20, 24 and 25 were also affected, it was observed that the effect was much lesser than those for suspenders 21 and 23. Their DIF and SIF were within a range of 1.06 to 1.18 and 1.00 to 1.07, respectively. Tension time histories of three suspenders 21' to 23', which are symmetric to suspenders 21 and 23, but in Cable Plane 2, are plotted in Figure 124(c). It is observed that the effect of the loss of suspender 22 on these suspenders is small, since their DIF and SIF are in a narrow range of 1.09 to 1.11 and 1.00 to 1.01, respectively.

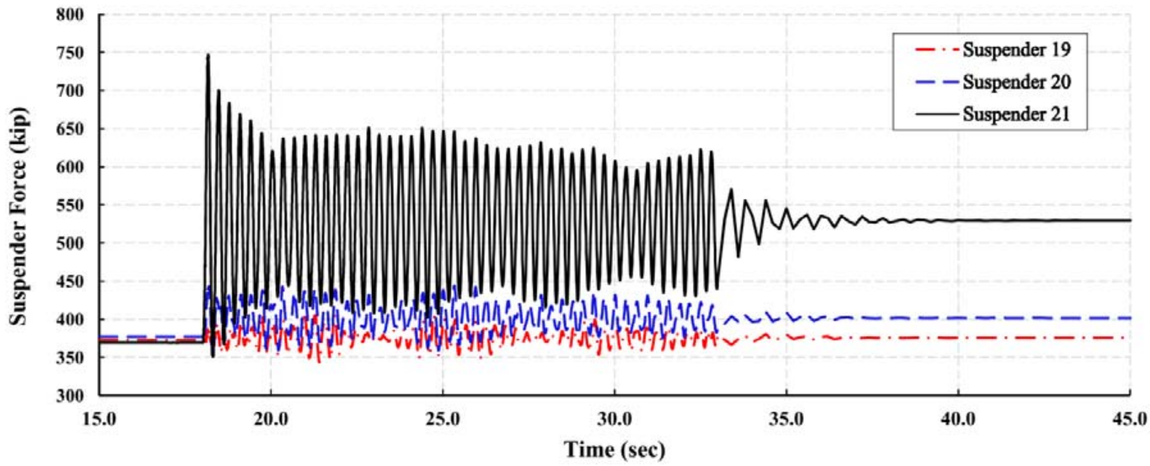

Source: FHWA.

(a) Suspenders at left side of suspender 22, in Cable Plane 1.

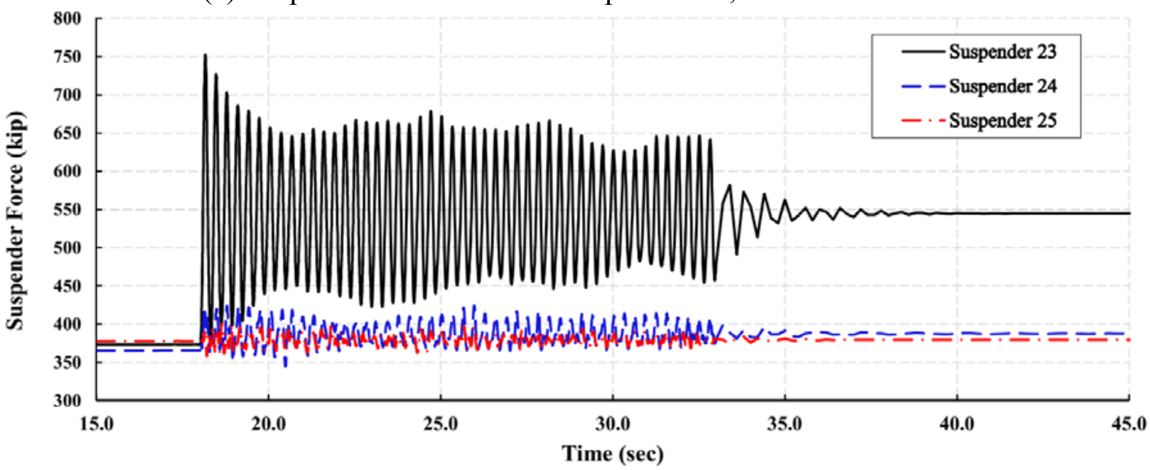

Source: FHWA.

(b) Suspenders at right side of suspender 22, in Cable Plane 1.

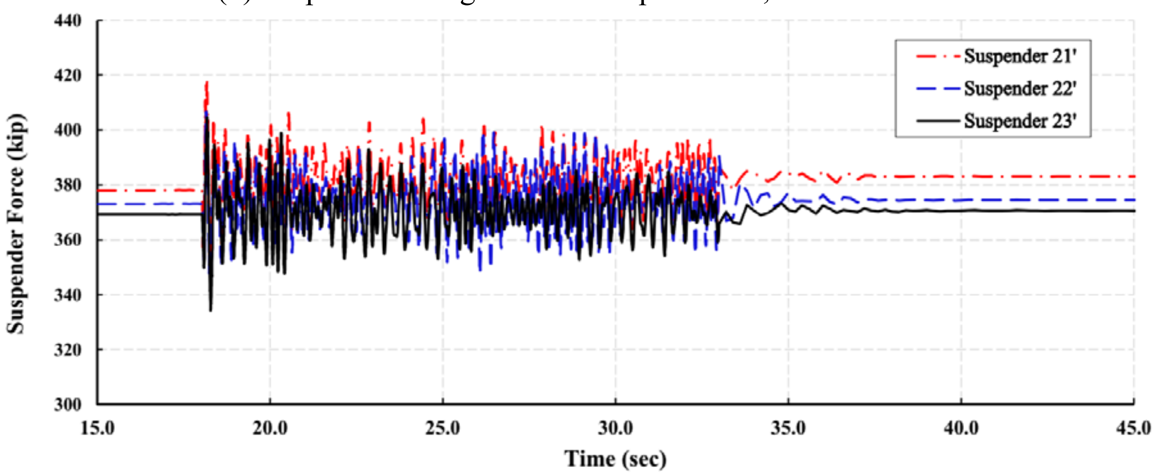

Source: FHWA.

(c) Suspenders near suspender 22, in Cable Plane 2.

Figure 124. Graphs. Time histories of tensions of the adjacent suspenders during the loss of suspender 22 under COMB1.

The simulation results above show that the entire bridge was only slightly affected by the removal of a single suspender, except for the two adjacent suspenders near the suddenly removed member. Therefore, in the following sections, the effect of single suspender loss on the entire bridge will be investigated with a focus on the behavior of suspenders.

Demand to Capacity Ratios (DCR)

The DCR envelope for 35 single-suspender loss cases under COMB1 is shown in Figure 125. For the intact bridge, the DCRs were relatively low and the maximum DCR_{intact} was 0.23 for suspenders 15 and 55. Due to sudden suspender removal, the DCRs of suspenders in the suspender removal zone (i.e., suspenders 1 to 36) increased significantly. It was observed that, except for suspenders 14 and 15, the DCR of all other suspenders (i.e., suspenders 1 to 13 and 16 to 29) increased by more than 90% and DCR_{damage_peak} was approximately 0.46 for suspender 22 because of loss of suspender 23. In suspenders 14 and 15, located at both sides of the tower, the constraints from the tower suppressed the vibration induced by sudden suspender loss to a certain degree. Therefore, their DCR_{damage_peak} values were smaller, but still around 0.35. With a relatively smaller cross-section, DCR_{damage_peak} of type-I suspenders were overall larger than those for type-II suspenders. When the bridge went into the new steady state once the vibration was damped out, DCR_{damage_steady} of all suspenders decreased, and the maximum value of DCR_{damage_steady} was approximately 0.34 for suspender 28.

Suspenders outside the suspender removal zone (i.e., suspenders 1 to 35) were only slightly affected and the effect decreased with an increase in the distance from the suspender removal zone. However, it is worth noting that the DCR envelope of suspenders in Figure 125 is based on the removal of suspenders 1 to 35. Based on symmetries of bridge and loading, the mirrored results can be obtained for suspender removals in other zones in Cable Plane 1 and 2. Therefore, only the results on suspenders in the removal zone in Figure 119 will be presented.

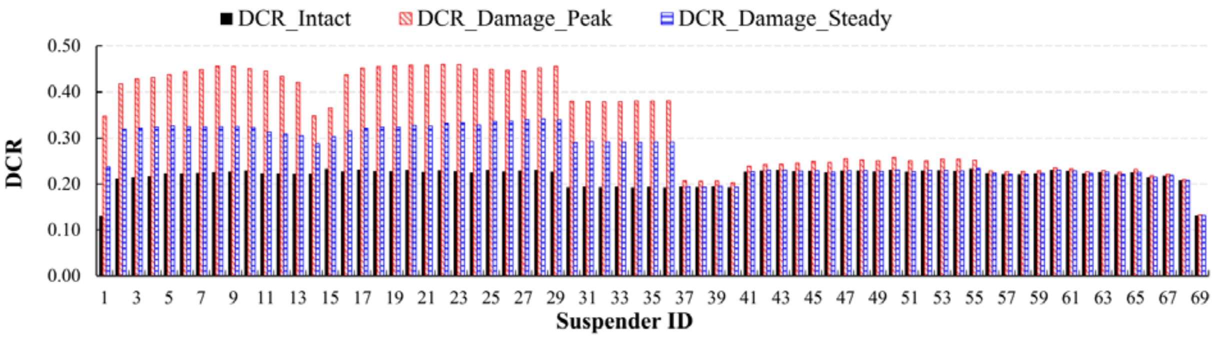

Source: FHWA.

(a) DCR Envelope of suspenders in Cable Plane 1.

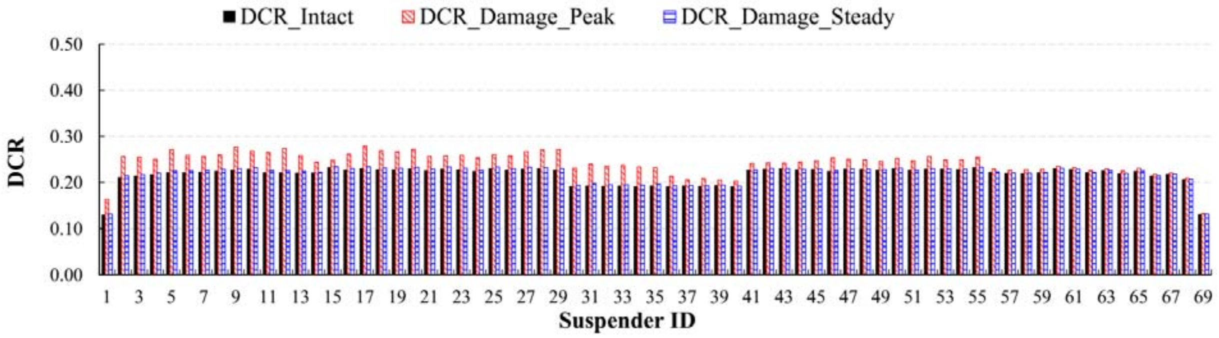

Source: FHWA.

(b) DCR Envelope of suspenders in Cable Plane 2.

Figure 125. Graphs. DCR Envelope of suspenders for bridge subject to single suspender loss under COMB1.

The DCR envelopes for the 35 single-suspender loss cases under load combinations COMB2 and COMB3 are shown in Figure 126 and Figure 127, respectively. For the intact bridge, the results of live load analysis have already demonstrated that the tension forces in the suspenders in the side span (i.e., suspenders 1 to 14) for the bridge under COMB2 and COMB1 are close to each other, and similarly the tension forces in the suspenders in the center span (i.e., suspenders 15 to 36) for the bridge under COMB3 and COMB1 are also close to each. Additionally, for these two load cases, the DCR envelopes were dominated by these suspenders in both the dynamic state associated with the removal process and the subsequent steady-state. For the bridge under COMB2, the maximum DCR_{damage_peak} was 0.46 for suspender 8 because of the loss of suspender 9. Similarly, the maximum DCR_{damage_steady} was 0.33 for suspender 5. For the bridge under COMB3, the maximum DCR_{damage_peak} was 0.46 for suspender 22 due to the loss of suspender 23 or for suspender 23 due to the loss of suspender 22, and the maximum DCR_{damage_steady} was 0.34 for suspender 28.

In summary, for the bridge subject to a sudden suspender loss under COMB1 through COMB3, the maximum of DCR for suspenders was 0.46 during the dynamic vibration phase and 0.34 in the subsequent steady-state phase. Therefore, all suspenders were still in the elastic range when the bridge was subject to a sudden single suspender loss.

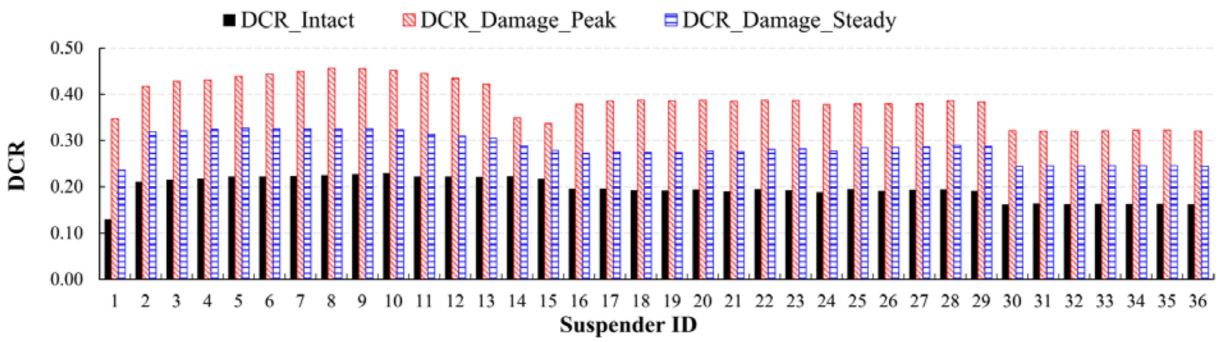

Source: FHWA.

Figure 126. Graph. DCR envelope of suspenders for bridge subject to single suspender loss under COMB2.

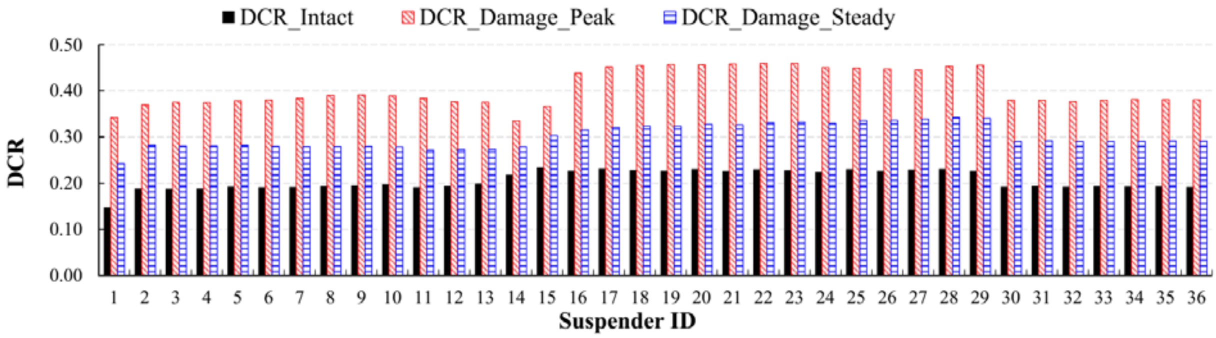

Source: FHWA.

Figure 127. Graph. DCR envelope of suspenders for bridge subject to single suspender loss under COMB3

Dynamic Increase Factor (DIF) and Static Increase Factor (SIF)

The DIF and SIF envelopes for the 35 single-suspender loss cases under COMB1 are shown in Figure 128. It is observed from this figure that only suspenders in the removal zone (i.e., suspenders 1 to 36) were affected significantly by sudden single suspender loss. There was no significant effect on suspenders in other zones in both Cable Planes 1 and 2. The maximum DIF and SIF were 2.66 and 1.81, respectively, for suspender 1 due to sudden loss of suspender 2. Because the tension of suspender 1 in the intact bridge was only around 60% of the tensions in other suspenders, the tension increase effect was more noticeable for this suspender. For all other suspenders within the removal zone, the DIFs were in the range of 1.57 ~ 2.03 and the maximum value of 2.03 was for suspender 21 because of the loss of suspender 22. The SIF values were in the range of 1.30 ~ 1.52 and the maximum value of 1.52 was for suspender 36 due to the loss of suspender 35. The minimum DIF and SIF values both occurred for suspender 15, since suspenders 14 and 15 were close to Tower 1 and the vibration effects were suppressed by the constraints imposed by the tower.

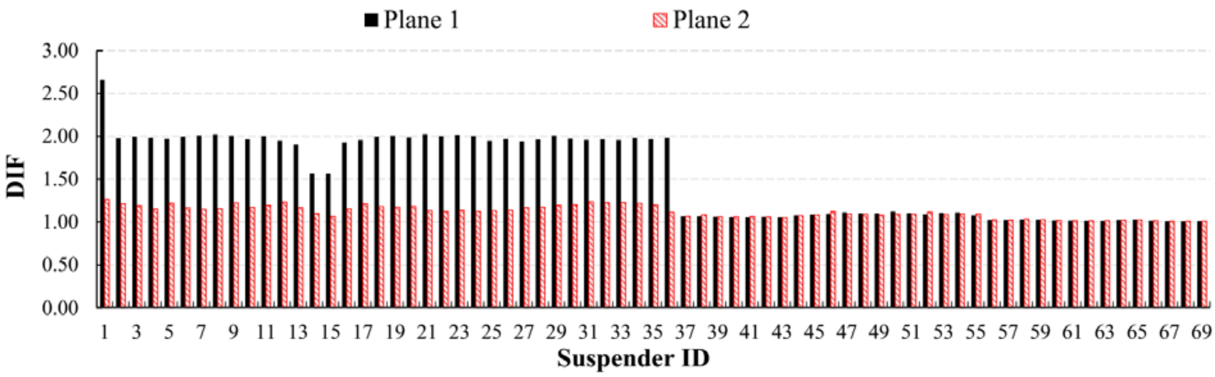

Source: FHWA.

(a) Envelope of DIF.

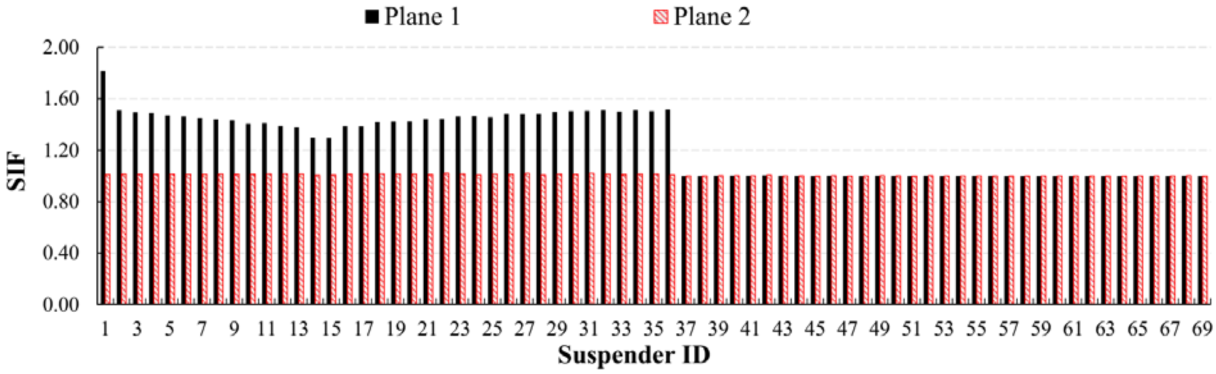

Source: FHWA.

(b) Envelope of SIF.

Figure 128. Graphs. DIF and SIF envelopes of suspenders for bridge subject to single suspender loss under COMB1.

The DIF and SIF envelopes of suspenders for the bridge subject to the 35 single-suspender loss cases under COMB2 and COMB3 are shown in Figure 129 and Figure 130, respectively. It should be noted that only the results of suspenders in the removal zone are presented and the results for the loss of suspenders in other zones can be obtained by symmetries of the bridge and loading. Overall, the trends of DIF and SIF envelopes are similar to those for the bridge under COMB1. Excluding suspender 1, the maximum DIF for the two load cases were both 2.0, for suspender 27 for load combination COMB2 and for suspender 21 for COMB3. The maximum SIF was 1.51 for suspender 2 for COMB2 and 1.52 for suspender 36 for COMB3.

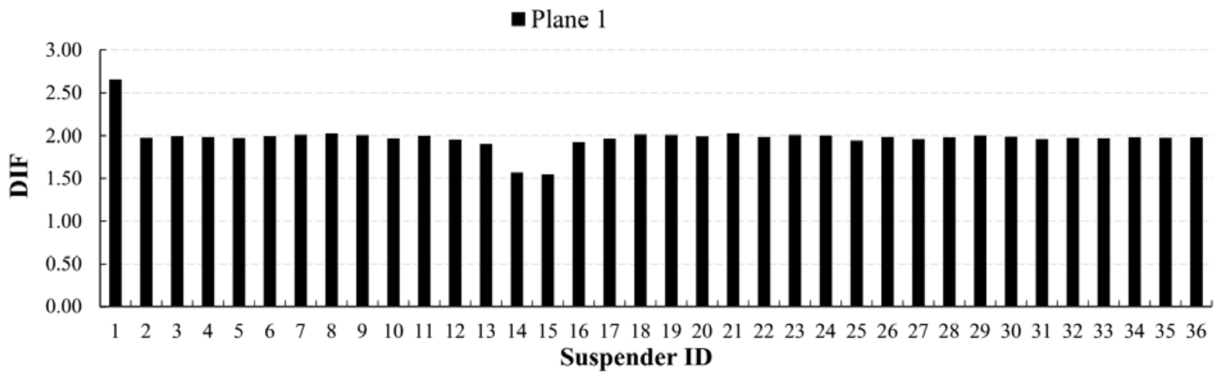

Source: FHWA.

(a) Envelope of DIF.

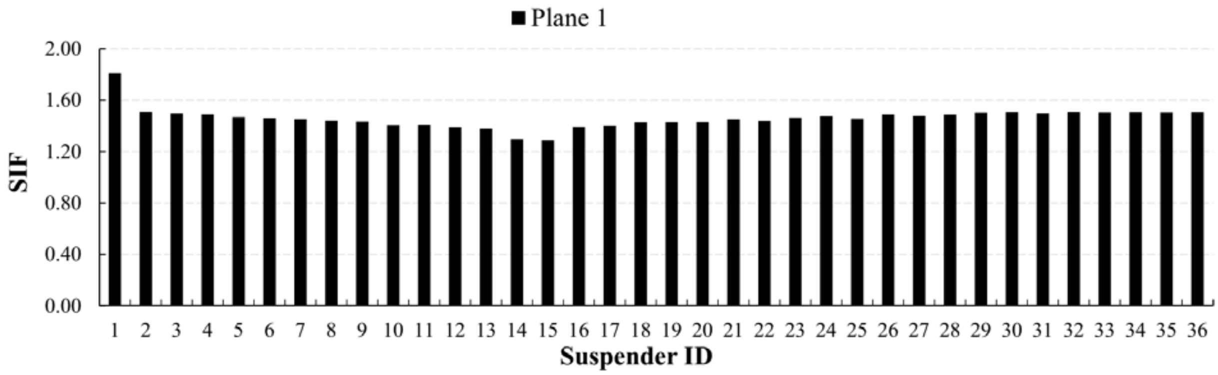

Source: FHWA.

(b) Envelope of SIF.

Figure 129. Graphs. DIF and SIF envelopes of suspenders for bridge subject to single suspender loss under COMB2.

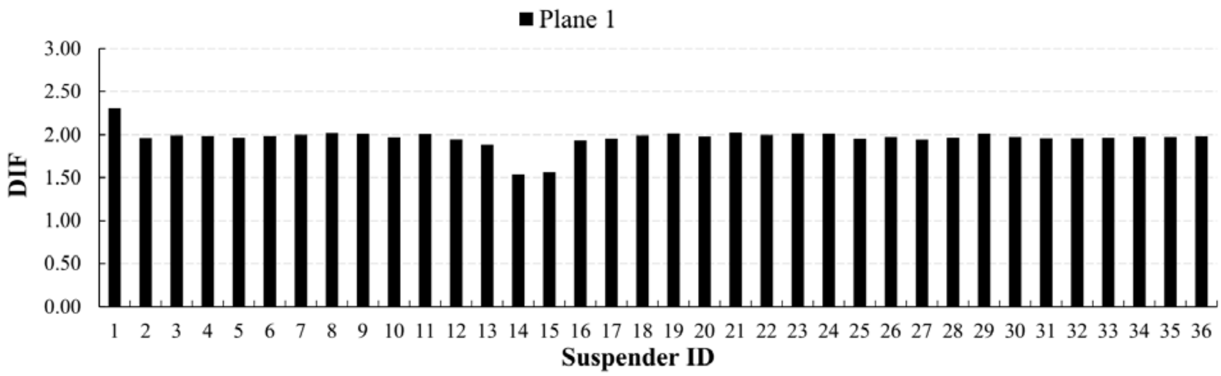

Source: FHWA.

(a) Envelope of DIF.

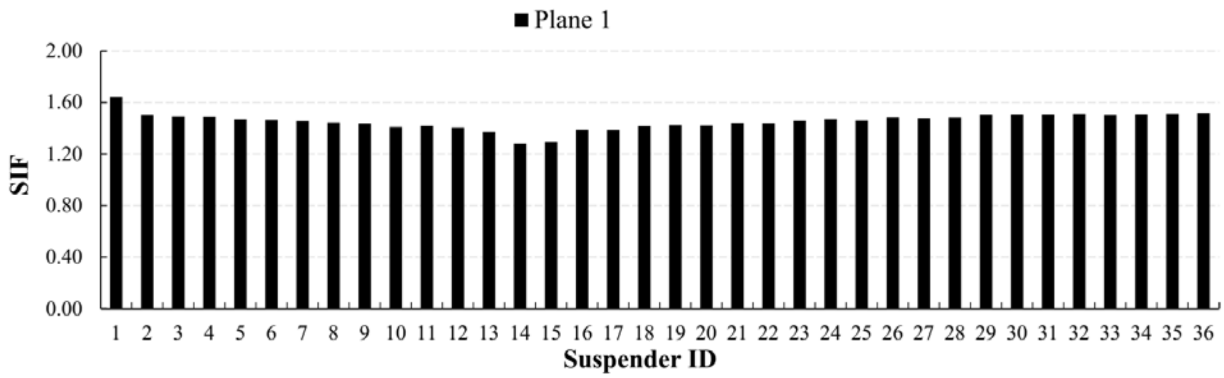

Source: FHWA.

(b) Envelope of SIF.

Figure 130. Graphs. DIF and SIF envelopes of suspenders for bridge subject to single suspender loss under COMB3.

Dynamic Amplification Factor (DAF)

The DAF envelopes of suspenders for the bridge subject to the 35 single-suspender loss cases under COMB1 through COMB3 are plotted in Figure 131. As shown in Figure 131(a), the dynamic effect of the suspenders in the removal zone (i.e., suspender 1 to 36) is more noticeable than for those in other zones. DAF of these suspenders are in the range of 1.30 ~ 1.47, except for suspenders 14 and 15, whose DAF are 1.21. For the suspenders near the removal zone in Cable Plane 2 (i.e., suspenders 01' ~ 36'), the DAF are mostly in the range 1.10 ~ 1.27, except for suspender 15'. Suspenders beyond the removal zone were only slightly affected and their DAFs are less than 1.10. It should be noted that the results shown in Figure 131(a) are based on the removal of suspenders 1 to 35. The results for suspender loss in other zones can be easily obtained by symmetries of the bridge and loading. Therefore, only the results in the suspender removal zone are presented for the bridge under COMB2 and COMB3 as shown in Figure 131(b)&(c). Overall, the DAF of suspenders for the bridge under load combinations COMB 2 and COMB 3 are quite similar to those for the bridge under the load combination COMB1.

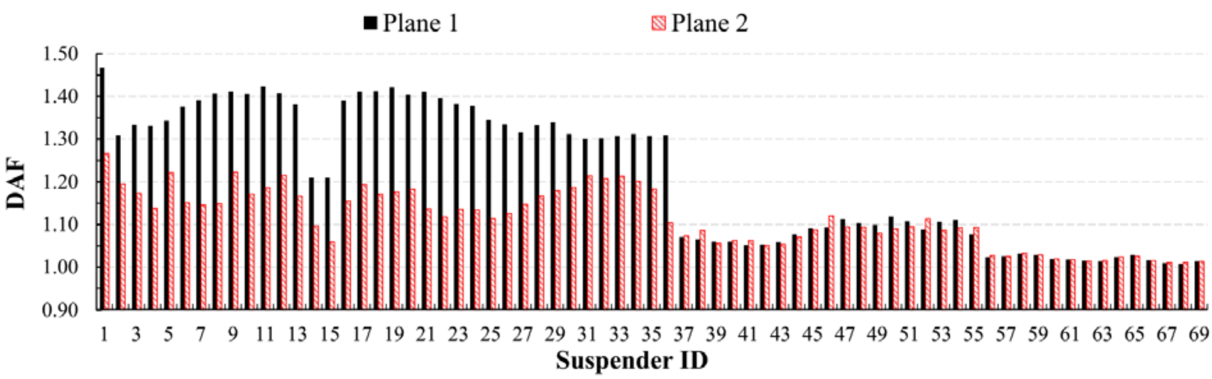

Source: FHWA.

(a) Bridge under COMB1.

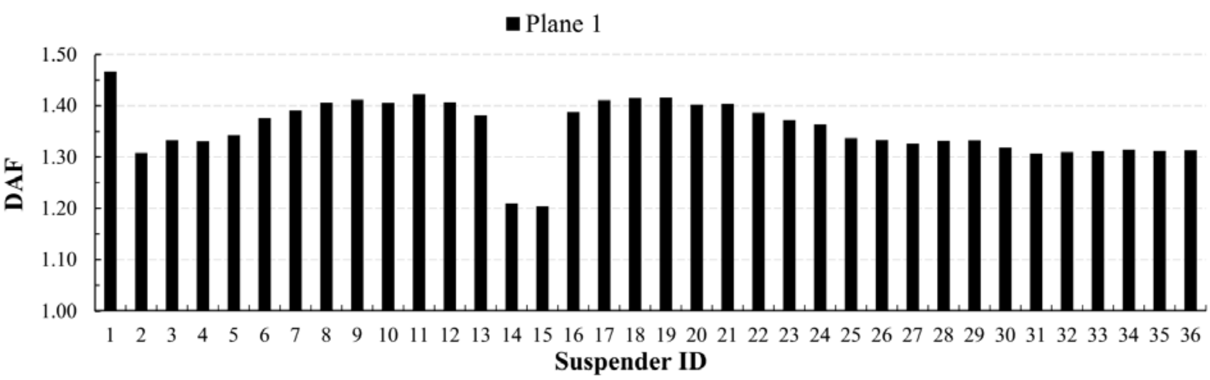

Source: FHWA.

(b) Bridge under COMB2.

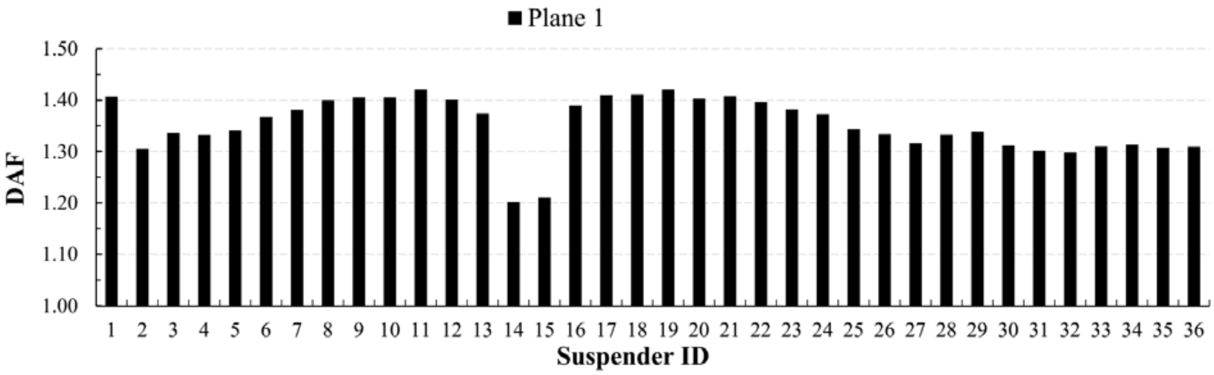

Source: FHWA.

(c) Bridge under COMB3

Figure 131. Graphs. Envelopes of DAF of suspenders for bridge subject to single suspender loss.

Progressive Collapse Behavior under Multiple-Suspender Loss Scenario

The progressive collapse behavior of the bridge due to the loss of multiple suspenders was investigated. The following assumptions were made:

(i) The applied live load was kept constant during the suspender loss event.
(ii) The suspenders were removed one by one, i.e., only one suspender was removed at a time, and the subsequent suspender removal process was performed only when the bridge went into its new steady-state condition, i.e., when the dynamic vibration was completely damped out.
(iii) Suspender removals were successively conducted until progressive collapse of the entire bridge was triggered.

Similar to the single suspender removal process, the global damping curve shown in Figure 111 was used to reduce the simulation time. Specifically, the global damping was kept constant at ζ = 2% for 10 seconds, which was long enough to capture the peak response of the entire bridge, especially the peak dynamic response of adjacent suspenders and main cables. Subsequently, the damping was increased suddenly to ζ = 100% and it was kept constant for 9.89 seconds to allow the dynamic vibration to be damped out, i.e., to allow the bridge response to reach a new steady-state. Once the bridge response reached its new steady-state, the damping was changed to ζ = 2% for the next suspender removal process. This procedure was repeated until progressive collapse of the entire bridge was triggered.

As shown in Figure 132, under COMB1, 8 type-II suspenders (i.e., suspenders 30 ~ 37 in Cable Plane 1) in the center span were removed by following the procedure discussed above.

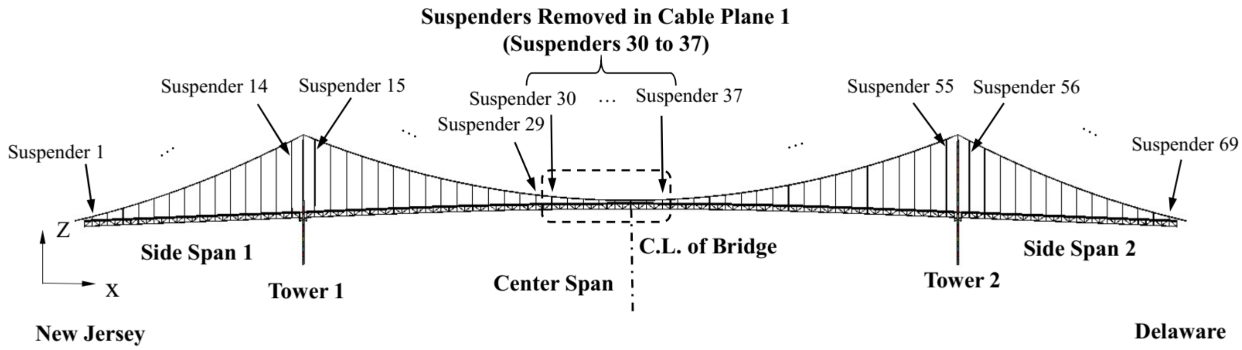

Sequence of suspender removals: 30 → 31→ 32→ 33 → 34 → 35 → 36 → 37

Source: FHWA.

Figure 132. Illustration. Multiple suspender removal scenario under load combination COMB1.

Under COMB1, most of the major structural components (except suspenders), such as main cables and towers, were in their elastic range, even for the damaged bridge during the multiple-suspender loss scenario. The progressive collapse process of the entire bridge was mainly due to the rupture of other suspenders. Therefore, the responses of the suspenders near the removal zone were focused during the simulation. The peak dynamic tension force and subsequent steady-state force in each suspender for each removal step are summarized in Table 26. Additionally, representative tension time histories of suspenders 28, 29, 36 and 37 are plotted in Figure 133. The simulation results show that an un-zipping type collapse of the entire bridge was triggered suddenly after the removal of the 8th suspender. Based on the number of suspenders removed (denoted by NSR), the bridge behavior during this multiple-suspender removal simulation can be roughly divided into the following three stages:

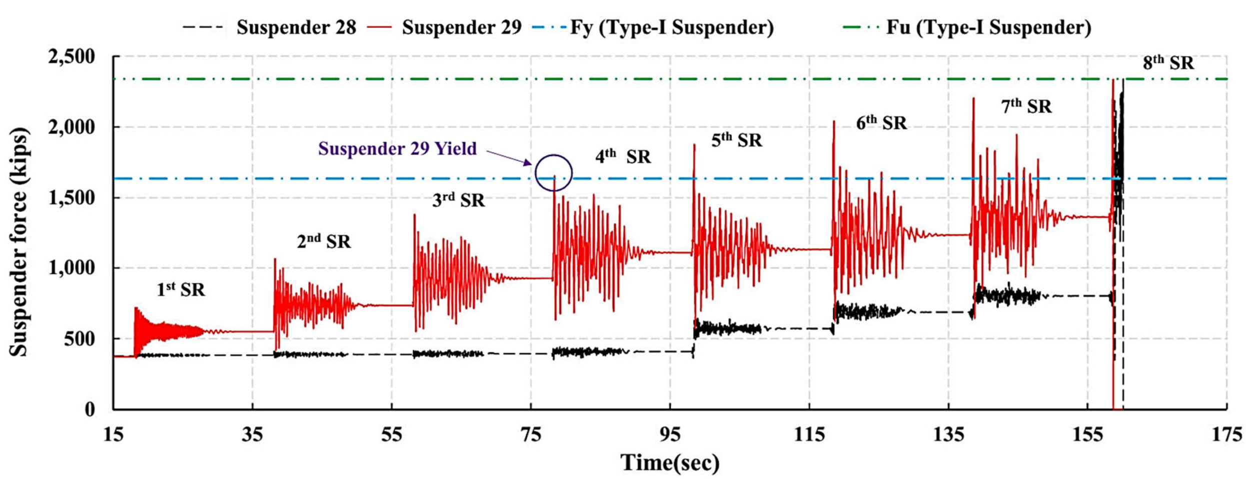

Source: FHWA.

(a) Tension of suspenders 28 and 29.

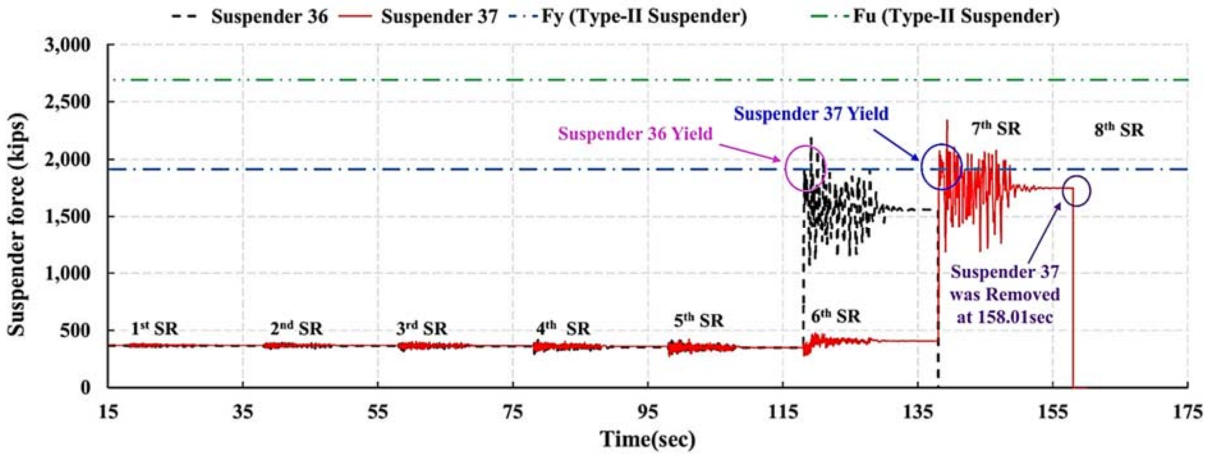

Source: FHWA.

(b) Tension of suspenders 36 and 37.

Figure 133. Graphs. Tension time histories of selected suspenders during multiple-suspender removals.

Table 26. Dynamic tension response of selected suspenders near the removal zone during multiple-suspender loss event.

Type	Suspender No.	COMB1 NSR= 0	NSR=1 Suspender 30		NSR=2 Suspenders 30~31		NSR=3 Suspenders 30~32		NSR=4 Suspenders 30~33		NSR=5 Suspenders 30~34		NSR=6 Suspenders 30~35		NSR=7 Suspenders 30~36		NSR=8 Suspenders 30~37
			P	S	P	S	P	S	P	S	P	S	P	S	P	S	
Type-I	28	376.4	398.5	383.2	408.8	388.7	417.7	392.3	445.4	407.8	641.9	570.9	767.7	687.2	897.2	801.2	
Type-I	29	371.0	719.1	548.9	1064.8	734.3	1382.5	925.3	1654.9	1107.4	1877.6	1129.2	2041.4	1236.8	2205.6	1364.4	
Type-II	30	368.4															
Type-II	31	370.9	726.6	556.7													
Type-II	32	368.4	391.9	371.9	1068.7	749.7											**Progressive Collapse.**
Type-II	33	370.1	386.1	369.0	403.2	372.4	1382.1	952.8									
Type-II	34	369.1	385.8	368.2	389.5	365.5	428.3	366.9	1637.2	1161.3							
Type-II	35	369.7	381.6	369.5	397.2	367.5	393.0	362.4	411.5	361.2	1843.5	1394.9					
Type-II	36	367.5	379.6	366.8	391.5	365.4	391.5	361.7	415.5	354.0	419.7	351.0	2185.6	1560.3			
Type-II	37	370.7	388.4	370.5	393.9	369.6	403.3	367.1	404.5	361.7	421.7	350.6	478.0	407.6	2342.5	1749.2	
Type-II	38	368.8	381.6	369.1	402.6	368.4	410.3	366.6	412.2	362.6	417.7	354.0	400.7	337.6	536.8	447.2	

Note: Unit for suspension tensions: kips.
NSR --- the total amount of suspenders removed.
P --- the peak of dynamic tension of suspender during each suspender removal.
S --- the tension of suspender in the subsequent steady-state after each suspender removal.

Stage One: 1st to 3rd Suspender Loss (NSR ≤ 3)

The simulation results for single suspender removal have already demonstrated that only the adjacent suspenders were affected significantly. Therefore, the tension in suspender 29, which was adjacent to suspender 30, was closely monitored during the simulation. As shown in Figure 133(a), after the 3rd suspender removal (i.e., removal of suspender 32), the peak of the dynamic tension force in suspender 29 was 1382.5 kips and was still below its yield strength of F_{y1} = 1635.8 kips. In addition, Table 26 shows that the peak of the dynamic tension force in suspender 33 was 1382.1

kips, which was also less than its yield strength of F_{y2} = 1912.5 kips. Thus, all suspenders in the damaged bridge at this stage were still behaving elastically.

The steady-state vertical displacement of the bridge in this stage is plotted in Figure 134, based on the displacements of the top chords of the stiffening truss. Since the side spans were only mildly affected in this stage, only the displacements of the center span are presented. Figure 134 shows that the displacements of the stiffening truss (both in Cable Plane 1 and 2) increased slightly, especially the local displacement around suspender 30. The maximum displacement at this stage was -1.38 feet in the middle of the center span. However, after the 2nd suspender was removed, the local displacement around suspenders 30 to 31 increased to -1.55 feet, developing into the maximum displacement of the entire bridge. Following this, the displacement of the removal zone dominated the displacement of the entire center span until the 8th suspender was removed.

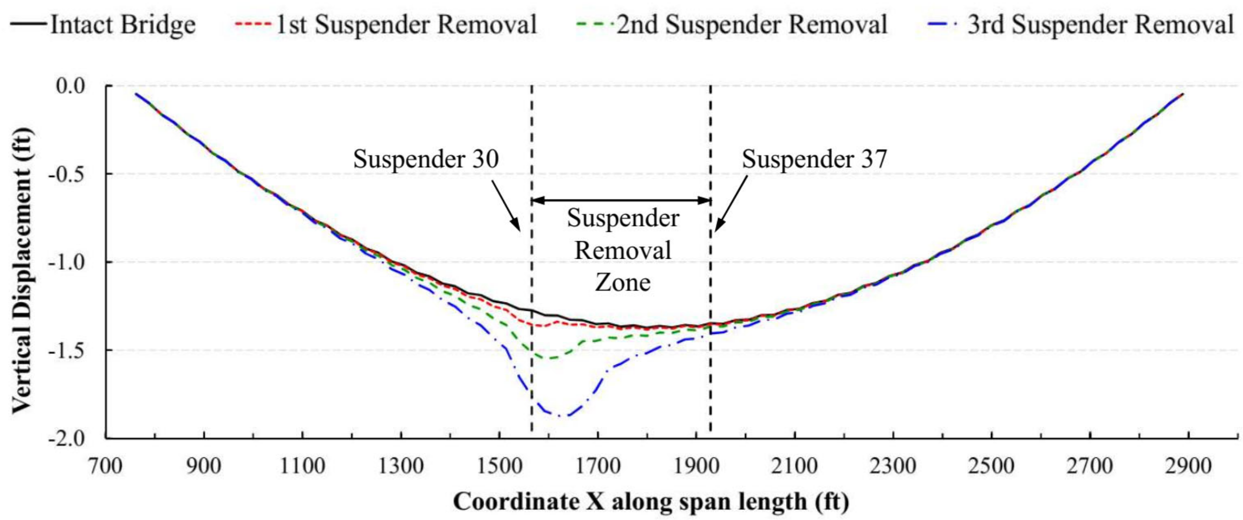

Source: FHWA.

(a) Cable Plane 1.

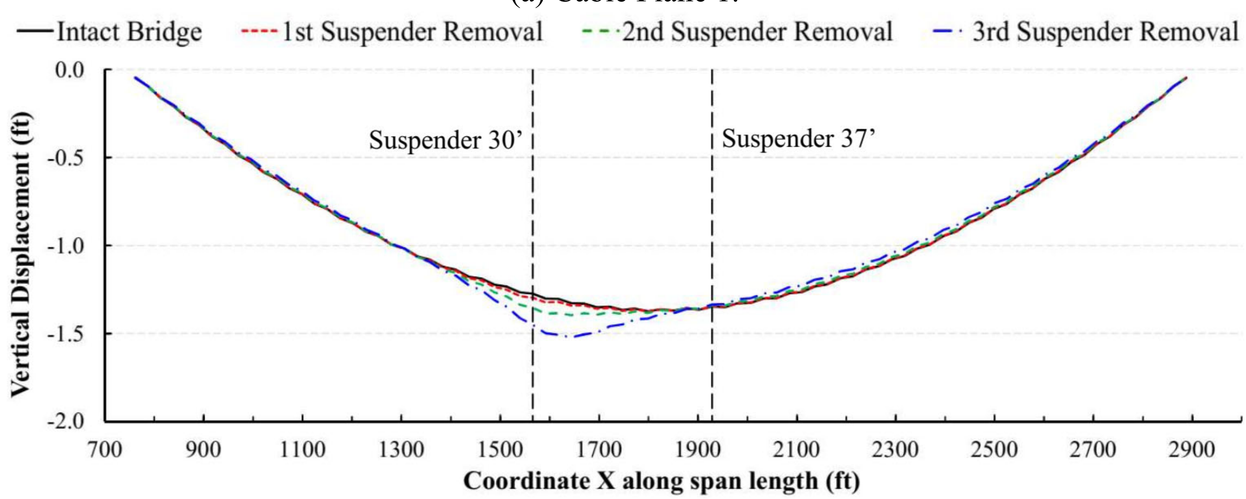

Source: FHWA.

(b) Cable Plane 2.

Figure 134. Graphs. Vertical displacements of stiffening trusses in center span during 1st to 3rd suspender removal steps.

Stage Two: 4th to 7th Suspender Loss (4 ≤ NSR ≤ 7)

After the 4th suspender was removed, the tension in suspender 29 increased significantly and the peak of the dynamic tension was approximately 1655 kips, which was slightly more than its yield strength F_{y1} of 1635.8 kips. However, it dropped to 1107.4 kips in the damaged steady-state condition. This type of behavior continued during the removal of the 5th to 7th suspenders. After the 5th suspender was removed, which was a type II suspender, the peak tension in suspender 35 was 1844 kips, which was still below its yield strength of F_{y2} = 1912.5 kips. After the 6th suspender was removed, the peak tension in suspender 36 was 2158.6 kips, which was more than its yield strength of F_{y2}. However, in the following steady state, the tension dropped to approximately 1560 kips. The tension in suspender 37 behaved similarly after the 7th suspender was removed.

The steady-state vertical displacement of the bridge in this stage is plotted in Figure 135, which is also based on the displacement of the top chords of the stiffening trusses in the center span. Since Cable Plane 1 dominates, only the vertical displacement of the stiffening truss in Cable Plane 1 is presented. It is observed that the displacement in the suspender removal zone increased progressively with the removal of more suspenders. After the 7th suspender was removed, the maximum displacement reached -8.50 feet in the damaged steady-state condition.

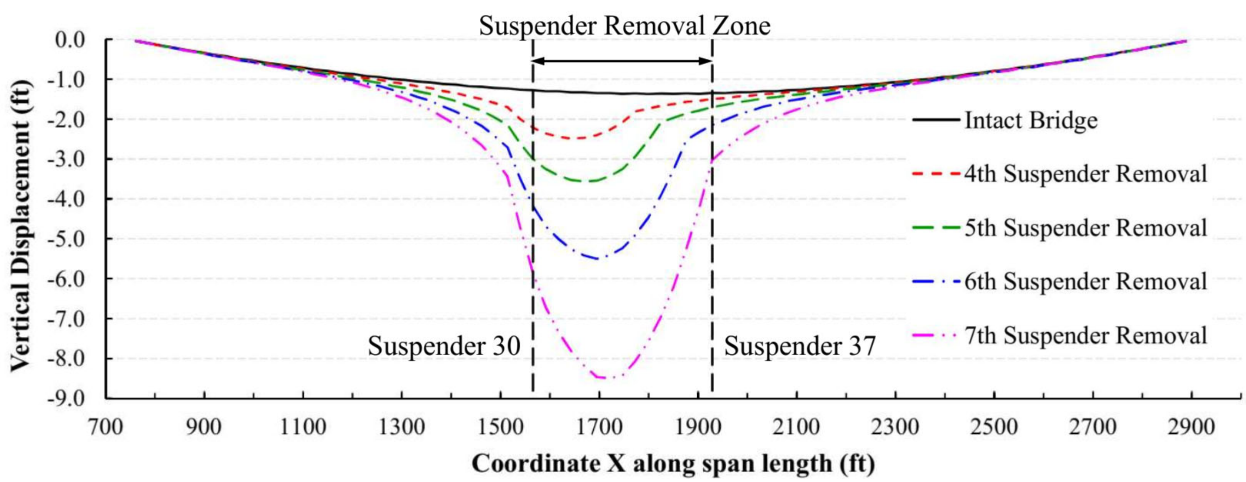

Source: FHWA.

Figure 135. Graph. Vertical displacements of stiffening truss in center span during 4th to 7th suspender removal steps.

Stage Three: 8th Suspender Loss (NSR = 8)

As shown in Figure 133(a), after the 8th suspender was removed (i.e., suspender 37), the tension in suspender 29 increased significantly and reached its ultimate strength of F_{u1} = 2300.9 kips, leading to sudden rupture of the suspender. Subsequently, more suspenders near the suspender removal zone in Cable Plane 1 ruptured one by one, leading to final collapse of the bridge. Figure 136 shows the entire collapse process of the bridge. In addition, the simulation results show that the main cables started to slip over the tower saddles after the 8th suspender was removed, which did not occur during the previous two stages. Time histories of cable slippages over the saddles are shown in Figure 137. As it shown, before loss of the 8th suspender (i.e., at t =158.01 seconds), the slippage of the main cables was zero, i.e., no slipping occurred. Afterwards, Main Cable 1 started to slip over Saddle 1 and 3 around t =159.58 seconds. Soon after, the un-zipping type of progressive collapse process was triggered. Due to the dynamic effect, Main Cable 2 started to slip over Saddle 2 at t =161.88 seconds and over Saddle 4 at t =161.96 seconds. The slipping of the main cables continued until the end of the simulation. It was clear that the slipping of main cables was not unidirectional, i.e., the main cables slipped back and forth over the saddles during the collapse process.

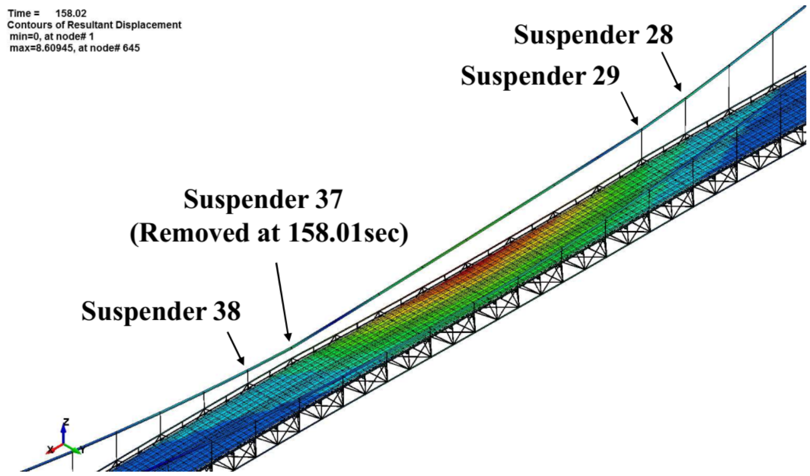

Source: FHWA.

(a) 8th SR.

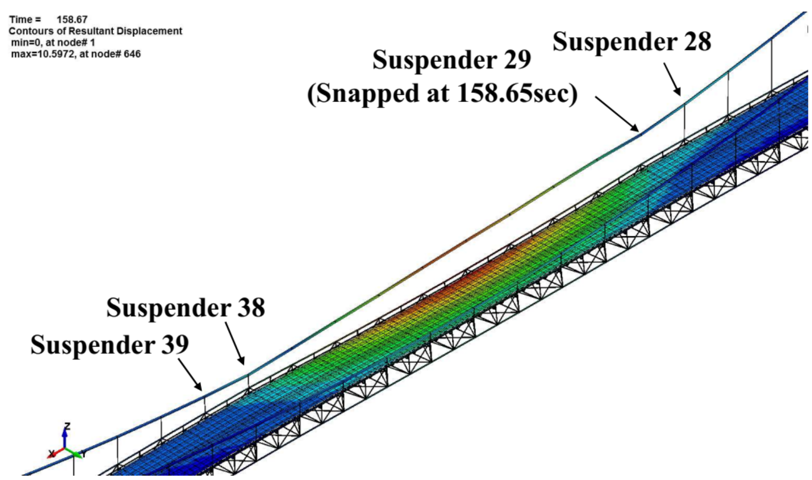

Source: FHWA.

(b) Suspender 29 snapped.

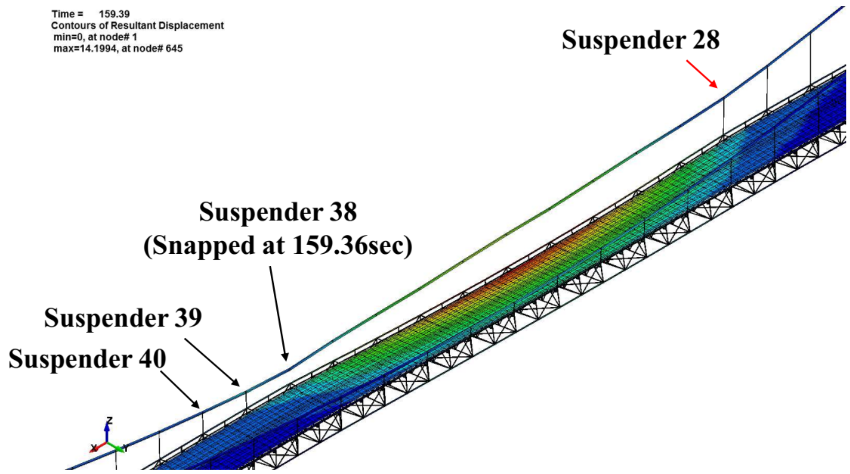

Source: FHWA.

(c) Suspender 38 snapped.

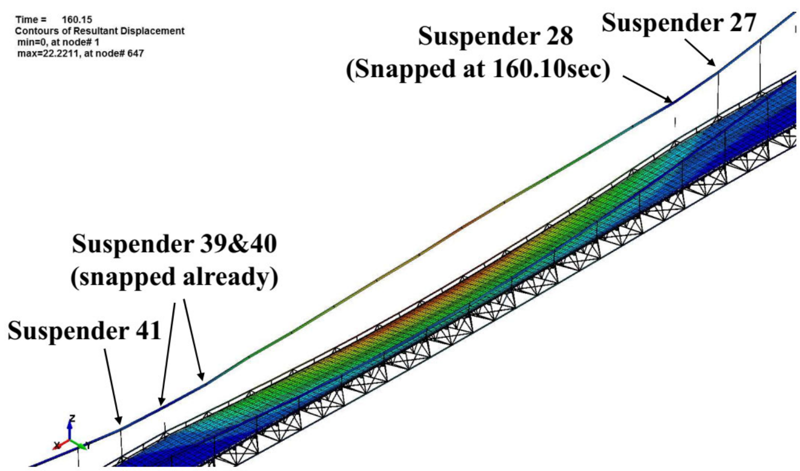

Source: FHWA.

(d) Suspenders 28 and 39 ~ 40 snapped.

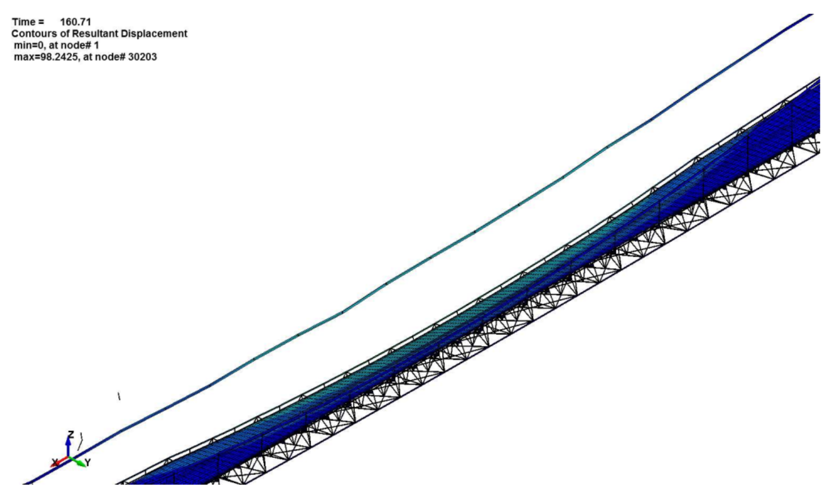

Source: FHWA.

(e) More suspenders snapped.

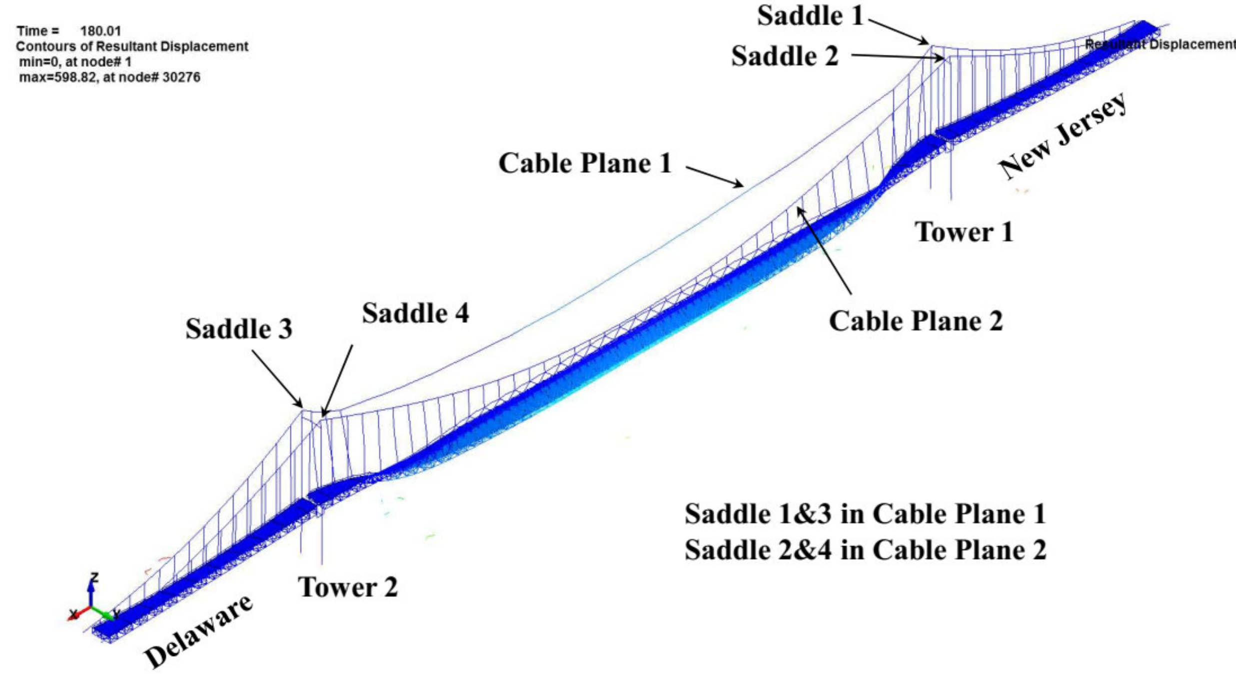

Source: FHWA.

(f) Bridge collapsed.

Figure 136. Illustrations. Progressive collapse of entire bridge after the 8th suspender loss.

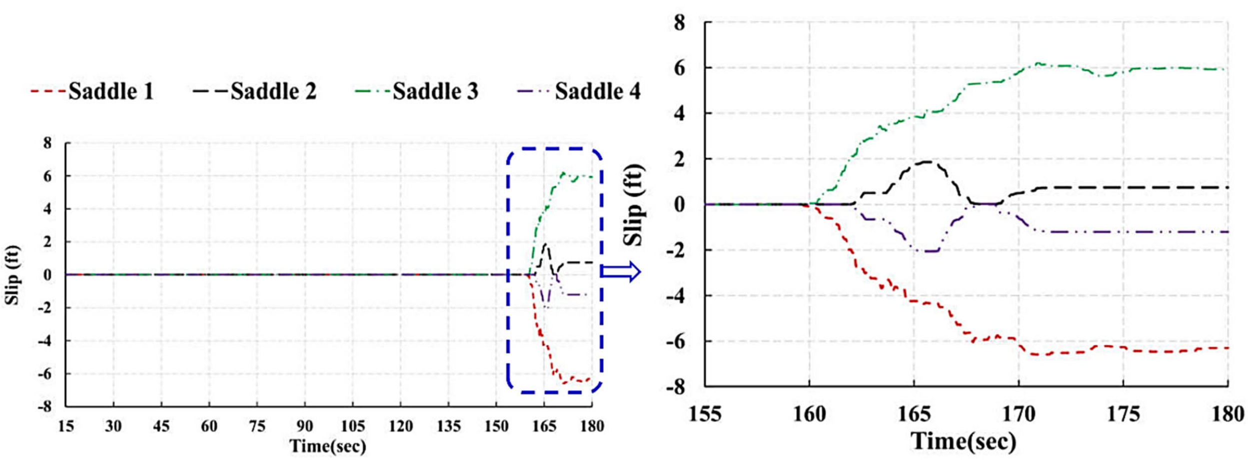

Source: FHWA.

Figure 137. Graphs. Slip of main cables over tower saddles during progressive collapse of entire bridge.

Based on the simulation results of the multiple suspender removal scenarios presented above, the following conclusions can be drawn:

(1) Only the suspenders near the removed suspender are substantially affectedly during each suspender removal step.

(2) For NSR ≤ 3. All the suspenders were in the elastic range.

(3) For NSR = 4. The adjacent type-I suspender yielded during the dynamic vibration state.

(4) For NSR = 6. The adjacent suspenders, both type-I and type-II, yielded during dynamic vibration.
(5) For NSR ≤ 6. No collapse event occurred.
(6) For NSR = 7. Both types of suspenders were very close to their ultimate capacities, i.e., up to 87% ~ 97% of F_u.
(7) For NSR ≥ 8. The un-zipping type of progressive collapse of the entire bridge commenced.

SUMMARY

Based on the explicit LS-DYNA models presented in Chapter 3, comprehensive investigations were conducted in this chapter on the behavior of the three example bridges subjected to sudden cable (i.e., stay cable/hanger/suspender) loss through member removal analyses. The key highlights from these studies are:

- For each example bridge, the intact bridge under various live load distributions was analyzed, and a comparison was made with the bridge's response under dead load only, focusing on the vertical displacement and cable forces/stresses.
- For each example bridge, various scenarios of single cable loss were simulated for several live load distributions. Four parameters-DCR (Demand Capacity Ratio), DIF (Dynamic Increase Factor), SIF (Static Increase Factor) and DAF (Dynamic Amplification Factor), were defined to evaluate the effect of cable loss.
- The simulation results show that only structural members in the vicinity of cable loss, especially the adjacent cables in the same cable plane, were primarily affected by the dynamic effects associated with sudden loss of a cable. The DCR of cables in the damaged bridge show that all the cables and other main steel structural members were still in their elastic range. Therefore, the effects on the overall performances of the three bridges due to loss of a single cable were very limited. This limited effect is attributed to the following considerations: (i) for the cable-stayed bridge, the loss of a single cable was already considered during design, for example, per recommendations in PTI (2001), (ii) for the tied-arch bridge, the structural system was designed to have a network of crossed, slanted hangers to enhance its visual appeal, therefore, it had more hangers than a typical tied-arch bridge, and (iii) for the suspension bridge, large safety factors (i.e., low DCR, around 0.2) were adopted for the design of the suspenders.
- For each example bridge, the behavior of the bridge subjected to multiple cable loss scenarios was also investigated under the most critical live load distribution. Specifically, the cables were removed one by one following the approach taken for single cable loss. During each cable removal step, the bridge was monitored closely, especially the response of key structural components, such as vertical displacement of the bridge, stress of main girder, stresses of adjacent stay cables or hangers, stress of main arch, tensions of adjacent suspenders, etc. Based on these, several limit states were identified for each bridge.
- Multi-cable loss scenarios show that, even with the loss of several cables sequentially, the three bridges could still carry the design live loads in spite of large deflections causing the bridge to reach its functional limit state. With the loss of more cables, the deflections increased significantly because some structural members reached their yield strengths, but the bridges still had reserve strength. Progressive collapse was eventually triggered after the loss of more cables.

CHAPTER 5. BRIDGE BEHAVIOR UNDER OVER-LOADING

INTRODUCTION

In this chapter, pushdown analyses were conducted for each of the three bridges discussed in Chapter 4 using the explicit models developed in Chapter 3. The failure of key structural components of the bridges was monitored closely during pushdown analyses and several failure events were selected as limit states, which were then focused upon in the redundancy analyses in Chapter 7. Bridges with single member loss (as discussed in Chapter 4) were also pushed down and their response compared to the behavior of the corresponding intact bridges to evaluate the effect of member loss on pushdown capacity in the context of the selected limit states.

CABLE-STAYED BRIDGE

In order to evaluate the ultimate load-carrying capacity and redundancy of the cable-stayed bridge, pushdown analyses were conducted on the intact bridge and the damaged bridge after being subjected to single sudden cable loss. Because of similarity in the analysis process and results of the pushdown analyses under different live load patterns, detailed pushdown analysis results under live load pattern 01 are introduced in this chapter. The results under other live load patterns are similar and are not presented in this report.

Pushdown Analysis of the Intact Bridge

Prior to increasing the live load during the pushdown analysis, the intact bridge should be in its equilibrium state. Therefore, the behavior of the bridge under both dead and live loads was simulated first, as introduced in Chapter 3 and Chapter 4. Then the live load was gradually increased until the intact bridge reached its ultimate limit state. The entire pushdown analysis process was simulated by considering a global damping of 2% of critical damping. The rate of increase in live load during the pushdown analysis significantly affected the results. Faster loading rates caused large dynamic effects that led to premature failure. On the other hand, too slow of a loading rate caused the analysis to take an excessive amount of time. A sensitivity analysis was therefore conducted to determine an optimum live load increase rate. The results of pushdown analysis under different live load increase rates and their required simulation times are shown in Figure 138. Based on the sensitivity analysis, it was observed that the difference between live load increase rates of 0.1LL/second and 0.2LL/second is small, with a value of 0.6%. Hence, a live load increase rate of 0.2LL/second was selected for the simulation. The live load curve for the pushdown analysis of the intact cable-stayed bridge is shown in Figure 139.

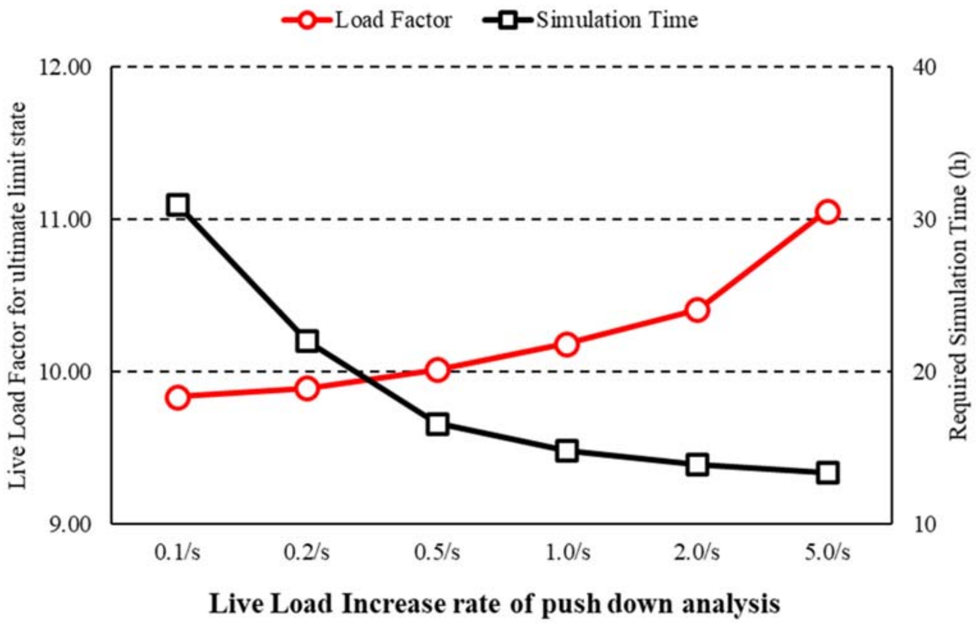

Source: FHWA.

Figure 138. Graph. Sensitivity of live load increase rate of pushdown analysis.

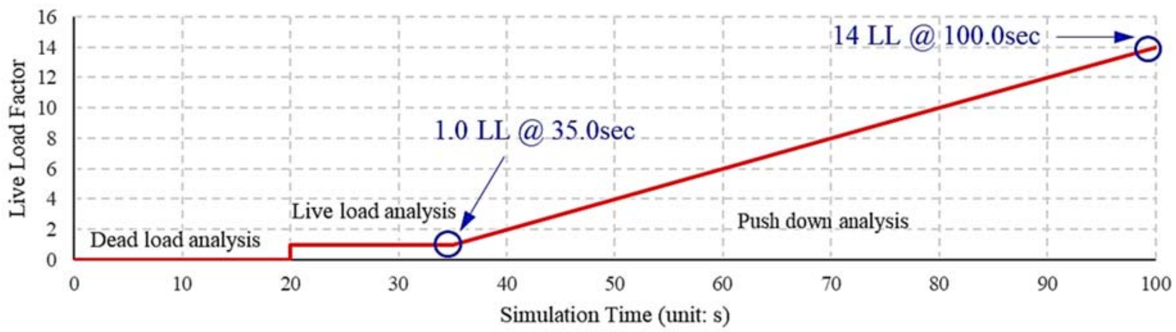

Source: FHWA

Figure 139. Graph. Live load curve of pushdown analysis of intact bridge.

Typical limit states and failure modes

Four typical limit states were identified as the live load was increased, as summarized in Table 27. A plot of the maximum vertical displacement of the deck with respect to the live load factor is shown in Figure 140. The first member failure limit state was cable yield. At this limit state, the first cable (Cable S.22) reached its yield strength at a live load factor of 7.95. The rate of displacement at the deck level remained steady after the first cable yielded. As the live load continued to increase, more cables yielded causing the main girder to become highly stressed as it lost support from the cables. When the first girder member yielded, which is the second limit state of interest, the maximum vertical displacement suddenly increased at a live load factor of 8.92. At this limit state, 46 cables had reached their yield strength. As the live load was further increased, more cables and girder members yielded, and the stiffness of the bridge decreased dramatically. The lateral bearing connecting the bridge pylon and girder failed when the live load factor reached 9.74, which was the third significant limit state. At this limit state, 80 cables had reached their yield strength. The first cable (Cable S.22) ruptured (the fourth limit state) when the live load factor reached 9.89 just after failure of the lateral bearing. With a further small increase in the live load factor, many more cables reached their ultimate strength and ruptured, leading to a collapse of the whole bridge. The collapsed state of the intact bridge is shown Figure 141.

Table 27. Typical limit states of pushdown analysis of the Cooper River Bridge.

Typical limit state	Live load factor	Displacement (feet)	Cable status
First cable yield	7.95	17.09	(1/128 cable yield)
First girder yield	8.92	20.42	(46/128 cable yield)
First lateral bearing failure	9.74	40.27	(80/128 cable yield)
First cable rupture	9.89	62.57	(84/128 cable yield)

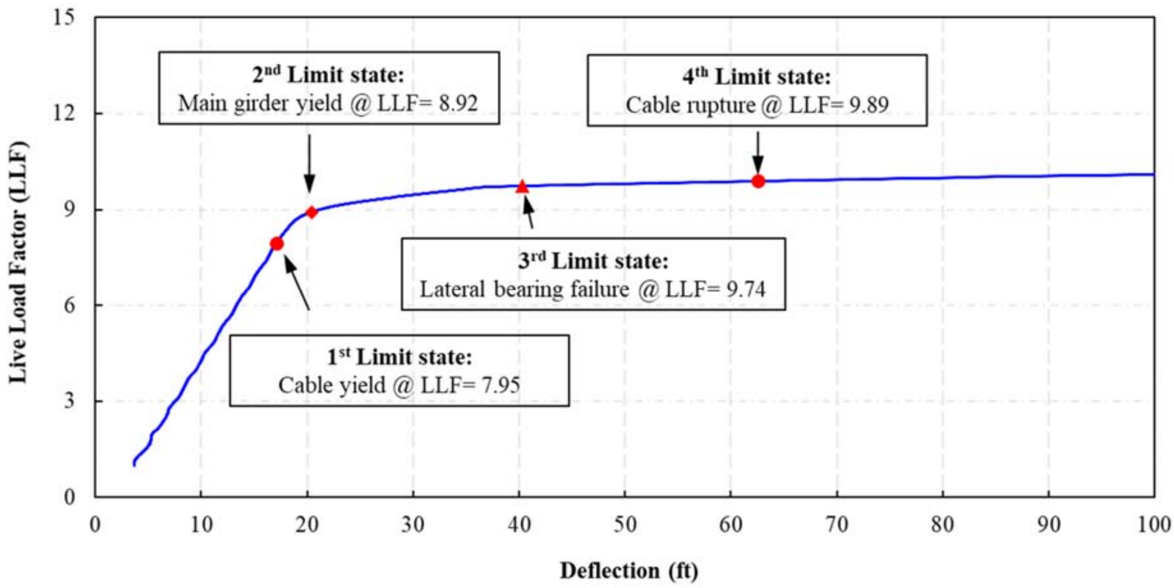

Source: FHWA.

Figure 140. Graph. Load-displacement curve of pushdown analysis of intact bridge.

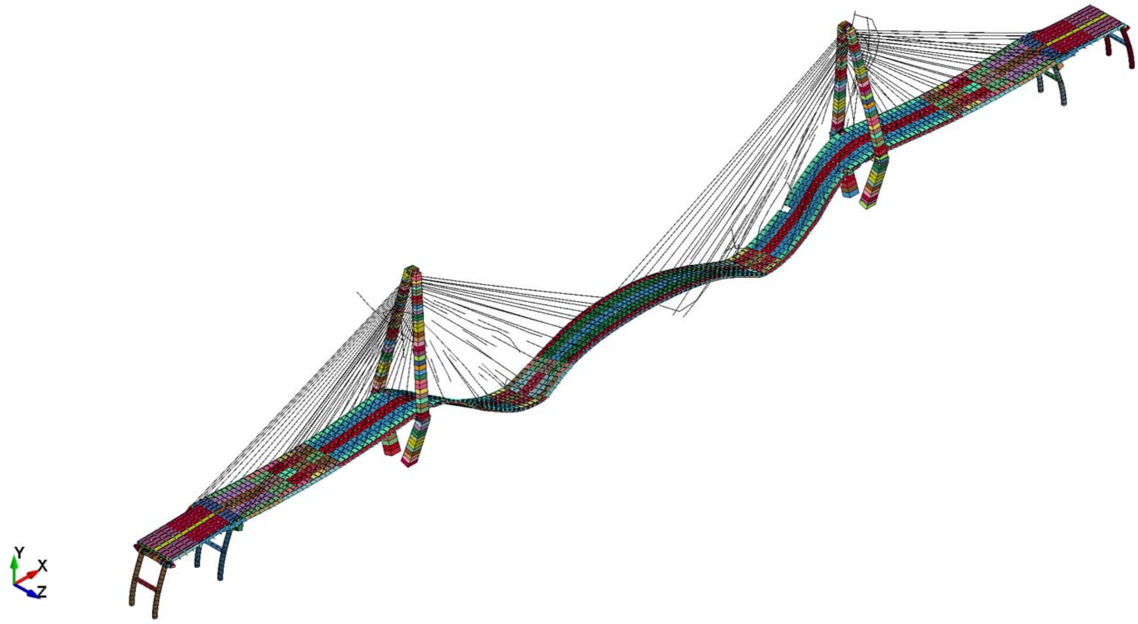

Source: FHWA.

Figure 141. Illustration. Ultimate progressive collapse state of the intact cable-stayed bridge under pushdown analysis.

Pushdown Analysis of the Damaged Bridge

Pushdown analysis was conducted for the damaged bridge. A single cable removal analysis was first performed after application of the dead and live loads. Once the bridge reached a new steady-state under the damaged condition, pushdown analysis was performed by increasing live load until the bridge reached its ultimate limit state. The rate of increase in live load in this case was chosen as 0.2LL/second as done for the intact bridge analysis. The overall simulation stages for the analysis are:

Stages 1-3: Application of dead and live loads till a simulation time of 30 seconds, as discussed earlier in Chapter 3 and Chapter 4.

Stages 4-6: Single cable removal analysis from 30 to 65 seconds, as discussed earlier in Chapter 4.

Stage 7: From 65 to 70 seconds, the large global damping was adjusted to the normal value of 2% of critical damping.

Stage 8: From 70 seconds onwards, pushdown analysis was conducted for the damaged bridge by increasing the live load at the rate of 0.2LL/second until the bridge collapsed.

The overall defined live load curve for the pushdown analysis of the damaged bridge is shown in Figure 142.

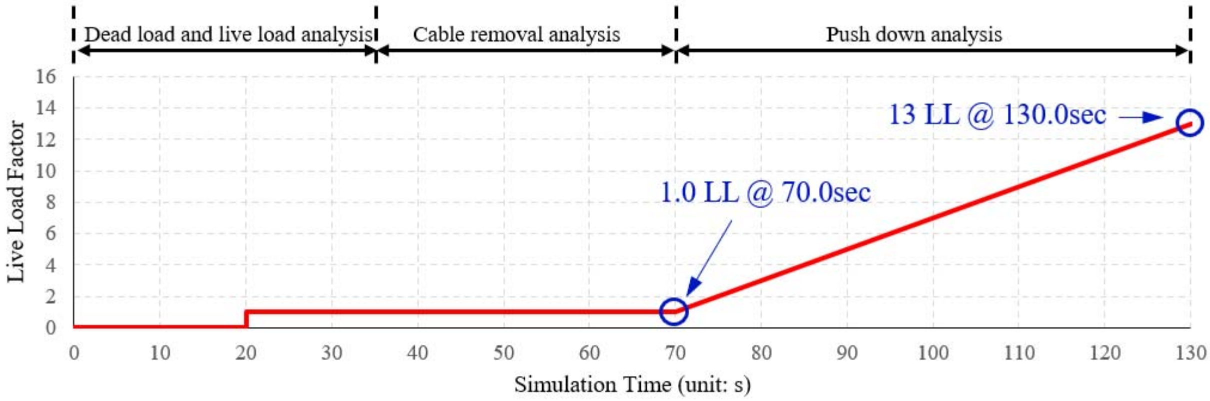

Source: FHWA.

Figure 142. Graph. Live load curve of pushdown analysis of damaged bridge.

Load factors of limit states

Pushdown analyses for the thirty-two single cable loss scenarios introduced in Chapter 4 were considered. The load factors for the four limit states identified earlier (first cable yield, first girder yield, first lateral bearing failure and ultimate collapse limit state) during the pushdown analysis of the damaged bridge are shown in Figure 143.

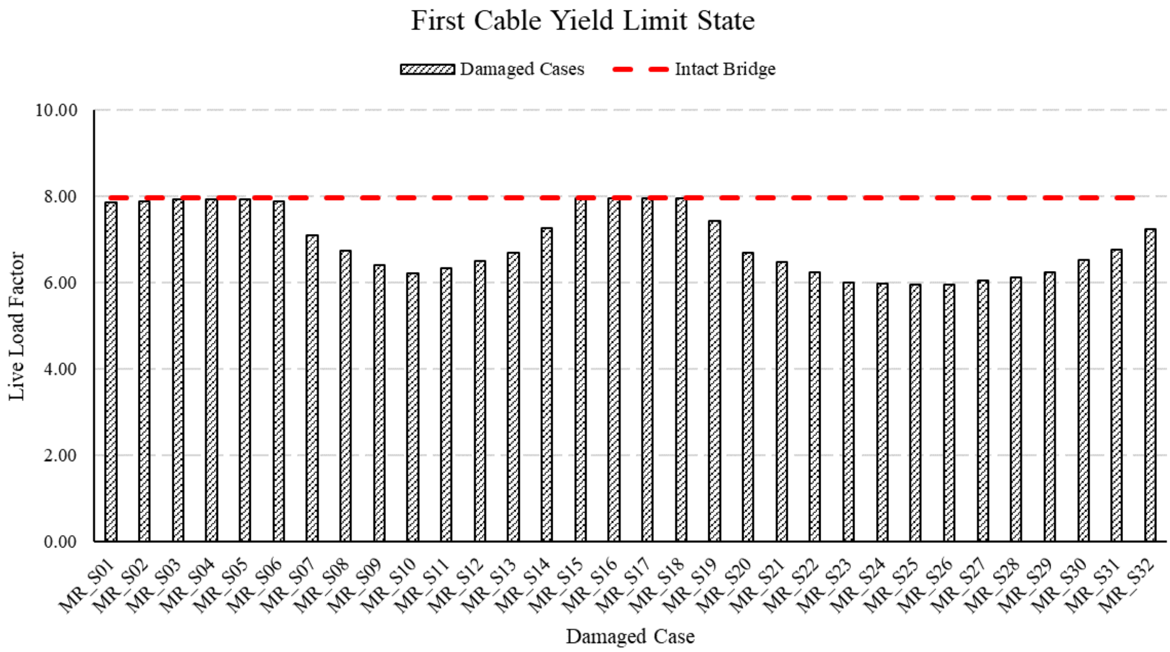

Source: FHWA.

(a) Live load factor of first cable yield limits state.

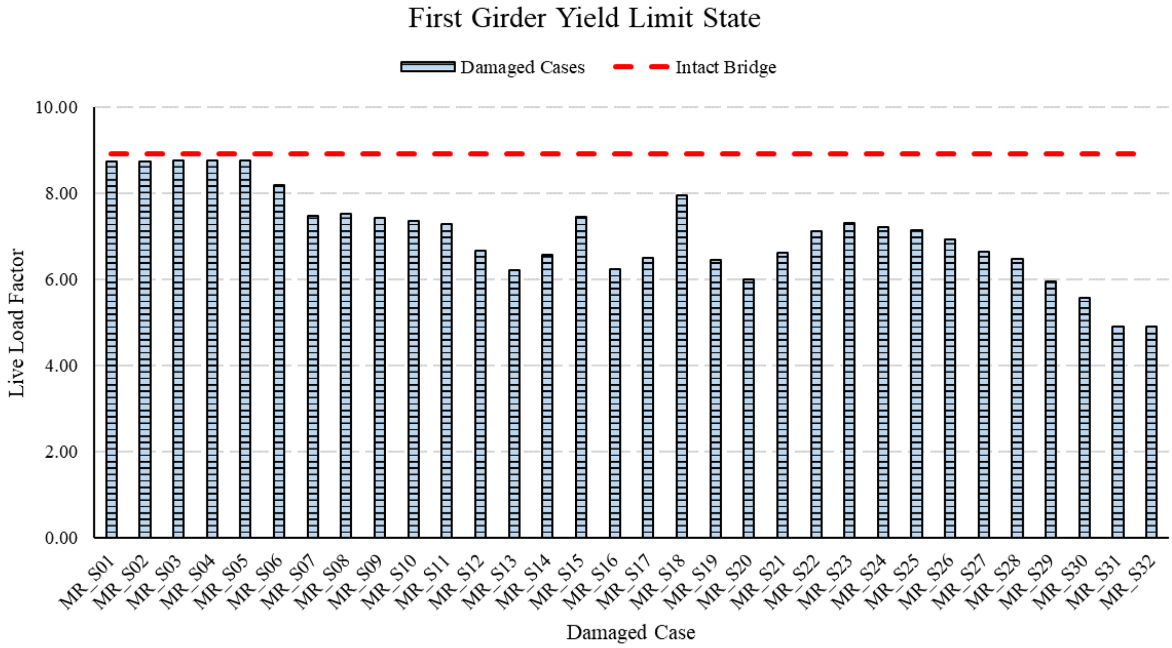

Source: FHWA.

(b) Live load factor of first girder yield limit state.

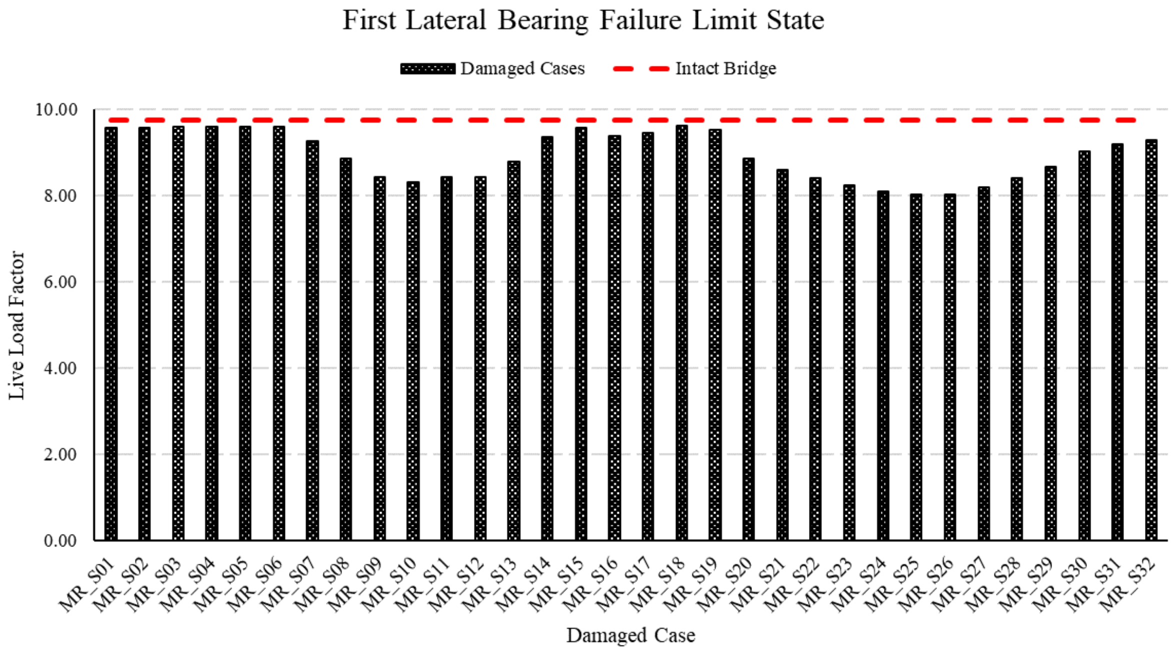

Source: FHWA.

(c) Live load factor of first lateral bearing failure limit state.

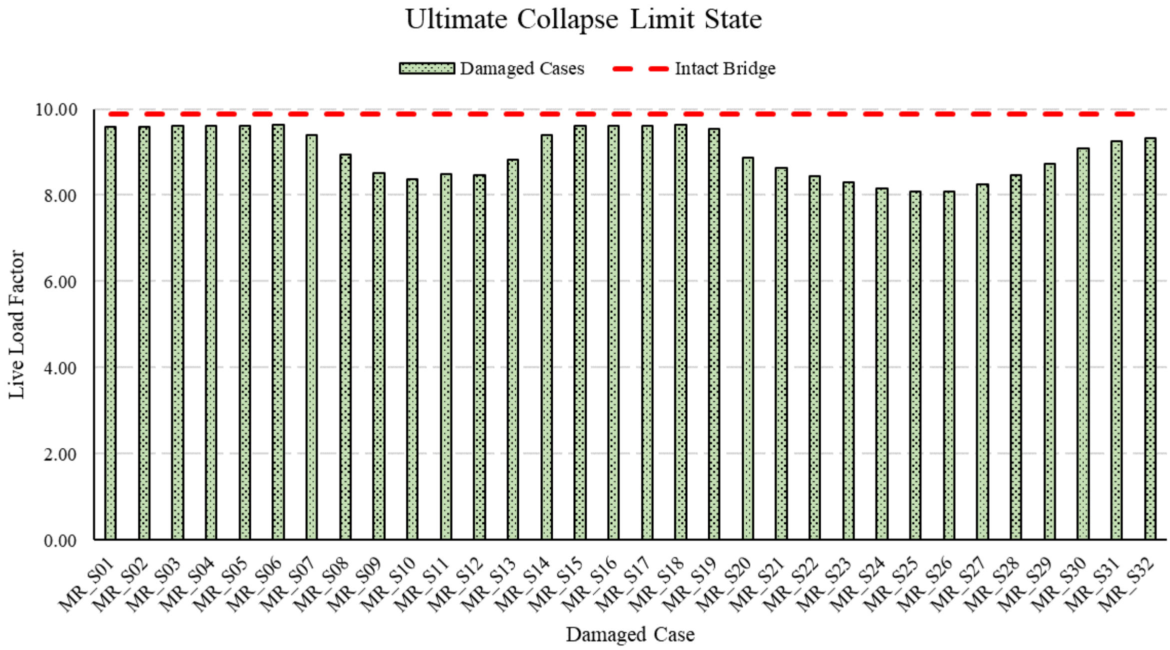

Source: FHWA.

(d) Live load factor of ultimate limit state.

Figure 143. Graphs. Pushdown analysis results of damaged bridge.

As shown in Figure 143, the live load factors corresponding to the various limit states show a similar trend. The loss of the longest cables at the side span (Cable S.01-S.06) had a relatively smaller effect on the live-load factor for the first cable yield, lateral bearing failure and ultimate collapse limit states, since these cables were near the support provided by the auxiliary pier. The loss of the cables near the bridge pylon (Cable S.15-S.18) also had a relatively smaller effect on these three limit states, because the cable forces in these cables were relatively smaller than the other cables. The loss of cables at the center of the side span and middle span caused a larger drop in the live-load factor for these three limit states. Loss of Cable S.10 in the side span and loss of Cable S.23-S.25 in the center span were the most critical cases with the lowest live load factors for the three limit states.

As shown in Figure 143(b), live load factors corresponding to first girder member yield limit state show a different trend. The loss of the longest cables at the side span (Cable S.01-S.06) had a relatively smaller effect on the live load factor for first girder member yield limit state, since these cables are near the support provided by the auxiliary pier. For other damaged cases with single cable loss, the live load factors corresponding to the first girder limit state were more related to the cable force in the suddenly removed cable, since the girder was supported by the cable. Loss of Cable S.31 and S.32 were the two most critical cases for this limit state.

TIED-ARCH BRIDGE

Similar to the cable-stayed bridge, pushdown analyses were conducted on both the intact and damaged (due to sudden single hanger loss) tied-arch bridge models. Based on the pushdown analysis results, typical limit states were identified for carrying out the redundancy analysis.

Pushdown Analysis of the Intact Bridge

As done for the cable-stayed bridge, live load was increased until both intact and damaged bridge reached their ultimate limit states. The live load was gradually increased until the bridge reached its ultimate limit state. The entire pushdown analysis process was simulated under a global damping of 2% of critical damping. As done earlier, a sensitivity analysis was conducted to determine the optimal live load increase rate. The results of these analyses are shown in Figure 144 and indicate that a live load increase rate of 0.2LL/second is reasonable. The overall live load curve for the pushdown analysis of the intact bridge is shown in Figure 145.

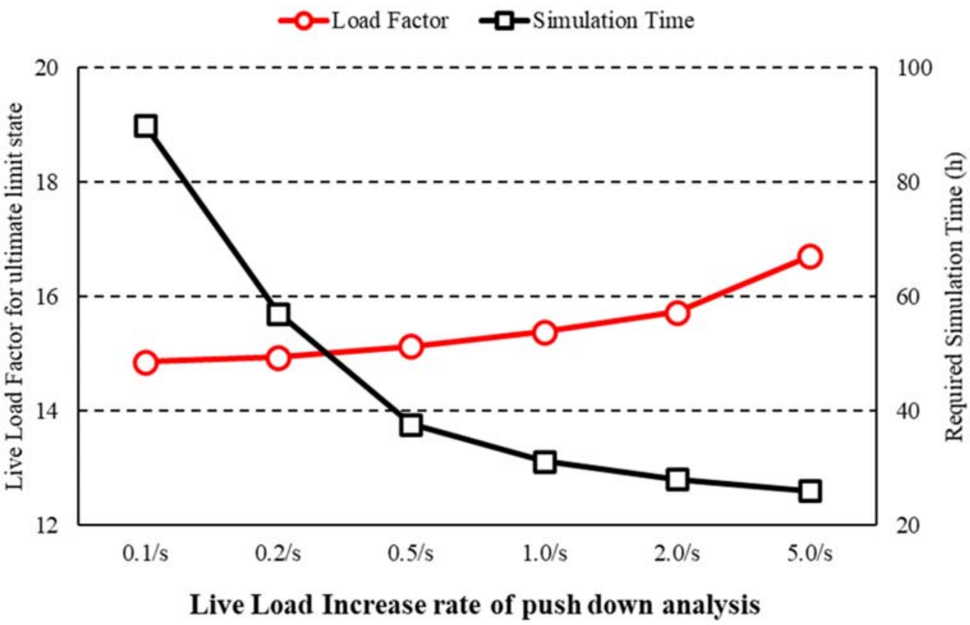

Source: FHWA.

Figure 144. Graph. Sensitivity of live load increase rate of pushdown analysis.

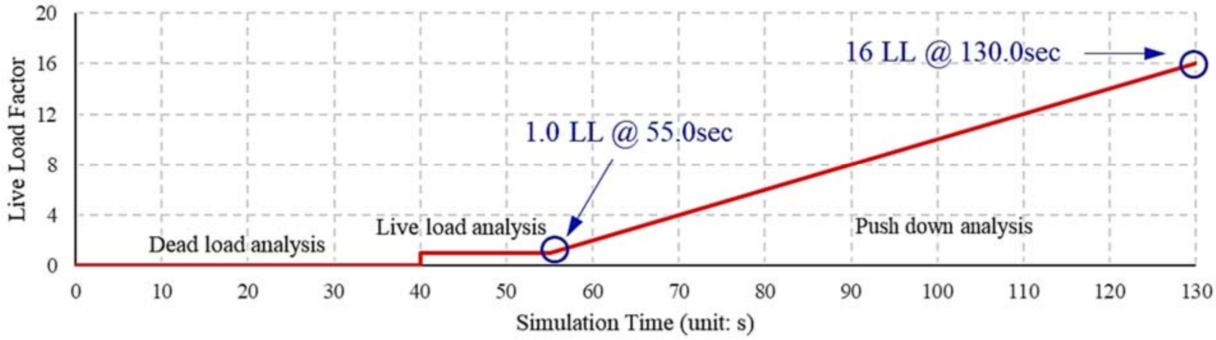

Source: FHWA.

Figure 145. Graph. Live load curve of pushdown analysis of intact bridge.

Typical limit states and failure modes

Three limit states were identified and shown in Figure 146, which plots the live load factor versus the maximum vertical deflection of the deck. The first limit state is hanger yield. The first hanger to reach its yield strength at a live load factor of 11.95 was W.03. As the live load was further increased, more hangers yielded and eventually the maximum vertical displacement increased suddenly as the live load factor reached 14.35. This corresponded to the second limit state-arch member yield. As the live load further increased, more hangers yielded and the yield zone in the arch spread causing the stiffness of the bridge to decrease significantly. Eventually, the third limit state was reached, i.e. hanger rupture. This occurred at W.03 at the live load factor of 15.01. With a small increase in live load factor at this point, many more hangers reached their ultimate strength and ruptured, leading to the collapse of the entire bridge. The girder members only reached their yield strength and ultimate strength after the bridge started to collapse. The collapse state of the intact tied-arch bridge is shown in Figure 147.

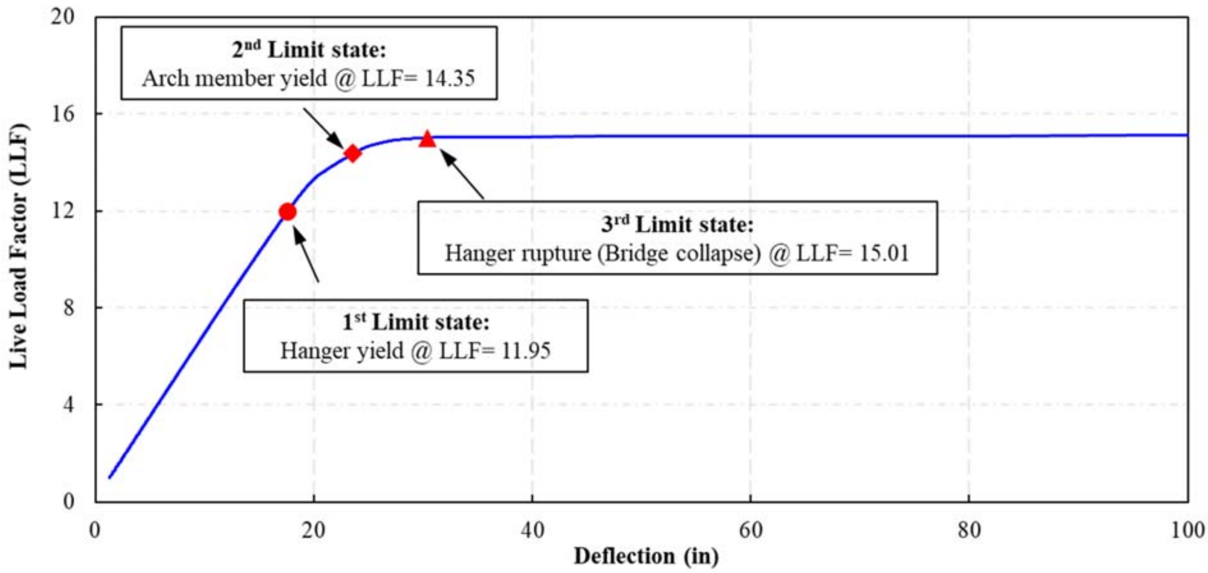

Source: FHWA.

Figure 146. Graph. Load-displacement curve of pushdown analysis of intact bridge.

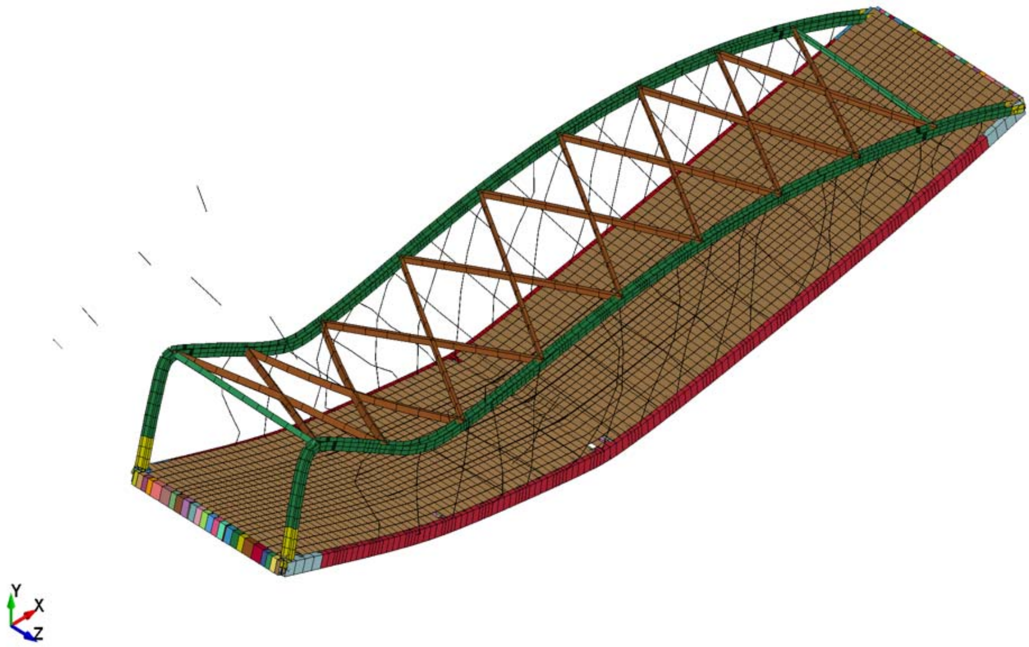

Source: FHWA.

Figure 147. Illustration. Ultimate progressive collapse state of the intact tied-arch bridge under pushdown analysis.

Deck behavior

As discussed earlier, the deck model accounts for concrete cracking in tension, concrete crushing in compression, and reinforcement yielding, hardening and fracture. The area of cracked deck elements as a percentage of the total area of the deck is computed and shown in Figure 148. It shows that the deck does not undergo cracking while the live load factor is below 4. As the live load exceeds this threshold, the deck starts cracking and the rate picks up when the live load factor reaches approximately 7. At the first hanger yield limit state, approximately 56% of the deck had undergone cracking. At the first arch member yield limit state, approximately 72% of the deck had undergone cracking. The overall deck cracking distribution at the first hanger yield limit state and the first arch member yield limit state are shown in Figure 149 and Figure 150, respectively.

In addition to the deck cracking behavior, deck damage behavior was also investigated. The deck is considered to be damaged or failed if the equivalent uniaxial compressive strain reached the concrete crushing strain (compressive failure) or the tensile strain in the reinforcement reached its yield strain. The deck damage percentage during the pushdown analysis is shown in Figure 151, where it is shown that the deck will only suffer damage after the bridge starts to collapse.

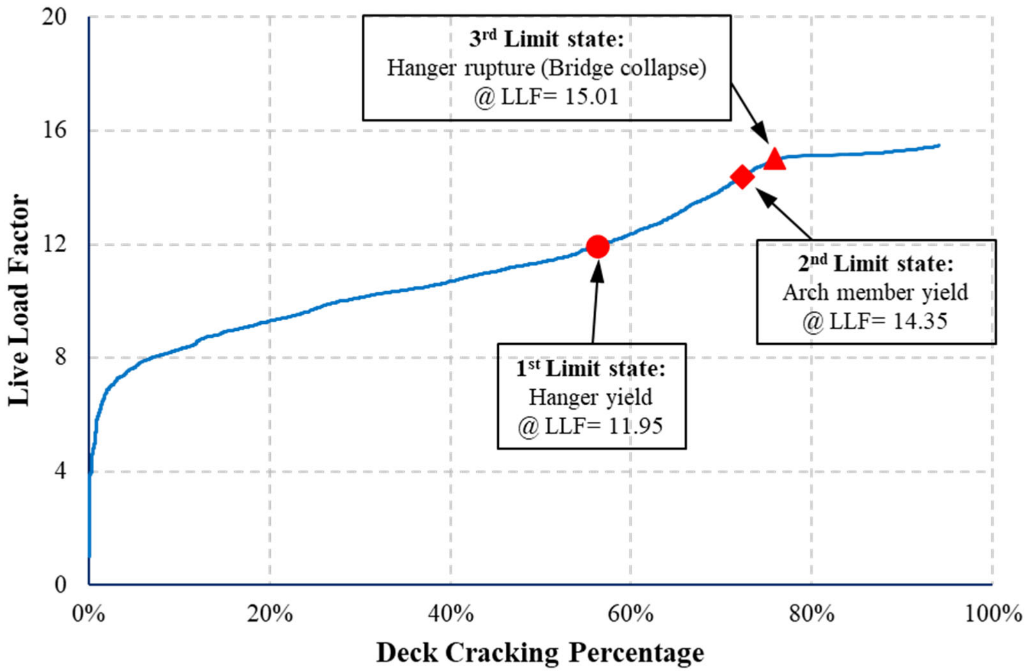

Source: FHWA.

Figure 148. Graph. Deck cracking percentage under pushdown analysis.

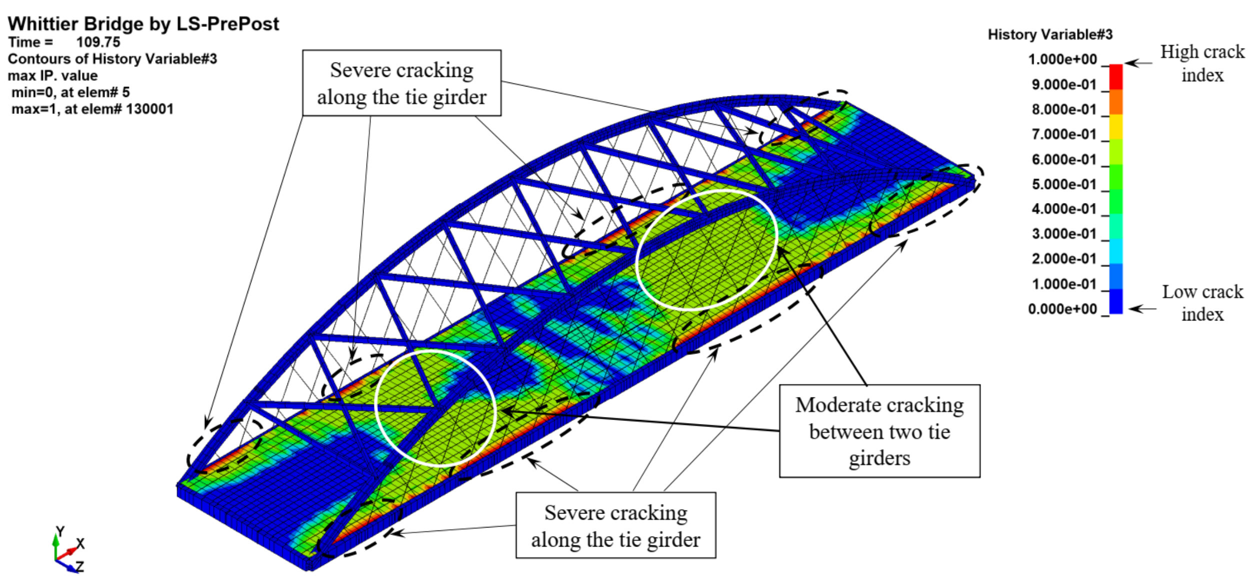

Source: FHWA.

Figure 149. Illustration. Deck cracking status at first hanger yield limit state.

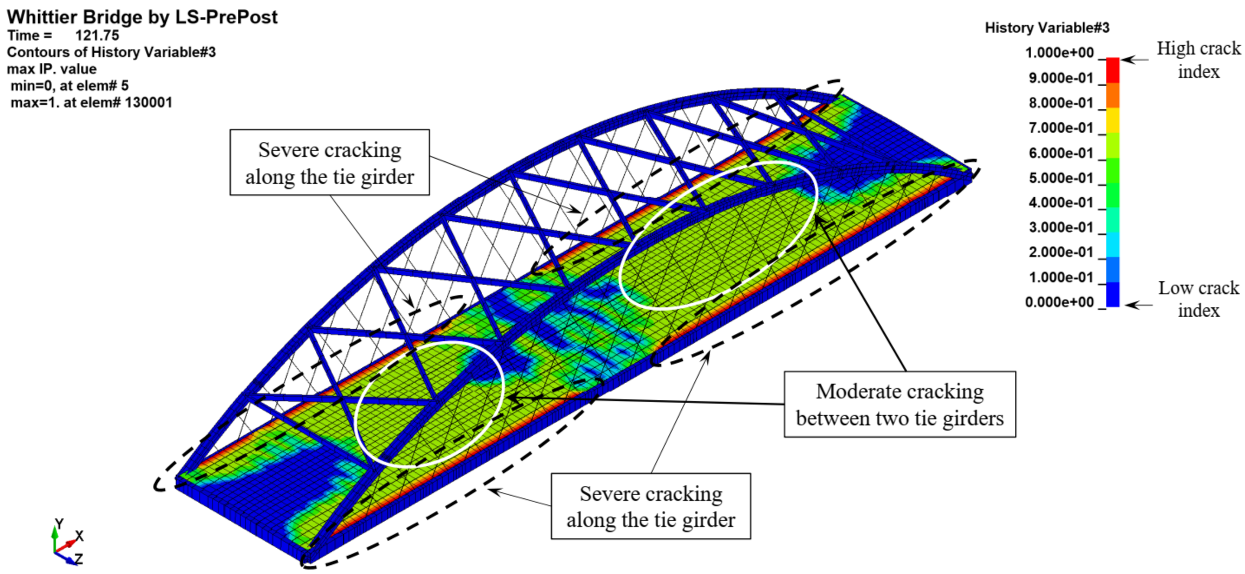

Source: FHWA.

Figure 150. Illustration. Deck cracking status at first arch member yield limit state.

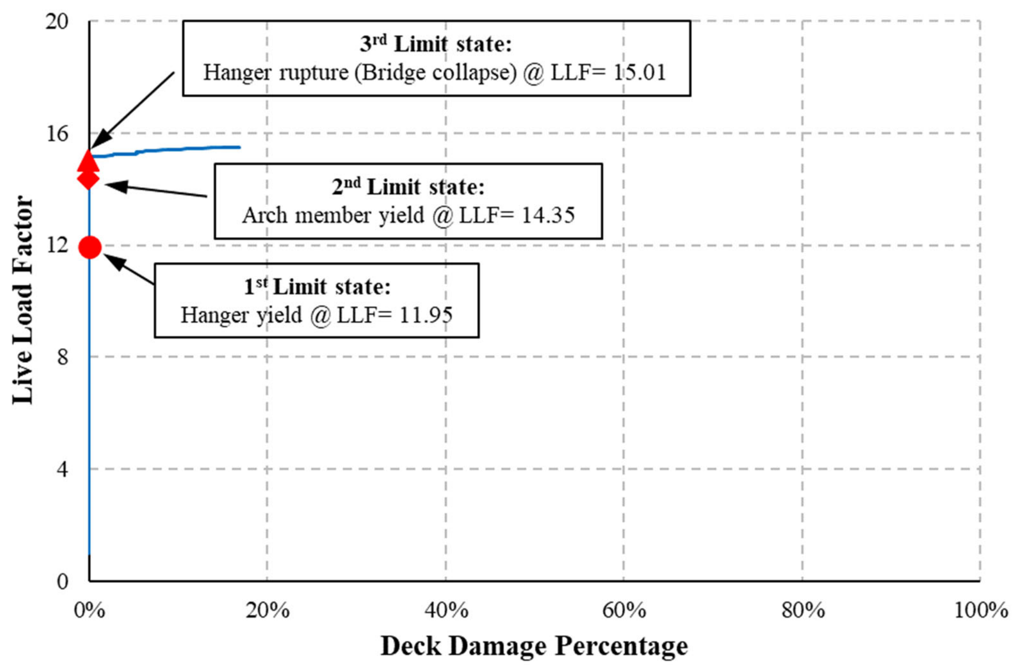

Source: FHWA.

Figure 151. Graph. Deck damage percentage under pushdown analysis.

Pushdown Analysis of the Damaged Bridge

Pushdown analysis was conducted for the damaged bridge. A single-hanger removal analysis was first performed after application of the dead and live loads. Once the bridge reached a new steady-state under the damaged condition, pushdown analysis was performed by increasing live load until the bridge reached its ultimate limit state. The rate of increase in live load in this case was chosen as 0.2LL/second as done for the intact bridge analysis. The overall simulation stages for the analysis are:

Stages 1-4: Application of dead and live loads until a simulation time of 50 seconds, as discussed earlier in Chapter 3 and Chapter 4.

Stages 5-7: Single hanger removal analysis from 50 to 75 seconds, as discussed earlier in Chapter 4.

Stage 8: From 75 to 80 seconds: The large global damping is adjusted back again to 2% of critical damping.

Stage 9: From 80 seconds: Pushdown analysis is performed on the damaged bridge by increasing the live load at the rate of 0.2LL/second until the collapse of the bridge.

The overall defined live load curve during the pushdown analysis of the damaged bridge is shown in Figure 152.

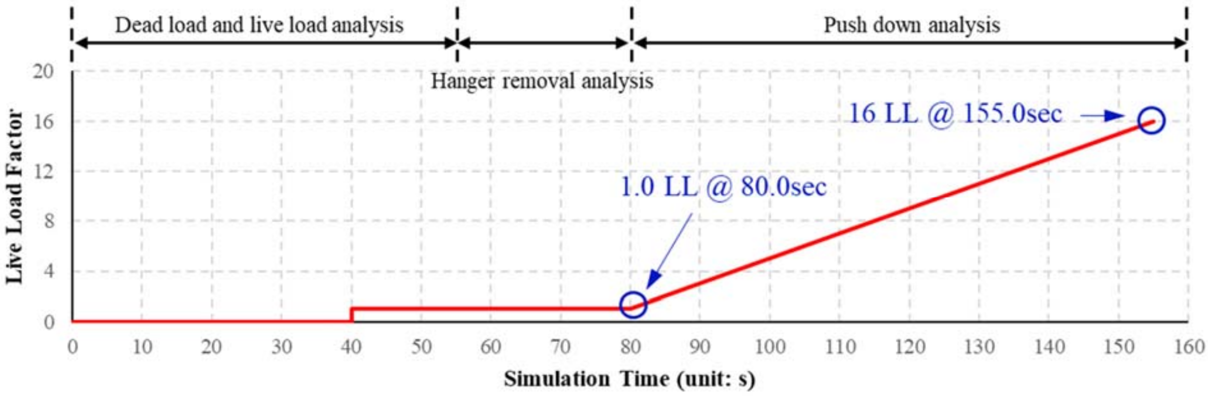

Source: FHWA.

Figure 152. Graph. Live load curve of pushdown analysis of damaged bridge.

Load factors corresponding to limit states

Pushdown analyses for the eighteen single hanger loss scenarios were considered. The eighteen single hanger loss scenarios were loss of W.01 to W.18. The load factors for the three limit states identified earlier during the pushdown analysis of the damaged bridge are shown in Figure 153.

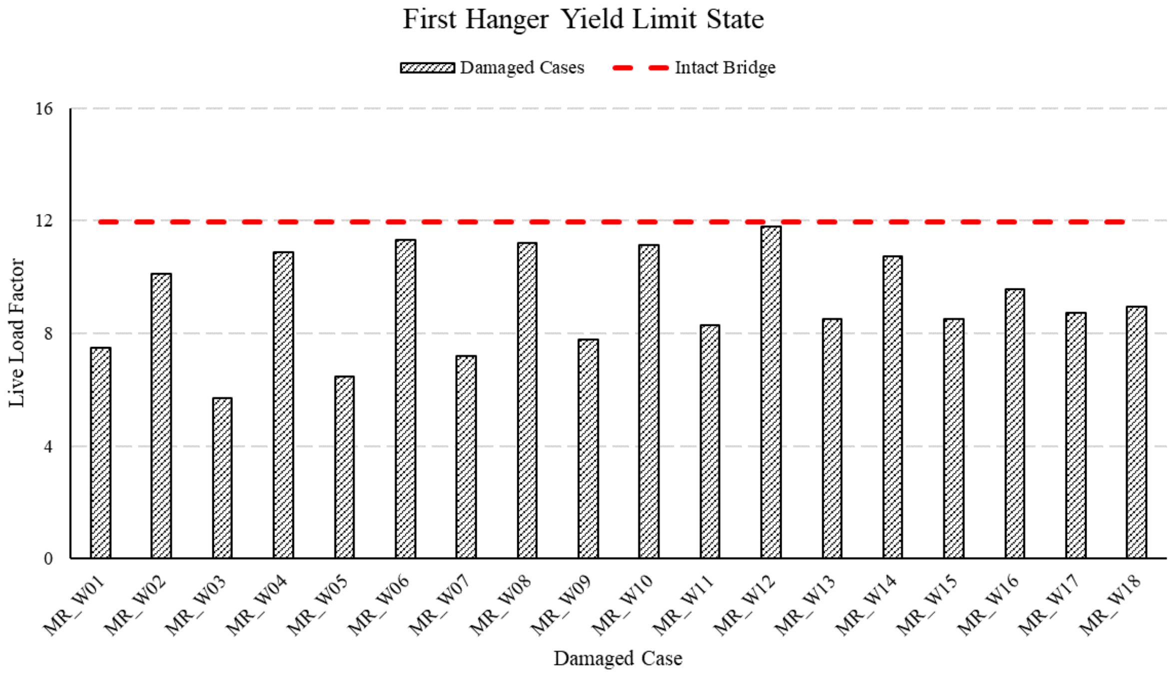

Source: FHWA.

(a) Live load factor of first hanger yield limits state.

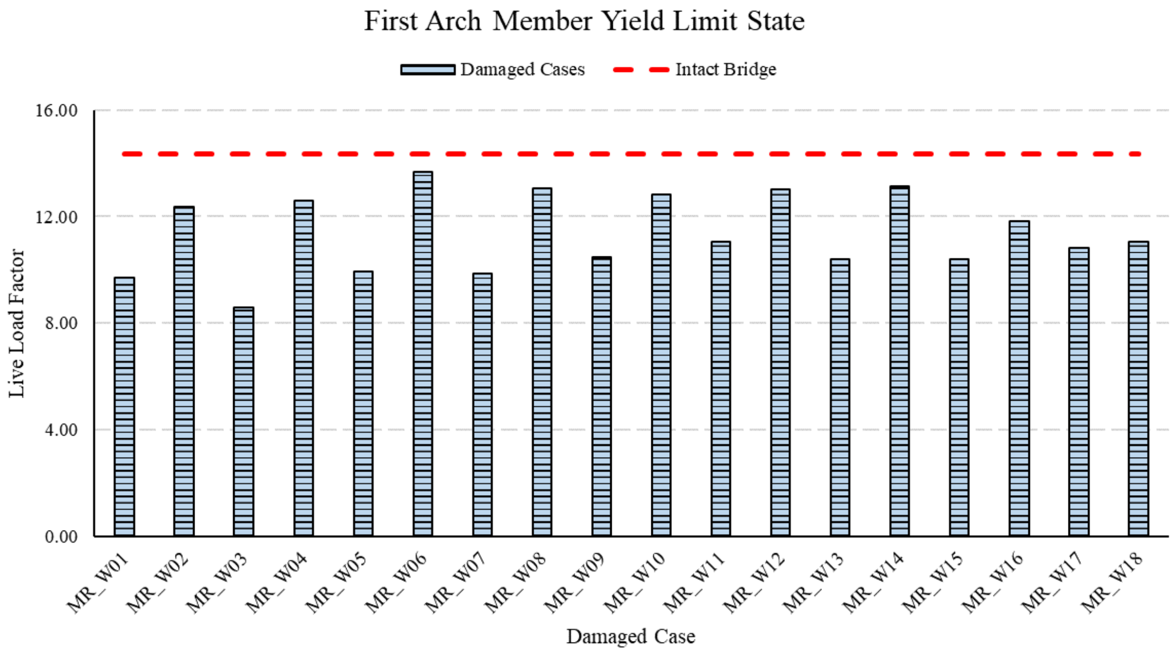

Source: FHWA.

(b) Live load factor of first arch member yield limits state.

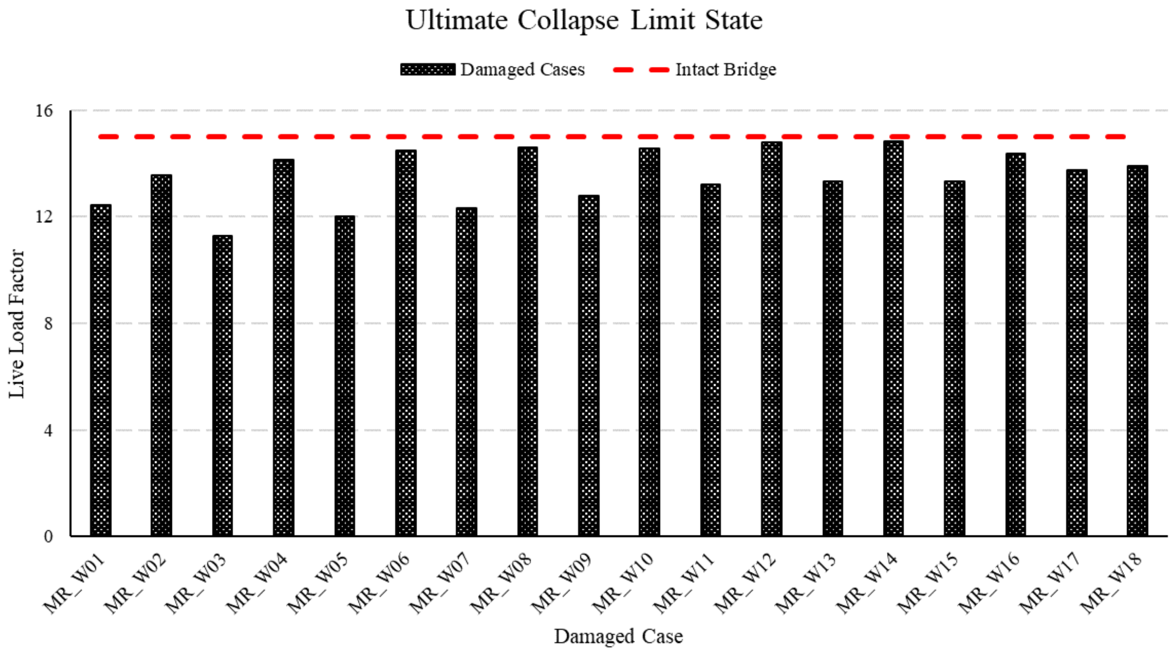

Source: FHWA.

(c) Live load factor of ultimate limit state.

Figure 153. Graphs. Load factor of pushdown analysis of damaged bridge.

The load factors corresponding to the first hanger yield, first arch yield and ultimate collapse limit states in Figure 153 show a similar trend for different hanger loss scenarios since these three limit states are correlated to each other. The simulations show that the arch moved upward during pushdown analysis and eventually yielded due to the combined effect of compressive force and biaxial bending moment in the arch member. Eventually, hangers reached their ultimate strength and underwent rupture, which eventually led to the collapse of the entire bridge. The loss of hangers slanted backwards, such as W.01, W.03, W.05, had a lower live load factor than loss of hangers slanted forward. Loss of the hangers in the middle was not as critical as the hangers in the end zone. Loss of W.03 was the most critical case with the lowest live load factor corresponding to the three limit states.

SUSPENSION BRIDGE

Pushdown analyses were conducted on the intact and damaged bridge subjected to single sudden cable loss in order to evaluate the ultimate load carrying capacity and redundancy of the suspension bridge. As done for the two earlier bridges, the live load was incrementally increased until the deflection of the bridge became extremely large and the bridge collapsed. The live-load distribution patterns LL1 to LL3, discussed in Chapter 4 previously, were investigated through the pushdown analyses.

Pushdown Analysis of the Intact Bridge

Following are the simulation steps during the pushdown analysis of the intact bridge:

1st Step: Dead load and live load analysis

Prior to increasing the live load during the pushdown analysis, the intact bridge should be in its equilibrium state. Therefore, the behavior of the bridge under both dead and live loads was simulated first. Similar to the simulations for sudden single suspender loss, both dead and live loads were applied together for the sake of reducing the computational time. Details can be found in Chapter 4. The live load was applied on the bridge within the first 2.0 seconds using the linear ramp curve shown in Figure 154(a), and the damping curve used to allow the bridge to reach the steady state quickly is shown in Figure 154(b). The simulation duration of the 1st step was set to 14.0 seconds based on trial simulations to achieve the steady-state.

2nd Step: Pushdown analysis

At the end of the 1st step, the live load applied on the bridge was increased gradually using the linear ramp curve shown in Figure 154(a). Initially, the live load factor (LLF) was increased linearly starting at t = 14.0 seconds at a rate of 1/3LL/second. After the LLF reached a value of 21.0 at t = 74.0 seconds, the increase rate was reduced to 1/10LL/second until t = 94.0 seconds, because the trial simulations showed that the bridge collapsed around a LLF of 23.0. This lower rate of increase in live load was selected to capture the ultimate state of bridge more accurately. Then, LLF was kept constant at a value of 23.0 until t = 120.0 seconds (the end of simulation time). During this step, the global damping of the bridge was kept constant at $\zeta = 2\%$.

Pushdown analysis simulations were conducted for the three cases of live loads following the steps described above. However, the loading curves and damping curve used during live load cases LL2 and LL3 were slightly different from those used during live load case LL1, as shown in Figure 155.

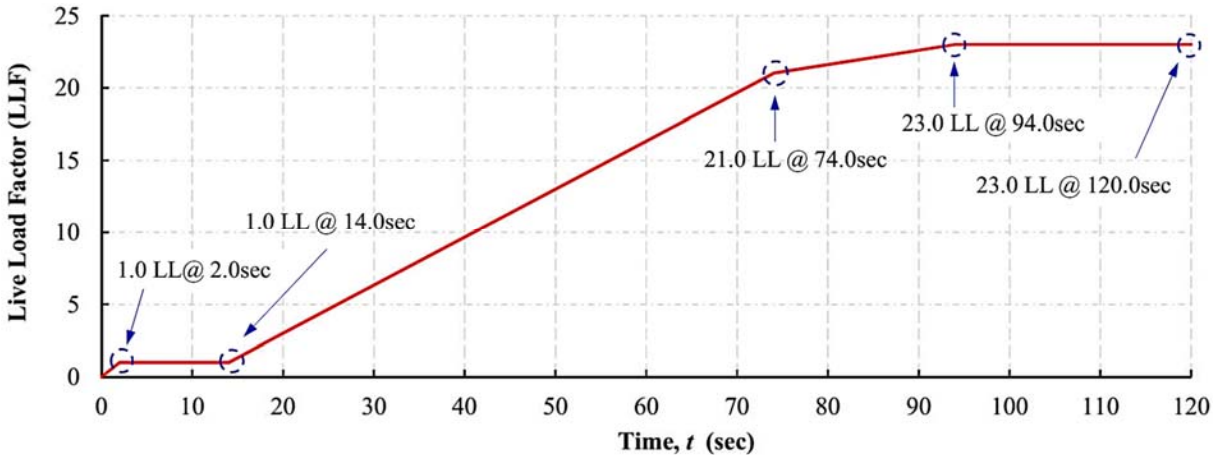

Source: FHWA.

(a) Loading curve.

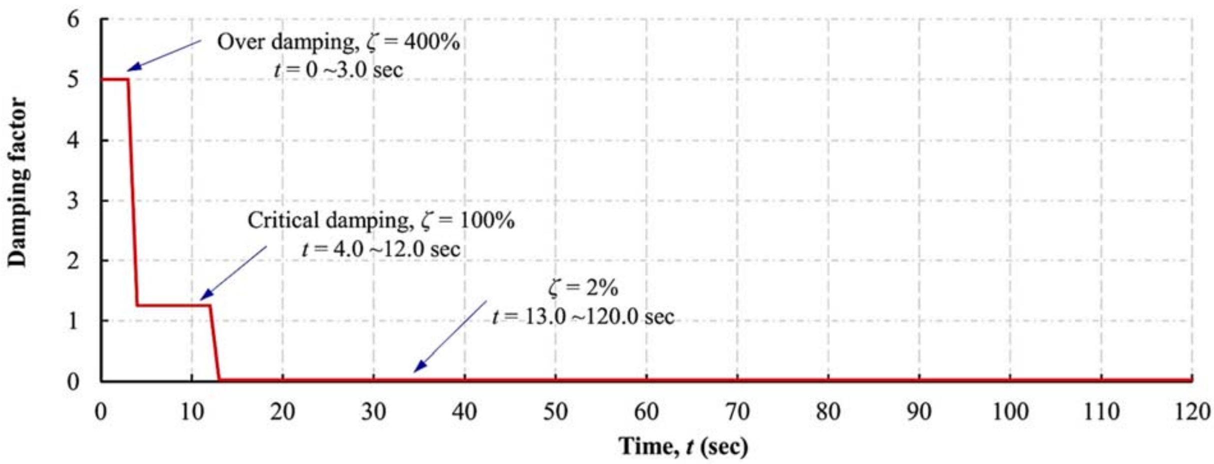

Source: FHWA.

(b) Global damping curve.

Figure 154. Graphs. Loading curve and damping curve for pushdown analysis of intact bridge under live load LL1 (case PDAI1).

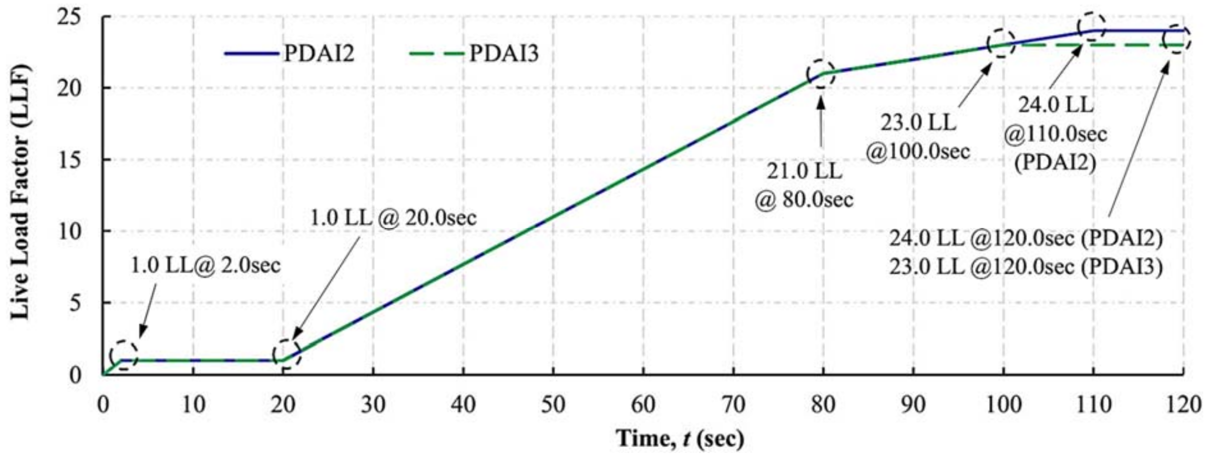

Source: FHWA.

(a) Loading curve.

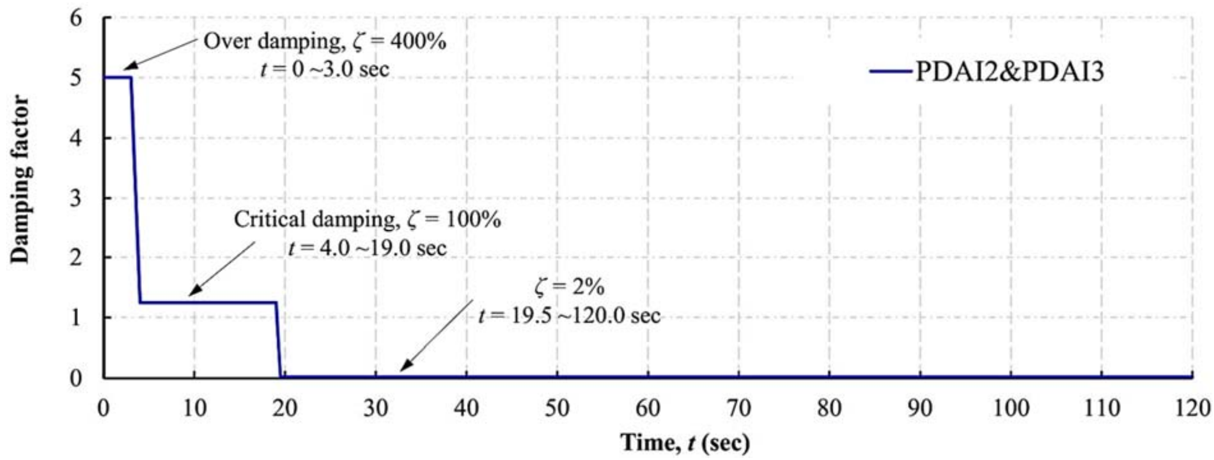

Source: FHWA.

(b) Global damping curve.

Figure 155. Graphs. Loading curve and damping curve for pushdown analyses of intact bridge under live load LL2 (case PDAI2) and live load LL3 (case PDAI3).

Pushdown Analysis of Intact Bridge under Live Load LL1 (Case: PDAI1)

Following the steps described above, pushdown analysis was conducted on the intact bridge for the LL1 case. With an increase in the live load, starting at simulation time of $t = 14.0$ seconds, both axial force in the main cables and the deflection of bridge increased till the main cable reached its ultimate capacity and ruptured at $t = 84.416$ seconds, which triggered collapse of the entire bridge. Before the collapse, the bridge had already experienced a large downward deflection, especially in the center span. The live load factor during the pushdown analysis is plotted against the maximum deflection of the bridge in Figure 156. Overall, the plot follows a "bilinear" behavior with the slope in the 1st stage (i.e., i.e., $1.0 \leq \text{LLF} \leq 8.25$, prior to main cable yield) being larger than that in the 2nd stage (i.e., $\text{LLF} > 8.25$, prior to main cable rupture). It is interesting to note that the bridge carried almost triple the live load that caused the main cable to yield prior to full failure of the system.

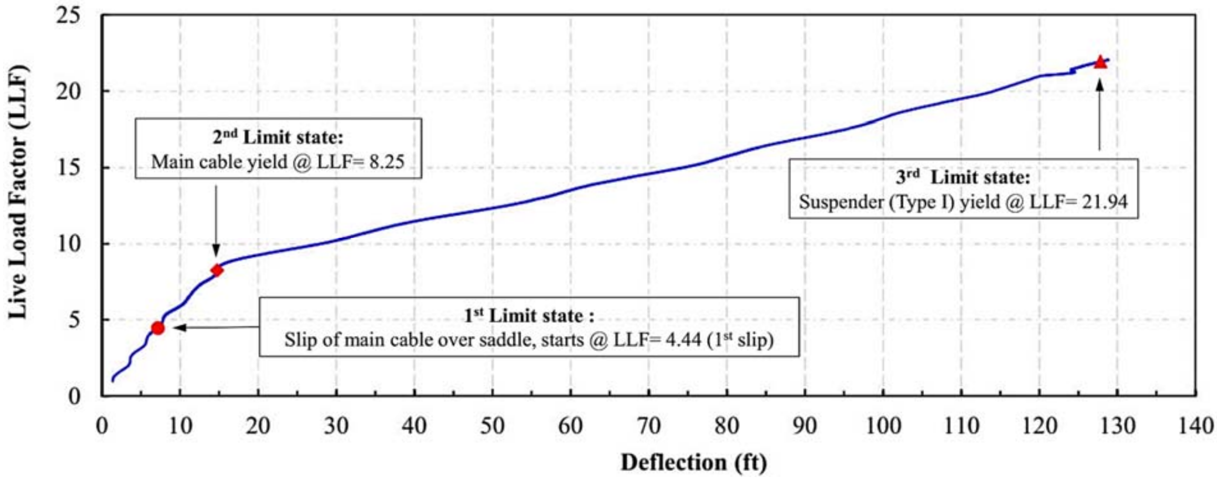

Source: FHWA.

Figure 156. Graph. Limit states for intact bridge during pushdown analysis - case PDAI1.

Table 28. Failure events for intact bridge during pushdown analysis - case PDAI1.

No.	Events	Deflection (feet)	LLF
1	**Slip of main cable over tower saddle, start (1st slip)**	7.14	4.44
2	**Yield of main cable**	14.75	8.25
3	Slip of main cable over tower saddle, end (1st slip)	14.82	8.32
4	Buckling of diagonal member, side span	15.22	8.59
5	Yield of top chord (type I)	40.63	11.53
6	Yield of bottom chord (Type II)	44.41	11.86
7	Yield of bottom chord (Type III)	44.73	11.89
8	Yield of bottom chord (Type I)	45.46	11.95
9	Buckling of diagonal member, main span	46.14	12.00
10	Buckling of tower link, main span	48.03	12.16
11	Yield of top chord (type II)	50.68	12.39
12	Yield of tower link buckling (Side Span)	78.42	15.50
13	Yield of vertical member (Type II)	103.19	18.71
14	Slip of main cable over tower saddle, start (2nd slip)	123.56	21.14
15	Slip of main cable over tower saddle, end (2nd slip)	124.45	21.21
16	**Yield of suspender (Type I)**	127.86	21.94
17	Rupture of main cable	128.86	22.04

The first member failure events captured during the pushdown analysis are summarized in Table 28 for live load LL1. For each type of structural components, only the 1st member failure is presented. As observed in Table 28, 17 failure events were captured for this load case.

The first failure event observed was the start of slip of the main cable over a tower saddle. In comparison with those on the side spans, more live load was applied on the center span during the pushdown analysis. This caused forces in the main cable in the center span to increase quicker than those in the side spans, especially in the cable segments around the towers. At lower live loads, there was no slipping of the main cable over the tower saddles because of friction. However, the unbalanced cable forces near the tower saddle increased gradually with a gradual increase in live loads and slipping initiated once the unbalanced forces breached the friction force threshold. Slipping over the saddles also led to readjustment in the cable configuration and internal axial forces. Once the unbalanced cable force fell below the friction threshold, slipping stopped and a rebalanced state of the cable configuration was achieved by the bridge.

For the live load case LL1, the slipping time-history of Main Cable 1 at Saddle 3 is plotted in Figure 157(a). It is observed from this figure that the main cable slipped three times during pushdown analysis. The plot of LLF against the slippage is shown in Figure 157(b). It is observed from this figure that the main cable started to slip for the first time when LLF increased from 1.0 to 4.44, and it continued to slip with increase of the live load until the slippage reached a value of 0.547 feet, because a rebalanced state was reached at LLF = 8.29. No further slipping occurred till the LLF reached 21.14, when the balanced state was again violated. The main cable slipped in this case until the slippage reached a value of 0.657 feet at LLF = 21.25. When the LLF was increased to 21.86, the main cable started to slip for the 3rd time until the LLF reached a value of 21.91. Finally, the main cable ruptured when the LLF reached a value of 22.04.

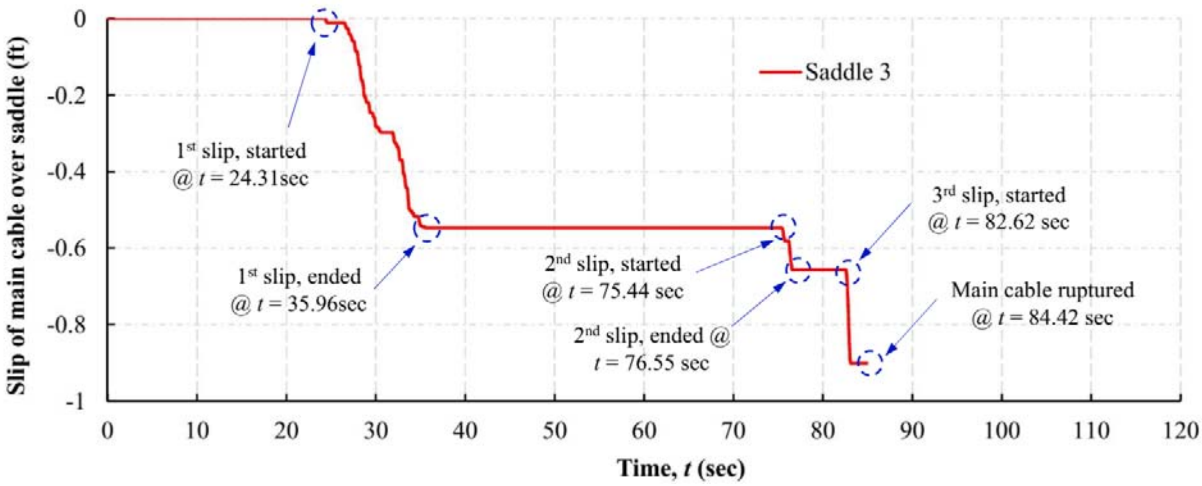

Source: FHWA.

(a) Slip time-history of Main Cable 1 over Saddle 3.

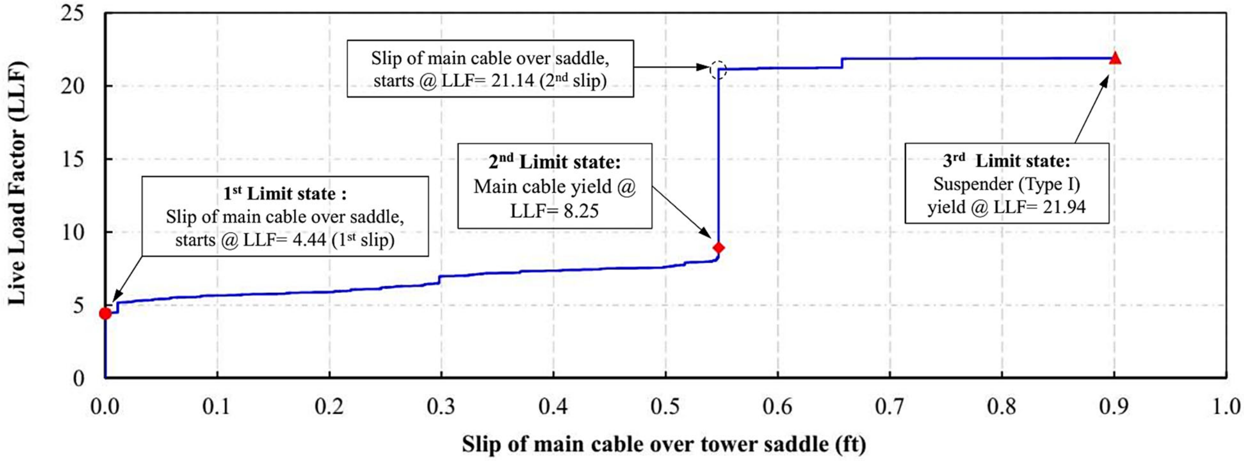

Source: FHWA.

(b) LLF vs. Slippage of Main Cable 1 over Saddle 3.

Figure 157. Graphs. Slip of main cable over tower saddle during the pushdown analysis of intact bridge - case PDAI1.

The second failure event observed was the yielding of the main cable, which occurred on cable segment MC60’ at a LLF of 8.25. The time history of the cable force in MC60’ (see Figure 158 for element location) during live load case LL1 is plotted in Figure 158. It is observed from this figure that the cable force in MC60’ increased with the increase of live load until it reached its yield force of 44,467 kips at t = 35.753 seconds, corresponding to LLF = 8.25. With further increase in live load, the cable force ruptured at its ultimate strength of 62,503.6 kips at t = 84.416 seconds, which is the 17th failure event listed in Table 28.

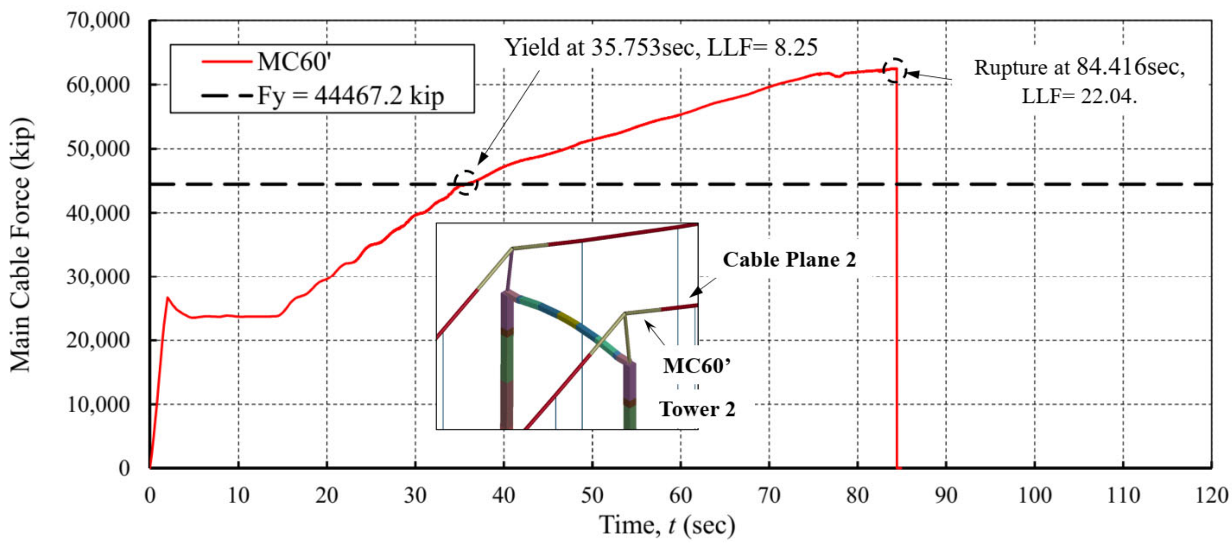

Source: FHWA.

Figure 158. Graph. Time history of cable force of segment MC60’ during the pushdown analysis of intact bridge - case PDAI1.

Axial forces in the suspenders were also monitored closely during the pushdown analysis. The time history of the axial force for suspender 28 is shown in Figure 159. As observed from this figure and Table 28, the first yielding occurred at LLF = 21.94 for type-I suspender 28. This LLF occurred just slightly before the collapse of the bridge. It is worth noting that the bridge had a large downward maximum deflection of approximately 128 feet at this point. All type-II suspenders behaved elastically during the entire pushdown analysis.

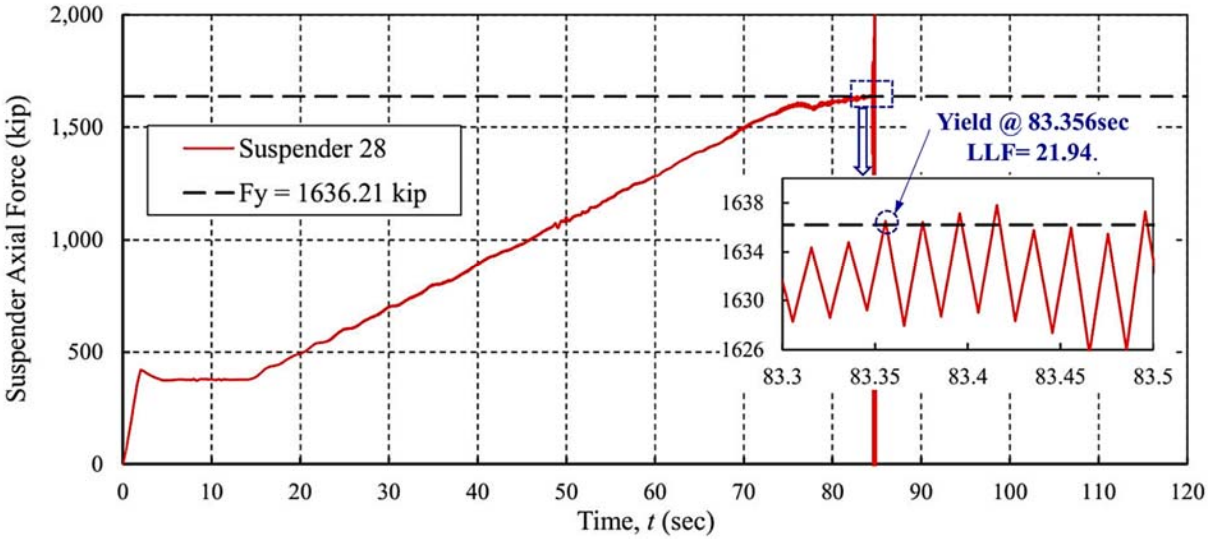

Source: FHWA.

Figure 159. Graph. Time history of axial force of suspender 28 during the pushdown analysis of intact bridge - case PDAI1.

The slipping of the main cable over a tower saddle was the first failure event related to key structural components that affected the behavior of the bridge significantly. Figure 156 shows that the bridge behavior changed significantly around LLF = 8.25 when the main cable yielded, which is also the 2nd event in Table 28. Thus, these two events were selected as limit states to investigate the bridge's redundancy in Chapter 7. In addition, although pushdown analysis for the live load case 1 shows that the yielding of a suspender occurred later than many other events in Table 28, a suspender is a key structural component that is vulnerable to sudden loss. Therefore, three events in total were selected as limit states: (i) slip of main cable over tower saddle, (ii) yielding of main cable and (iii) yielding of suspender.

Pushdown Analysis of Intact Bridge under Live Load LL2 (Case: PDAI2)

Under LL2, the side spans had a downward deflection whereas the center span had an upward deflection, as shown in Figure 160, since the live loads were only applied on side spans. These deflections continued to increase with increase in live loads, especially after the main cables in the center span started to slip towards side spans over the tower saddles. At this instant, the upward deflection in the center span was found to decrease temporarily because of slippage of the main cables, as shown in Figure 160(b). For the simulation start time until $t = 120.0$ seconds, the bridge did not collapse, although the bridge had extremely large deflections at this instant with the maximum downward deflection in the side spans being 47.25 feet and the maximum upward deflection in the center span being 59.53 feet. The sudden start of slipping of the main cable also caused the stiffening trusses in the center span to vibrate.

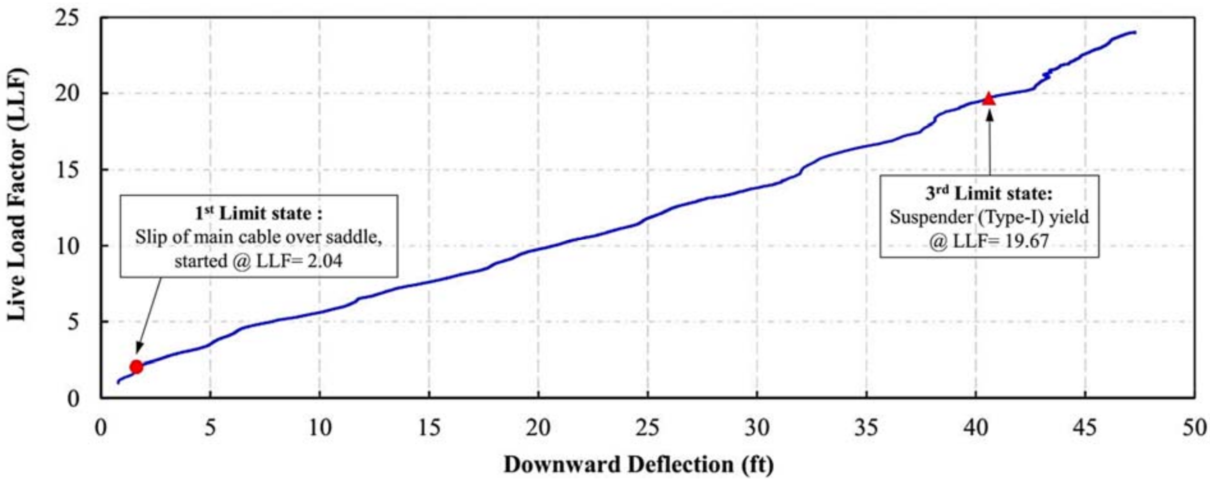

Source: FHWA.

(a) Side spans.

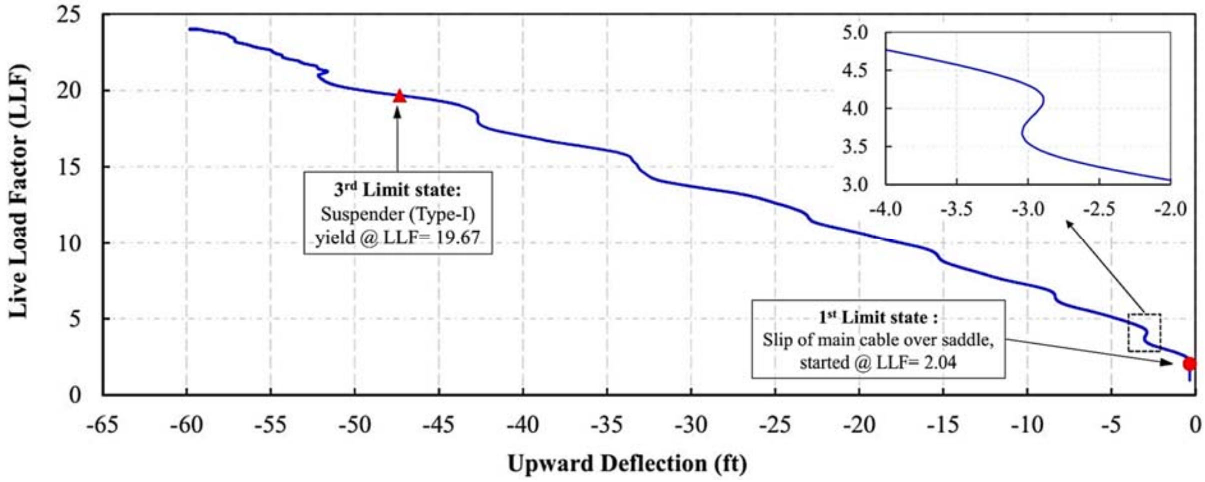

Source: FHWA.

(b) Center span.

Figure 160. Graphs. Limit states for intact bridge during the pushdown analysis - case PDAI2.

Unlike case PDAI1, only two limit states, the 1st and 3rd limit states, were observed during the pushdown analysis for LL2. The 1st limit state, i.e. slipping of main cable over tower saddle, occurred at LLF = 2.04. This limit state was reached much earlier than that in case PDAI1, since the unbalanced main cable force near the tower saddle increased more quickly in this case because of the increase of the live loadd on the side spans. The slippage time-histories of the main cables over the four tower saddles (i.e., pulley elements) are plotted in Figure 161(a). It is observed from this figure that the two main cables started to slip over the the four tower saddles simulatanously at t = 23.12 seconds and continued to slip until the end of simulation t =120.0 seconds. This is different from what occurred in case PDAI1, where the slippage occurred in spurts. LLF is plotted against the slippage of Main Cable 1 over Saddle 1 in Figure 161(b). It is observed from this figure that no slippage occurred before a LLF of 2.04 and afterwards, the slippage continued to increase monotonically with LLF.

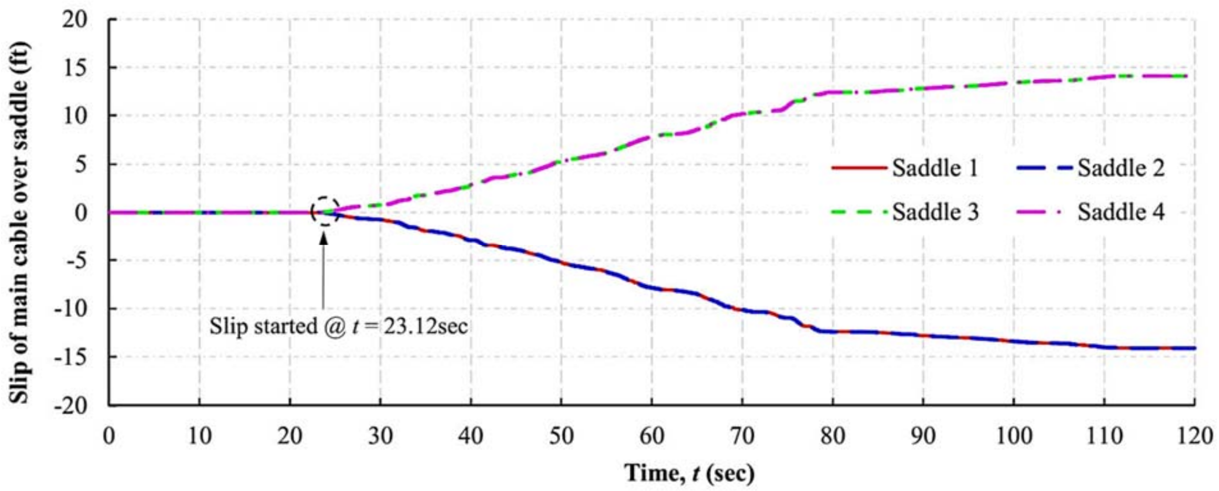

Source: FHWA.

(a) Slip time-history of main cable over saddles.

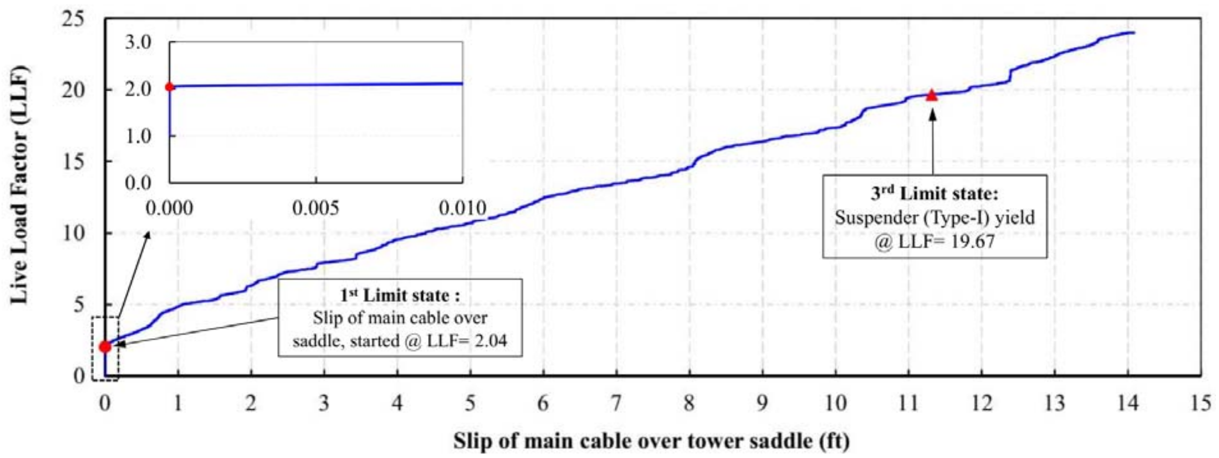

Source: FHWA.

(b) LLF vs. Slippage of Main Cable 1 over Saddle 1.

Figure 161. Graphs. Slip of main cable over tower saddle during the pushdown analysis of intact bridge - case PDAI2.

Another limit state reached during the pushdown analysis is the 3rd limit state-yielding of suspender, which occurred in suspender 15 near Tower 1 in the center span. The slipping of the main cables from the center span to the side spans caused the axial forces in four suspenders 15, 15’, 55 and 55’, to increase quicker than that in other suspenders. The axial force time-history for suspender 15 is plotted in Figure 162. It is observed from this figure that the suspender force reached the yield strength at t =76.02 seconds, corresponding to a LLF of 19.67 and it fluctuated around the yield strength until the end of the simulation.

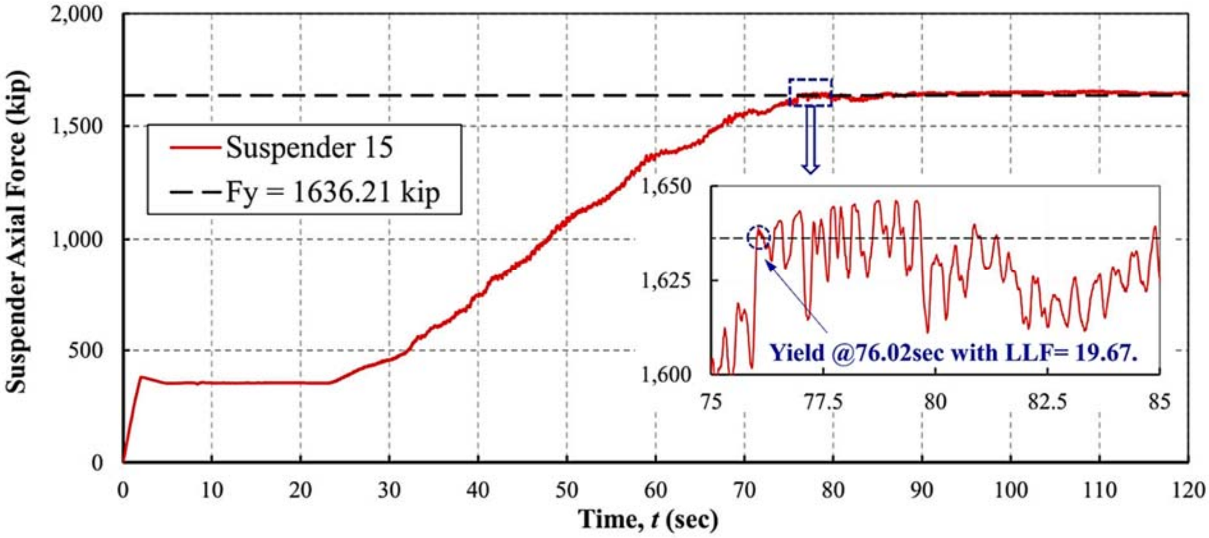

Source: FHWA.

Figure 162. Graph. Time history of axial force of suspender 15 during the pushdown analysis of intact bridge - case PDAI2.

Pushdown Analysis of Intact Bridge under Live Load LL3 (Case: PDAI3)

In this case, the center span had a downward deflection and the side spans had an upward deflection, since the live load was applied only on the center span. LLF is plotted against the maximum downward deflection in the center span and the maximum upward deflection in the side spans in Figure 163. The downward deflection in the center span is similar to that from pushdown analysis for live load case LL1, exhibiting an approximately "bilinear" trend with the two phases of linear behavior being distinguished by the 2nd limit state (i.e., yielding of main cable). However, the downward deflection increased more quickly in this case, since there was no live load on the side spans to counteract the slipping of the main cables from the side spans towards the center span. The trend of the upward deflection in the side spans is similar to that of the center span in LL2, but much smaller in magnitude. It increased quickly after the 2nd limit sate was reached and the maximum was -13.55 feet when the simulation was terminated at t = 103.71 seconds.

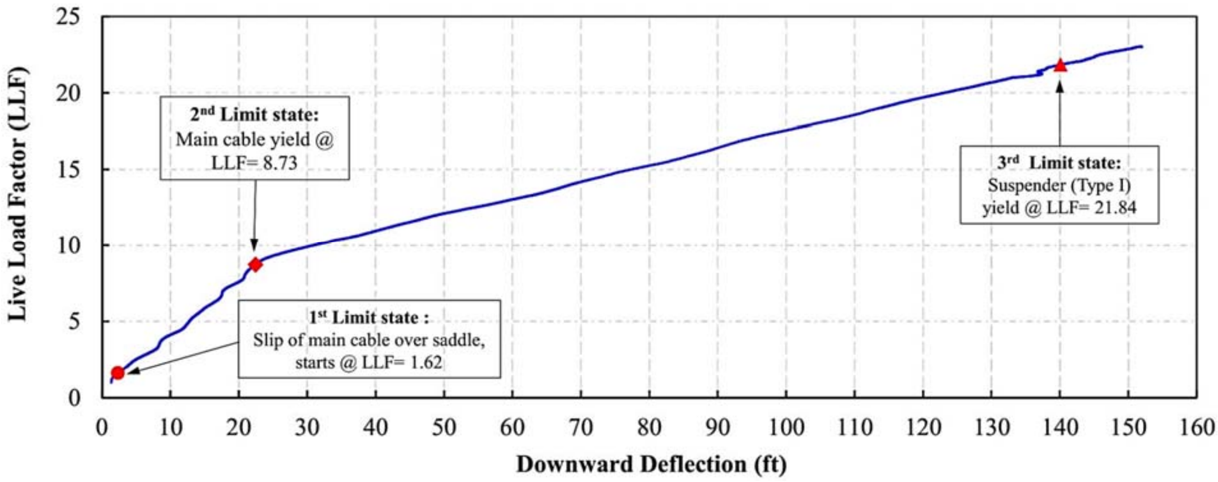

Source: FHWA.

(a) Center span.

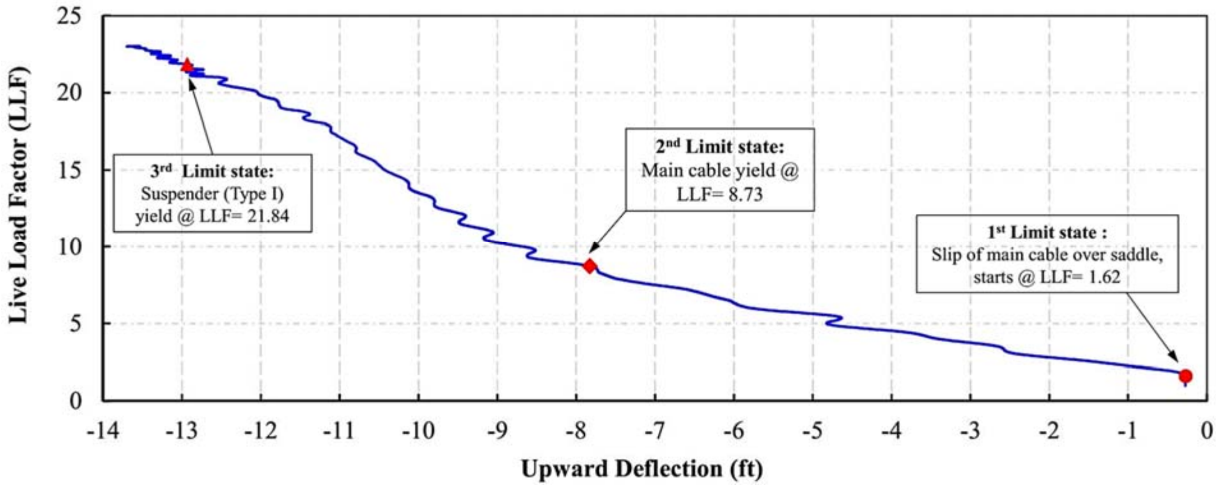

Source: FHWA.

(b) Side spans.

Figure 163. Graphs. Limit states for intact bridge during pushdown analysis - case PDAI3.

All the three limit states were reached during the pushdown analysis for LL3. Since there were no live loads on side spans, the unbalanced cable force at each tower saddle increased more quickly than that in case LL1. Therefore, the main cables were more prone to slipping from the side spans towards the center span over the tower saddles. The slippage time-history of the main cables at four tower saddles (i.e., pulley elements) are plotted in Figure 164(a). It is observed from this figure that the main cables started to slip simultaneously at t = 21.86 seconds, corresponding to a LLF of 1.62. After this, they continued to slip until the end of the simulation. LLF is plotted against the slippage of Main Cable 1 at Saddle 1 in Figure 164(b). It is observed from this figure that the slippage was faster after it reached 4 feet, corresponding to a LLF of 16.64.

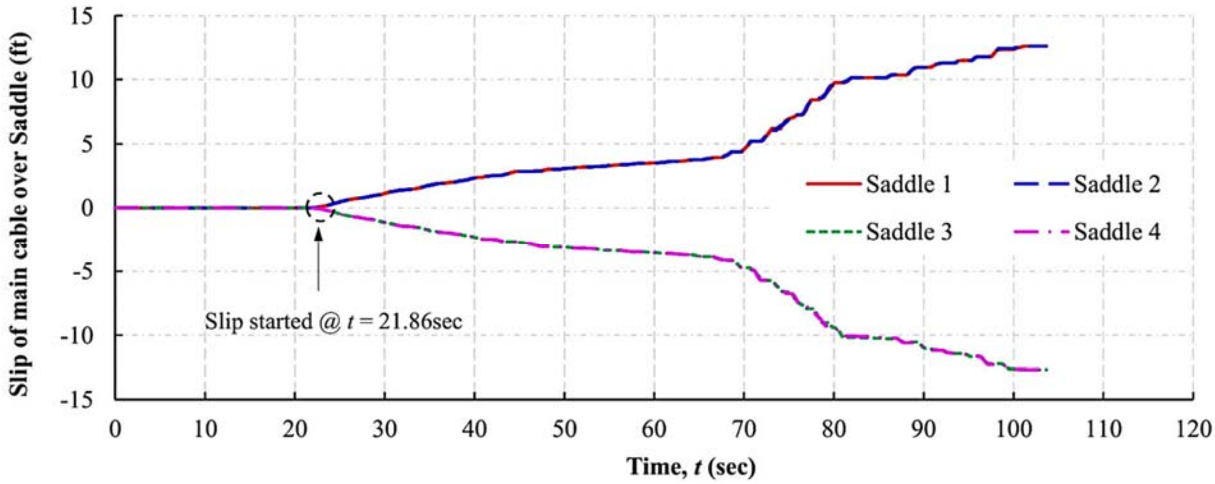

Source: FHWA.

(a) Slip time-history of main cables over saddles.

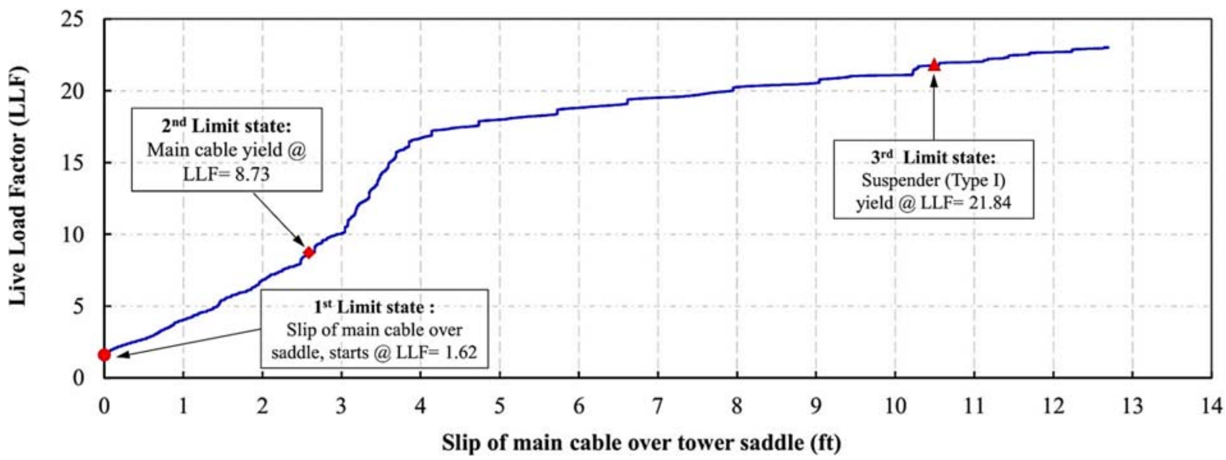

Source: FHWA.

(b) LLF vs. Slippage of Main Cable 1 over Saddle 1.

Figure 164. Graphs. Slip of main cable over tower saddle during the pushdown analysis of intact bridge - case PDAI3.

With an increase in live load on the center span, the axial force in the main cable in the center span increased quickly, especially for the cable segments near towers. The force time-history of segment MC60’ is plotted in Figure 165. It is observed from this figure that the cable force reached the yield strength at t = 43.187 seconds, corresponding to a LLF of 8.73.

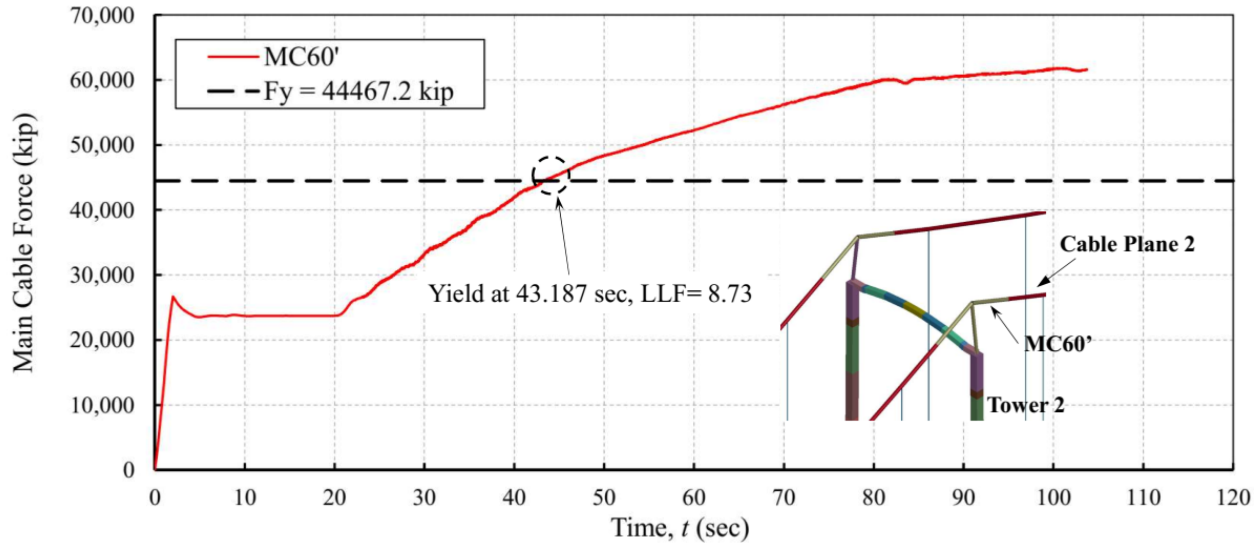

Source: FHWA.

Figure 165. Graph. Time history of cable force of segment MC60' during the pushdown analysis of intact bridge - case PDAI3.

Due to the slippage of the main cable, the axial force in the suspenders near towers in the side spans increased more quickly than others. During the pushdown analysis, the type-I suspender 14 yielded first at $t = 88.35$ seconds corresponding to a LLF of 21.84. The force time-history of this suspender is shown in Figure 166.

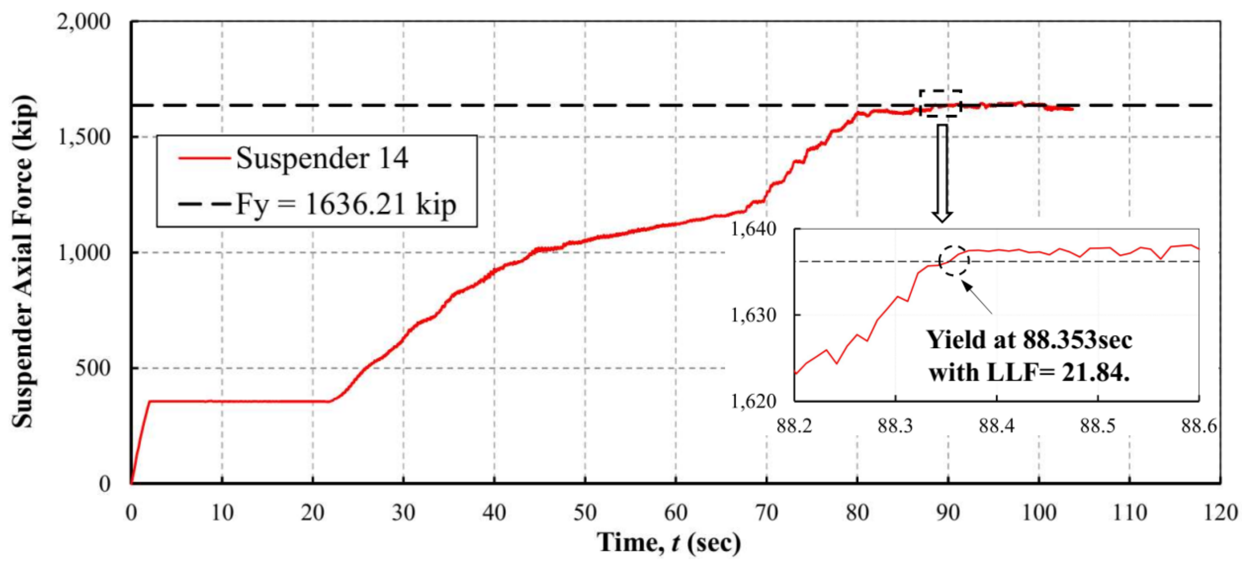

Source: FHWA.

Figure 166. Graph. Time history of axial force of suspender 14 during the pushdown analysis of intact bridge - case PDAI3.

Typical Limit States

Three limit states for the intact suspension bridge are summarized in Table 29, based on the sequence of their occurrence during the pushdown analyses. These limit states will be used for redundancy analysis of the bridge in Chapter 7.

Table 29. Limit states from pushdown analysis on the intact suspension bridge.

No.	Limit States	LLF		
		LL1	LL2	LL3
1	Slip of main cable over tower saddle	4.44	2.04	1.62
2	Yield of main cable	8.25	N.A.	8.73
3	Yield of suspender	21.94	19.67	21.84

Pushdown Analysis of the Damaged Bridge

Following the stimulation steps described for the intact bridge, pushdown analysis was also conducted on damaged suspension bridges, i.e., after they suffered single sudden suspender loss. All 35 suspender-loss scenarios discussed in Chapter 4 were investigated for three live-load distribution patterns LL1 to LL3. The suspender loss was simulated using the member removal process described in Chapter 4, and the lost suspender was removed when the 1st simulation step was almost finished, i.e., at t = 12.01 seconds for the bridge under LL1 and at t = 18.01 seconds for the bridge under LL2 and LL3. Pushdown simulation cases on the damaged bridge are termed "PDADX-SRY", in which X represents the live load pattern and Y is the ID number of the removed suspender. For example, case PDAD2-SR20 means the pushdown analysis of the bridge with suspender 20 removed under the live load pattern LL2. The three limit states identified in the pushdown analysis of the intact bridge are also used for the pushdown analysis of the damaged bridge.

Pushdown Analysis of the Damaged Bridge under LL1 (Cases PDAD1-SR01~35)

Similar to the pushdown analysis of the intact bridge under LL1, all three limit states were reached for all damaged bridge cases under LL1. The live load factors for these limit states are plotted in Figure 167 to Figure 169, including the relative difference with respect to the LLF of the intact bridge under LL1 (i.e., case PDAI1).

For the 1st limit state, the LLFs of all damaged bridge cases are in a narrow range of 4.35 to 4.45, very close to the LLF of the intact bridge. The relative differences are less than 2.0%, as shown in Figure 167. For the 2nd limit state, the LLFs of the damaged bridge are in the range of 8.13 to 8.32. They are also very close to the LLF of intact bridge with the maximum relative difference being around 1.5%, as shown in Figure 168. Hence, single suspender loss has little effect on the 1st and 2nd limit states of the bridge under LL1.

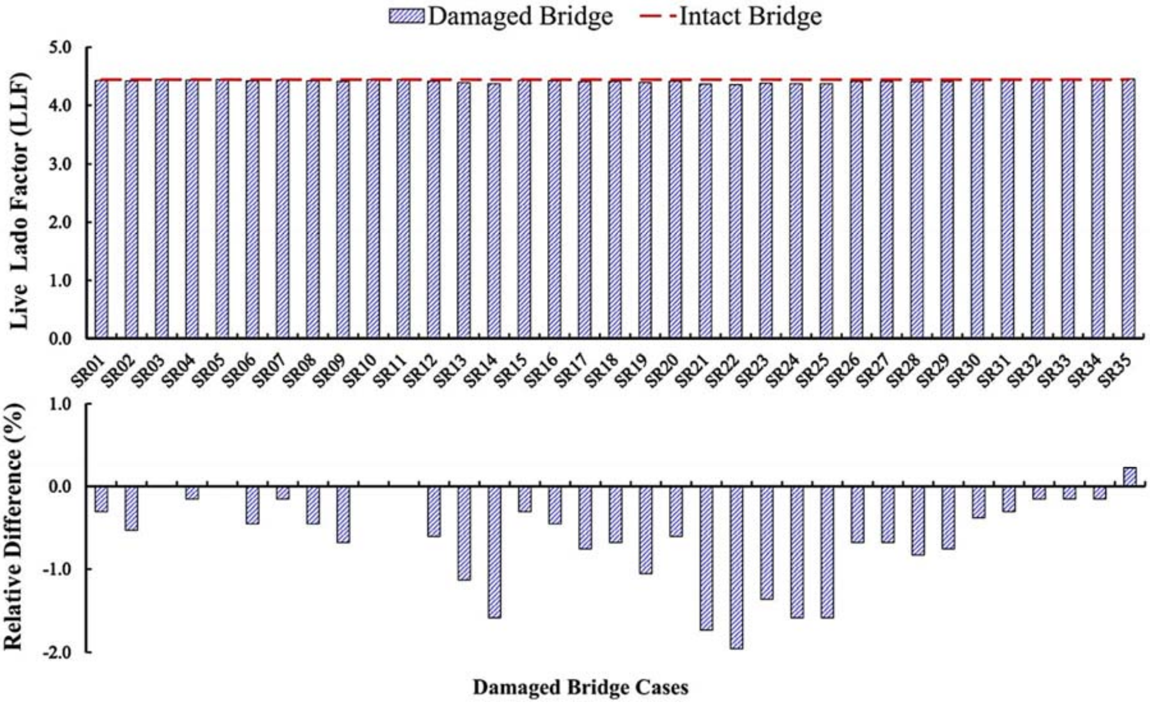

Source: FHWA.

Figure 167. Graph. Live load factor of 1st limit state of damaged bridge during pushdown analyses – cases PDAD1.

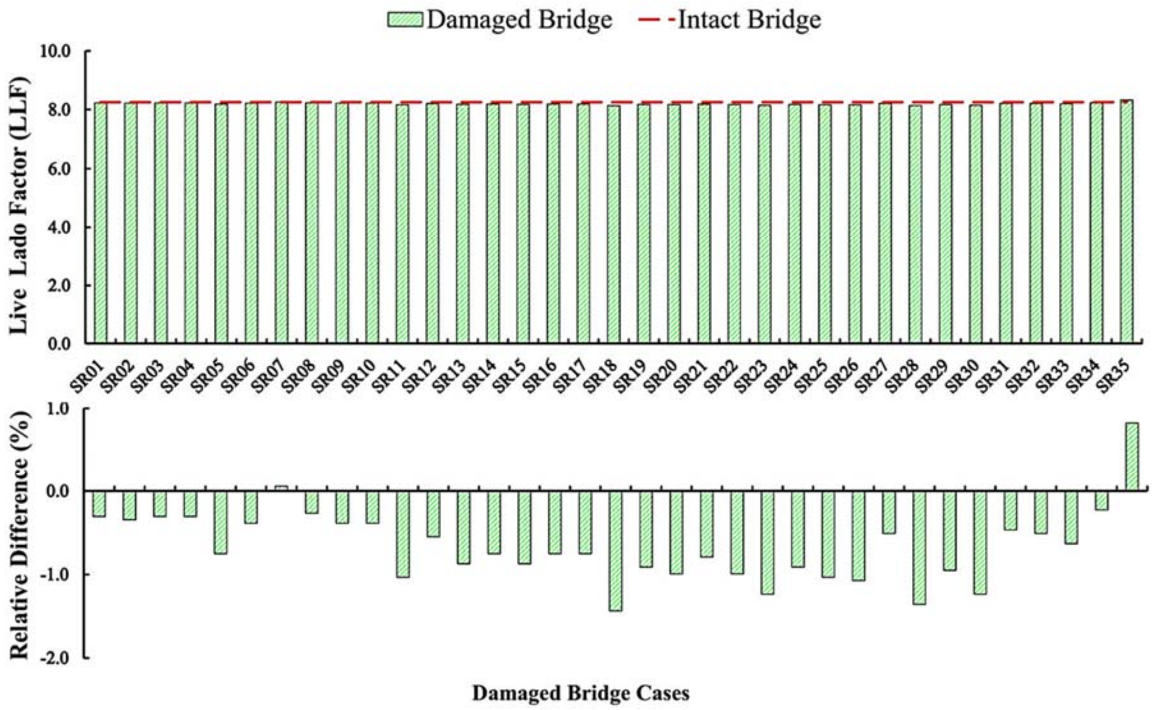

Source: FHWA.

Figure 168. Graph. Live load factor of 2nd limit state of damaged bridge during pushdown analyses – cases PDAD1.

However, single suspender removal has a significant effect on the 3rd limit state. As shown in Figure 169, except for case SR35, the LLFs of all other damaged bridge cases are lower than that of the intact bridge and the relative differences are in the range of -41.2% to -12.5%. For each damaged bridge case, suspenders adjacent to the removed suspender dominate the 3rd limit state. Thus, for cases SR01 to SR30, the LLFs are dominated by the type-I suspenders and for cases SR31 to SR35, the LLFs are dominated by the type-II suspenders. Since the type-II suspenders have a larger cross-section, the LLFs for cases SR31 to SR34 increase by approximately 3 with respect to those for cases SR24 to SR30. Due to the support provided by the bridge towers, the influence of single suspender loss on the LLFs of the cases with suspender loss close to bridge towers is found to be less significant. Therefore, the LLFs of cases SR14 and SR15 are larger than the LLFs of other cases nearby. Additionally, from case SR08 to case SR14, The LLF increases gradually whereas the LLF decreases gradually from case SR15 to case SR27.

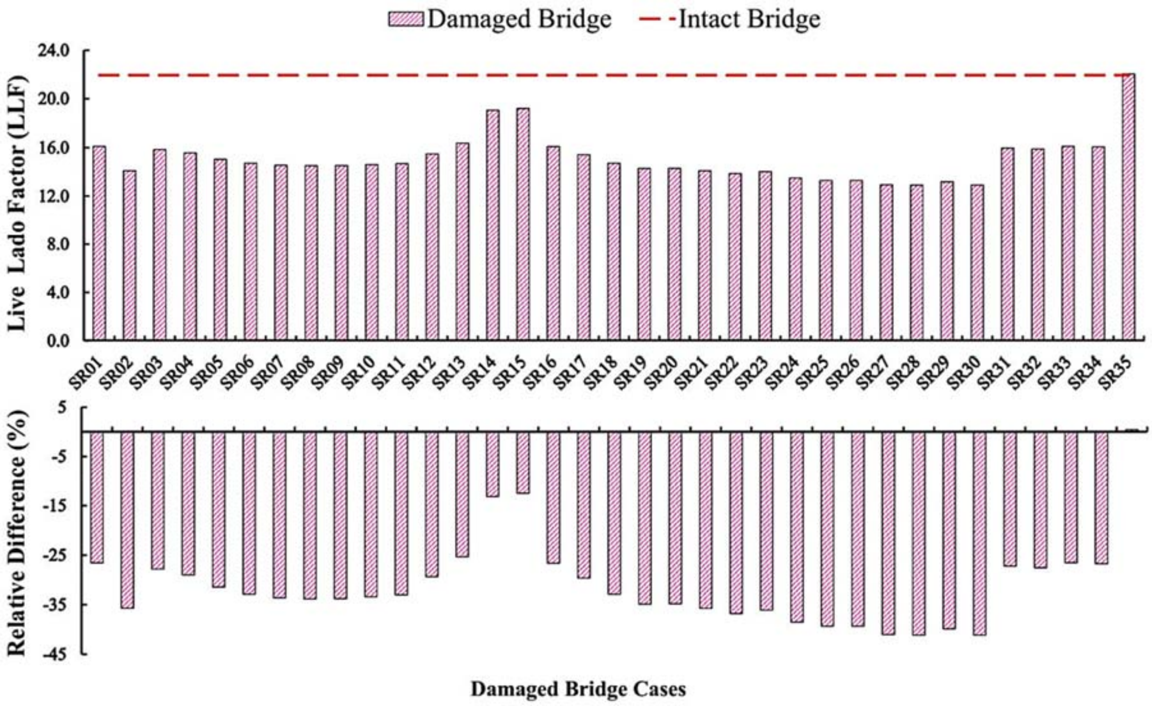

Source: FHWA.

Figure 169. Graph. Live load factor of 3rd limit state of damaged bridge during pushdown analyses – cases PDAD1.

Pushdown Analysis of the Damaged Bridge under LL2 (Cases PDAD2-SR01~35)

Similar to the pushdown analysis for the intact bridge, only two limit states (i.e., the 1st and 3rd limit states) were reached for all damaged bridge cases under LL2. The LLFs corresponding to these limit states are plotted in Figure 170 and Figure 171, including their relative difference with respect to the LLF of the intact bridge under LL2 (i.e., case PDAI2).

In comparison with the intact bridge, the 1st limit state was slightly affected when single suspender loss occurred in the side span. As shown in Figure 170, the LLFs of the damaged bridge cases for cases SR1 to SR14 are very close to that for the intact bridge with the maximum relative difference being less than 2.3%. However, for a single suspender loss in the center span, the 1st limit state was affected significantly. The LLFs of cases SR15 to SR35 are less than that for the intact bridge, with the maximum relative difference being around -19.0%. The minimum LLF is 1.65 in case SR28.

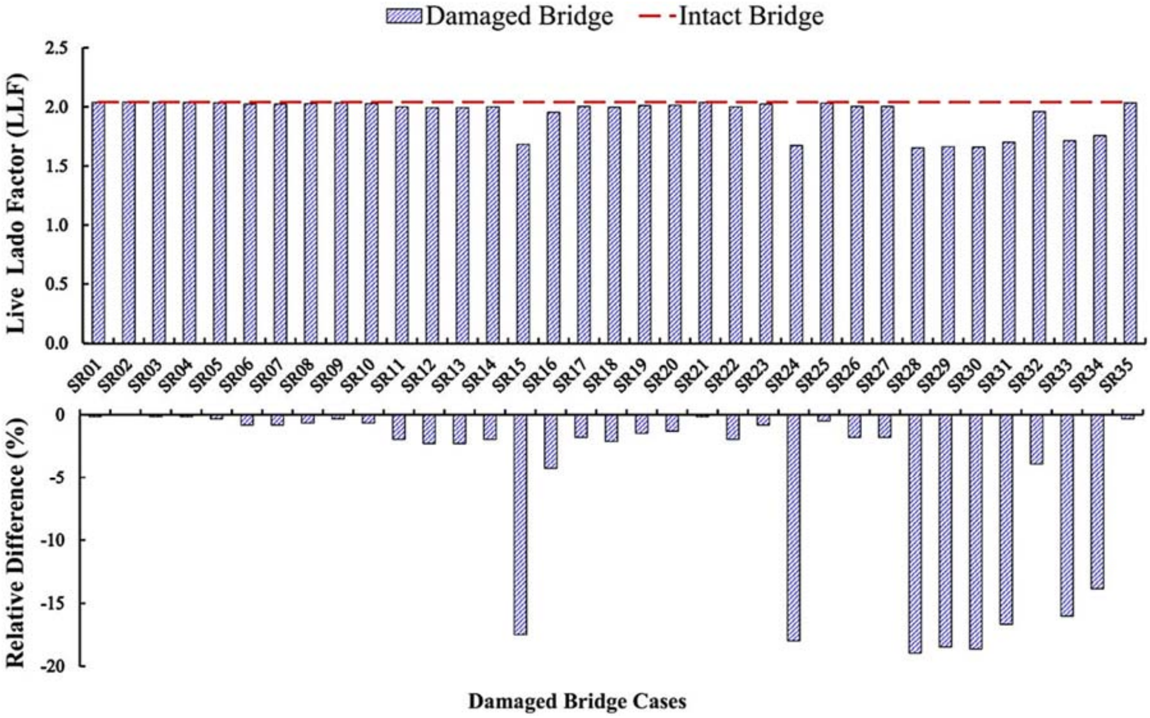

Source: FHWA.

Figure 170. Graph. Live load factor of 1st limit state of damaged bridge during pushdown analyses – cases PDAD2.

The influence of single suspender loss on the 3rd limit state is mainly observed in the side spans where the live loads were applied. As shown in Figure 171, the LLFs of cases SR01 to SR14 are less than 19.67 (i.e., the LLF of for the intact bridge). The minimum LLF is 13.70, which occurred in case SR08, with a difference of -30.4% with respect to that of the intact bridge. Similar influence is also found in the center span, but for cases with suspender loss very close to the tower, such as cases SR15 and SR16. The LLFs for other suspender loss scenarios in the center span, i.e., cases SR17 to SR35, are very close to that for the intact bridge.

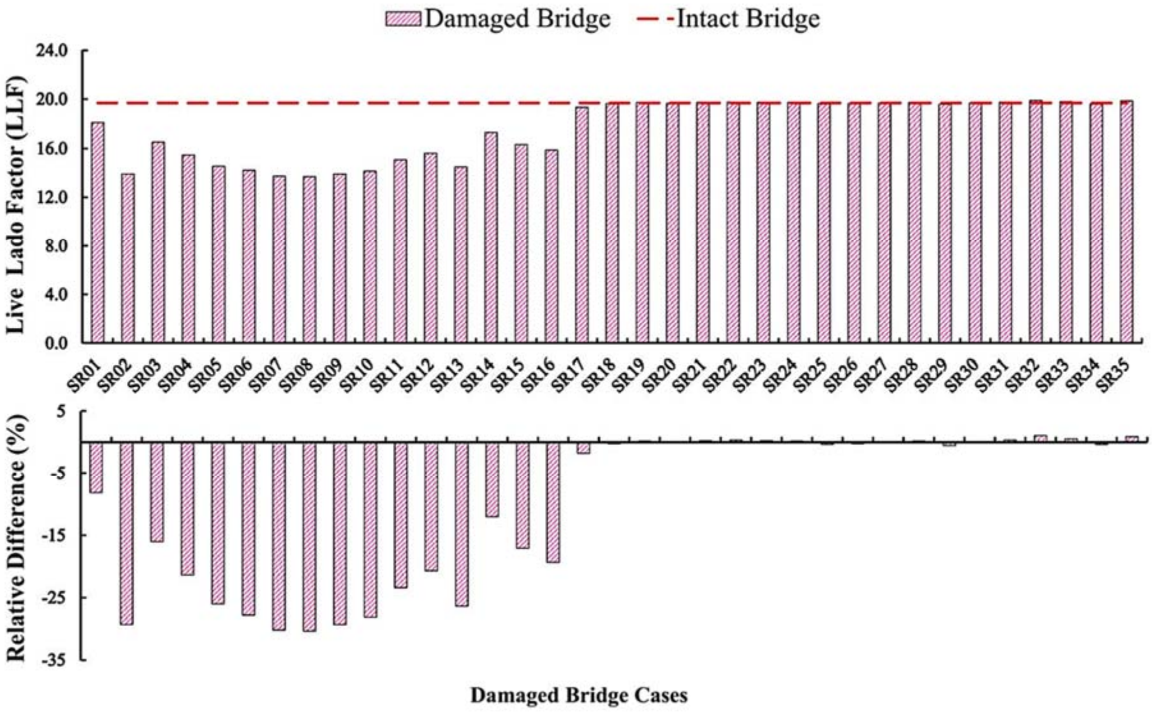

Source: FHWA.

Figure 171. Graph. Live load factor of 3rd limit state of damaged bridge during pushdown analyses – cases PDAD2.

Pushdown Analysis of the Damaged Bridge under LL3 (Cases PDAD3-SR01~35)

Similar to the pushdown analysis of the intact bridge under LL3, all three limit states were reached for all damaged bridge cases under LL3. The LLFs corresponding to these limit states and their relative differences with respect to that for the intact bridge (i.e., case PDAI3) are plotted in Figure 172 to Figure 174.

For the 1st limit state, the LLFs of all damaged bridge cases are in a narrow range of 1.58 to 1.64, which are very close to that for the intact bridge. For the 2nd limit state, the LLFs of all damaged bridge cases are also in a narrow range of 8.71 to 8.74, which are very close to the LLF of intact bridge. Hence, single suspender loss has small effect on the 1st and 2nd limit states of the bridge under LL3.

However, the effect of suspender loss on the 3rd limit state varies significantly with the location of suspender loss. Specifically, only a slight effect is observed when the suspender loss occurs in the side spans (e.g., cases SR01 to SR12), while a significant effect is observed when it occurs in the center span. However, for cases SR13 and SR14, although the suspender loss occurs in the side span, the influence increases because of their location close to the tower and the LLF drops to around 19.0 from 21.84 (i.e., the LLF for the intact bridge). A more noticeable effect of suspender loss on the 3rd limit state is observed in the center span. From case SR15 to case SR30, the LLF decreases monotonically first and then fluctuates slightly around 13.0. The minimum LLF is 12.96, which occurred in case SR27 with a relative difference of -40.6% with respect to that of the intact case. The declining trend terminates at case SR30. After this, the LLF increases abruptly and stays around 16.0 from case SR31 to case SR35, since type-II suspenders start to dominate the 3rd limit state from case SR31.

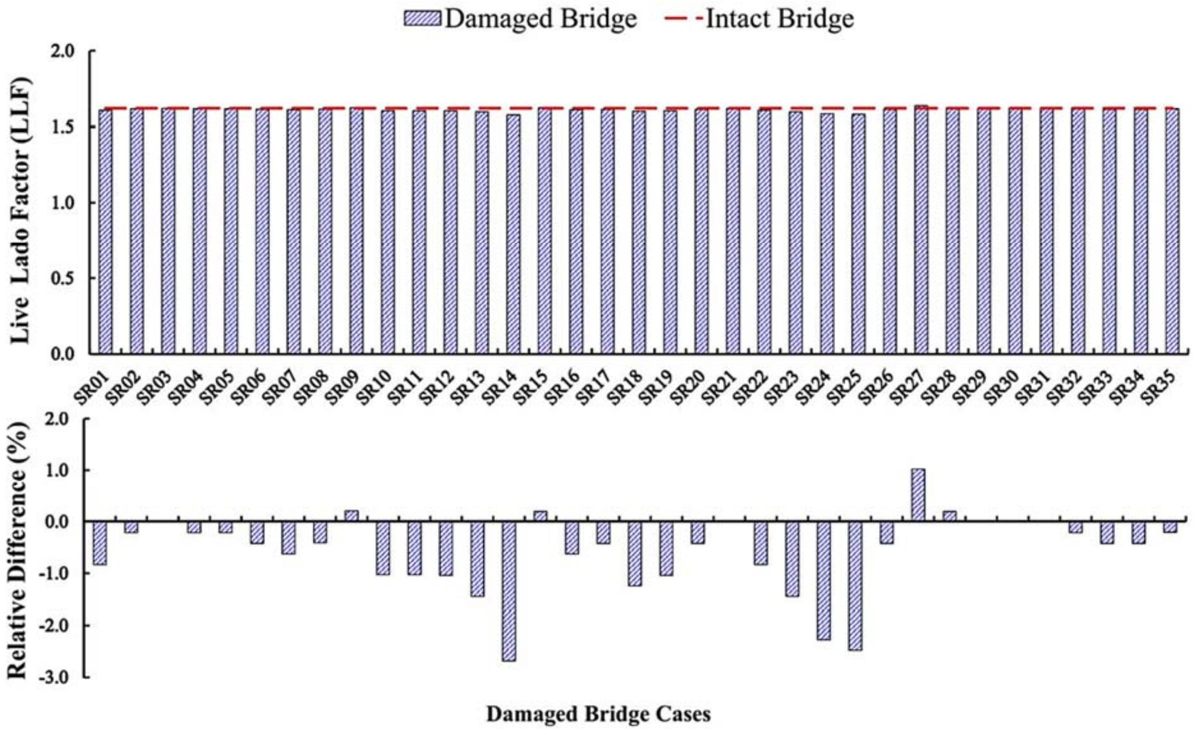

Source: FHWA.

Figure 172. Graph. Live load factor of 1st limit state of damaged bridge during pushdown analyses – cases PDAD3.

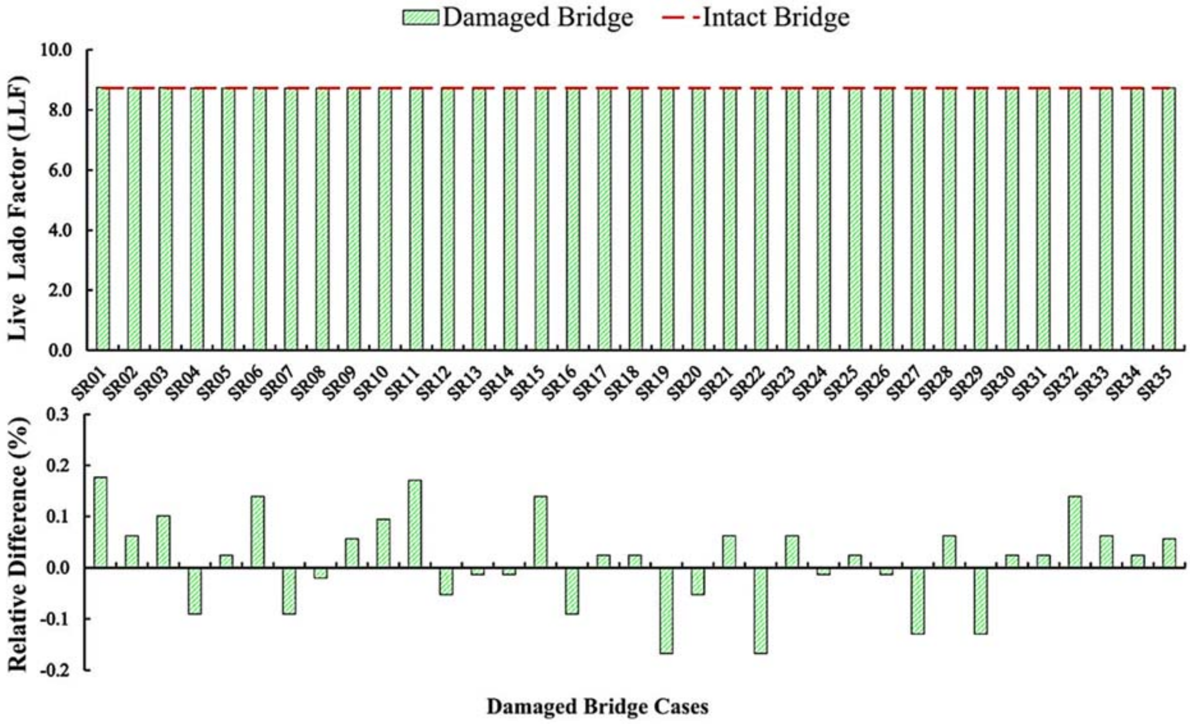

Source: FHWA.

Figure 173. Graph. Live load factor of 2nd limit state of damaged bridge during pushdown analyses – cases PDAD3.

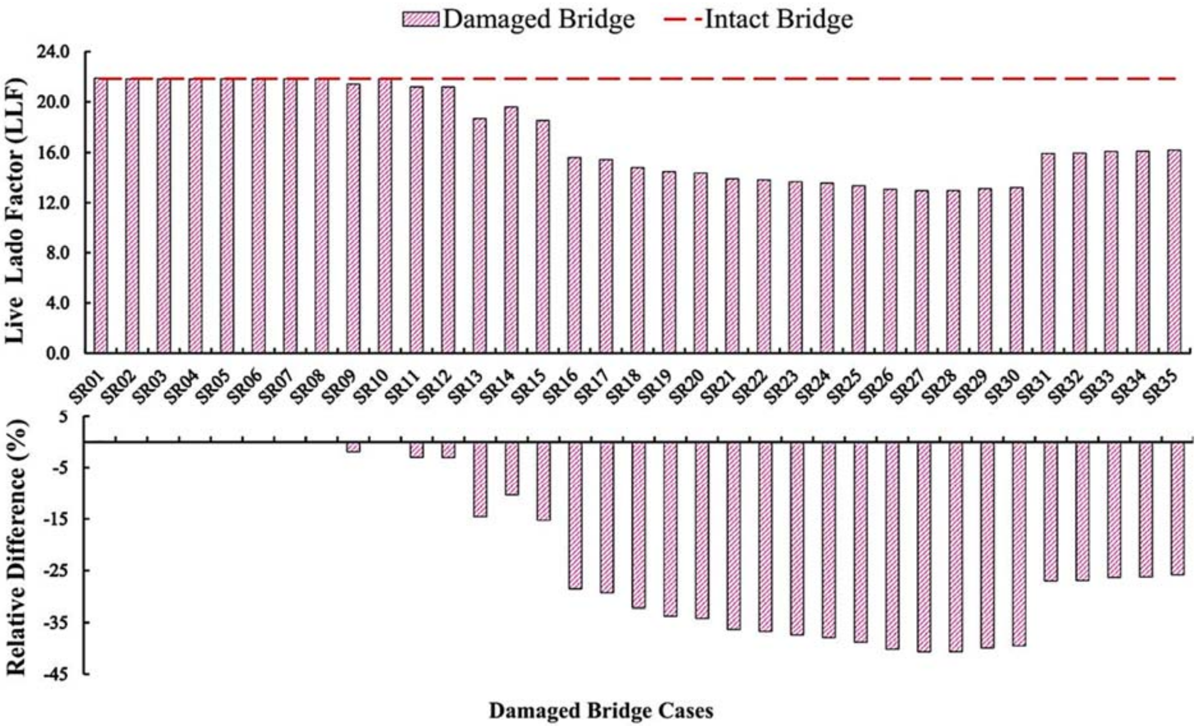

Source: FHWA

Figure 174. Graph. Live load factor of 3rd limit state of damaged bridge during pushdown analyses – cases PDAD3.

SUMMARY

Using the explicit models developed in Chapter 3, the behavior of the three bridges under over-loading was investigated through pushdown analyses in this chapter, for both the intact states and the damaged states due to single cable loss. Based on the pushdown analyses, typical limit states and failure modes of the bridges under over-loading were identified, and in Chapter 7, they were used to evaluate the reliability and robustness of the bridges. The highlights of this chapter includes,

- For each example bridge, pushdown analysis was conducted on the intact bridge under the selected live-load distributions. Key structural components of the bridge were monitored closely during the push down process, such as stay cables/hangers/suspenders, main girders, main arches, etc. Important failure events for each key component were selected to serve as the limit states of the bridges.
- For the cable-stayed bridge, four limit states were identified: (1) stay cable yield, (2) main girder yield, (3) lateral bearing failure and (4) stay cable rupture. For the tied-arch bridge, three limit states were identified: (1) hanger yield, (2) main arch yield and (3) hanger rupture. For the suspension bridge, three limit states were identified: (1) slip of main cable over tower saddle, (2) main cable yield and (3) suspender yield. LLF (live load factor) corresponding each limit state was recorded as the index to evaluate the limit state quantitatively.
- Pushdown analyses were also performed on each example bridge in its damaged state (induced by single cable loss), and all scenarios of single cable loss and live-load distribution patterns discussed in Chapter 4 were simulated.
- The limit states identified from the intact bridges were also investigated during the pushdown analyses on the damaged bridge, and the corresponding LLF were compared with the LLF of the intact bridges. The results showed that: (1) all three bridges have very high capacity for the design live loads, (2) the overall performances of bridges were affected negatively by cable loss and the effects varied with the location of cable loss and live distribution patterns, and (3) even with such adverse effects, the capacities of the damaged bridge were not reduced significantly.

CHAPTER 6. COMPARISON OF PROPOSED ROBUSTNESS METHOD AND CURRENT REDUNDANCY METHOD

INTRODUCTION

As introduced in the previous chapters, a robust structure should not suffer disproportionate collapse due to a local damage. Traditional design approaches are unable to provide explicit measures of residual safety. In this chapter, a structural redundancy evaluation method is introduced, and a robustness index is proposed to fill the current gap in the state of the art.

CURRENT REDUNDANCY METHOD IN NCHRP REPORT

The redundancy evaluation method proposed in the NCHRP Report 406 is one of the most popular approaches for assessing bridge redundancy. In this technique, structural redundancy is evaluated from load multipliers computed from a nonlinear deterministic pushdown analysis. The load multipliers are LF_1, LF_u, LF_f and LF_d, which are illustrated in Figure 175. LF_1 is defined as the load factor at first member failure, LF_u is the load factor at the ultimate capacity of the intact system, LF_f is the load factor at the loss of functionality, and LF_d is the load factor at the ultimate capacity of the damaged system. Using these load factors, the structural redundancy is characterized by three redundancy ratios given by Equation (20).

$$R_u = \frac{LF_u}{LF_1}\,;\ R_f = \frac{LF_f}{LF_1}\,;\ R_d = \frac{LF_d}{LF_1}. \tag{20}$$

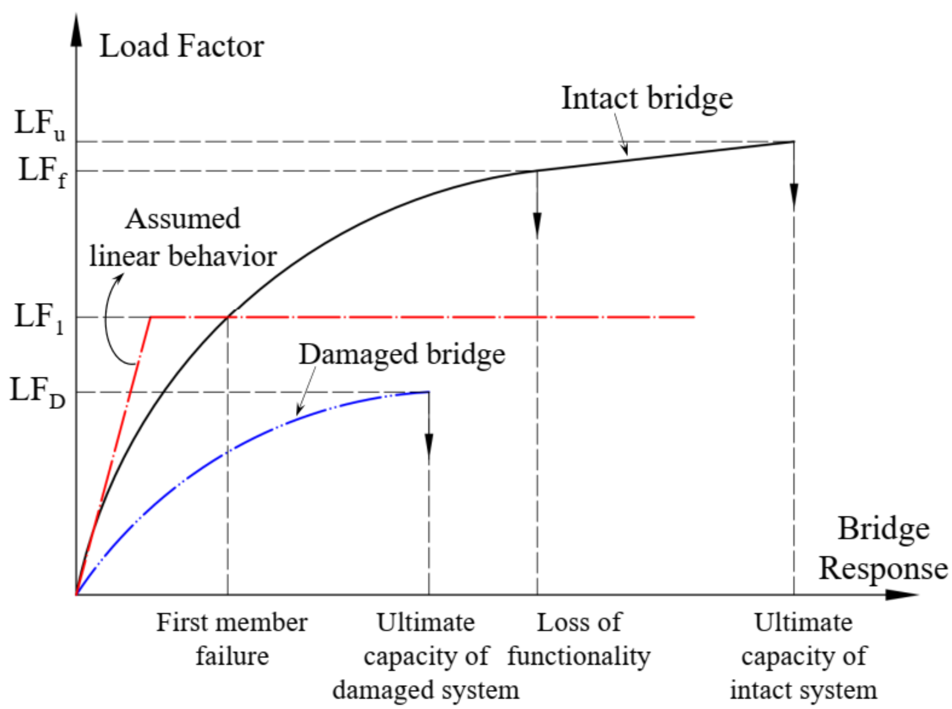

Source: National Academy of Sciences.

Figure 175. Illustration. Typical behavior of bridge systems during push down analysis.

A set of system factors were also proposed and calibrated for steel and pre-tensioned I-beam slab bridges in NCHRP 406. Similarly, another report, NCHRP 458, applied the same procedure to bridge substructures, such as confined and unconfined piers, spread footings, drilled shafts, and piles. Their descendant, NCHRP 776, extends the work to bridges like multi-cell box girder bridges and considers the interaction between the superstructure and substructure.

Based on the NCHRP 406, a bridge is considered redundant if the calculated redundancy ratios meet the conditions listed in Equation (21),

$$R_u \geq 1.30;\ R_f \geq 1.10;\ R_d \geq 0.50. \tag{21}$$

These limits were obtained from reliability analyses of typical simply supported steel and concrete I-girder bridges with four or more girders. Three relative reliability indexes given by Equation (22) were used in the reliability analysis-based procedure,

$$\begin{aligned} \Delta\beta_u &= \beta_{ult} - \beta_{member} \\ \Delta\beta_f &= \beta_{funct} - \beta_{member} \\ \Delta\beta_d &= \beta_{damaged} - \beta_{member} \end{aligned} \tag{22}$$

where β_{member} is the reliability index of the first member failure for the intact bridge, β_{funct} is the reliability index of the functional limit state for the intact bridge, β_{ult} is the reliability index of the ultimate limit state for the intact bridge, and $\beta_{damaged}$ is the reliability index of the ultimate limit state of the damaged bridge.

A simplified calibrated method was used to calculate these three relative reliability indexes in the NCHRP 406 report, given by Equation (23),

$$\begin{aligned} \Delta\beta_u &= \frac{\ln R_u}{\sqrt{V_{LF}^2 + V_{LL}^2}} \\ \Delta\beta_f &= \frac{\ln R_f}{\sqrt{V_{LF}^2 + V_{LL}^2}} \\ \Delta\beta_d &= \frac{\ln R_d \dfrac{\overline{LL_{75}}}{\overline{LL_2}}}{\sqrt{V_{LF}^2 + V_{LL}^2}} \end{aligned} \tag{23}$$

where R_u, R_f and R_d are the redundancy ratios in Equation(20), V_{LF} is the coefficient of variation (COV) of the load factor, V_{LL} is the COV of the live load, $\overline{LL_{75}}$ is the mean value of the maximum expected lifetime live load and $\overline{LL_2}$ is the mean value of live load for a 2-year inspection period.

Based on results in the NCHRP 406 report, the relative reliability indexes ($\Delta\beta_u$, $\Delta\beta_f$ and $\Delta\beta_d$) are summarized in Table 30. These values can be used to compute the redundancy ratios for a bridge, which should then meet the requirements in Equation (21).

Table 30. Relative reliability indexes in NCHRP Report 406.

		$\Delta\beta_u$(Ultimate Limit)	$\Delta\beta_f$ (Functionality)	$\Delta\beta_d$ (Damaged Condition)
Steel I-Girder Bridges	Range	0.46 ~ 0.94	0.41 ~ 0.62	-5.00 ~ -1.15
	Average	0.72	0.53	-2.96
Pre-stressed Concrete I-Girder Bridges	Range	0.70 ~ 1.28	-0.17 ~ 0.41	-4.79 ~ -0.9
	Average	0.97	0.0	-2.40
Target value for redundant		0.85	0.25	-2.70

These redundancy criteria, the limit value of load factor ratios, in the NCHRP reports were obtained from reliability analyses of typical simply supported steel and concrete I-girder bridges with four or more girders, which are classified as redundant bridges. Therefore, their applicability to long-span cable supported bridges, which could potentially be not redundant, needs to be further examined in detail. Another limitation of the NCHRP approach is that the degree of redundancy measured by the redundancy ratios only provides limited information. For example, two structures with same $R_u = 2$ (one has $LF_u = 2.0$ and $LF_1 = 1.0$, while the other has $LF_u = 3.0$ and $LF_1 = 1.5$) and same COVs may have different levels of redundancy, which is not well-explained or represented by these ratios. Moreover, the only randomness considered in this simplified reliability method are the load factors LF and live load LL, while randomness should also be considered for dead loads, material properties, and geometric variables. One more important limitation of the NCHRP approach is that it considers only one limit state. However, long-span cable-supported bridges, which are much more complex than the simply supported girder bridges used to calibrate the NCHRP approach, have a multitude of initiating events and limit states as discussed in the previous chapters. Questions, such as "which initial damage is most critical?", "How severe a damage can a bridge take but still stand safely?", need to be further evaluated. In order to address these limitations, a new robustness evaluation method is proposed next.

PROPOSED ROBUSTNESS EVALUATION METHOD

For a given example bridge, the probability of exceeding any limit state of interest, such as collapse, critical member failure, serious cracking or functional loss, could be evaluated by $P_F = P[F; L]$, where "F" implies the failure corresponding to the limit state "L". For any initial damage "A" inflicted on the bridge, the probability of exceeding the same limit state under the damaged condition could also be evaluated by $P_F' = P[F|A; L]$. If $P_F' \rightarrow 1$, it implies "A" is a critical damage corresponding to the limit state "L" and the structure has negligible redundancy against damage "A" for the limit state "L". On the other hand, if $P_F' \rightarrow P_F$, it implies "A" is a local damage corresponding to the limit state "L" and the structure is fully robust against the damage "A" for the limit state "L". The probabilities of failure in intact and damaged conditions are related to the generalized reliability indexes $\beta_0 = \Phi^{-1}(1 - P_F)$ and $\beta' = \Phi^{-1}(1 - P_F')$, respectively, where Φ is the normal distribution function. Based on these reliability indexes β_0 and β', an exponential form of robustness index is proposed by Equation (24), which is a function of the initial damage "A" and is contextualized by the limit state "L",

$$R_b(A; L) = exp\left(\frac{\beta' - \beta_0}{\beta_0}\right) \quad (24)$$

This formulation grows out of system reliability-based importance measures and distances between the intact and damaged structures in probability space (Bhattacharya 2021). It is appropriate for high reliability structures and can be applied to any limit state of interest and any credible initial damage. In addition, this measure is bounded between 0 and 1: $R_b(A;L) \to 0$ implies the structure has no robustness against the initial damage "A" in the limit state "L"; and $R_b(A;L) \to 1$ implies the structure is fully robust against the initial damage "A" in the limit state "L", or the structure is insensitive to the initial damage "A" for the limit state "L". This measure also does not suffer from the shortcomings of existing reliability-based robustness measures.

For member failure limit states, AASHTO LRFD (2017) is calibrated with a required member reliability index of 3.50, and the target values for relative reliability indexes $\Delta\beta_u$ and $\Delta\beta_d$ are 0.85 and -2.70, respectively, according to the NCHRP Report 776. Thus, a redundant bridge should have a required reliability index of $\beta_u = 3.50 + 0.85 = 4.35$ for the intact bridge and $\beta_d = -2.70 + 3.50 = 0.8$ for the damaged bridge. Then, the minimum acceptable value for the proposed robustness index should be $R_{b,\ target} = \exp\left(\frac{\beta' - \beta_0}{\beta_0}\right) = \exp\left(\frac{0.80 - 4.35}{4.35}\right) = 0.44$ for small-to-medium span bridges.

RELIABILITY METHOD AND CALIBRATION

Considering the high computational cost for member removal analysis in LS-DYNA®, a generalized first-order reliability method is proposed to evaluate the reliability index. This approach avoids expensive Monte Carlo simulations, while preserving good accuracy.

Generalized First-Order Reliability Method

Typically, there are several limit states associated with the design of a structure, such as serviceability, member yield or ultimate strength. Each of these limit states can be expressed by a limit state equation of the corresponding failure surface, in terms of the basic variables $V_1, V_2, \cdots, V_m$, i.e.,

$$g(V_1, V_2, \cdots, V_m) = R(V_1, V_2, \cdots, V_m) - S(V_1, V_2, \cdots, V_m) = 0 \tag{25}$$

where *g* is the limit state function, *R* is the resistance and *S* is the structural response.

In structural safety check format, the corresponding design equation can be written as,

$$R^n = R(V_1^n, V_2^n, \cdots, V_m^n) \geq S^n = S(V_1^n, V_2^n, \cdots, V_m^n) \tag{26}$$

where R^n is the nominal structural resistance, S^n is the corresponding nominal structure response, and $V_1^n, V_2^n, \cdots, V_m^n$ are the nominal values of the basic variables that define the corresponding structural limit state.

If all the random variables (i.e., basic variables) in Equation (25) are normally distributed (independent or otherwise), and if the limit state function "*g*" is linear in the random variables, the reliability index is simply the ratio,

$$\beta = \frac{\mu_g}{\sigma_g} \tag{27}$$

where μ_g and σ_g are the mean and standard deviation of the function "g", respectively.

However, for most structures, the limit state function "g" is nonlinear and it may not have an explicit solution. The generalized first-order reliability method allows the nonlinear limit state function $g\ (V_1, V_2, \cdots, V_m)$to be linearized using the first-order Taylor series expansion at point $\mathbf{v}^* = (v_1^*, v_2^*, \cdots, v_m^*)$, i.e.,

$$g(V_1, V_2, \cdots, V_m) \ = g(v_1^*, v_2^*, \cdots, v_m^*) + \textstyle\sum_{i=1}^{m} \frac{\partial g}{\partial V_i}\Big|_{\text{at } \mathbf{V}^*} (V_i - v_i^*) \quad (28)$$

The partial differential coefficients $\frac{\partial g}{\partial V_i}\Big|_{\text{at } \mathbf{V}^*}$ can be obtained from finite element analysis based on Equation (29).

$$\frac{\partial g}{\partial V_i}\Big|_{(v_1^*, v_2^*, \cdots, v_m^*)} = \lim_{\Delta v_i^* \to 0} \frac{g(v_1^*, v_2^*, \cdots, v_i^* + \Delta v_i^*, \cdots, v_m^*) - g(v_1^*, v_2^*, \cdots, v_i^*, \cdots, v_m^*)}{\Delta v_i^*} \quad (29)$$

The first two moments of the limit state equation can be calculated by Equation (30) and (31) as,

$$\mu_g = \ g(v_1^*, v_2^*, \cdots, v_m^*) + \textstyle\sum_{i=1}^{m} \frac{\partial g}{\partial V_i}\Big|_{(v_1^*, v_2^*, \cdots, v_m^*)} \left(\mu_{V_i} - v_i^*\right) \quad (30)$$

$$\sigma_g = \sqrt{\textstyle\sum_{i=1}^{m} \left[\sigma_{V_i} \frac{\partial g}{\partial V_i}\Big|_{(v_1^*, v_2^*, \cdots, v_m^*)}\right]^2} \quad (31)$$

Then, the approximate reliability index can be calculated based on Equation (27). However, this estimate can be significantly affected by the selection of the point of linearization $\mathbf{v}^*$. In most cases, the point where the maximum likelihood on the limit state function occurs is selected. In practice, an iterative process is needed to identify this maximum likelihood point $(v_1^*, v_2^*, \cdots, v_m^*)$ and safety index β. However, considering extremely high simulation costs for member removal analysis in LS-DYNA® for complex cable-supported bridges, the linearization point $(v_1^*, v_2^*, \cdots, v_m^*)$ is chosen directly based on the nominal values of the random variables. For the random variable of live load, the Δv_L^* is chosen as $(LF - 1)\, v_L^n$, where LF is the live load factor of any limit state of interest from the pushdown analysis. Only one pushdown analysis till structure failure and m separate finite element analysis at normal conditions are required to calculate the reliability index β.

In the following, the proposed simplified reliability method is validated using a simple truss in which geometric nonlinearity is included in the analysis.

Simple Truss Example

The proposed generalized first-order reliability method was calibrated by the simple truss shown in Figure 176. It is simply supported and subjected to a concentrated load at the middle node. The load P, Young's modulus E and yield stress Y are chosen as random variables, and their distribution properties are shown in Table 31.

It is assumed that both members have fully correlated material properties, which means that the yield strength of both members follows a normal distribution with a mean of 400 MPa and a COV of 10%, and the elastic modulus also follows a normal distribution with a mean of 200 GPa and a COV of 5%. The geometry is assumed to be deterministic. The truss was modeled using truss elements with *MAT_PLASTIC_KINEMATIC in LS-DYNA®. The reliability indexes of the first member yield limit state and system failure (member rupture) were calculated by the proposed simplified method. By comparison, reliability indexes obtained from Monte Carlo simulations with 100 million trails were compared to the calculated results, as listed in Table 32. Results in this table show that the proposed simplified reliability method can capture results accurately with minor differences with respect to computation intensive approaches such as the Monte Carlo approach.

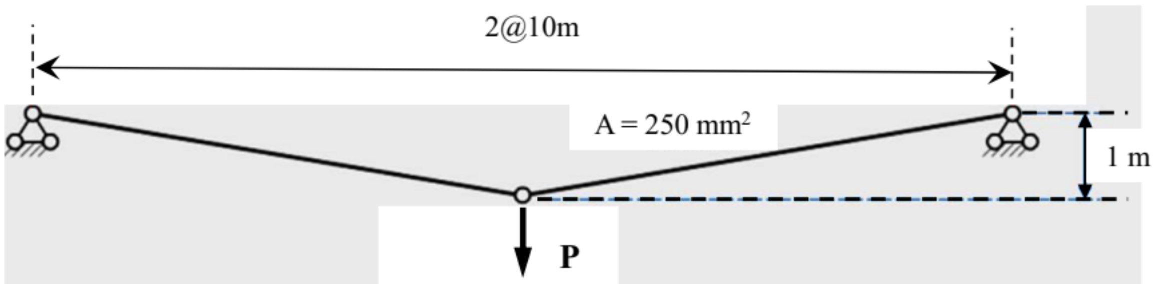

Source: FHWA.

Figure 176. Illustration. Geometrically nonlinear truss.

Table 31. Distribution properties of random variables of the truss.

Random Variables	Mean Value	COV	Distribution Type
Load P (kN) (Different Load Levels)	9.0 13.5 18.0	50%	Normal
Modulus of Elasticity *E* (GPa)	200	5%	Normal
Yield Stress *Y* (MPa)	400	10%	Normal

Table 32. Reliability indexes with respect to the two limit states versus mean load.

Load Level (kN)	**Limit State**	**Reliability Index**	**Reliability Index (Monte Carlo)**	**Difference** (%)
P = 9.0	Yield (in Tension)	2.66	2.78	-4.3
P = 13.5	Yield (in Tension)	1.33	1.38	-3.6
P = 18.0	Yield (in Tension)	0.58	0.59	-1.7
P = 9.0	system failure	8.02	8.78	-8.7
P = 13.5	system failure	6.74	7.10	-5.1
P = 18.0	system failure	5.51	5.77	-4.5

COMPARISON BETWEEN THE PROPOSED REDUNDANCY METHOD AND THE NCHRP 776 APPROACH

The proposed robustness evaluation method has been applied to a three-span continuous composite steel I-girder bridge investigated in the NCHRP Report 776 (Ghosn et al. 2014) to compare the two approaches.

Steel I-Girder Bridge Example

The cross section of the selected bridge is shown in Figure 177. The total length of the bridge is (50+80+50) feet = 180 feet. No transverse bracing is present in this bridge.

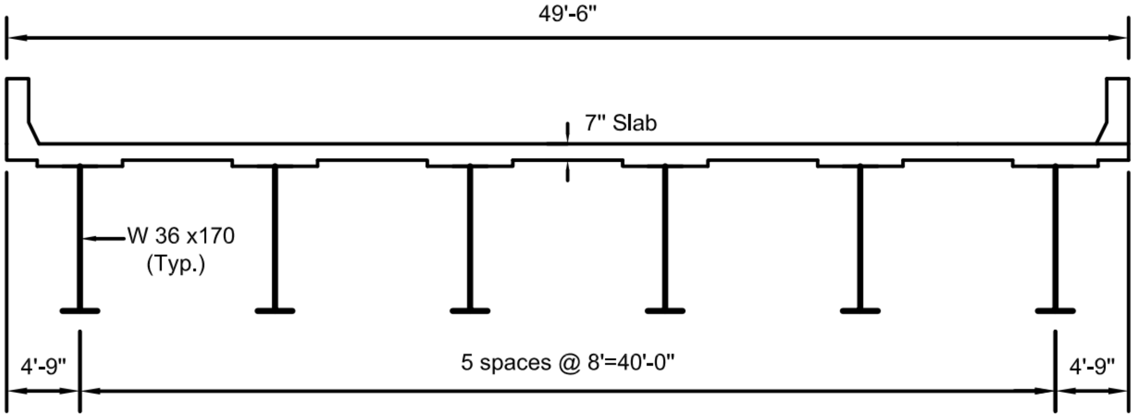

Source: FHWA.

Figure 177. Illustration. Cross section of the three-span steel I-girder bridge.

A FE model was built for this bridge using the grillage analogy method, as shown in Figure 177. The longitudinal elements represent the composite section of the steel-I girder and concrete deck, labeled as Side01 to Side06 in the side span and Mid01 to Mid06 in the middle span. The moment curvature curve of the composite girder section is shown in Figure 179. Two standard trucks arranged side by side (see Figure 178) were considered as the live load. More detailed information on this bridge can be found in the NCHRP Report 776 (Ghosn et al. 2014).

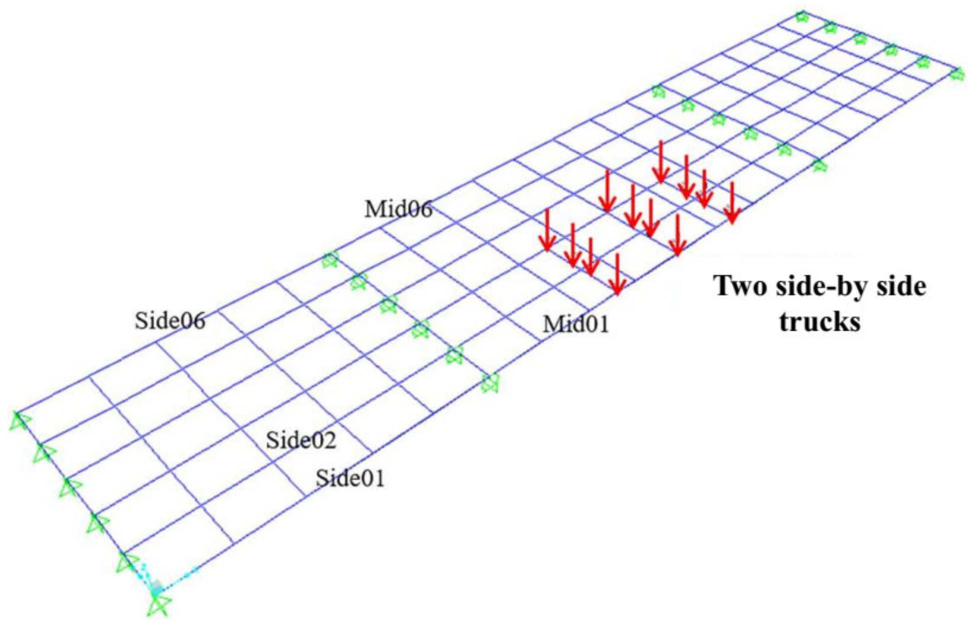

Source: FHWA.

Figure 178. Illustration. FE model of the example three-span steel I-Girder bridge.

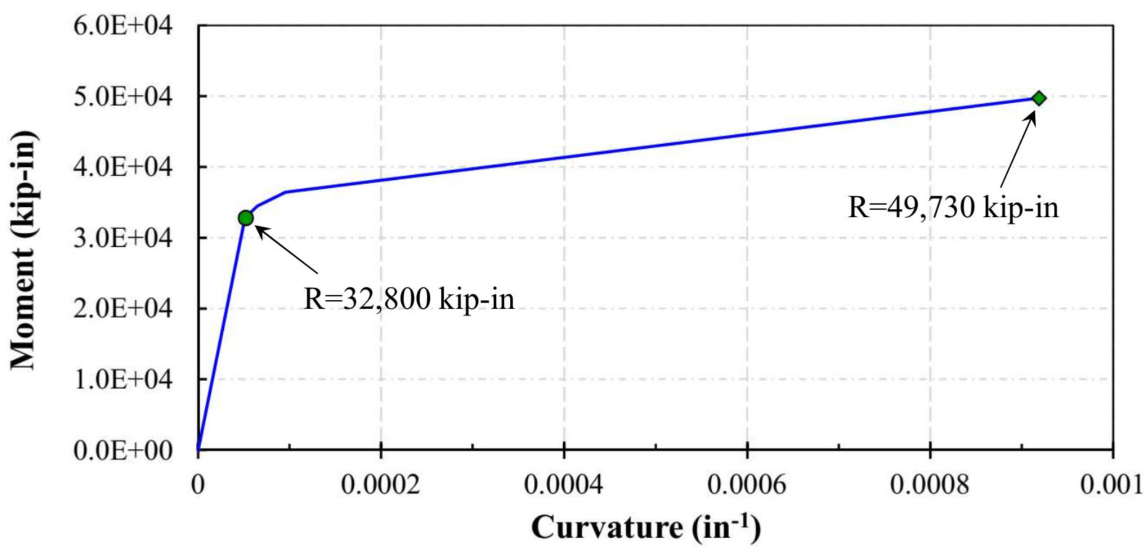

Source: FHWA.

Figure 179. Graph. Moment-Curvature curve of composite longitudinal steel I-Girder section.

The maximum moments in the longitudinal beams was D = 4,860 kip-inch and L = 6,450 kip-inch under dead load only and live loads only, respectively. Based on the approach in the NCHRP report, the resistance of longitudinal beams was selected as the ultimate moment capacity of R = 49,730 kip-inch. Thus, the load factor against first member failure LF_1 was,

$$LF_1 = \frac{R - D}{L} = \frac{49730 - 4860}{6450} = 6.96$$

Pushdown analysis was also conducted for this bridge under intact state by increasing the live load on the bridge until the collapse of the entire bridge. The load displacement curve from the pushdown analysis is shown in Figure 180. The first limit state during the pushdown analysis was the appearance of the first plastic hinge within the longitudinal beams at LF = 4.64, corresponding to the maximum moment of 32,800 kip-inch. As the live load was increased, more elements reached the yield strength and the stiffness of entire bridge also decreased. The bridge reached its ultimate limit state at LF of 8.70, when the maximum moment of the longitudinal beams reached its ultimate capacity of 49,730 kip-inch and the bridge could not carry any more live load.

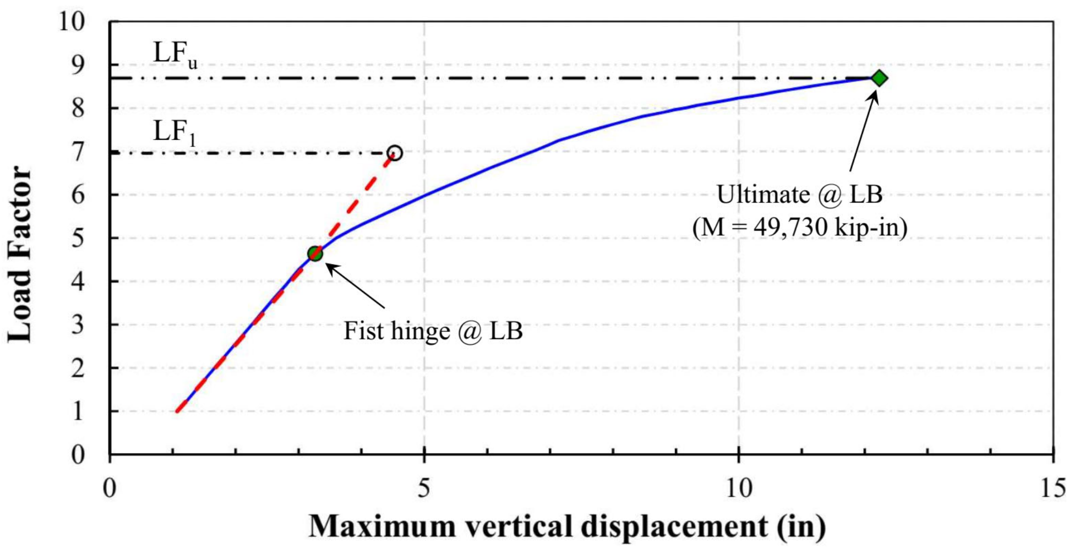

Source: FHWA.

Figure 180. Graph. Load-displacement curve of intact bridge.

Based on the results of pushdown analysis and the calculated load factor against first member failure LF_1 above, the redundancy ratio per the NCHRP approach is,

$$R_u = \frac{LF_u}{LF_1} = \frac{8.70}{6.96} = 1.25 < 1.30$$

The calculated redundancy ratio is less than the required value of 1.30. However, is the bridge really deficient in redundancy? Based on further reliability analysis results introduced in the NCHRP Report, the reliability index for the first member failure is $\beta_1 = 6.68$ and the reliability index for the ultimate limit state is $\beta_u = 7.71$. Thus, the relative reliability index $\Delta\beta_u = \beta_{ult} - \beta_{member} = 7.71 - 6.68 = 1.03$, which is larger than the required value of 0.85. In this case, the redundancy ratio R_u is an incomplete representation of bridge redundancy.

The proposed robustness approach was applied to this bridge for comparison. First, pushdown analyses were conducted on the bridge in both intact and damaged states with various damage scenarios. Two limit states, (i) the occurrence of the first plastic hinge in any longitudinal beams and (ii) attainment of the ultimate limit state of the bridge, were identified during the pushdown analyses. Then, reliability indexes of these two limit states were calculated for both intact and damage states based on the simplified reliability method (Equation (27)-(31)). Finally, the robustness indexes for these two limit states were calculated for different damage scenarios.

The load factor results are shown in Figure 181, the reliability indexes are shown in Figure 182 and the robustness indexes are shown in Figure 183. It is observed that the load factors, reliability indexes, and the robustness indexes have similar trends for different damage scenarios, implying that they are positively correlated. The damage case MR_Mid01 had the smallest load factor, reliability index, and robustness index against the first plastic-hinge limit state and the ultimate limit state among all the damage scenarios, indicating that member Mid01 of this example bridge is the most critical single member for the damage state under the live load applied, because this member is located within the zone where the live load was applied. For damage scenarios MR_Side01 to MR_Side06 and MR_Mid04 to MR_Mid06, the load factors and beta indexes were similar to those of the intact bridge. Since these members are far away from the live load zone, loss of these members had a relatively small effect on the entire bridge. Besides that, Figure 183 shows that all damage scenarios with single member removal had robustness indexes larger than 0.44, indicating that this bridge is robust against single member loss in both the first plastic-hinge limit state and the ultimate limit state. Hence, the proposed approach provides bridge engineers with a significantly better representation of the redundancy and robustness of the bridge than the traditional approaches. The application of the proposed robustness method will be introduced in the next chapter.

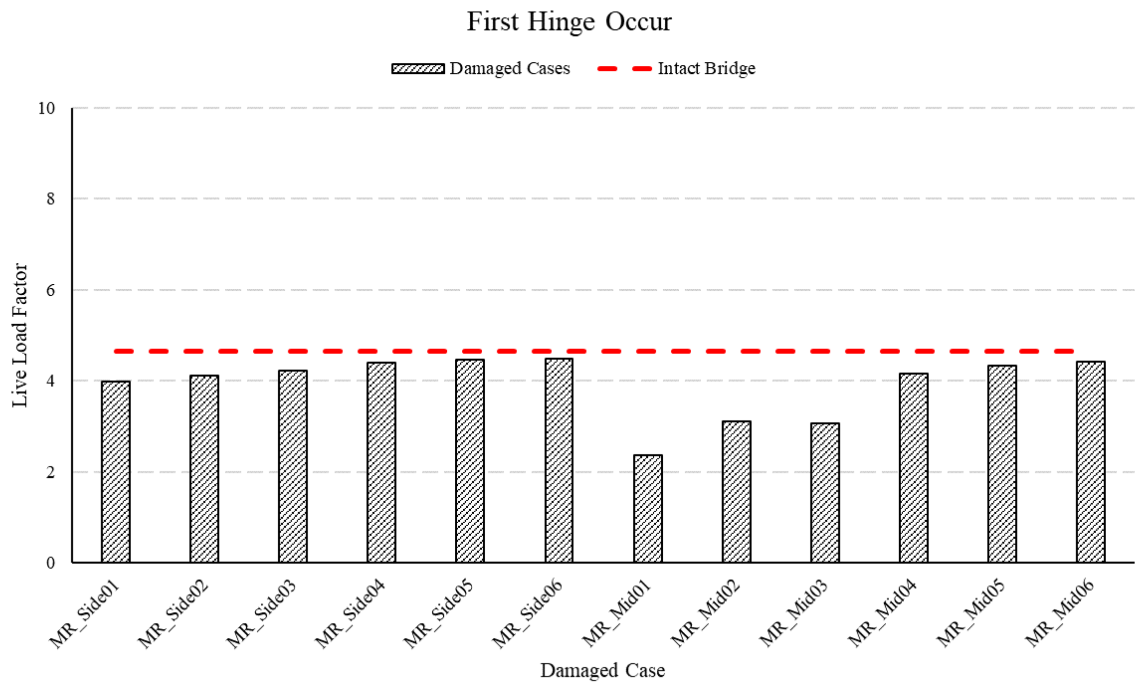

Source: FHWA.

(a) Load factor for first hinge formation.

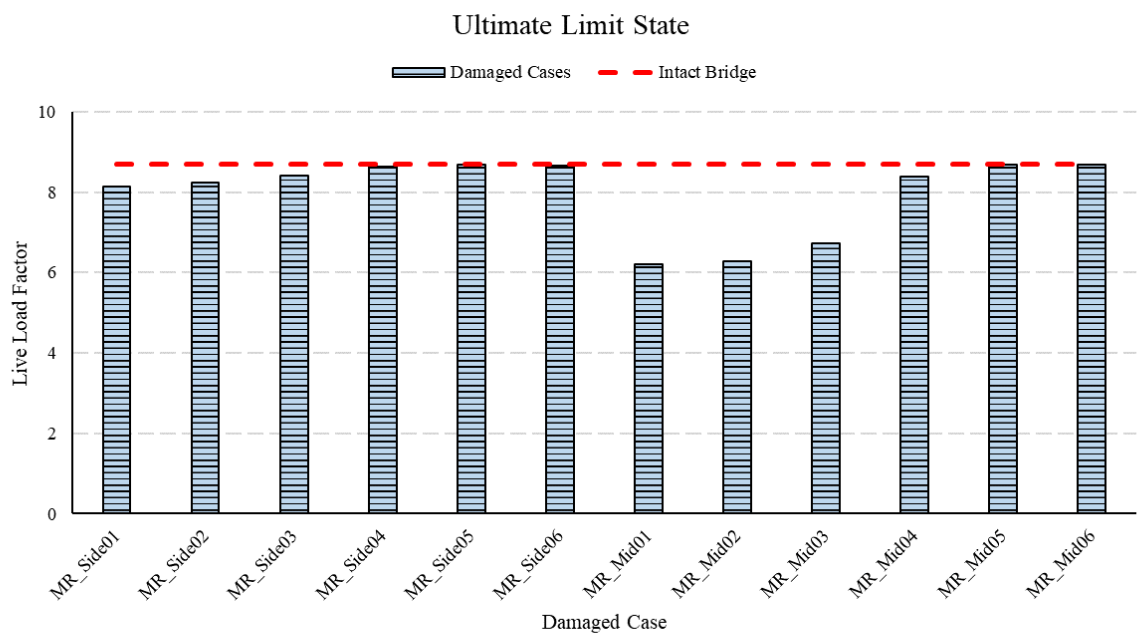

Source: FHWA.

(b) Load factor for ultimate limit state.

Figure 181. Graphs. Load factor of push down analysis of damaged bridge.

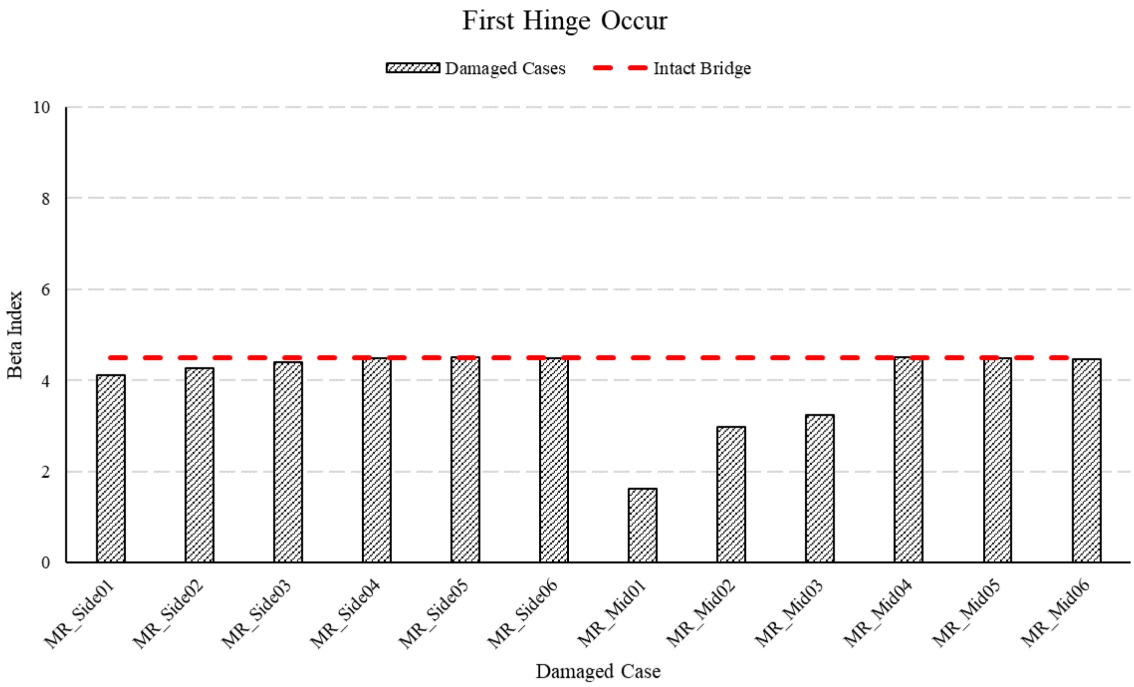

Source: FHWA.

(a) Beta indexes for first hinge formation.

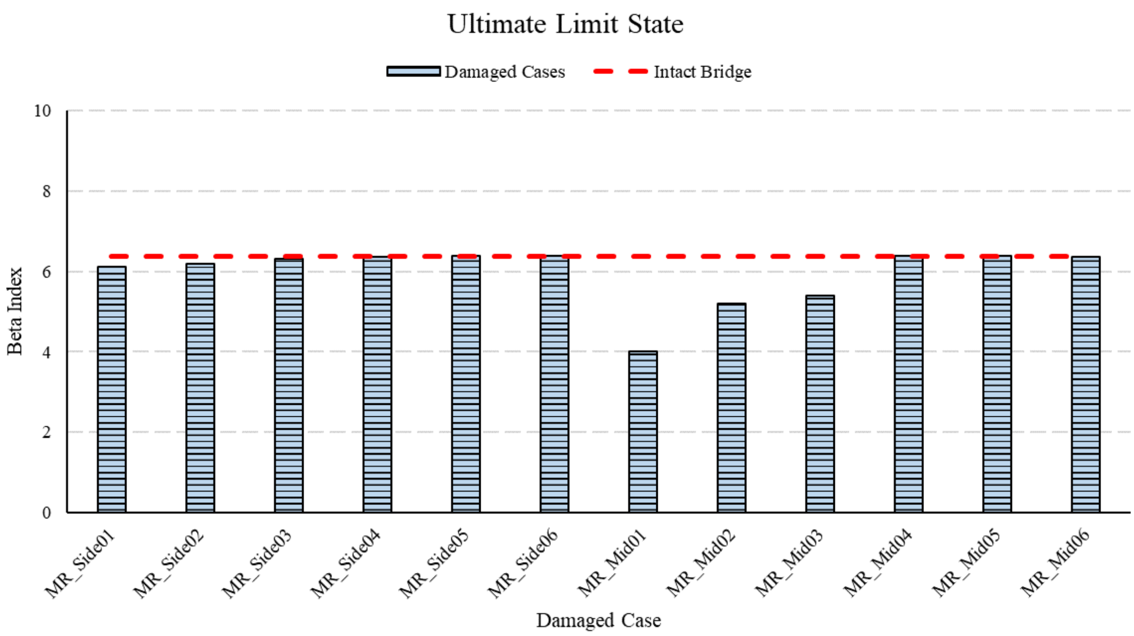

Source: FHWA.

(b) Beta indexes for ultimate limit state.

Figure 182. Graphs. Beta indexes of damaged bridge.

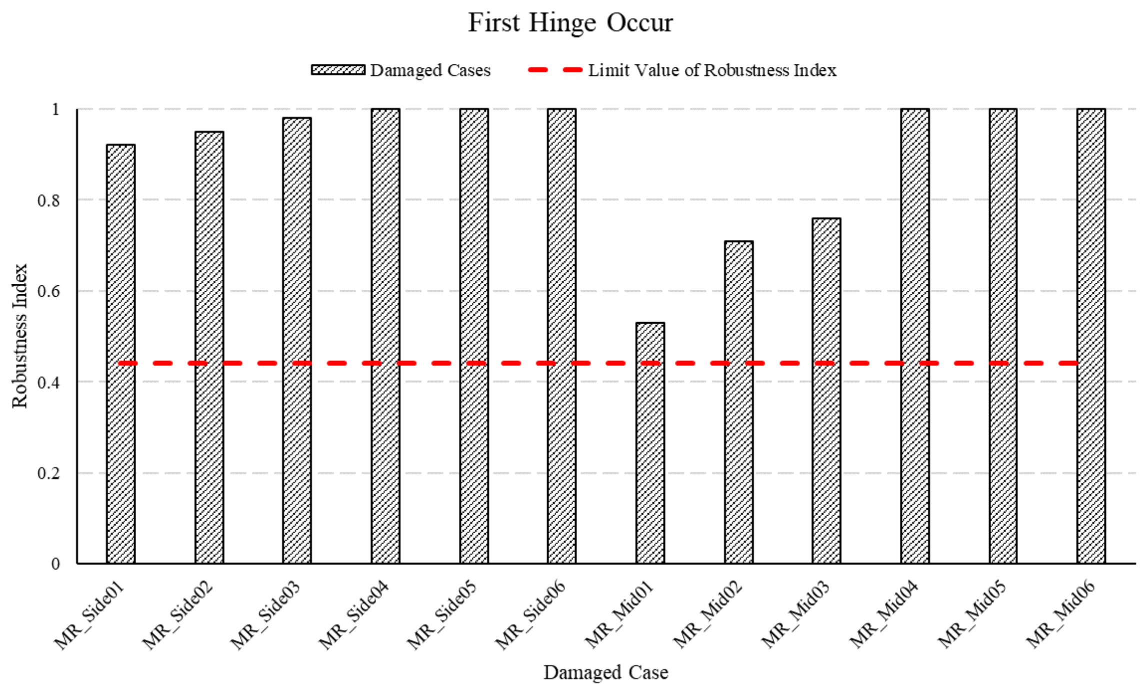

Source: FHWA.

(a) Robustness indexes for first hinge formation

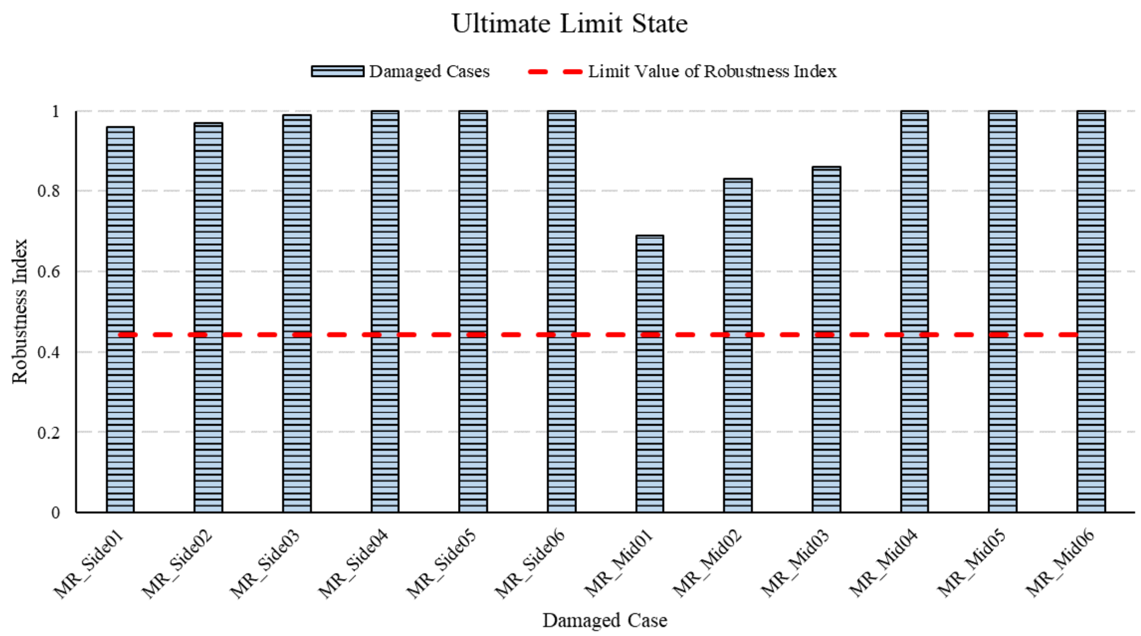

Source: FHWA.

(b) Robustness indexes for ultimate limit state

Figure 183. Graphs. Robustness indexes of different damage scenarios.

SUMMARY

In this chapter, the current redundancy evaluation method suggested by the NCHRP Report 776 was introduced, and its limitations, especially for long-span bridges, were discussed. Then, a new generalized first-order reliability evaluation method was proposed and exercised on a simple truss structure. A robustness index was proposed based on the results of the new reliability evaluation method. The new robustness evaluation method was applied to a three-span continuous composite steel I-Girder bridge investigated in the NCHRP Report 776 and a comparison was made between these two methods. The results demonstrated that the new robustness evaluation method performed in a more reasonable manner than the NCHRP method, especially for the damaged bridge. Specifically, for each limit state, the effect of damages can be clearly identified, and the robustness of the damaged bridge can be quantified in a more precise manner. Therefore, it can be used to explicitly assess the residual safety of damaged bridge.

CHAPTER 7. ROBUSTNESS OF LONG-SPAN CABLE-SUPPORTED BRIDGES

INTRODUCTION

The proposed robustness evaluation method is applied in this chapter to the three long-span cable-supported bridges introduced in earlier chapters. Due to similarity, only the results under a representative live load pattern are introduced. For each example bridge, the reliability indexes in the intact state are computed for the specified limit states identified from the push down analyses in Chapter 5. The reliability indexes of the damaged bridge (due to single cable loss) are also calculated and compared with those from the intact bridge. The robustness indexes are then calculated for the specified limit states under different damage scenarios.

ROBUSTNESS OF THE CABLE-STAYED BRIDGE

As introduced in Chapter 6, the generalized first-order reliability method was applied to the cable-stayed bridge to calculate the reliability indexes for both intact bridge and damaged bridge due to single cable loss. Two limit states-cable yield and girder yield, were investigated and the robustness indexes for these two limit states were calculated. Steps for calculating the robustness indexes are presented next.

Random Variables in the Cable-Stayed Bridge

Randomness related to the load, section properties and material properties was considered in order to perform the reliability analysis. It was assumed that all cross-sections had fully correlated material properties in the main structural steel members. This means all steel members had a yield strength that followed a normal distribution with a bias factor of 1.10 and a coefficient of variation (COV) of 10% and an elastic modulus that also followed a normal distribution, but with a bias factor of 1.0 and a COV of 2%. The cables were assumed to have fully correlated section properties and their area followed a normal distribution with a bias factor of 1.05 and a COV of 5%. The random variables considered in the cable-stayed bridge are summarized in Table 33.

Table 33. Random variables in the cable-stayed bridge.

RV No.	Random Variables	Distribution	Bias Factor	COV
RV1	Dead Load	Normal	1.00	10%
RV2	Live Load	Normal	0.90	20%
RV3	Cable Area	Normal	1.05	5%
RV4	Steel Elastic Modulus	Normal	1.00	2%
RV5	Steel Yield Strength	Normal	1.10	10%
RV6	Cable Elastic Modulus	Normal	1.00	2%
RV7	Cable Yield Strength	Normal	1.15	10%
RV8	Deck Concrete Compressive Strength (Main span)	Normal	1.20	15%
RV9	Deck Concrete Compressive Strength (Side spans)	Normal	1.20	15%
RV10	Main Girder Web Depth	Normal	1.00	2%
RV11	Main Girder Top Flange	Normal	1.00	2%
RV12	Main Girder Bottom Flange	Normal	1.00	2%
RV13	Pylon Concrete Compressive Strength	Normal	1.20	15%
RV14	Pylon Reinforcement yield Strength	Normal	1.10	10%

Note: Bias factor is the ratio of the mean to the nominal value; COV is the coefficient of variation.

Reliability Index of Typical Limit States

Based on the generalized first-order reliability method introduced in Chapter 6, reliability indexes were calculated for the cable yield and girder yield limit states. To do this, a basic case with all the random variables equal to their nominal value was simulated first. Then, a group of simulation cases with changes in one random variable at a time were carried out. Following this, the partial differential coefficients were calculated due to the change in a random variable based on the Equation (29) in Chapter 6. Finally, the reliability index was calculated for a specified limit state based on Equations (27), (30) and (31). This entire process of calculating the reliability index was carried out in MATLAB®. A MATLAB code for this is enclosed in Appendix A of this report. These calculation steps were repeated for both cable yield and girder yield limit states for the intact bridge and the damaged bridge with different cable loss scenarios. For the cable stayed bridge, 32 sudden cable removal cases were performed. In addition, for the structural behavior under each cable removal case, two types of structural responses were considered: the dynamic peak response after sudden member removal and the steady-state response after the structure reached its new equilibrium state following the sudden member removal. The reliability indexes for first cable yield and first girder yield limit states under load combination COMB01 (i.e., dead load plus live load pattern 01) are shown in Figure 184 and Figure 185.

Cable Yield Limit State

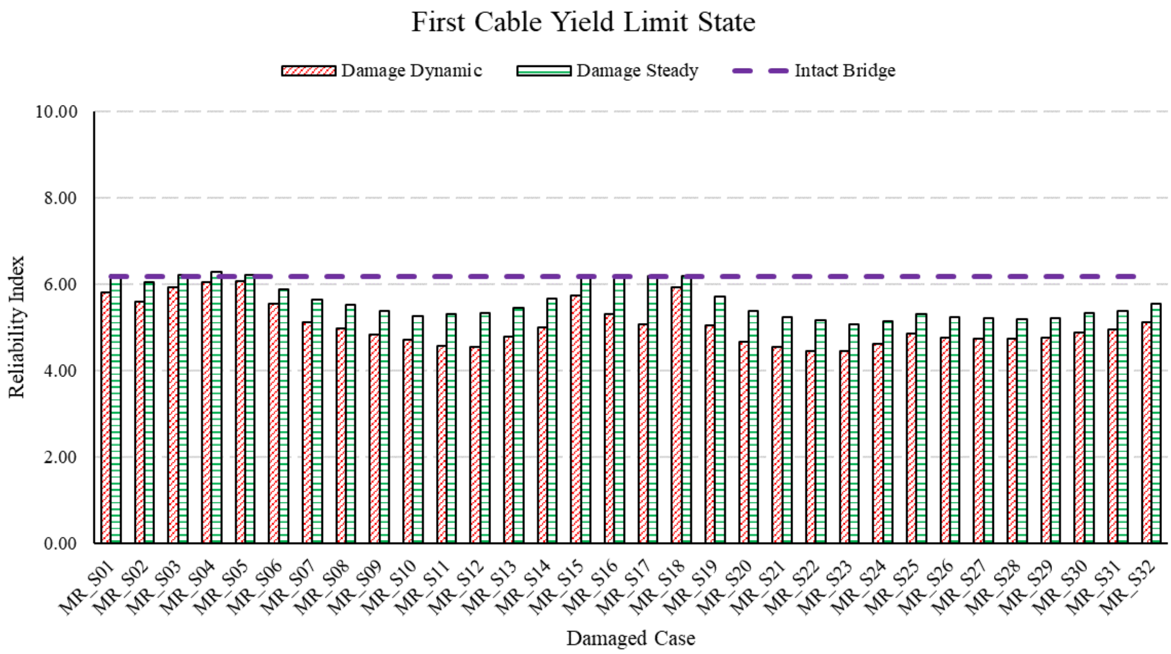

Source: FHWA.

Figure 184. Graph. Reliability index for cable yield limit state under single cable loss.

The reliability indexes for the cable yield limit state for the bridge in the intact and the damaged states (due to single cable loss) are shown in Figure 184. For the intact bridge under COMB01, the reliability index for this limit state (Intact Bridge in Figure 184) is 6.18. Due to single cable loss, the reliability indexes decrease. During the dynamic phase due to sudden cable removal, the reliability indexes (Damage Dynamic in Figure 184) range from 4.44 to 6.05. The minimum value of the reliability indexes occurs for the loss of cables S.22 and S.23. This indicates that the loss of either of these two cables is most critical in the sense that their loss has the highest chance of causing other cables to reach their yield strength. The maximum reliability index occurred for the loss of cables S.04 and S.05. These two cables are near the middle auxiliary pier and the spacing between cables in this area is smaller. Hence, loss of cables in this area may have relatively lesser effect on other cables.

The bridge reached a new equilibrium state after the dynamic effect of sudden cable removal was damped out. In the new steady-state, the reliability indexes (Damage Steady in Figure 184) range from 5.06 to 6.27. The minimum value of the reliability index occurs for the loss of cable S.23. It is observed that the reliability indexes for cable loss cases near the bridge pylon or near the middle auxiliary pier have relatively larger values than those of other cable loss cases because of transfer of some of the forces to the support rather than to adjacent cables. The maximum value of the reliability indexes in the new steady-state equilibrium state is 6.27, which occurs for the loss of cable S.04. This indicates that the loss of cable S.04 would result in a reliability index that is slightly larger than that of the intact bridge, which means that the loss of this cable would have a positive effect for the other cables. However, this does not imply that this cable is not important. During the dynamic phase due to the loss of this cable, there is a larger possibility to cause yielding in other cables when compared with the intact bridge. Loss of this cable would also result in a larger probability of reaching other limit states, such as the girder yield limit state, which indicates that this cable is important for other limit states. Finally, this reliability index is for a specified live load pattern, which is the fully applied live load in all spans. Loss of this cable may become critical for the cable yield limit state in other live load patterns.

Girder Yield Limit State

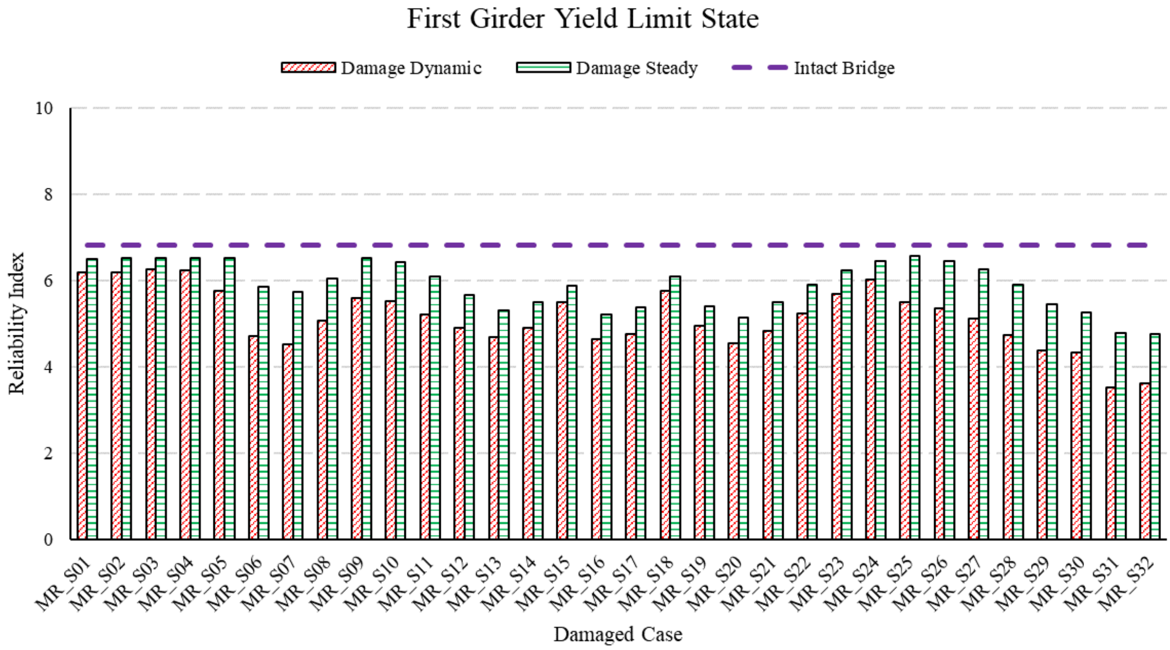

Source: FHWA.

Figure 185. Graph. Reliability index for girder yield limit state under single cable loss.

The reliability indexes for the girder yield limit state for the bridge in the intact state and the damaged states due to a sudden loss of a single cable are shown in Figure 185. For the intact bridge under COMB01, the reliability index of this limit state (Intact Bridge in Figure 185) is 6.81 and it is larger than the reliability index of the cable yield limit state, indicating that the cable yielding has a higher probability of occurring compared to the girder yielding. Due to the loss of a single cable, the reliability indexes of the girder yield limit state decrease compared to that for the intact bridge. During the dynamic response phase due to sudden cable removal, the reliability index of the girder yield limit state (Damage Dynamic in Figure 185) range from 3.52 to 6.27. The minimum value occurs for the loss of cables S.31 and S.32. These two cables are the longest cables in the center span. Compared to the reliability index of the cable yield limit state due to same cable loss (cable S.31 or cable S.32), which has a value of 4.94, the girder yield limit state becomes the dominant limit state due to loss of these cables. The longest cables in the center are strong and the cable forces in these cables are large. Hence, loss of any of these cables would cause a larger change of stress in the main girder. Besides that, the reliability indexes for the loss of cables near the bridge pylon also have relatively small values, even though forces in these are relatively small. Because the main girder near the bridge pylon has the largest compressive force and the girder is the most critical of the intact bridge. Hence, the loss of a cable in this area would also make the unsupported length of main girder increase significantly, resulting in a lower reliability index for this case.

The bridge will reach a new equilibrium state after the vibration induced by sudden cable removal is damped out and the bridge settles down into the new damaged state. In the new steady-state, the reliability indexes (Damage Steady in Figure 185) range from 4.76 to 6.57. The trend of reliability indexes in this steady state has the same trend to those during the dynamic phase. The minimum value of the reliability index occurs for the sudden loss of cable S.32.

Robustness Index against Single Cable Loss

For each specified limit state, the robustness indexes were calculated based on Equation (24) in Chapter 6. The robustness indexes for the cable yield limit state and girder yield limit state under COMB01 are introduced next.

Cable Yield Limit State

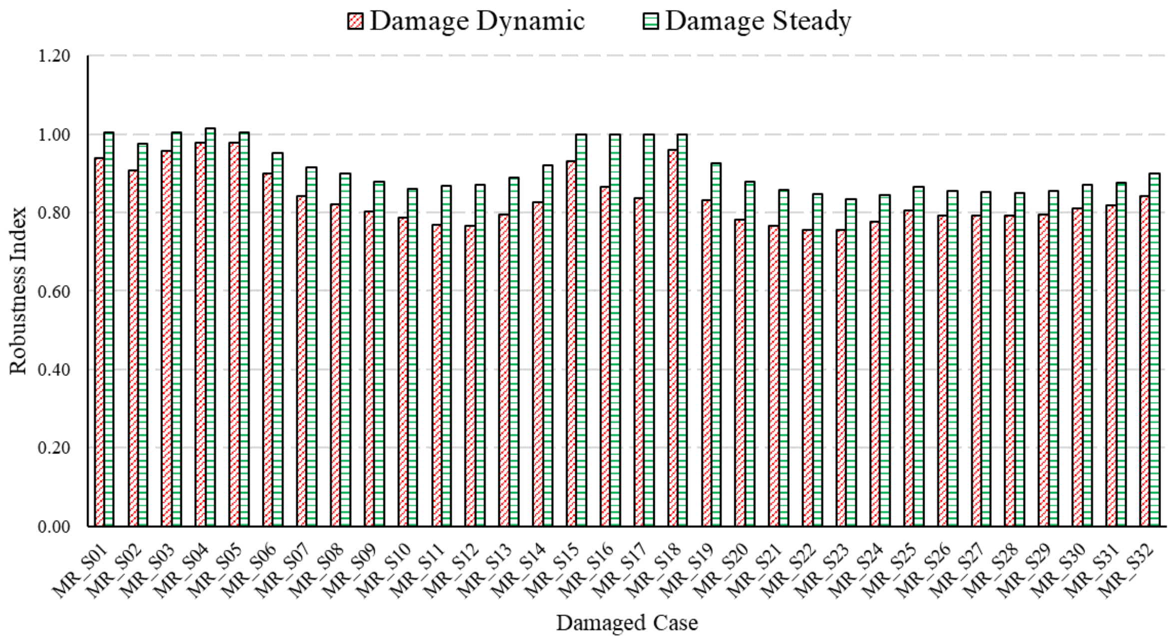

Source: FHWA.

Figure 186. Graph. Robustness index for cable yield limit state against single cable loss.

The robustness indexes for the cable yield limit state under COMB01 due to single cable loss are shown in Figure 186. It is observed that the robustness indexes during the dynamic phase due to sudden loss of single (Damage Dynamic) range from 0.75 to 0.98, whereas the robustness indexes in the steady state after sudden cable loss (Damage Steady) range from 0.83 to 1.01. Since the robustness indexes represent comparisons between the reliability indexes for intact and damaged conditions, the trend of the robustness indexes is the same as that for the reliability indexes discussed in the previous paragraphs. It is further observed that the most critical cable loss case for the cable yield limit state is the sudden loss of cables S.22 and S.23.

Girder Yield Limit State

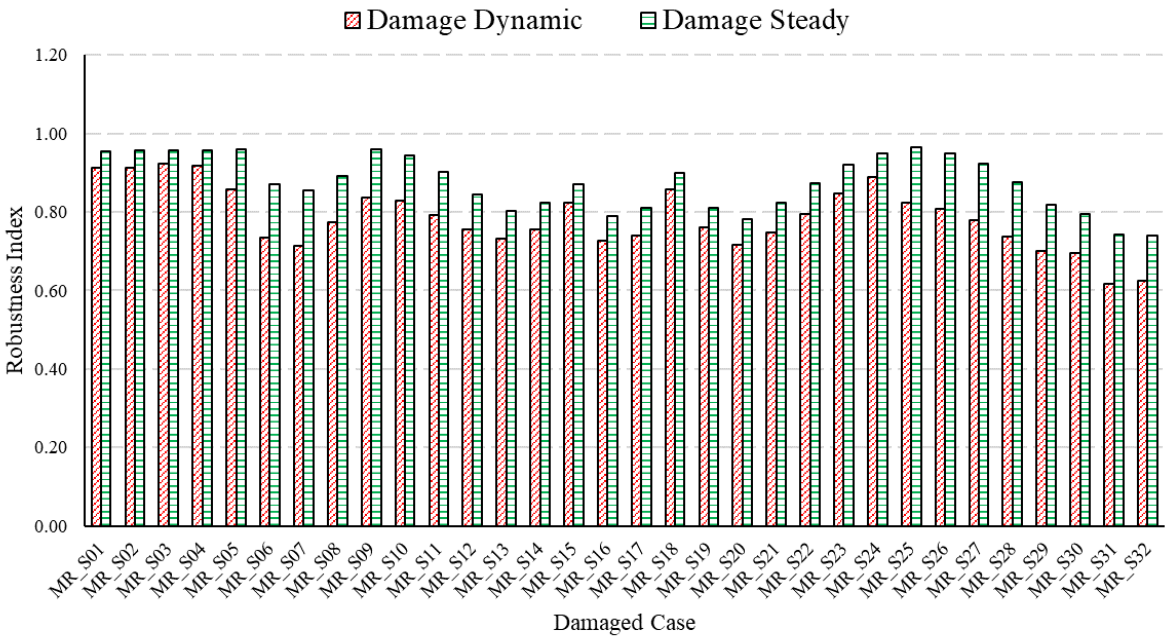

Source: FHWA

Figure 187. Graph. Robustness index for girder yield limit state against single cable loss.

The robustness indexes for the girder yield limit state under COMB01 due to single cable loss are shown in Figure 187. The robustness indexes during the dynamic phase due to single cable loss (Damage Dynamic) range from 0.62 to 0.92, whereas the robustness indexes in the steady state (Damage Steady) range from 0.74 to 0.97. The most critical cases for the girder yield limit state are the loss of cables S.31 and S.32.

ROBUSTNESS OF THE TIED-ARCH BRIDGE

Similar to the case of the cable-stayed bridge in the previous section, the reliability and robustness indexes were calculated for the tied-arch bridge. Three limit states (i.e., hanger yield, arch yield and girder yield) were investigated for this bridge.

Random Variables in the Tied-Arch Bridge

The random variables considered in the tied-arch bridge are shown in Table 34. It is assumed that all the main structural members have fully correlated material properties.

Table 34. Random variables in the tied-arch bridge.

RV No.	Random Variables	Distribution	Bias Factor	COV
RV1	Dead Load	Normal	1.00	10%
RV2	Live Load	Normal	0.90	20%
RV3	Steel Yield Strength (Arch)	Normal	1.10	10%
RV4	Steel Yield Strength (Other)	Normal	1.10	10%
RV5	Steel Elastic Modulus (All)	Normal	1.00	2%
RV6	Hanger Yield Strength	Normal	1.15	10%
RV7	Arch Flange Width(Knuckle)	Normal	1.00	2%
RV8	Arch Web Height	Normal	1.00	2%
RV9	Arch Web Height (Knuckle)	Normal	1.00	2%
RV10	Girder Height	Normal	1.00	2%
RV11	Girder Flange Width	Normal	1.00	2%
RV12	Girder Flange Width (Knuckle)	Normal	1.00	2%
RV13	Concrete Deck Compressive Strength	Normal	1.20	15%
RV14	Reinforcement Yield Strength	Normal	1.10	10%

Reliability Index of Typical Limit States

Reliability indexes were calculated for the tied-arch bridge by investigating 18 hanger removal cases for the selected three limit states. Reliability indexes for the limit states of hanger yield, arch yield and girder yield are shown in Figure 188, Figure 189, and Figure 190, respectively.

Hanger Yield Limit State

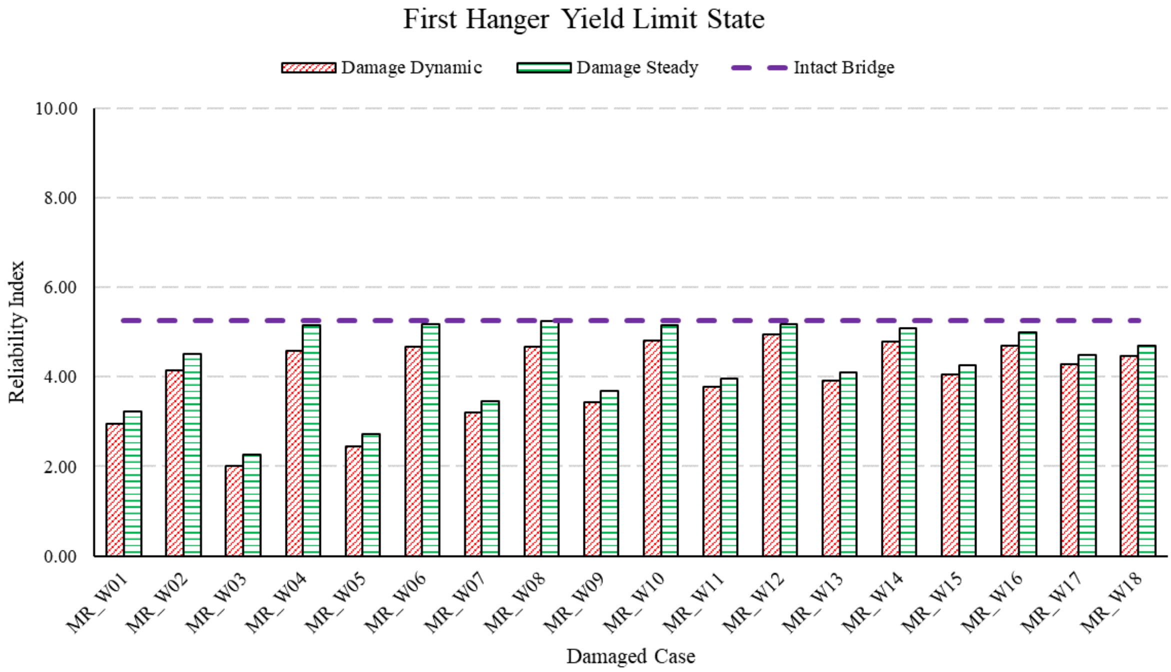

Source: FHWA.

Figure 188. Graph. Reliability index for hanger yield limit state under single hanger loss.

The reliability indexes for the hanger yield limit state for the bridge in the intact state and the damaged states due to sudden loss of a single hanger are shown in Figure 188. For the intact bridge, the reliability index for this limit state (Intact Bridge in Figure 188) is 5.26. Due to single hanger loss, the reliability indexes decrease. During the dynamic response due to sudden hanger removal, the reliability indexes (Damage Dynamic in Figure 188) range from 2.00 to 4.94. The minimum value of the reliability indexes occurs in the case of sudden loss of single hanger W.03. This indicates that the loss of this hanger is the most critical case that could result in another hanger reaching its yield strength.

The bridge reached a new equilibrium state after the dynamic effects due to sudden hanger removal were damped out. In the new steady-state, the reliability indexes (Damage Steady in Figure 188) range from 2.26 to 5.25. The minimum value of the reliability indexes occurs when hanger W.03 is lost.

Arch Yield Limit State

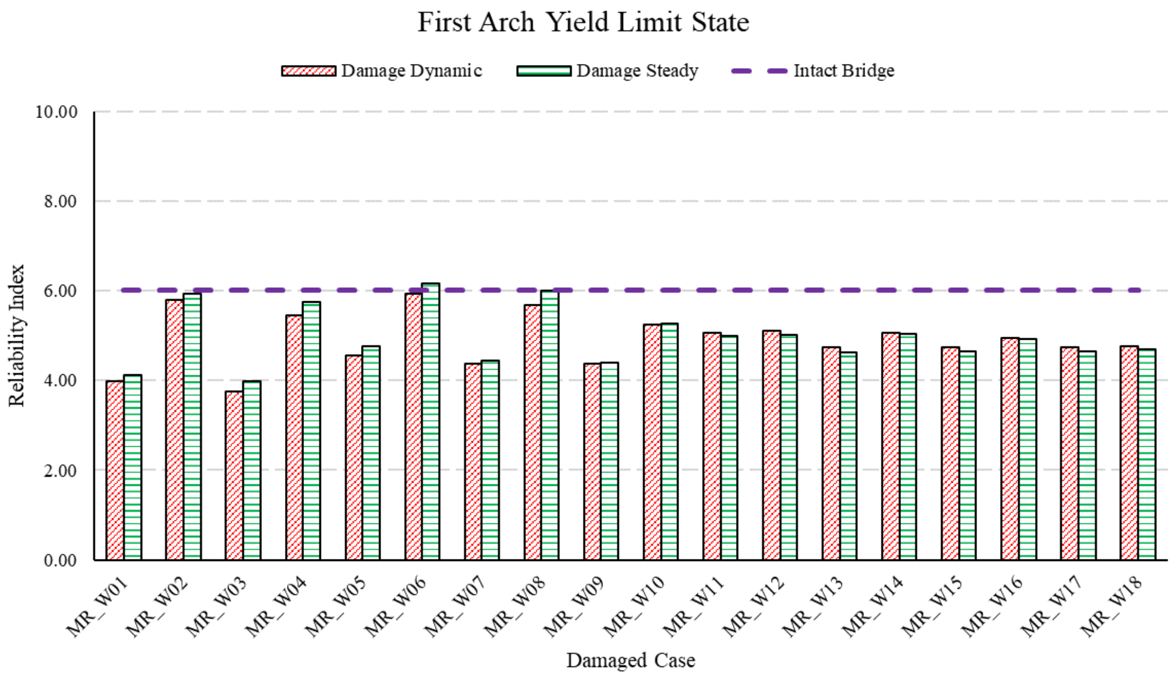

Source: FHWA.

Figure 189. Graph. Reliability index for arch yield limit state under single hanger loss.

The reliability indexes for the arch yield limit state for the bridge in the intact state and the damaged states are shown in Figure 189. For the intact bridge, the reliability index for this limit state (Intact Bridge in Figure 189) is 6.02. Due to sudden loss of a single hanger, the reliability indexes decrease. In the dynamic response stage, the reliability indexes (Damage Dynamic in Figure 189) range from 3.75 to 5.93. The minimum value of the reliability index occurs for the case of sudden loss of hanger W.03. This is the most critical case of hanger removal for the arch yield limit state. It should be noted that this hanger is also the most critical for the hanger yield limit state.

The bridge reached a new equilibrium state after the dynamic effect due to sudden loss of a hanger was damped out. In the new steady-state, the reliability indexes (Damage Steady in Figure 189) range from 3.97 to 6.16. The minimum value of the reliability index occurs for the sudden loss of hanger W.03.

Girder Yield Limit State

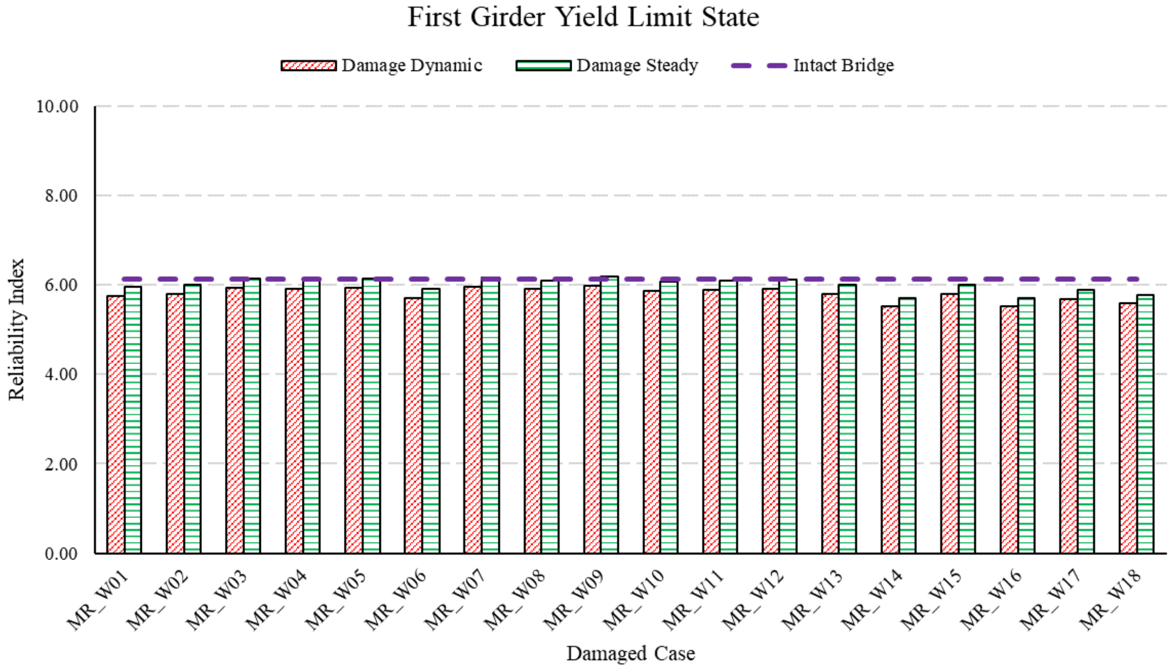

Source: FHWA.

Figure 190. Graph. Reliability index for girder yield limit state under single hanger loss.

The reliability indexes for the girder yield limit state for the bridge in the intact state and the damaged states due to single hanger loss are shown in Figure 190. For the intact bridge, the reliability index for this limit state (Intact Bridge in Figure 190) is 6.13. Due to sudden loss of a single hanger, the reliability indexes decrease. During the dynamic response due to sudden loss of a hanger, the reliability indexes (Damage Dynamic in Figure 190) range from 5.51 to 5.98. Since the tied-arch bridge has cross hangers, loss of one hanger did not significantly affect the reliability index for the girder yield limit state. The bridge reached a new equilibrium state after the dynamic effect due to sudden hanger removal was damped out. In the new steady-state, the reliability indexes (Damage Steady in Figure 190) range from 5.70 to 6.13.

Robustness Index against Single Hanger Loss

For a specified limit state, the robustness indexes were calculated based on Equation (24) in Chapter 6 using the reliability indexes computed for the intact and damaged conditions.

Hanger Yield Limit State

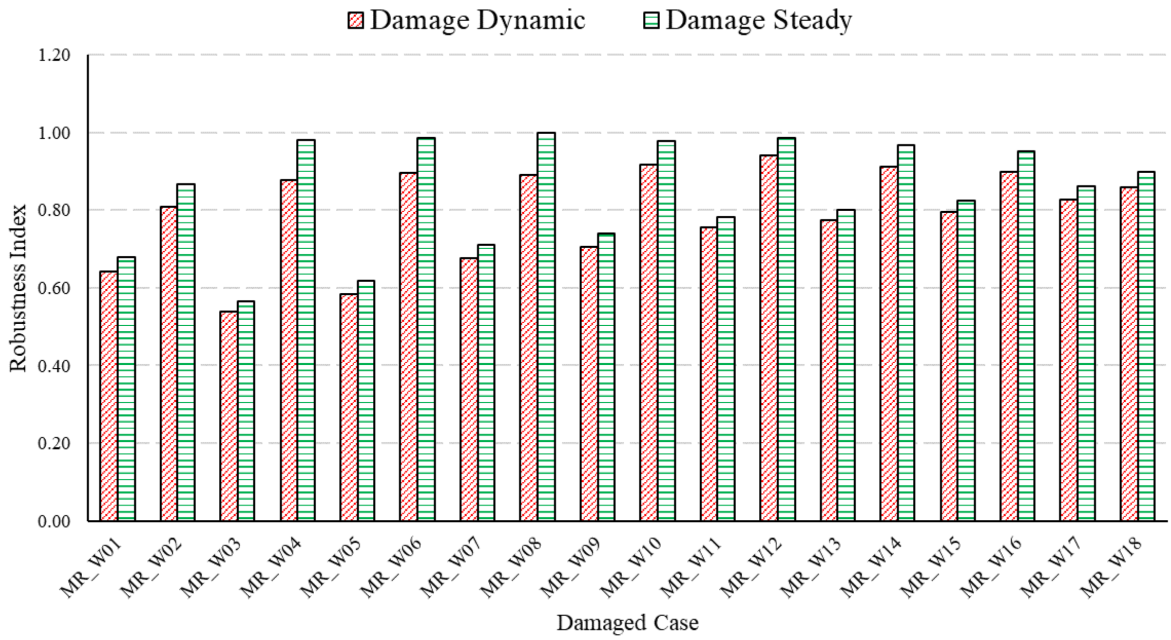

Source: FHWA

Figure 191. Graph. Robustness index for hanger yield limit state against single hanger loss.

The robustness indexes for the hanger yield limit state under dead load and live load due to single hanger loss are shown in Figure 191. It is observed that the robustness indexes of the hanger yield limit state during the dynamic phase due to single hanger loss (Damage Dynamic) range from 0.54 to 0.94, whereas those in the steady state (Damage Steady) range from 0.57 to 1.00. The most critical hanger loss case for the hanger yield limit state is the loss of hanger W.03.

Arch Yield Limit State

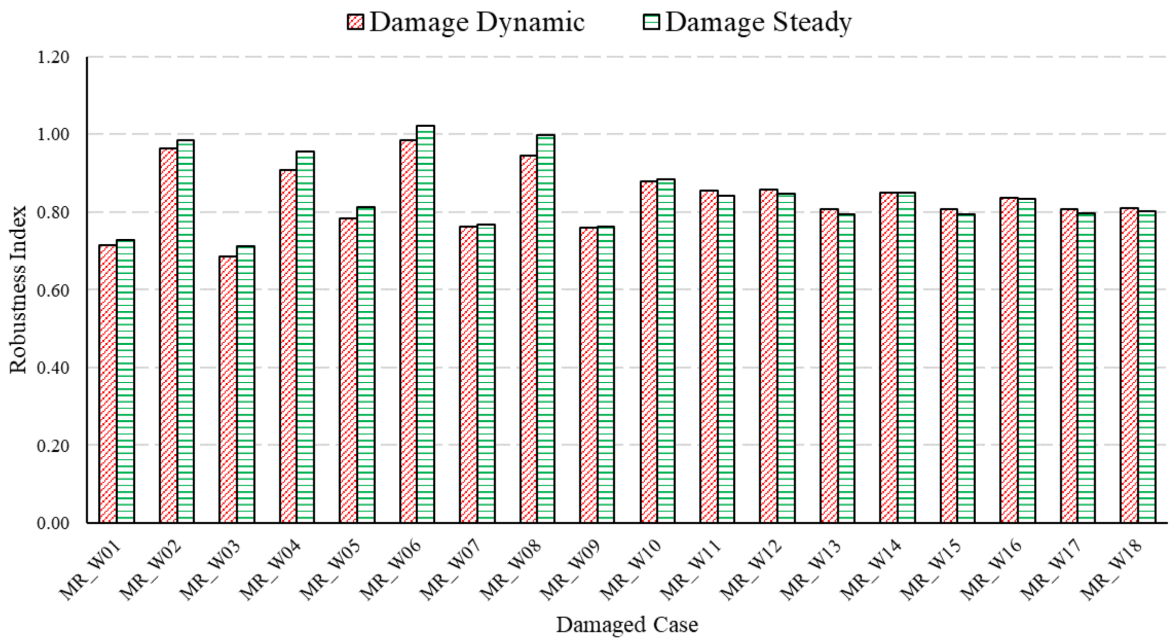

Source: FHWA.

Figure 192. Graph. Robustness index for arch yield limit state against single hanger loss.

The robustness indexes for the arch yield limit state for the bridge under dead load and live load due to single hanger loss are shown in Figure 192. It is observed that the robustness indexes during the dynamic phase due to single hanger loss (Damage Dynamic) range from 0.66 to 0.99, whereas they range from 0.71 to 1.00 in the steady state (Damage Steady).

Girder Yield Limit State

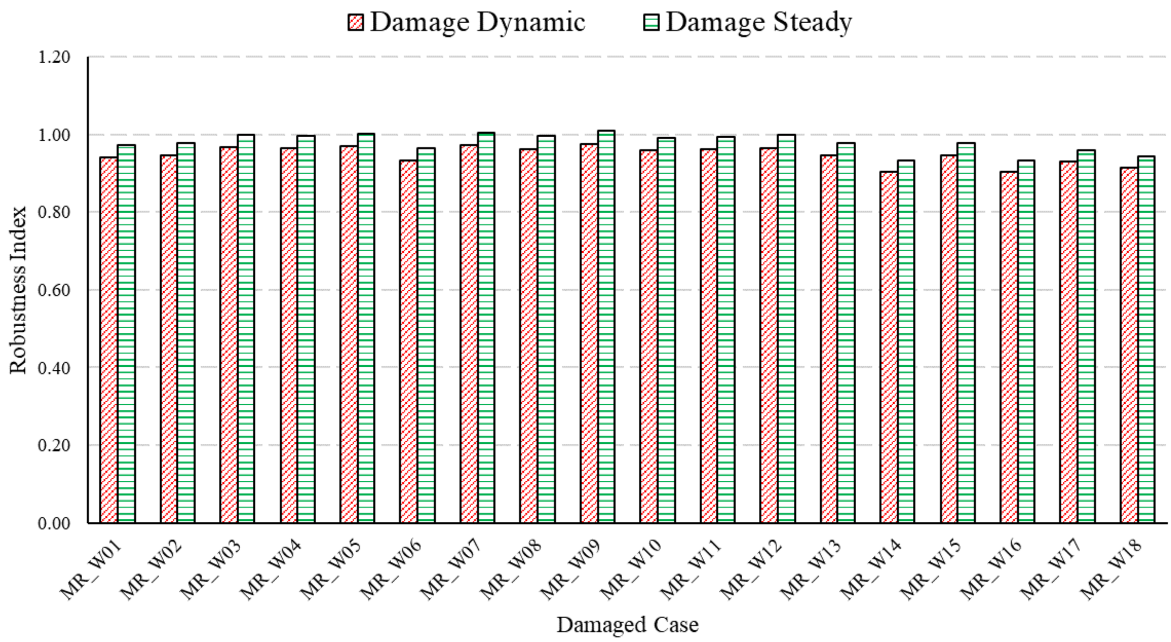

Source: FHWA.

Figure 193. Graph. Robustness index for girder yield limit state against single hanger loss.

The robustness indexes for the girder yield limit state for the bridge under dead load and live load due to single hanger loss are shown in Figure 193. It is observed that the robustness indexes during the dynamic phase due to single hanger loss (Damage Dynamic) range from 0.90 to 0.98, whereas they during the steady state (Damage Steady) range from 0.93 to 1.00.

ROBUSTNESS OF THE SUSPENSION BRIDGE

In this section, both reliability and robustness indexes were calculated for the suspension bridge. Two limit states-cable yield and suspender yield, were investigated.

Random Variables in the Suspension Bridge

Randomness related to the load, section properties and material properties were considered as shown in Table 35. Similar to the other two bridges, it was assumed that all cross-sections had fully correlated material properties.

Table 35. Random variables in the suspension bridge.

RV No.	Random Variables	Distribution	Bias Factor	COV
RV1	Dead Load	Normal	1.00	10%
RV2	Live Load	Normal	0.90	20%
RV3	Cross-section Area of Main Cable	Normal	1.05	5%
RV4	Yield Stress of Main Cable	Normal	1.00	10%
RV5	Cross-section Area of Suspender	Normal	1.10	5%
RV6	Yield Stress of Suspender	Normal	1.00	10%
RV7	Yield Stress of Stiffening Truss	Normal	1.15	10%
RV8	Yield Stress of Tower	Normal	1.20	10%
RV9	Friction coefficient	Normal	1.20	25%

Reliability Index of Typical Limit States

The reliability indexes for the suspension bridge were calculated for 35 cases of sudden suspender removal for the two selected limit states and plots of the reliability indexes are shown in Figure 194 and Figure 195.

Main Cable Yield Limit State

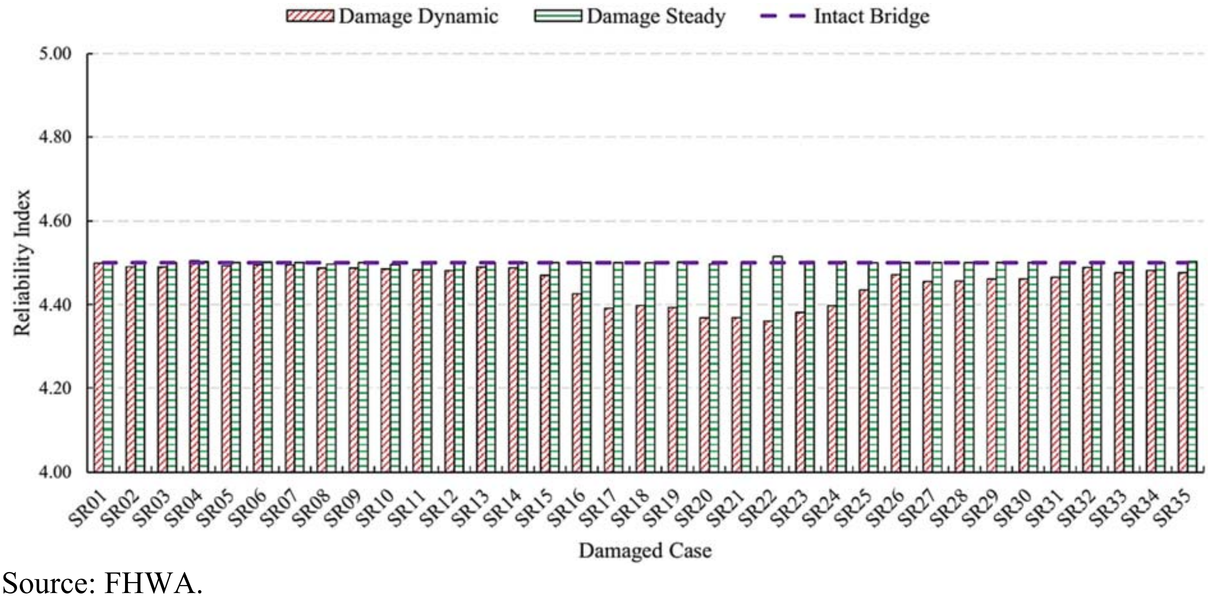

Source: FHWA.

Figure 194. Graph. Reliability index for main cable yield limit state under single suspender loss.

The reliability indexes for the main cable yield limit state for the bridge in intact and damaged conditions due to a sudden loss of a single suspender are shown in Figure 194. The reliability index for the main cable yield limit state of the intact bridge under load combination COMB1 (i.e., dead load and live load pattern LL1) is 4.5. The reliability indexes of the main cable yield limit state decrease during the dynamic response due to sudden loss of a single suspender. However, they return back to the value of the intact bridge once the bridge reaches its new equilibrium state after the dynamic effects are damped out. During the dynamic response phase, the reliability indexes (Damage Dynamic in Figure 194) range from 4.36 to 4.50. For the cases with a suspender removal in the side span, the reliability indexes are close to 4.5. For the cases with a sudden suspender removal close to the bridge tower, the reliability indexes are relatively low. The minimum value of the reliability index occurs in case SR22, i.e., the loss of suspender 22 is the most critical in causing the main cable to reach its yield strength under COMB1.

Suspender Yield Limit State

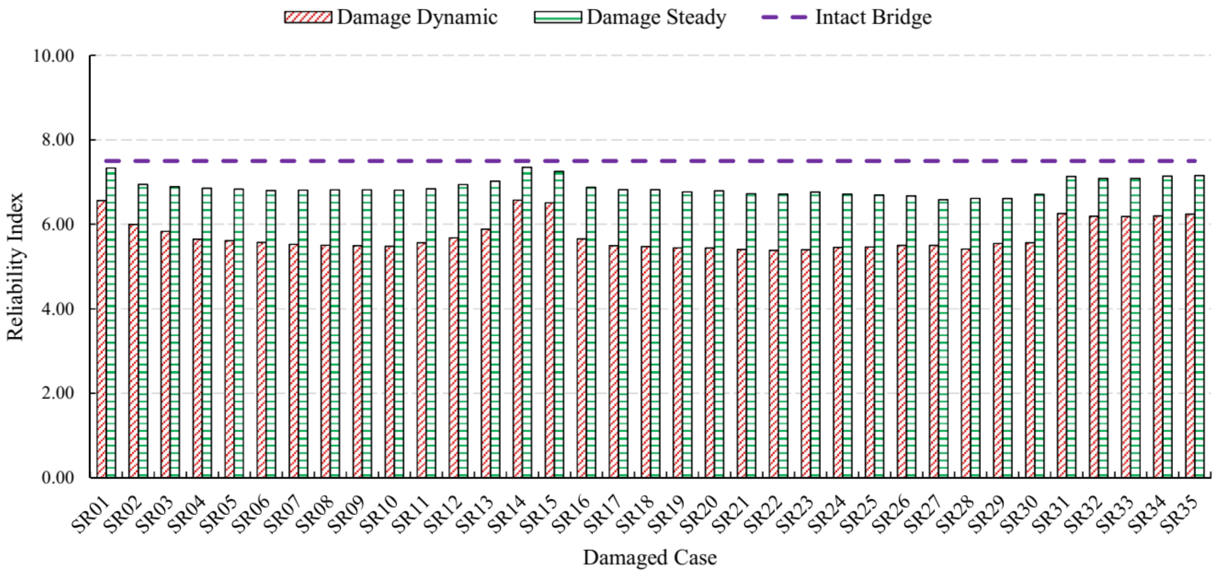

Source: FHWA.

Figure 195. Graph. Reliability index for suspender yield limit state under single suspender loss.

The reliability indexes for the suspender yield limit state for the bridge in intact and damaged conditions due to a sudden single suspender loss are shown in Figure 195. For the intact bridge under COMB1, the reliability index for this limit state is 7.50. It generally decreases because of a sudden single suspender loss. During the dynamic response because of sudden suspender loss, the reliability indexes (Damage Dynamic) range from 5.38 to 6.57. Suspenders in the bridge are categorized into three groups when calculating the reliability indexes of suspender yield. The 1st group is close to the support, including suspenders 01, 14, and 15. The reliability indexes are the largest one with a value around 6.57 in cases of loss of these suspenders, since the forces carried by these suspenders were transferred to the nearest support after the loss of any of these suspenders. The 2nd group consists of five suspenders in the center of the main span, i.e., suspenders 31 to 35. As discussed in Chapter 3, two types of suspenders were used in the suspension bridge. Eleven type-II suspenders in the center of main span have a larger cross section. These suspenders are stronger and loss of their adjacent suspenders would have lower probability of causing yielding of these suspenders. Sudden loss of any of these five suspenders results in the reliability indexes around 6.2 for the suspender yield limit state. The 3rd group of suspenders has relatively lower reliability indexes, with values ranging from 5.38 to 6.0. The minimum value of the reliability index occurs in case SR22, i.e., sudden loss of suspender 22. It indicates that losing suspender 22 is the most critical case that may result in another suspender reaching its yield strength. The bridge reached a new equilibrium state after the dynamic effect due to sudden loss of a single suspender was damped out. In the new steady-state, the reliability indexes (Damage Steady) range from 6.58 to 7.35, specifically, around 7.3 for the 1st group of suspenders, around 7.1 for the 2nd group, and 6.58 to 6.95 for the 3rd group.

Robustness Index against Single Hanger Loss

For a specified limit state, the robustness indexes were calculated based on Equation (24) in Chapter 6 and the reliability indexes for the bridge in both intact and damaged conditions. The robustness indexes for the two selected limit states (i.e., main cable yield and suspender yield) for the bridge under COMB1 were calculated and are presented in the following.

Main Cable Yield Limit State

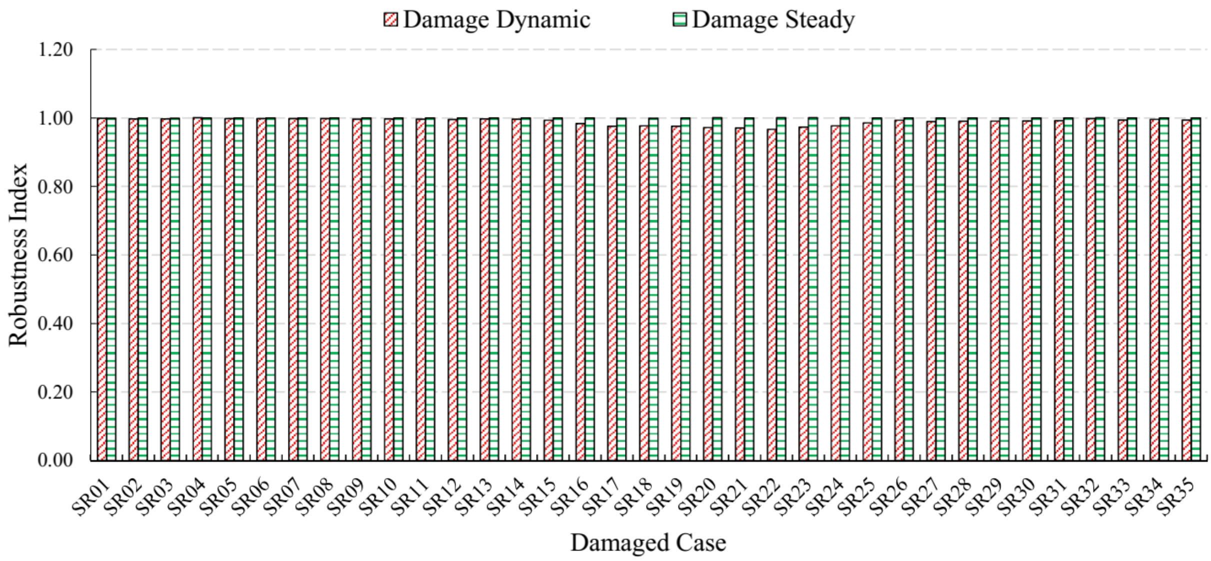

Source: FHWA.

Figure 196. Graph. Robustness index for main cable yield limit state against single suspender loss.

The robustness indexes for the main cable yield limit state for the bridge under COMB1 due to single cable loss range from 0.97 to 1.00, as shown in Figure 196. It is noted that robustness indexes of the bridge in the damaged steady-state after sudden loss of a suspender are around 1.00 for all cases of single suspender removal. This shows that the bridge is robust against main cable yielding due to a single suspender loss. Under COMB1, the most critical suspender loss case for the main cable yield limit state is case SR22, i.e., the loss of suspender 22.

Suspender Yield Limit State

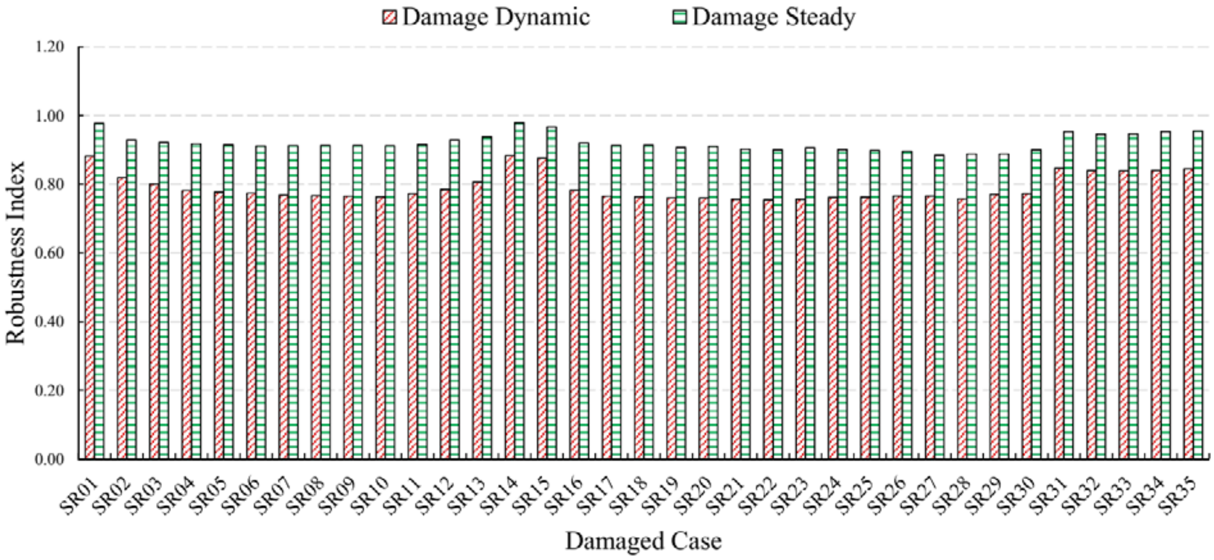

Source: FHWA

Figure 197. Graph. Robustness index for suspender yield limit state against single suspender loss.

The robustness indexes for the suspender yield limit state for the bridge under COMB1 due to a single suspender loss are shown in Figure 197. It is observed that the robustness indexes during the dynamic phase range from 0.75 to 0.88, whereas they range from 0.88 to 0.98 during the steady-state phase. The most critical suspender loss case for this limit state is case SR22 too.

APPLICATION OF NCHRP REDUNDANCY METHOD FOR THE THREE LONG-SPAN BRIDGES

Application in the Cable-Stayed Bridge

Based on the pushdown analysis results of the intact bridge, the bridge reached its first member failure limit state (first cable yield) at LF_1 of 7.95 and reached its ultimate limit state (cable rupture and bridge collapse) at LF_u of 9.89. Based on the pushdown analysis results of the damaged bridge with different cable loss cases, the most critical case for the ultimate limit state was loss of Cable S.26 with LF_d of 8.02.

Then, the redundancy ratios per the NCHRP approach are,

$$R_u = \frac{LF_u}{LF_1} = \frac{9.89}{7.95} = 1.24 < 1.30$$

$$R_d = \frac{LF_d}{LF_1} = \frac{8.02}{7.95} = 1.01 > 0.50$$

The calculated redundancy ratio R_u is less than the required value of 1.30, while redundancy ratio R_d is larger than the required value of 0.50. However, is the bridge really deficient in redundancy?

As observed in previous chapters, the cable-stayed bridge had a large reserve capacity in the presence of cable loss and even multiple cable loss events.

Application in the Tied-Arch Bridge

Based on the pushdown analysis results of the intact bridge, the bridge reached its first member failure limit state (first hanger yield) at LF_1 of 11.95 and reached its ultimate limit state (hanger rupture and bridge collapse) at LF_u of 15.01. Based on the pushdown analysis results of the damaged bridge with different cable loss cases, the most critical case for ultimate limit state was loss of Hanger W.03 with LF_d of 11.29.

Then, the redundancy ratios per the NCHRP approach are,

$$R_u = \frac{LF_u}{LF_1} = \frac{15.01}{11.95} = 1.26 < 1.30$$

$$R_d = \frac{LF_d}{LF_1} = \frac{11.29}{11.95} = 0.94 > 0.50$$

The calculated redundancy ratio R_u is less than the required value of 1.30, while redundancy ratio R_d is larger than the required value of 0.50. As noted for the cable-stayed bridge, these numbers are misleading because simulations results indicated that the bridge had extensive reserve capacity in the presence of hanger loss.

Application in the Suspension Bridge

Based on the pushdown analysis results of the intact bridge, the bridge reached its first member failure limit state (main cable yield) at LF_1 of 8.25 and reached its ultimate limit state (cable rupture and bridge collapse) at LF_u of 22.04. Based on the pushdown analysis results of the damaged bridge with different cable loss cases, the most critical case for ultimate limit state was loss of Suspender 22 with LF_d of 12.96.

Then, the redundancy ratios per the NCHRP approach are,

$$R_u = \frac{LF_u}{LF_1} = \frac{22.04}{8.25} = 2.67 > 1.30$$

$$R_d = \frac{LF_d}{LF_1} = \frac{12.96}{8.25} = 1.57 > 0.50$$

The calculated redundancy ratio R_u is larger than the required value of 1.30, and the redundancy ratio R_d is larger than the required value of 0.50 too.

Clearly, as demonstrated for the three long-span bridges in this work, the NCHRP method provides overly conservative results about the redundancy and robustness of long span bridges. As noted earlier, this is primarily due to the fact that the method was developed for and calibrated against shorter span bridges.

SUMMARY

In this chapter, robustness indexes of the three long-span bridges were investigated using the proposed robustness method. For the sake of comparison, application of the NCHRP redundancy method in these bridges were also presented. The highlight of this chapter includes:

- Based on the identified typical limit states in Chapter 5 and proposed generalized first-order reliability method, reliability indexes of these limit states were calculated for both intact bridge and the bridge with single cable loss damage. For the cable-stayed bridge, two limit states-first cable yield and first girder yield, were analyzed. For the tied-arch bridge, three limit states-first hanger yield, first arch member and first girder member yield, were analyzed. For the suspension bridge, two limit states-main cable yield and suspender yield, were analyzed. Uncertainties such as the applied load, section properties, and material properties were considered. Based on the calculated reliability indexes for both intact bridge and damaged bridge, robustness indexes of the identified limit states were calculated for each bridge.

- For the cable-stayed bridge, the robustness indexes of the cable yield limit state during the dynamic phase due to sudden loss of a single cable range from 0.75 to 0.98, whereas the robustness indexes in the steady state after sudden cable loss range from 0.83 to 1.01, the most critical cable loss case for the cable yield limit state is the sudden loss of cables S.22 and S.23. The robustness indexes of the girder yield limit state during the dynamic phase due to single cable loss range from 0.62 to 0.92, whereas the robustness indexes in the steady state range from 0.74 to 0.97. The most critical cases for the girder yield limit state are the loss of cables S.31 and S.32.
- For the tied-arch bridge, the robustness indexes of the hanger yield limit state during the dynamic phase due to single hanger loss range from 0.54 to 0.94, whereas those in the steady state range from 0.57 to 1.00. The most critical hanger loss case for the hanger yield limit state is the loss of hanger W.03. The robustness indexes of the arch yield limit state during the dynamic phase due to single hanger loss range from 0.66 to 0.99, whereas they range from 0.71 to 1.00 in the steady state. The robustness indexes of the girder yield limit state during the dynamic phase due to single hanger loss range from 0.90 to 0.98, whereas those during the steady state range from 0.93 to 1.00.
- For the suspension bridge, the robustness indexes for the main cable yield limit state due to single cable loss range from 0.97 to 1.00, the robustness indexes of the bridge in the steady state after sudden loss of a single suspender are around 1.00. The robustness indexes of the suspender yield limit state during the dynamic phase range from 0.75 to 0.88, whereas they range from 0.88 to 0.98 during the steady state. The most critical suspender loss case for the suspender yield limit state is observed to be the loss of suspender 22.
- For comparison purposes, the NCHRP redundancy method was also applied to the three case study bridges. For the cable-stayed bridge and the tied-arch bridge, the calculated redundancy ratios R_u are less than the required value of 1.30, while the redundancy ratios R_d - computed by considering the most critical member loss case - are larger than the required value of 0.50.

CHAPTER 8. CONCLUSIONS, LIMITATIONS AND FUTURE WORK

SUMMARY AND CONCLUSIONS

Based on three example long-span cable-supported bridges: the Cooper River Bridge (cable-stayed bridge), the new Whittier Bridge (suspended tied-arch bridge) and the 2nd structure of the Delaware Memorial Bridge (suspension bridge), a comprehensive investigation has been conducted on the robustness of long-span cable supported-bridges, especially when these bridges are subjected to sudden loss of one or more of their critical members (i.e., stay cables of cable-stayed bridges, hangers of suspended tied-arch bridges and suspenders of suspension bridges). The work in this research presents detailed information on: (1) development of finite element models of the three example bridges, (2) investigation of the bridges' behavior under sudden loss of single or multiple cables, (3) investigation of the bridges' behaviors under over-loading through pushdown analyses, (4) a new structural robustness evaluation method and a robustness index which are applicable for long-span bridges, and (5) investigation on the robustness of the three example bridges using the proposed robustness evaluation method. The key highlights and conclusions of this research are as follows:

- Detailed implicit and explicit finite element models were developed for each of the three long-span cable-supported bridges. All explicit models were developed in LS-DYNA® and the implicit models were developed in other FEM platforms (i.e., Midas Civil, SAP 2000® and ANSYS® Mechanical). Comparisons were made between results from both explicit and implicit models for each bridge through dead load analysis and modal analysis. The results from the explicit and implicit models agreed well with each other and these results were also consistent with the results from implicit models provided by HNTB. In addition, the nonlinear material behaviors were included and validated with test results from the literatures and analytical calculations. The results from the explicit models were able to capture the behavior of all bridges very well.
- The behavior of the bridges under sudden loss of a single cable (i.e., stay cable / hanger / suspender) was investigated thoroughly by using the explicit LS-DYNA models through member removal analyses. Various scenarios of cable loss were simulated with the several critical live load distribution patterns. The results show that structural members in the vicinity of cable loss, especially the adjacent cables, were primarily affected to a certain degree due to the dynamic effect of sudden loss of cable. The demand capacity ratios (DCRs) of cables of damaged bridge show that all the cables and other main steel structural members were still in their elastic ranges. Therefore, the effects on the overall performances of the three bridges due to loss of a single cable were very limited. For the cable-stayed bridge, this could be attributed to the fact that the loss of a single cable was already considered during design as per the recommendation in PTI (2001). For the tied-arch bridge, this could be attributed to design of the bridge as a network arch bridge with more hangers adopted than regular tied-arch bridges with evenly distributed vertical hangers. For the suspension bridge, this could be attributed to large safety factors (i.e., low DCRs around 0.2) of the suspenders.
- The behavior of the three bridges under multiple cable loss was also investigated under the most critical live load distributions. Specifically, the cables were removed one by one following the approach similar to that for single cable loss. With the loss of several cables

sequentially, the bridges could still carry the design live loads, in spite of large deflections reaching the functional limit state. With the loss of yet more cables, the deflections increased significantly because some structural members reached their yield strengths. With the loss of even more cables, progressive collapse of the entire bridge, similar to un-zipping collapse, was triggered in the cable-stayed bridge and the suspension bridge. Progressive collapse of the tied-arch bridge did not occur with the loss of many more cables, because the bridge was already damaged severely because of yielding of the main arch.

- The behavior of the three bridges under over-loading was investigated thoroughly in both the intact and damaged states with various cable loss scenarios through pushdown analyses. Typical limit states and failure modes of each type of bridges under over-loading were identified. The results show that: (1) all three bridges have very high capacity for the design live loads, (2) the overall performances of bridges were affected negatively by cable loss and the effects varied with the location of cable loss and live load distribution patterns, and (3) even with such adverse effects, the performances of damaged bridge were not reduced significantly.
- The current redundancy evaluation method proposed in the NCHRP Report 776 was developed based on short-to-medium span highway bridges and was found not appropriate for long-span bridges. Therefore, a new structural robustness evaluation method was proposed, which is applicable for both short-to-medium span and long-span bridges. This method was validated using a short-span example bridge in the NCHRP Report 776. A robustness index was also proposed to explicitly measure the residual safety of damaged bridge.
- Using the proposed robustness evaluation method, the robustness of the three long-span cable-supported bridges was evaluated for the typical limit states identified from pushdown analyses. The results show that: (1) the effect of various scenarios of single cable loss on each bridge can be captured explicitly, demonstrating the applicability of the robustness evaluation method and the robustness index proposed, especially for long-span bridges, and (2) in spite of the adverse effect of single cable loss, there was no significant reduction on the reliability and robustness in all three long-span bridges, i.e., they are very robust against single cable loss scenarios.

LIMITATIONS AND FUTURE WORK

Some limitations of this research and possible suggestions for future work are noted in the following.

- To evaluate of the reliability and robustness of long-span bridges comprehensively, all load combinations recommended in design manuals and guidelines should be examined. Although several critical live load distributions were included, they were all related to the design traffic load. Other load effects such as wind load, temperature changes, etc., and their combination were not considered. Therefore, a comprehensive examination on load effects and their combinations is highly recommended. For an existing bridge, finite element models of the bridge should be based on as-built design drawings and should be calibrated using monitoring data, if available.
- This research shows that the current long-span cable-supported bridges were designed with high reliability and they are robust against various single cable loss scenarios. Although

multiple cable loss scenarios were also investigated, more detailed simulation scenarios can be considered. For example, some simple assumptions were adopted in this research, i.e., the cables were removed one by one in a scheduled sequence, and the cable loss occurred only when the bridges reached their steady-state from the previous cable loss. Random cable loss for the bridge in transit state from the previous cable loss, or multiple simultaneous cable loss should also be investigated.

- The structural robustness method and robustness index proposed were tentatively applied on the three example bridges selected in research. However, in order to propose an acceptable limit value of the robustness index for long-span bridges, they need to be extended to other types of long-span bridges.
- More research can be performed to develop a simplified deterministic method which can be used to evaluate the robustness index of bridges in design office, since the proposed approach is probabilistic and requires significant levels of computation, which may not be feasible for design offices.
- Further research is also needed for bridge load rating, inspection frequency and depth, and management activity decision making for long-span bridges with different robustness and redundancy. These results will be very useful for bridge operation and asset management.

ACKNOWLEDGMENTS

The authors sincerely acknowledge the review comments and feedback from the expert technical group members, Dr. Ayman Shama (Parsons), Dr. Zhiuhua Yi (New York City Department of Transportation), Dr. Degang Li (Stantec), Mr. Bill Moreau (Atane Consulting), Mr. Thomas Macioce (Pennsylvania Department of Transportation), Mr. Alexander Bardow (Massachusetts Department of Transportation), Mr. Jia-Dzwan Shen (Federal Highway Administration), Mr. Arthur D'Andrea (Louisiana Department of Transportation), Mr. Theodor Zoli (HNTB), Mr. Terry Koon (South Carolina Department of Transportation) and Mr. Vincent Chiarito (Federal Highway Administration). The authors are also very grateful to the project manager, Mr. Waider Wong, for feedback and help with management of the project.

Finally, the authors acknowledge the partial support through grant from the University Transportation Research Center (UTRC). UTRC is the designated United State Department of Transportation University Transportation Center (UTC) for the federal region 2 and is housed at the City College of New York.

REFERENCES

AASHO. (1961). Standard Specifications for Highway Bridges, 8th Edition. American Association of State Highway Officials, Washington, D.C.

AASHTO. (2012). *AASHTO LRFD Bridge Design Specifications*, 6th Edition. American Association of State Highway and Transportation Officials, Washington, D.C.

AASHTO. (2014). *AASHTO LRFD Bridge Design Specifications*, 7th Edition. American Association of State Highway and Transportation Officials, Washington, D.C.

AASHTO. (2017). *AASHTO LRFD Bridge Design Specifications*, 8th Edition. American Association of State Highway and Transportation Officials, Washington, D.C.

AASHTO. (2018a). *Analysis and Identification of Fracture Critical Members and System Redundant Members*. American Association of State Highway and Transportation Officials, Washington, DC.

AASHTO. (2018b). *Guide Specifications for Internal Redundancy of Mechanically-Fastened Built-up Steel Members*. American Association of State Highway and Transportation Officials, Washington, DC.

AASHTO. (2020). *AASHTO LRFD Bridge Design Specifications*, 9th Edition. American Association of State Highway and Transportation Officials, Washington, D.C.

Adam, J.M., Parisi, F., Sagaseta, J. and Lu, X. (2018). "Research and practice on progressive collapse and robustness of building structures in the 21st century. " *Engineering Structures*, 173, 122-149.

Agrawal, A.K., Ettouney, M., Chen, X., Li, H. and Wang, H. (2020). *Steel Truss Retrofits to Provide Alternate Load Paths for Cut, Damaged, or Destroyed Members*. Report No. FHWA-HRT-20-055. Federal Highway Administration, Washington, D.C.

Alashker, Y., Li, H., and El-Tawil, S. (2011). "Approximations in progressive collapse modeling." *Journal of Structural Engineering*, 137(9): 914-924.

Allen, D.E. and Schriever, W.R. (1972). "Progressive collapse, abnormal loads, and building codes." In *Structural failures: Modes, causes, responsibilities* (pp. 21-47), ASCE.

ANSYS Inc. (2013). *ANSYS® Academic Research Mechanical*, Release 15.0. ANSYS Inc., Pittsburg, USA.

ASCE. (2013). "Minimum Design Loads for Buildings and Other Structures." *ASCE/SEI 7-10*, Reston, VA.

ASCE (2020). "ASCE/SEI 76-XX Standard for Mitigation of Disproportionate Collapse Potential in Buildings and Other Structures" (under development).

Barth, K., Michaelson, G. and Gonano, D. (2014). "Assessment of redundancy protocols for short-span steel truss bridges." *Bridge Structures*, 10(2, 3):105-114.

Beauchamp, J. C., Chan, M. Y. T. and Pion, R. H. (1984). "Repair and evaluation of a damaged truss bridge—Lewes, Yukon River." *Canadian Journal of Civil Engineering*, 11(3): 494-504.

Bhattacharya, B. (2021). "A reliability based measure of structural robustness for coherent systems. " *Structural Safety*, 89:102050.

Bi, K., Ren W.X., Cheng P.F., and Hao H. (2015). "Domino-type progressive collapse analysis of a multi-span simply-supported bridge: A case study. " *Engineering Structures*, 90:172-182.

Björnsson, Í. (2010). *Robust Design of Bridges: Robustness Analysis of Sjölundaviadukt Bridge*. MSc Thesis, Lund University, Division of Structural Engineering.

Blockley, D. (1992). *Engineering Safety*. McGraw-Hill, London.

Bojanowski, C., and M. Balcerzak. "Response of a large span stay cable bridge to blast loading." Proceedings of the 13th International LS-DYNA Users Conference, Dearborn, MI, USA. 2014.

Brett, C. and Lu, Y. (2013). "Assessment of robustness of structures: Current state of research." *Frontiers of Structural and Civil Engineering*, 7(4): 356-368.

Calvi, G. M., Moratti, M., O'Reilly, G. J., Scattarreggia, N., Monteiro, R., Malomo, D., Calvi, P. M. and Pinho, R. (2019). "Once upon a time in Italy: The tale of the Morandi Bridge." *Structural Engineering International*, 29(2): 198-217.

CEN. (2006). Eurocode 1: Actions on Structures. Part 1-7: General actions -Accidental actions. EN 1991-1-7. European Committee for Standardization, Brussels, Belgium.

CEN. (2004). Eurocode 2: Design of Concrete Structures. Part 1: General Rules and Rules for Buildings. EN 1992-1-1. European Committee for Standardization, Brussels, Belgium.

CEN. (2019). Eurocode — Basis of structural and geotechnical design. prEN 1990:2019. CEN/TC 250.

Cha, H., Lyrenmann, L., Connor, R. J. and Varma, A. H. (2014). "Experimental and numerical evaluation of the postfracture redundancy of a simple span truss bridge." *Journal of Bridge Engineering*, 19(11): 04014048.

Cho, H. N., Lim, J. K. and Choi, H. H. (2001). "Reliability-based fatigue failure analysis for causes assessment of a collapsed steel truss bridge." *Engineering Failure Analysis*, 8(4): 311-324.

Chopra, A. K. (2012). *Dynamics of Structures: Theory and Applications to Earthquake Engineering*. Pearson, Upper Saddle River, NJ.

CSA. (2014). *Canadian Highway Bridge Design Code* (CAN/CSA-S6-14). Canadian Standards Association, Toronto, Ontario, Canada.

Csagoly, P.F. and Jaeger, L.G. (1979). "Multi-load-path structures for highway bridges." *Transportation Research Record,* 711: 34–39, National Academy of Sciences, Washington, D.C.

CSI. (2019). *CSI Analysis Reference Manual for SAP2000®, ETABS®, SAFE® and CSiBridge®*. Computers and Structures, Inc., Berkeley, CA.

Das, R., PANDEY, S.A., MAHESH, M., Saini, P. and Anvesh, S. (2016). "Effect of dynamic unloading of cables in collapse progression through a cable stayed bridge." *Asian Journal of Civil Engineering (Building and Housing)*, 17(4): 397-416.

DelGrego, M.R., Culmo, M.P. and DeWolf, J.T. (2008). "Performance evaluation through field testing of century-old railroad truss bridge." *Journal of Bridge Engineering*, 13(2): 132-138.

Diggelmann, L.M., Connor, R.J., Sherman, R.J. and Beshah, F. (2013). *Evaluation of Member and Load-Path Redundancy on the US-421 Bridge over the Ohio River*. Report No. FHWA-HRT-13-104. Federal Highway Administration, Washington, D.C.

DOD. (2009). *Unified facilities criteria: Design of buildings to resist progressive collapse*. Report No. UFC 4-023-03. United States Department of Defense, Washington, D.C.

El-Tawil, S., Khandelwal, K., Kunnath, S. and Lew, H.S. (2007). "Macro models for progressive collapse analysis of steel moment frame buildings." In *Structural Engineering Research Frontiers*: 1-12.

Ellingwood, B. R. (2006). "Mitigating risk from abnormal loads and progressive collapse." *Journal of Performance of Constructed Facilities*, 20(4): 315-323.

Ellingwood, B.R. and Dusenberry, D.O. (2005). "Building design for abnormal loads and progressive collapse." *Computer-Aided Civil and Infrastructure Engineering*, 20(3): 194-205.

Ellingwood, B. , Smilowitz, R. , Dusenberry, D. , Duthinh, D. , Lew, H. and Carino, N. (2007). *Best Practices for Reducing the Potential tor Progressive Collapse in Buildings.* NIST Interagency/Internal Report (NISTIR) No. 7396. National Institute of Standards and Technology, Gaithersburg, MD.

Ernst, H. J. (1965). "Der E-Modal von Seilen unter Berücksichtigung des Durchhanges." *Der Bauingenieur*, 40(2): 52-55.

FHWA (2013). TechBrief: *Evaluation of Member and Load Path Redundancy on the US-421 Bridge over the Ohio River*. Report No. FHWA-HRT-13-105. Federal Highway Administration, Washington, D.C.

FHWA (2017). *Closure of I-276 Delaware River Bridge (PA Turnpike and NJ Turnpike)*. Event Report, January 20, 2017, FHWA Office of Bridges and Structures, Washington, D.C.

Fisher, J.W., Roberts, R. and Pense, A.W. (1977). "Evaluation of fracture of Lafayette Street bridge." *Journal of the Structural Division*, 103(7): 1339-1357.

Frangopol, D.M. and Curley, J.P. (1987). "Effects of damage and redundancy on structural reliability." *Journal of structural engineering*, 13(7): 1533-1549.

Ghosn, M. and Moses, F. (1998). *Redundancy in Highway Bridge Superstructures*. NCHRP Report No. 406. Transportation Research Board, Washington, D.C.

Ghosn, M., Yang, J., Beal, D. and Sivakumar, B. (2014). *Bridge System Safety and Redundancy*. NCHRP Report No. 776. Transportation Research Board, Washington, D.C.

Gimsing, N. J., & Georgakis, C. T. (2011). Cable supported bridges: Concept and design. John Wiley & Sons.

Gross, J. L. and McGuire, W. (1983). "Progressive collapse resistant design." *Journal of Structural Engineering*, 109(1): 1-15.

Grubb, M. A., Wilson, K. E., White, C. D. and Nickas, W. N. (2015). *Load And Resistance Factor Design (LRFD) for Highway Bridge Superstructures-Reference Manual*. Report No. FHWA-NHI-15-047. Federal Highway Administration, Washington, D.C.

GSA. (2003). *Progressive Collapse Analysis and Design Guidelines for New Federal Office Buildings and Major Modernization Projects.* General Services Administration, Washington, D.C.

Hallquist, J. O. (2006). *LS-DYNA Theory Manual*. Livermore software Technology Corporation, Livermore, CA.

Hartmann, J. and Weingroff, R. (2021). *Happy 50th Anniversary. National Bridge Inspection Standards.* https://www.fhwa.dot.gov/highwayhistory/national_bridge_inspection_standards.cfm

Hashemi, S. K., Bradford, M. A. and Valipour, H. R. (2016). "Dynamic response of cable-stayed bridge under blast load." *Engineering Structures*, 127: 719-736.

HNTB. (2016). *Private Correspondence*. HNTB, New York, NY.

IAEA. (2016). Safety of Nuclear Power Plants: Design. IAEA Safety Standards Series No. SSR-2/1 (Rev. 1). International Atomic Energy Agency, Vienna International Centre, Vienna, Austria.

Imai, K. and Frangopol, D.M. (2000). "Geometrically nonlinear finite element reliability analysis of structural systems. II: applications." *Computers & Structures*, 77(6): 693-709.

Izzuddin, B.A., Vlassis, A.G., Elghazouli, A.Y. and Nethercot, D.A. (2008). "Progressive collapse of multi-storey buildings due to sudden column loss—Part I: Simplified assessment framework." *Engineering structures*, 30(5): 1308-1318.

JSCE. (2007a). *Standard Specification for Concrete Structures -2007 "Design"*. Japan Society of Civil Engineers, Tokyo, Japan.

JSCE. (2007b). *Standard Specifications for Steel and Composite Structures*. 1st Editon. Japan Society of Civil Engineers, Tokyo, Japan.

Jelinek, J. and Bartlett, F.M. (2002). "Material properties of historical bridge steel." In *Proceedings of 30th Annual Conference of the Canadian Society of Civil Engineering*, Canadian Society for Civil Engineering, June 5-8, 2002, Montreal, Quebec, Canada.

Kawai, Y., Siringoringo, D. and Fujino, Y. (2014). "Failure analysis of the hanger clamps of the Kutai-Kartanegara Bridge from the fracture mechanics viewpoint." *Journal of JSCE*, 2(1): 1-6.

Kent, Dudley Charles, and Robert Park. (1971). "Flexural members with confined concrete." Journal of the Structural Division 97.7: 1969-1990.

Kokot, S. and Solomos, G. (2012). *Progressive Collapse Risk Analysis: Literature Survey, Relevant Construction Standards and Guidelines*. ISPRA: Joint Research Centre, European Commission, Ispra, Italy.

Lind, N. C. (1995). "A measure of vulnerability and damage tolerance." *Reliability Engineering & System Safety*, 48(1): 1-6.

Liu, S., Bartlett, F. M. and Zhou, W. (2013). "Alternative load paths in steel through-truss bridges: Case study." *Journal of Bridge Engineering*, 18(9): 920-928.

Liu, W. D., Neuenhoffer, A., Ghosn, M. and Moses, F. (2001). *Redundancy in Highway Bridge Substructures*. NCHRP Report No. 458, Transportation Research Board, Washington, D.C.

Lonetti, P. and Pascuzzo, A. (2014). "Vulnerability and failure analysis of hybrid cable-stayed suspension bridges subjected to damage mechanisms." *Engineering Failure Analysis,* 45: 470-495.

Lwin, M. (2012). *Clarification of Requirements for Fracture Critical Members*. FHWA Memorandum HIBT 10. Federal Highway Administration, Washington, D.C.

Mayrbaurl, R. M. and Camo, S. (2004). *Guidelines for Inspection and Strength Evaluation of Suspension Bridge Parallel-Wire Cables*. NCHRP Report No. 534. Transportation Research Board, Washington, D.C.

MIDAS IT. (2012). *MIDAS Civil 2012 User Manual*, MIDAS Information Technology, Seoul, Korea.

Nagavi, R.S. and Aktan, A.E. (2003). "Nonlinear behavior of heavy class steel truss bridges." *Journal Of Structural Engineering*, 129(8): 1113-1121.

Narita, N., and Yokoyama, K., (1991), "A summarized account of damping capacity and measures against wind action in cable-stayed bridges in Japan", Cable-stayed bridges: recent developments and their future (M. Ito, editor), Elsevier Science Publishers.

NTSB. (2008a). *Safety Recommendation (H08-1)*. National Transportation Safety Board, Washington, D.C.

NTSB. (2008b). *Structural Investigation Group Chairman Factual Report*. NTSB Report No. 08-015. National Transportation Safety Board, Washington, D.C.

NTSB. (2008c). *Data Report: State-by-State Bridge Counts*. Case No. HWY07MH024. National Transportation Safety Board, Washington, D.C.

NTSB. (2008d). *Collapse of I-35W Highway Bridge, Minneapolis, Minnesota, August 1, 2007*. NTSB/HAR-08/03. National Transportation Safety Board, Washington, D.C.

Pearson, C. and Delatte, N. (2005). "Ronan point apartment tower collapse and its effect on building codes." *Journal of Performance of Constructed Facilities*, 19(2): 172-177.

PTI. (2001). *Recommendations for Stay Cable Design, Testing and Installation*. 4th edition. Post-Tensioning Institute, Phoenix, AZ.

Qiu, W., Jiang, M. and Huang, C. (2014). "Parametric study on responses of a self-anchored suspension bridge to sudden breakage of a hanger." *The Scientific World Journal, 2014.*

Rackauskaite, Egle, Panagiotis Kotsovinos, and Guillermo Rein. (2017). "Model parameter sensitivity and benchmarking of the explicit dynamic solver of LS-DYNA for structural analysis in case of fire." Fire Safety Journal 90: 123-138.

Rodrigue, J.P. (2020). *The geography of transport systems*, Fifth Edition. Routledge.

Sanders Jr, W.W., Klaiber, F.W., Elleby, H.A. and Timm, L.W. (1975). *Ultimate Load Behavior of Full-Scale Highway Truss Bridges: Phase I. Ultimate Load Tests of the Hubby Bridge, Boone County*. Interim Report, Report No. ISU-ERL-AMES-75101. Iowa State Highway Commission, Ames, IA.

SETRA. (2002). *Cable Stays: Recommendations of French Interministerial Commission on Prestressing*. SETRA - Centre des Techniques des Ouvrages d'Art, France.

Sirisak, S. (1996). *Structural Integrity Evaluation of Truss Bridges*. PhD thesis. Vanderbilt University, Nashville, TN.

Starossek, U. (2009). *Progressive Collapse of Structures*. Thomas Telford, London.

Starossek, U., and Haberland, M. (2008). "Measures of structural robustness—Requirements and applications." In *Structures Congress 2008*: Crossing Borders (pp. 1-10).

Starossek, U., and Haberland, M. (2009). "Evaluating measures of structural robustness." In *Structures Congress 2009*: *Don't Mess with Structural Engineers: Expanding Our Role* (pp. 1-8).

Starossek, U., and Haberland, M. (2010). "Disproportionate collapse: terminology and procedures." *Journal of Performance of Constructed Facilities*, 24(6): 519-528.

Takena, K., Sasaki, M., Hata, K. and Hasegawa, K. (1992). "Slip behavior of cable against saddle in suspension bridges." *Journal of Structural Engineering*, 118(2):377-391.

TTSB. (2020). *Final Report on Nanfangao Sea-Crossing Bridge Collapse*. Report no. TTSB-HOR-20-11-001. Taiwan Transportation Safety Board. Taiwan.

Vasudevan, Anirudha Kadambi. Finite element analysis and experimental comparison of doubly reinforced concrete slabs subjected to blast loads. University of Missouri-Kansas City, 2012.

Vecchio, F.J. and Shim, W. (2004). "Experimental and analytical reexamination of classic concrete beam tests." *Journal of Structural Engineering*, 130(3): 460-469.

Williamson, E.B., Bayrak, O., Williams, G.D., Davis, C.E., Marchand, K.A., McKay, A.E., Kulicki, J.M. and Wassef, W. (2010). *Blast-Resistant Highway Bridges*: *Design and Detailing Guidelines*, NCHRP Report No. 645. Transportation Research Board, Washington, D.C.

Wolff, M. and Starossek, U. (2009). "Cable loss and progressive collapse in cable-stayed bridges." *Bridge Structures*, 5(1): 17-28.

Wolff, M. and Starossek, U. (2010). "Cable-loss analyses and collapse behavior of cable-stayed bridges. Bridge Maintenance, Safety, Management and Life-Cycle Optimization." In *Proceedings of the Fifth International IABMAS Conference*, Philadelphia, USA, 11-15 July 2010, CRC Press.

Xu, G. and Ellingwood, B.R. (2011). "An energy-based partial pushdown analysis procedure for assessment of disproportionate collapse potential." *Journal of Constructional Steel Research*, 67(3): 547-555.

Zoli, T.P. and Steinhouse, J. (2007). "Some considerations in the design of long span bridges against progressive collapse.", HNTB, New York, NY.

Appendix A: Matlab Code to Calculate Reliability Index

The following Matlab code shows the detail steps about how to calculate the reliability index of cable yield limit state during sudden cable loss in cable stayed bridge. The sentences starting with "%" are comments for the Matlab code.

```
clear;
clc;
format long;

%COV information for each random variable
cov = [0.10;0.20;0.05;0.02;0.10;0.02;0.10;0.15;0.15;0.02;0.02;0.02;0.15;0.10];
% Import Cable Area information
Cable_Area = importdata('H:\00CableStayedBridge\ReliabilityBeta\CableLimit\CableArea.csv');

%%Step1: Original structural response without random variable change
%Import data to MATLAB, for example, axial forces time history for cable elements.
fid_cable = importdata('F:\04Reliability\LL05_MR_Results\MR32\V_00\00Cable.csv');
Cable_Force=fid_cable.data;
Cable_Force(:,1)=[]; %Delete first column (time value)
n_row=size(Cable_Force,1);

%Each cable is modeled by 10 elements, get the information for each element for each cable
Cable_E01=Cable_Force(:,1:10:end);%1st Element for each cable
Cable_E02=Cable_Force(:,2:10:end);%2nd Element for each cable
Cable_E03=Cable_Force(:,3:10:end);
Cable_E04=Cable_Force(:,4:10:end);
Cable_E05=Cable_Force(:,5:10:end);
Cable_E06=Cable_Force(:,6:10:end);
Cable_E07=Cable_Force(:,7:10:end);
Cable_E08=Cable_Force(:,8:10:end);
Cable_E09=Cable_Force(:,9:10:end);
Cable_E10=Cable_Force(:,10:10:end);%10th Element for each cable

% Find the max force time history for each cable (Maximum value in 10 elements in each cable)
Cable_Max = max(cat(10, Cable_E01, Cable_E02, Cable_E03, Cable_E04, Cable_E05,
Cable_E06, Cable_E07, Cable_E08, Cable_E09, Cable_E10), [], 10);

Cable_Area_Matrix=repmat(Cable_Area,n_row,1);

Cable_ksf=Cable_Max./Cable_Area_Matrix; %calculate stress for each cable(unit:ksf)
Cable_ksi=Cable_ksf/144; %Convert stress unit to ksi
Cable_ksi(1:35,:)=[]; %Delete first 35 rows (Under DL and Live Load), start from MR
Cable_MR_ksi=max(Cable_ksi); %Maximum value in each cable during MR

[a00 b00]=max(Cable_MR_ksi); %Find Maximum cable stress and cable No.
```

```
%Based on limit state function, calculate the safety margin.
%243ksi is the cable yield stress, a00 is the maximum cable stress during cable removal
g00=243-a00;


%%Step2: With random variable V1(DL) change, repeat the previous process and calculate the safety margin
%Import data to MATLAB, for example, axial forces time history for cable elements.
fid_cable = importdata('F:\04Reliability\LL05_MR_Results\MR32\V_01\00Cable.csv');
Cable_Force=fid_cable.data;
Cable_Force(:,1)=[]; %Delete first column (time value)
n_row=size(Cable_Force,1);

%Each cable is modeled by 10 elements, get the information for each element for each cable
Cable_E01=Cable_Force(:,1:10:end);%1st Element for each cable
Cable_E02=Cable_Force(:,2:10:end);%2nd Element for each cable
Cable_E03=Cable_Force(:,3:10:end);
Cable_E04=Cable_Force(:,4:10:end);
Cable_E05=Cable_Force(:,5:10:end);
Cable_E06=Cable_Force(:,6:10:end);
Cable_E07=Cable_Force(:,7:10:end);
Cable_E08=Cable_Force(:,8:10:end);
Cable_E09=Cable_Force(:,9:10:end);
Cable_E10=Cable_Force(:,10:10:end);%10th Element for each cable

% Find the max force time history for each cable (Maximum value in 10 elements in each cable)
Cable_Max = max(cat(10, Cable_E01, Cable_E02, Cable_E03, Cable_E04, Cable_E05,
Cable_E06, Cable_E07, Cable_E08, Cable_E09, Cable_E10), [], 10);

Cable_Area_Matrix=repmat(Cable_Area,n_row,1);

Cable_ksf=Cable_Max./Cable_Area_Matrix; %calculate stress for each cable(unit:ksf)
Cable_ksi=Cable_ksf/144; %Convert stress unit to ksi
Cable_ksi(1:35,:)=[]; %Delete first 35 rows (Under DL and Live Load), start from MR
Cable_MR_ksi=max(Cable_ksi); %Maximum value in each cable during MR

[a01 b01]=max(Cable_MR_ksi); %Find Maximum cable stress and cable No.
%Based on limit state function, calculate the safety margin.
%243ksi is the cable yield stress, a01 is the maximum cable stress during cable removal
g01=243-a01;
%Calculate the partial differential coefficients
delta_v01= cov(1);
cof_g_v01=(g01-g00)/ delta_v01;
```

```
%%Step3: With random variable V2 (LL) change, repeat the previous process and calculate the safety margin
%Import data to MATLAB, for example, axial forces time history for cable elements.
fid_cable = importdata('F:\04Reliability\LL05_MR_Results\MR32\V_02\00Cable.csv');
Cable_Force=fid_cable.data;
Cable_Force(:,1)=[]; %Delete first column (time value)
n_row=size(Cable_Force,1);

%Each cable is modeled by 10 elements, get the information for each element for each cable
Cable_E01=Cable_Force(:,1:10:end);%1st Element for each cable
Cable_E02=Cable_Force(:,2:10:end);%2nd Element for each cable
Cable_E03=Cable_Force(:,3:10:end);
Cable_E04=Cable_Force(:,4:10:end);
Cable_E05=Cable_Force(:,5:10:end);
Cable_E06=Cable_Force(:,6:10:end);
Cable_E07=Cable_Force(:,7:10:end);
Cable_E08=Cable_Force(:,8:10:end);
Cable_E09=Cable_Force(:,9:10:end);
Cable_E10=Cable_Force(:,10:10:end);%10th Element for each cable

% Find the max force time history for each cable (Maximum value in 10 elements in each cable)
Cable_Max = max(cat(10, Cable_E01, Cable_E02, Cable_E03, Cable_E04, Cable_E05,
Cable_E06, Cable_E07, Cable_E08, Cable_E09, Cable_E10), [], 10);

Cable_Area_Matrix=repmat(Cable_Area,n_row,1);

Cable_ksf=Cable_Max./Cable_Area_Matrix; %calculate stress for each cable(unit:ksf)
Cable_ksi=Cable_ksf/144; %Convert stress unit to ksi
Cable_ksi(1:35,:)=[]; %Delete first 35 rows (Under DL and Live Load), start from MR
Cable_MR_ksi=max(Cable_ksi); %Maximum value in each cable during MR

[a02 b02]=max(Cable_MR_ksi); %Find Maximum cable stress and cable No.
%Based on limit state function, calculate the safety margin.
%243ksi is the cable yield stress, a02 is the maximum cable stress during cable removal
g02=243-a02;
%Calculate the partial differential coefficients
delta_v02= LF-1;% LF is the live load factor related to the cable yield limit state
cof_g_v02=(g02-g00)/ delta_v02;


%%Step4: For other random variables similar to V1, repeat the process introduced in step 2 and calculate the relate safety margins (g03, g04, …, g14) and partial differential coefficients (cof_g_v03, cof_g_v04, …, cof_g_v14).


%% Step5: Calculate the reliability index
```

```
% partial differential coefficients for each random variable
cof_g=[cof_g_v01;cof_g_v02;cof_g_v03;cof_g_v04;cof_g_v05;cof_g_v06;cof_g_v07;cof_g_v0
8;cof_g_v09;cof_g_v10;cof_g_v11;cof_g_v12;cof_g_v13;cof_g_v14];
% Bias factor for each random variable
Bias_Factor=[1.00;0.90;1.05;1.00;1.10;1.00;1.15;1.20;1.20;1.00;1.00;1.00;1.20;1.10];
%Calculate the first two moments of the limit state equation.
mu_g=g00+cof_g'*(Bias_Factor-1);
sigma_g=sqrt(sum((cof_g.*cov).^2));
%Calculate the reliability index
beta=mu_g/sigma_g;
```